PERFORMANCE OF TENSION PILES DURING SIMULATED GROUND SHAKING AND SEAQUAKES

A Report to

the Minerals Management Service of the

United States Department of the Interior

Herndon, Virginia

by

Pramod M. Rao, Cumaraswamy Vipulanandan and Michael W. O'Neill

Department of Civil and Environmental Engineering

University of Houston

Houston, Texas 77204-4791

August, 1997

Table of Contents

9 SUMMARY, CONCLUSIONS AND RECOMMENDATIONS

LIST OF TABLES

LIST OF FIGURES

xix

Chapter 1

INTRODUCTION

1.1 Research Problem

Tension piles are used to anchor offshore structures such as tension leg platforms and appear in terrestrial structures subjected to large permanent overturning moments [Poulos (1988)]. Although the piles for these structures are designed with a margin of safety, degradation in frictional capacity of the soil and overloading of the piles due to the feedback from the superstructure may cause them to deform excessively or undergo complete extraction. In the worst case scenario, this may affect the stability of the superstructure, rendering it unserviceable. The actual cause of such failures is not clear from observations of failure of piled structures during the 1985 Mexico City earthquake and the recent Kobe earthquake in Japan [Matso (1995)]. This research program is focussed on assessing the behavior of piles subjected to tensile loading during simulated seismic events in a laboratory.

In the event of an earthquake, seismic waves propagating through the soil deposits excite the structure. (See Fig. 1.1.) The presence of frequency components of the structure in the ground motion frequency distribution may cause magnification of the dynamic loads on the foundation piles as a result of structural feedback. In addition, the seismic waves may also induce pore water pressure changes in the soil, leading to liquefaction or cyclic mobility conditions. An equally important phenomenon that affects soil-pile interaction at an offshore site is the effect of the seismic motion of the seabed. There are reports that the seismic motion of the seabed produces waves that propagate through seawater to cause strong impacts on fixed bodies and sometimes damage to ships passing near sites of earthquakes. This phenomenon is the so-called "seaquake" [Ambraseys (1985)]. The loads imposed by seaquakes may be tremendously large; however, although much focus has

1
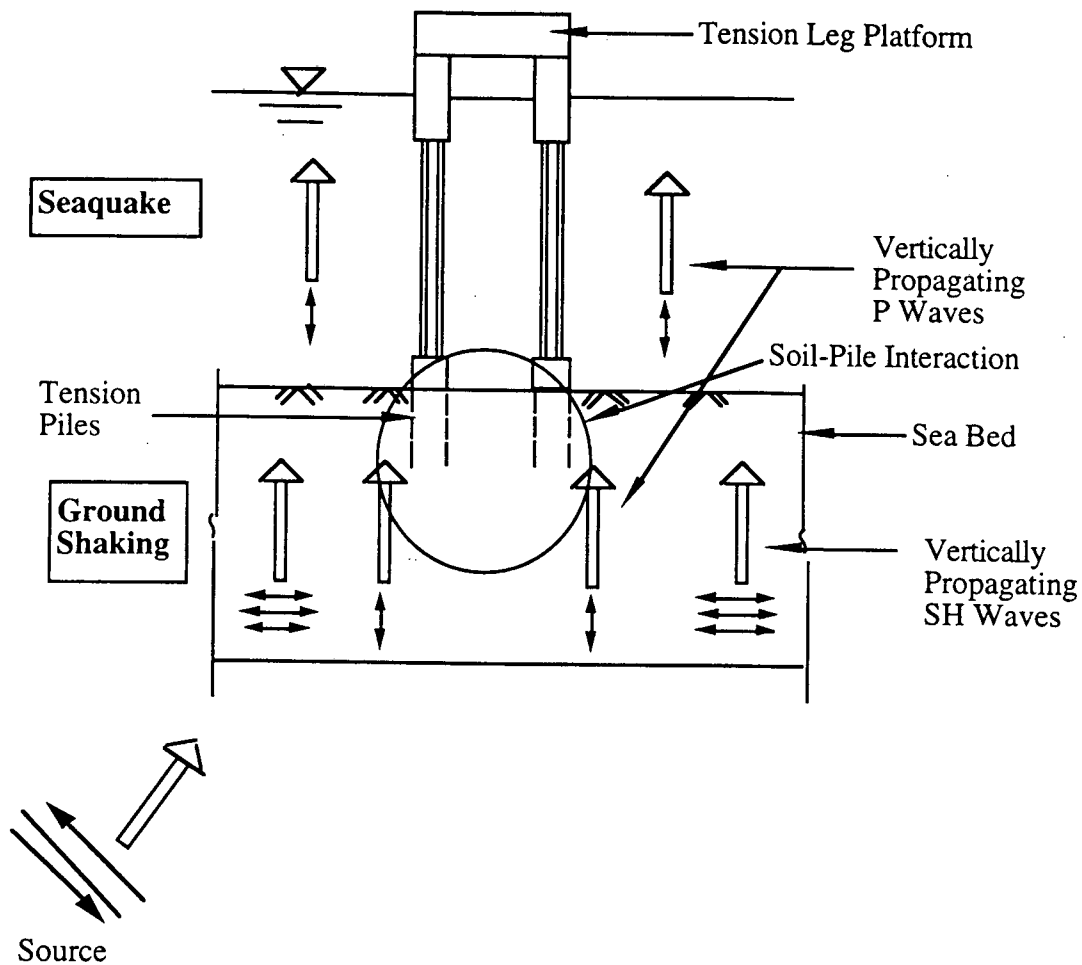
Fig. 1.1: Elements of Earthquake Response Phenomenon of Tension Piles

been given to the effects of seaquakes on marine structures, not much attention has been given to the changes induced by these seaquakes in the pore water pressure in soils underlying the sea due to the coupling of compression waves into the water.

It must be recognized that the response of a pile to soil-induced excitation depends on the characteristics of the ground motion (duration of shaking, magnitude of the earthquake, and the frequency content), dynamic characteristics of the pile and the superstructure that the pile supports [Tazoh et al. (1987)], the magnitude of the bias loading on the pile and soil properties. Very little field data exist on pile response to soil-induced excitation because of the expense involved in maintaining instrumentation on structures and

2

their foundations. Most laboratory test data focus on cyclic loading of the pile rather than the soil. These tests focus mainly on wind- and wave-induced cyclic loading; hence, the frequencies of loading are somewhat lower than for earthquake loading (0.02 Hz - 0.2 Hz) and the durations of cylic loading are greater than for a typical earthquake. Other studies do not use actual earthquake records but rely on excitation techniques to simulate earthquakes [Whitman and Klapperich (1987)]. These differences may create difficulties in interpreting the results for use in earthquake loading situations.

This study intended to overcome the deficiences in the previous studies by considering all the relevant variables and was aimed at understanding the effects of ground excitation and pore water pressure loading produced by p waves in the ocean on the behavior of tension piles in saturated sands in a laboratory

1.2 Objectives

In a previous study conducted at the University of Houston [Ochoa (1990)], laboratory model tests were performed on tension piles subjected to simulated seismic loading through the soil. The objective of that study was to establish an experimental procedure for the process and to investigate experimentally the stability of driven, permanently plugged pipe piles in saturated sand under the horizontal and vertical components of one generic seismic event for which three-dimensional accelerograms were available at an offshore site in California. Those experiments were conducted with mass-spring feedback loadings in the vertical direction on the pile heads, in which the resonance frequency of the mass-spring system was within the frequency range of the applied seismic event, and the generic seismic record was scaled to simulate earthquakes of high magnitude. Initial effective stresses in that study were kept low so as to simulate skin friction behavior in piles in the upper 7 - 14 meters of the seafloor. In that study, effects of

3

other events (different signatures) and of sea-seabed interaction (seaquake) were not considered.

The objectives of the present study were as follows :

(i) *Signature Effects* - To study experimentally, at model scale, the effect of shaking events produced by distant earthquakes of similar magnitudes, durations of shaking, and epicentral distances from the recording site but with different source mechanisms on the axial response of piles subjected to biased (static) tension, driven into a confined bed of medium-dense saturated sand.

(ii) *Seaquake Effects* - To design, construct and employ an experimental model capable of applying hydrodynamic pressure on the surface of a confined bed of saturated medium-dense sand, so as to investigate the pore pressure induced in the soil mass due to the application of the hydrodynamic pressure from a simulated seaquake and to assess its potential influence on the axial response of tension piles.

(iii) *Safety Criteria* - To develop criteria for stability and failure for model tensioned piles for the conditions modeled based on performance during earthquakes that was studied for various combinations of scaled simulated Richter magnitudes of two distinct seismic events and biased (static) tension loads on the pile and on performance during loading of the soil surface by simulated standing p-waves in the water (seaquake phenomenon).

(iv) *Degradation Factors* - To utilize an existing program for analysis of pile performance under dynamic axial loading (PAR) in a straightforward deconvolution process to ascertain appropriate degradation factors for analysis using the results of the small-scale model tests.

1.3 Research Approach

1.3.1 Experimental Study

The experimental study was divided into two phases. In phase I, piles under biased tension loads were subjected to ground excitations from different seismic events of similar magnitudes, durations of shaking and at the same epicentral distance from the foundation site, but with different focal mechanisms. The ability of piles to sustain biased tension loads during and after such events was assessed from these experiments. In particular, the effect of "event signature" (frequency content) on the condition of pile extraction was investigated.

Two California seismic events, the Oceanside event of 07-13-86 and the Upland event of 02-28-90, were selected for this purpose. The horizontal components of the ground motion for these events were scaled to simulate higher magnitude events (7.0, 7.5 and 8.0 Richter magnitude) in such a way as to preserve the phasing from the original records. The scaled accelerograms were converted to base movement at the pile toe by integrating twice. In order to model the diffusion characteristics of the pore water, both displacement and time axes of the records were scaled down by a factor of 0.19. A description of the model-prototype similitude is presented in Chapter 4.

The performance of piles in saturated sand subjected to earthquake loading was studied through model tests conducted in a vibrated pressure chamber. A closed-ended steel pipe pile, 25.4 mm in diameter and 405 mm in length with a wall thickness of 1.2 mm was driven by impact into a bed of saturated medium-dense sand deposited in the chamber that was consolidated under an isotropic effective stress of 17.24 kPa, representing the mean depth-averaged effective stress around a 4.5 -m- long prototype pile or the top 4.5 m of a longer pile. The test pile was subjected to bias tension load through a spring-mass system to which the pile was tethered to simulate structural feedback. The natural period of the

spring-mass system was about 2 sec, which was above the longest period in the model wave train for the simulated seismic event.

Seismic loading tests were performed on the model test pile by applying the magnitude (7.0, 7.5 and 8.0), geometric- and time-scaled soil displacement-time histories for the Upland and the Oceanside events to the base of the soil chamber while the pile was held under biased uplift load by the spring mass system. Several tests were conducted by varying the magnitude of the scaled earthquake and the magnitude of the applied biased load on the pile (45% - 90% of the static uplift capacity of the pile) for each of the two events. When the pile did not fail during a seismic event, static loading was performed to failure to define the post-shaking capacity of the pile. Based on the pile performance during the events, contours plots for stability, mobility, and failure conditions were established for the piles.

In phase II, pore water loading in the seabed due to seaquakes induced in the water overlying the ocean was investigated. This study was further extended to assess the behavior of tension piles during the pore water loading of the seabed. The testing assembly used in phase I was modified to enable application of hydrodynamic pressure to the surface of the saturated sand contained in the pressure chamber. Details are provided in Chapter 4. Initial tests were conducted in the absence of the pile to study the pore water pressure response of the soil as a function of the frequency of the hydrodynamic pressure, number of cycles of loading, and mean effective stress in the soil for typical water depths. Pore water pressures were measured at the $1/3^{rd}$ and $2/3^{rd}$ depths from the surface of the sand column in the test chamber (simulated depths of 1.5 m and 3.0 m for mean effective stress of 17.24 kPa in the test chamber). Tests were also performed to investigate the pile response due to the seaquake effect during typical M = 8.0 earthquakes for typical water depths. This was accomplished by applying the cyclic water pressure to the surface of a confined sand bed into which the model pile was driven and held under tension by a spring

mass system. These tests were carried out for varying magnitudes of bias load ratioed to the static capacity of the pile and varying magnitudes of mean effective stresses simulating prototype pile segment depths ranging from 4.5 m to 36 m.

Pile response during the signature studies and the hydrodynamic studies were monitored by measuring time histories of pile-head load, pile-head movement and pore water pressures. Scaling rules were established in order to extrapolate approximately the results from model to prototype conditions. In addition, laboratory index tests such as monotonic triaxial compression, direct steel-sand interface shear, torsional resonant column and one-dimensional cyclic confined compression tests were conducted on the test soil under medium-dense conditions.

1.3.2 Numerical Study

Ground Excitation Tests

The pile response measured during the ground excitation tests (signature tests) was utilized to develop degradation factors for analysis of piles using an existing program for dynamic analysis of axially loaded piles, PAR (Pile Analysis Routines) [PMB (1994)]. The pile was modeled as a one-dimensional linear elastic beam-column element, and discrete soil-resistance springs and dashpots were used to model the interaction between the pile and the soil. The non-linear axial and lateral soil-resistance springs were represented by "t-z" and "p-y" curves, respectively. Experimental data from static uplift tests were used to deconvolve the t-z curves (and p -y curves) using API (1993).

The axial response of prototype piles during ground excitation from both events was modeled numerically by initially conducting a static analysis where the pile was subjected to the bias load ratioed to the scaled capacity obtained from the tests. The deconvolved virgin soil-resistance curves were used (verified and modified, if necessary)

7

during this analysis. Subsequently, a dynamic analysis was carried out using "full-degraded" soil resistance curves where in the pile response under dynamic loads applied on the pile-head was obtained. The full-degraded curves were obtained by degrading the soil strength and stiffness using a degradation factor derived per Finn and Martin (1979), which is related to the pore water pressure developed in the soil and mean ambient effective stress during the shaking. These degradation factors were then "fined-tuned" empirically so that the displacement of the pile-head obtained from the analysis matched the measured values from the simulated seismic loading tests.

The phenomenon of residual pore water pressure buildup during ground excitations was explained using the theory provided by Seed et al. (1978) for soil response during cyclic shear stress loading. A method such as this can be used to estimate the pore water pressure buildup during seismic events if results of cyclic shear strength tests are available for the soil in question.

Seaquake Tests

The hydrodynamic pressure induced on the surface of the seabed due to the vertical motion of seabed during earthquakes was computed using the solution provided by Kobayashi et al. (1992) to the wave propagation problem. The phenomenon of pore water loading in the soil due to seaquake loading of the seabed was explained using a finite difference solution of modified one-dimensional consolidation equation [Zen et al. (1990b)].

1.4   Scope and Assumptions

The following constraints define the scope of this study.

(i)   This study was restricted to the axial response of tension piles only.

8

(ii) The effect of signature of an event was studied only for the horizontal component of the ground motion since Ochoa (1990) concluded that the vertical component of ground motion did not influence the pile response significantly.

(iii) The effects of ground excitations and seaquakes on the response of simulated offshore piles during seismic events were decoupled and studied independently.

(iv) The primary tool for applying effective stresses to the soil was a pressure chamber which can be used to simulate average effective stresses around a pile segment correctly but which does not simulate vertical stress gradients. The results must therefore be considered approximate at prototype scale.

The following assumptions were made :

(i) Preserving the phasing of the original records during the scaling process for the earthquakes ensures preservation of the source mechanisms of the earthquakes.

(ii) The pile-soil interaction phenomenon is governed by the depthwise mean effective stress around the pile.

(iii) The dynamic characteristics of the superstructure can be adequately reproduced by simulating only the fundamental frequency of the entire superstructure system.

(iv) The pore-water pressure diffusion characteristics are modeled satisfactorily by scaling the permeability of the soil and the frequency of the seismic record.

(v) The pile-soil flexibility is not a significant factor. (The test pile was relatively rigid, hence the results may be unconservative for long, flexible piles.)

(vi) The direction of wave propagation is mainly vertical. Therefore, the vertical component of ground motion is represented the p-wave particle motion, and the horizontal component of the ground motion is represented the s-wave particle motion.

9

(vii) The pore-water motion generated in the seabed as a result of standing p-waves generated in the sea due to seismic motion of the seabed is one-dimensional (vertical), resulting in the zero lateral strain condition.

(viii) The effect of surface waves generated during the seismic motion is minor and is neglected.

(ix) The vertical displacement motion of the seabed during a seismic event is idealized by a sine wave motion that is used in the computation of the hydrodynamic pressure for the seaquake studies.

1.5 Organization of Text

The document has been divided into nine chapters. Chapter 2 summarizes the literature reviewed on experimental and numerical studies that have been conducted so far in relation to the behavior of offshore piles under dynamic loadings. The characteristics of the seismic events and the scaling process employed to generate higher magnitude seismic events is explained in detail in Chapter 3. Following that chapter, a description of the scaling rules, test controls, testing assembly and testing methods is provided in Chapter 4. Chapter 5 discusses the results from the ground shaking tests, in particular the effects of the signature of seismic events on tension pile behavior and design implications. Results of the PAR analyses and degradation factors for strength are dealt in Chapter 6. The theoretical basis for the selection of the applied hydrodynamic pressure amplitudes and for interpretation of the pore water pressure response during seaquakes is dealt with in Chapter 7. The effect of the standing p-wave component of seaquakes on the behavior of piles and comparative effects due to ground excitations and seaquakes are explained in Chapter 8. Finally, conclusions and recommendations for future studies are presented in Chapter 9.

Chapter 2

LITERATURE REVIEW

A study of the axial response of offshore tension piles to seismic excitation requires an insight into the following phenomena.

a. Ground motion,

b. Soil response to dynamic loadings,

c. Physical models,

d. Pile response to cyclic loading,

e. Mathematical modeling of dynamic soil-pile interaction.

2.1 Ground Motion

The frequency content, duration of shaking, and peak ground acceleration are the three most important parameters of ground motion of interest to engineers.

The frequency distribution of energy of an earthquake is a function of the mechanism and depth of seismic rupture, orientation of the fault and the direction of the fault rupture with respect to the site of interest, crustal heterogenity which controls the rupture process of faults, the transmission characteristics of the propagation paths, topographic relief of the region and geometry of the basin [Gazetas (1990)].

The duration of motion is associated with the length of fault rupture. The longer the rupture, the longer is the duration of the ground motion [Bureau (1978)].

Peak ground acceleration is the earthquake parameter that is most frequently considered for the earthquake-resistant design of structures and civil works. Peak

acceleration is generally assumed to be magnitude-dependent and is primarily influenced by the site conditions (e.g., natural frequency of overburden soils in shearing mode deformation) and topography [Boore (1973), Schnabel et al. (1972)]. A wide range of attenuation relationships between earthquake magnitude, maximum acceleration and distance are available [Seed et al. (1976), Trifunac and Brady (1976)].

Current methods do not allow for the prediction of either the temporal occurrance or the magnitude of an earthquake. This makes the design of earthquake resistant structures difficult. Therefore, design of earthquake resistant structures in a particular region is based on the design response spectra of free-field motion for that particular region. Response spectra represent the nature and severity of the dynamic motions that can take place at the base or foundation of a structure as a result of an earthquake. The response spectrum is a useful indicator of several characteristics of the ground motion and its effect upon structures with varying natural modal frequencies.

The selection of a design response spectrum for a particular region depends on the seismicity of the region and the seismic risk levels associated with the structure. The steps involve identifying the credible earthquakes associated with the active faults in the nearby regions and selecting the appropriate earthquake records based on the risk levels and their magnitude, distance, source and frequency of occurrence [Bell (1978)]. In the absence of actual records, time histories are synthesized from geologic evidence, or selection is made from a database of recorded motions by matching the local soil conditions and the nature of characteristic earthquakes (magnitude, duration of shaking). The selected time histories are scaled to match an estimated peak ground acceleration at the particular site.

2.2 Soil Response to Dynamic Loading

During cyclic loading, the behavior of saturated sands is largely governed by the pore water pressure developed. The pore water pressure response to dynamic loading consists of two components, i) transient and ii) residual. The transient pore water pressures result from the coupled instantaneous response of the sand skeleton and the pore water to cyclic loads. Residual pore water pressures are caused by the cyclic shear stresses varying in space and time. They are not uniquely related to the instantaneous values of the cyclic induced stresses but depend on the intensity and duration of loading and the drainage characteristics of the seafloor [Finn and Siddharthan (1983)].

During earthquakes, the sea floor is subjected to earthquake-induced cyclic shear stresses, standing wave loading and surface wave loading due to the overlying water. Most of the literature on wave interaction problems is concentrated on surface wave loading. Hence, emphasis is given here to earthquake induced loading on the soils and standing wave loading. The nature of the problem of surface wave loading and standing wave loading are closely related, since both induce cyclic wave loading on the ocean floor. Under surface or standing wave loading or under earthquake loading, the soil may develop any of the following three conditions, depending upon the effective stress condition: i) liquefaction; ii) cyclic mobility; iii) densification.

Liquefaction: In this condition the soil undergoes continued deformation at a constant low residual resistance or with no residual resistance due to the buildup and maintenance of high pore water pressures which ultimately reduce the effective confining pressure to a very low value. Liquefaction of near-surface layer of silty or sandy soils has occurred during the 1990 Manjil earthquake in Iran and the 1989 Loma Prieta earthquake in California [Ishihara and Haeri (1990)], among other cases.

Cyclic mobility: In this condition cyclic shear stress application produces initial liquefaction, and subsequent cyclic shear stress application develops limited strains which cause the pore water pressure to drop due to dilation of the soil, resulting in slight regain in soil strength. This strength is also referred to as the steady-state strength. While the soil never truly liquefies, large deformations are often associated with cyclic mobility. Zeghal et al. (1994) reported a site behavior that was characterized by large strains and displayed hardening behavior with small restoring shear stresses.

Densification: Densification of soil during dynamic loading has been observed during surface-wave-induced loading on the seafloor. Densification results when the wave-associated vertical effective stress exceeds the vertical effective stress of the seafloor in calm seas [Zen and Yamazaki (1990a)]. Densification, however, may be preceded by liquefaction or cyclic mobility.

Castro and Poulos (1976) recognized that the potential for liquefaction or cyclic mobility is dependant on the soil mineralogy, its structure, its initial state (sustained static shear stress), stress level, volume change characteristics (contractive or dilative behavior) and method of loading.

Liquefaction and cyclic mobility conditions are critical to the stability of any foundation, including pile foundations. A variety of deterministic models have been developed to predict the actual level of pore pressure generation and liquefaction potential due to seismic and wave loading in the free field. These models are based on uniform strain or stress-controlled cyclic behavior, wherein a nonuniform transient loading was replaced by an equivalent cyclic loading. The assumption is made that pore pressure developed is based on cumulative damage accumulation and is not affected by the sequence of loading pulses and the magnitude of the applied cyclic stress ratio. The rate of generation of pore water pressure is related to the cyclic stress ratio (ratio of cyclic shear stress induced to the effective overburden stress) and the ratio of the number of uniform stress cycles to the

14

number of stress cycles required for the liquefaction, and dissipation is based on the theory of consolidation. Seed and Idriss (1971), Martin and Seed (1978), Chameau and Clough (1983), and Wang and Kavasanjian (1989) have provided solutions for pore water pressure in soil deposits during seismic loading. Zen and Yamazaki (1990b) and Barends (1990) have provided such solutions under surface wave loading assuming the problem condition to be one-dimensional plane strain.

The mechanism of liquefaction induced by small-amplitude and vertical surface wave loading in the ocean (standing p-waves from seaquakes) is different from earthquake loading. For vertical surface wave loading with small amplitude there is no shear on the seafloor, and the seafloor deformation is very small. In this case, the wave-associated bottom pressure excites an oscillatory excess pore pressure in the seabed with some damping and phase lag without any residual buildup in pore pressure if the soil structure is elastic. Contrary to this, earthquake-induced loading induces cyclic shear stress, which induces high residual pore water pressure [Foda , Tzang and Maeno (1991)].

The preceding brief summary from the literature pertains to soils in the free field. When a pile is introduced, stress conditions and state properties in the soil are changed in the vicinity of the pile, and the presence of the pile influences the way in which both shear stresses and cyclic pore water pressures develop during earthquake and seaquake loading. One of the objectives of this study was to investigate experimentally the effects on the soil that have been summarized when biased-loaded tension piles are present.

2.3   Physical Models

Physical models can be important sources for data on dynamic pile-soil interaction. Extensive reference has been made to two types of physical models in the literature: 1) centrifuge models, and 2) 1-g models. A third class of modeling, pressure chamber

15

modeling, combines the features of both, in that it is executed at 1-g but confining pressures are applied to simulate depth effects.

The basic principle of centrifuge modeling is that when a soil sample confined in a chamber is accelerated to n times the earth's gravitational acceleration, it essentially represents a (1/n)th scale model of a prototype system. This is primarily done to produce effective stress levels in the model that are as close as possible to those of the prototype, since the behavior of a soil mass is a function of effective stress level within that mass [Schofield (1980)].

Tests conducted in the centrifuge have raised important questions concerning scaling, since inertial and consolidation phenomena require different scaling of time if water is used as a pore fluid. To circumvent the problem, the viscosity of the pore fluid has been scaled - most commonly using silicone oil. The scale effect caused by relative model to grain size ratio is unimportant for clay soils [Randolph (1979)] but can be critical for granular soils. Another problem associated with this technique is the difficulty of satisfying the similitude between the relative pile/soil flexibility and its effects on load deformation behavior of piles [Lambson (1988)]. Modeling effects of installation of foundations and seismic loading also become difficult in a centrifuge.

By constrast, in a 1-g environment scaling to prototype effective stress levels is ignored. This creates difficulty in establishing model-prototype similitude because the ratios of stress developed when loading a model foundation to effective stress in the soil, and corresponding strains, particularly around peak or ultimate load, are not unique [Iai (1989)]. 1-g models, however, are much better adapted to studying the effects of seismic loading and pore water diffusion than are centrifuge models. Shaking tables, which have been used widely in the study of the seismic performance of structures, are examples of 1-g models. Ground motion in such devices are often simulated by using piezoelectric shakers, toggle and spring mechanisms, and hammer-plate exciters.

16

A problem that affects both types of physical models is the influence of shear resistance between the soil and the internal chamber wall on the vertical stress distribution in the chamber. Another major concern that plagues the modeling of dynamic soil-structure interacting systems is the reflection of stress waves occurring from the boundaries of the chamber. Approaches that have been successfully followed in mitigating this problem [Coe et al. (1985); Cheney et al. (1990)] include i) attenuation of such waves at the chamber boundaries using an absorptive material, and ii) selection of an appropriately large-sized chamber for the particular dynamic test to be performed. A small-size chamber increases the useful range of frequency, however, it may adversely affect the dynamic and static properties of the soil-structure model (i.e., stress distribution, dynamic stiffness factor(s), damping properties etc.).

In spite of all the above factors, model tests continue to provide insight and better understanding of the physical processes because they have the advantage of permitting parameter studies. Several model tests have been conducted to study the dynamic behavior of saturated soil masses [Hushmand et al (1988), Arulanandan et al. (1983)]. Forced vibration of footings and other structures have been studied in models in an attempt to verify and calibrate numerical models and to obtain an estimate of damping and dynamic stiffness in prototypes [Weissman and Prevost (1989)]. Finn and Gohl (1987) have demonstrated the utility of the centrifuge to measure pile-head response and bending moment distribution in model piles and pile groups under toe-level seismic excitation in both dry and saturated sand, respectively. However, the problems of ground response and soil-structure interaction response has not been studied extensively using actual earthquake records.

Experimental modeling of transient pore fluid flow or sea-seafloor interaction requires that similitude laws be satisfied between two physical conditions. In addition to the

geometric similarity, the Froude (Fr) and the Mach (Ma) numbers should be the same for the scale model and the corresponding prototype condition [Yamamoto et al. (1983)].

The third category of model testing, pressure chamber or "calibration chamber" testing, has been employed primarily for the calibration of *in situ* testing devices, such as the cone penetrometer and the pressuremeter against known conditions of soil density and effective stress. Ochoa (1990) pioneered the use of the pressure chamber for examining dynamic pile-soil interaction problems by using a closed-loop testing machine to impose complex shearing motion to the soil column in the pressure chamber near the toe of the pile.

The pressure chamber is a 1-g device in which prescribed isotropic or anisotropic effective stress conditions are applied at the boundaries, or in which prescribed stresses are applied to some boundaries (for example, the top boundary) and zero deformation conditions are imposed at the other boundaries. Drainage conditions can be established at the desire of the user. While long pressure chambers have been constructed with boundaries for varying lateral soil pressures with depth to simulate vertical gradients in mean effective stress in the soil mass [O'Neill and Raines (1991)], most pressure chambers are designed to permit only one stress state within the entire soil mass. This is the inherent disadvantage of pressure chamber testing, because the stress condition that is imposed represents a vertically averaged stress in the soil around a pile (or *in situ* testing device), and scaling to prototype scale must be predicated on the assumption that similitude of vertically averaged effective soil stresses is sufficient to ensure similitude in foundation performance.

2.4 Pile Response to Cyclic Loading

Limited experimental investigations generally have indicated that 'two-way' cyclic loading (involving load reversal) has a significant effect in reducing pile capacity and stiffness, whereas 'one-way' cyclic loading has a much smaller effect. On the other hand,

the relatively high frequency of earthquake loading and the resulting rapid rate of load application to the pile tends to cause an increase in both load capacity and pile stiffness.

2.4.1   Cyclic Degradation

Bea et al. (1982) suggest that cyclic loading causes only a maximum 10-20% reduction in axial capacity in clay, with a trend for increasing pile head settlement with increasing numbers of cycles and magnitude of cyclic loading. For piles in sand, the limited information available on the degradation effects of cyclic loading indicates that remarkable reduction in load capacity and pile head stiffness can occur. Chan and Hanna (1980) and Gudehus and Hettler (1981) describe laboratory model centrifuge tests which demonstrate conditions under which pile failure can occur with biased compression loading with cyclic loads of 30% or less of the ultimate static load for one way loading and even smaller values for two-way cyclic loading. Permanent settlements of the pile continued to increase, even after a very large number of cycles.

Small-scale pressure chamber model tests on piles in silica sand and calcareous sand, reported by Poulos (1984) and on piles in clay [Poulos (1981)], showed that the amount of degradation of skin friction was related to the amplitude of cyclic displacement, and that degradation did not commence until the cyclic displacement amplitude reached the displacement required to cause static slip.

Field tests on grouted piles in calcareous sand loaded in biased compression by Nauroy et al. (1986) have shown that the larger both the mean (biased) load and the cyclic load, the greater is the rate of accumulation of permanent settlement. As the cyclic load level approaches that required to cause failure during cycling, the rate of increase of settlement with increasing numbers of cycles may become very large.

2.4.2 Loading Rate Effects

For piles in silica sand, there appears to be little or no effect of loading rate on either skin friction or pile head stiffness, but for piles in calcareous sand, some slight rate effects are evident, typically with a 2-4 % increase in resistance for a ten-fold increase in loading rate [Poulos (1988)].

2.5 Mathematical Modeling of Dynamic Soil-Structure Interaction

Schnabel et al. (1972) developed a computer program called "SHAKE" to evaluate the response of homogeneous soil deposits of infinite lateral extent subjected to vertically propagating shear waves. The nonlinearity in the soil behavior was incorporated using an equivalent linear approach. The method was based on a total stress analysis. Finn et al. (1977) employed an effective stress approach and developed a program called "DESRA" for earthquake ground response analyses. A nonlinear hyperbolic stress -strain model using the masing rule for the hysteresis was used for the soil. The program allowed for degradation of the material properties based on the pore pressure generation and dissipation. Harrop-Williams (1988) developed a closed-form solution for the earthquake-induced cyclic shear stress distribution in a soil. The above methods assume the ground response problem to be a one-dimensional vertically propagating shear wave problem.

In modeling dynamic soil-pile interaction problems, an important factor is the energy dissipation (and perhaps absorption) characteristics of the foundation-soil system. There are two important sources of energy dissipation in the soil. The hysteretic component of damping, which is due to the inelastic behavior of the soil. The other source of damping, geometric or radiation damping, is due to the energy that is radiated away from the structure pile system by elastic wave propagation. A question to be addressed in mathematical modeling is whether the geometric damping is significant enough to be considered important in the response of pile-supported offshore platforms. Analytical and experimental

work by Novak (1974b) and Ross (1970) provide mixed indications. The contradictory results may be attributed to the relative magnitude of loading used in their work. Higher geometric damping values (10% - 30% of critical) resulted from tests where small loads were applied such that very little inelastic-hysteretic soil action was observed, and low geometric damping occurred where the loading range was high enough to cause hysteretic soil action [Arnold et al. (1977)]. Therefore, it is sufficient to say that questions regarding the importance and proper simulation of geometric damping are not fully resolved.

The general approaches that have been developed to consider dynamic pile-soil interaction are the following: the continuum approach [Novak (1974a)], lumped-mass model [Matlock et al. (1978)], finite element method [Blaney et. al (1976)] and mixed lumped parameter - continuum approach [Otani (1990)]. Finite element methods have practical drawbacks when modeling soil-structure interactions in that energy radiating into the soil from the structure reflects off the boundaries unless either very large meshes with damping geomaterial or energy-absorbing boundary elements are used. Lumped-mass models use simple semi-empirical formulations for soil stiffness and hysteretic energy dissipation but do not directly model radiation damping. The mixed model permits modeling of hysteresis in the soil near the pile through the use of lumped parameter elements at the soil-pile boundary and radiation damping through continuua elements located beyond the lumped-parameter elements.

A mixed model for piles [Chen and Penzien (1984)] involves application of the dynamic load through the pile head for soil undergoing seismic excitation. Lumped mass models [Matlock et al. (1978), Bea (1992)] that are used for the lateral (SPASM) and axial (PAR) response analysis, respectively, have provisions for applying time histories of lateral or axial motion to the support points of nonlinear springs representing the soil. The soil in turn loads the pile, whose inertial and dynamic stiffness response is appropriately represented. These models require that crude assumptions be made regarding the radiation

21

damping but are capable of simulating soil degradation and hysteretic damping accurately based on time history response of nonlinear uncoupled unit load transfer curves along the pile length. They are generally more appropriate for modeling large amplitude loading than for small amplitude loading.

While the continuum and finite element models permit more rational assessment of geometric damping and soil-pile coupling, the SPASM/PAR approach has been the most popular state-of-the-practice pile analysis method for seismic loading since it can simulate the soil degradation and hysteritic damping in terms familiar to geotechnical and structural engineers.

There are other less sophisticated models that consider soil-pile interaction under cyclic loading based on a quasi-static analysis that neglects the inertial resistance of the pile-soil system. These are essentially based on the degradation of semi-empirical unit load transfer curves at the end of every loading cycle, resulting reduction of shearing resistance around the pile and redistribution of load between the tip and shaft in dry soils [Swiniaski and Sawicki (1991)] and due to the effect of excess pore pressure generated around a pile in saturated sands [Lee and Poulos (1988)].

When a relatively few cycles of strong shaking occur without seaquake effects, full cyclic degradation of the soil will not occur around a pile, unless the static (biased) load is near the soil failure load. Therefore, in a time domain analysis, it is appropriate to degrade the backbone static soil resistance curves (e.g., t-z curves) during every cycle. For dealing with unit axial pile shaft response relations, Matlock and Foo (1979) proposed degradation factors to be used as multiplicative corrections to the limiting skin friction values after every cycle. They argued that the cyclic degradation occurs at a point on the shaft when that point is subjected to reverse slip, and that each application of reverse slip causes an additional degradation until some lower limiting value of skin friction is reached. Poulos (1988) later incorporated the strengthening effect due to the loading rate by introducing another factor in

addition to the degradation factor in his model. Other degradation models have been proposed for quantifying changes in soil stiffness and resistance [Pyke (1979), Matasovic and Vucetic (1993)].

Another aspect of the problem of offshore piles is the fluid-structure interaction problem. Williams and Mau (1988) have presented the hydrodynamic pressure distribution on a submerged arc due to vertical earthquake excitations. A Green's function for a fluid is used in conjunction with a Green's function for the arch to solve the coupled fluid-structure interaction problem. Assuming the seabed to be impermeable and deformations to be low and using the Williams-Mau (1988) solution with an arch of infinite radius, an earthquake-producing vertical motion on the seafloor in sediments in a 300 m depth of water can induce total hydrodynamic pressures up to 3 times the soil effective stress at a depth of 7 m below the sea bed (Ochoa, 1990). That is, pressures of 30 - 60 kPa can be produced. Whether these pressures, which are total pressures applied at relatively high frequencies, affect pore pressures and total stresses equally, as would be the case for application of a static water pressure on the seafloor, depends upon the compressibility of the soil framework, the viscosity and inertial properties of the water, the drag properties of the soil pores and perhaps other factors. For this reason, further exploration of the phenomenon is justified.

Hydrodynamic pressure produced by horizontal earthquake motion acting on axisymmetric offshore and coastal structures was explored using a semi-analytical and semi-numerical approach by Sun et al. (1991). Body waves developed hydrodynamic pressures with amplitudes as high as 50% of the hydrostatic pressure at the base of structures at resonance.

Liou et al. (1988) analyzed the response of tension-leg platforms to vertical seismic excitations using a substructuring technique. They analyzed the vertical motion, tendon forces and the foundation uplift of a tension leg platform under vertical excitation of the

seafloor. Their study for a typical tension leg platform revealed that the maximum combined dynamic excursions in the tendon force in all the tendons can be as high as 70% of the initial combined tendon force for vertical excitation of the seafloor corresponding to p wave velocities in the soil of 610 m/sec. Their study incorporated multiple interactions among the soil, foundation, fluid and platform. The superstructure feedback loading due to wave-induced loading independent of the pile movement may have a significant contribution to the pile response. The contribution of superstructure feedback due to pile movement during ground loading has been found to be not more than 10% based on experimental studies by Ochoa (1990). If the time histories of 1) the superstructure feedback load on the piles produced by the movement of the piles in response to seismic loading, and 2) the load on the piles produced by water wave action on the structure can be estimated, it can be assumed that they can be superimposed to obtain the complete load history on the pile heads. The experiments described in the present study will directly address only issue 1).

2.6 Inferences

The following can be inferred from the literature review.

i)   The ground motion is influenced by the earthquake source, transmission pathways and soil mechanisms.

ii) Soil response to water wave or seismic loading is influenced considerably by the background pore water pressure build-up during the loading event. This may result in liquefaction (complete failure in terms of load carrying capacity), cyclic mobility (considerable strains without complete loss in capacity) or densification (resulting in gain in capacity).

iii) Physical models, despite their shortcomings, provide a qualitative and an approximate quantitative understanding of the physical phenomena with an opportunity for conducting parametric studies, if the phenomena are modeled properly.

iv) Soil-structure interaction during dynamic loading in saturated sands may have two effects on the pile capacity: i) degradation in the pile capacity ii) increase in capacity due to rate of loading effects.

v) Existing mathematical models for dynamic soil-pile interaction problems can be used for design purposes provided they are calibrated based on experimental results.

vi) Wave-induced pressure by the overlying water in the ocean can produce significant pressures on the seafloor that may further degrade the shear strength of the soil.

Chapter 3
SEISMIC EVENTS

3.1 Event Description

The "signature effect," or the effect of earthquakes with similar magnitudes, peak ground accelerations and durations of shaking but different source mechanisms, on the response of tension piles was studied for two seismic events. The two events chosen for the study were the Oceanside, California, event of July 13, 1986, and the Upland, California, event of February 28, 1990. Three-dimensional acceleration-time histories were available for these events at a deep soil site offshore, the Seafloor Measurement Systems (SEMS) site, maintained by the Minerals Management Service of the U.S. Department of the Interior near Long Beach, California. The locations of the event epicenters and the SEMS unit are shown in Fig. 3.1. Acceleration time histories at this site were measured at about 76 m below the shallow sea surface, 3 m below the sea floor.

No detailed soil data exist for the SEMS site. Borings taken there indicated that the soil is primarily a fine, medium dense sand, and that at least 120 m of sand is present above bedrock. However, the depth of the bedrock-sand interface has not been established.

The Fourier amplitude spectra of the resultant horizontal component of ground motion in the major principal direction of motion for both the Upland and the Oceanside events are shown in Fig. 3.2. The acceleration spectrum for the Oceanside event is essentially monomolal, with a primary peak at about 3.5 Hz. The acceleration spectrum for the Upland event is essentially bimodal, with peaks near 1 Hz and 3 Hz. More of the energy in the Upland event is contained in the lower frequency components than in the Oceanside event. Table 3.1 shows the characteristics of the two earthquakes. The two earthquakes had similar magnitudes (M_L = 5.2, where M_L is defined as the body wave

magnitude), peak ground accelerations (PGA = 0.028g) and durations of shaking (80 - 90 secs). The difference in signatures resulted from the difference in the focal mechanisms associated with the two events and the directions in which the seismic energy traveled relative to the strikes of the regional formations to reach the recording site.
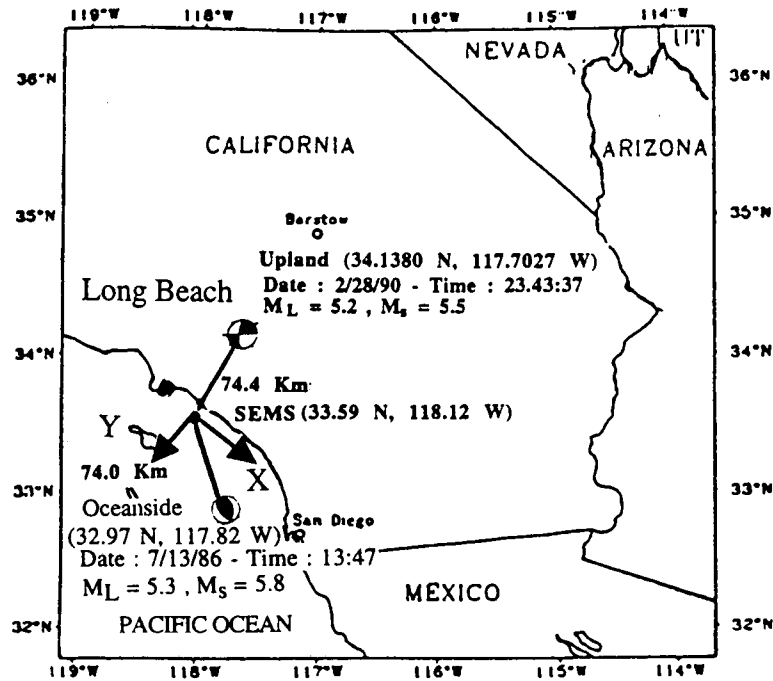
Fig. 3.1: **Map Showing the Locations of the Oceanside and Upland Event Epicenters and the SEMS Unit**

The Oceanside event had a reverse thrust faulting mechanism, whereas the Upland event had a left-lateral strike-slip mechanism. The Oceanside event occurred on the San Diego Trough-Bahia Soledad fault zone, one of the four major active north-west trending sub-parallel faults in the region west of the cities of Oceanside and San Diego. The Upland event occurred in the eastern part of the Los Angeles basin, northeast of Oceanside. Several major reverse thrust faults occur in the southern front of the transverse mountain ranges,
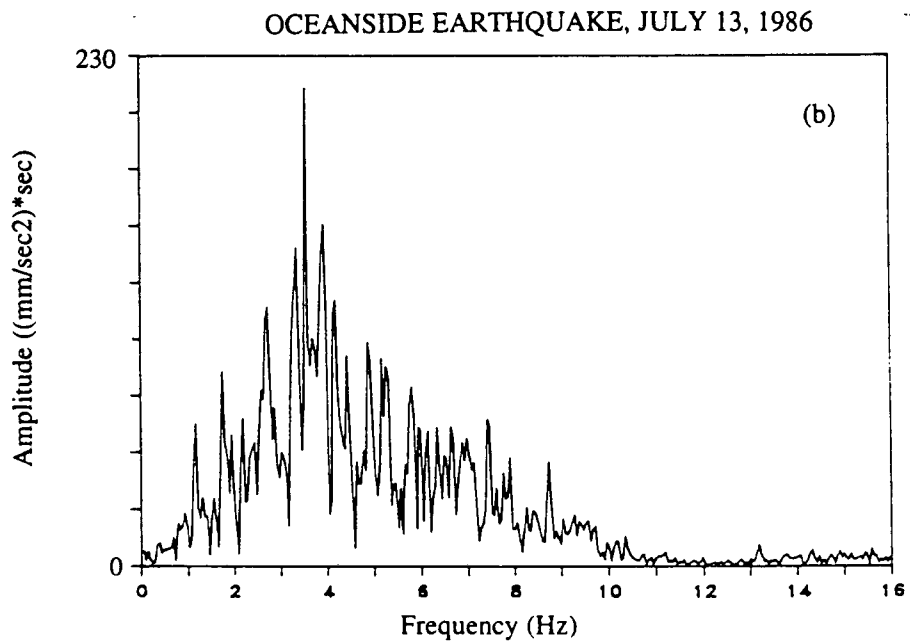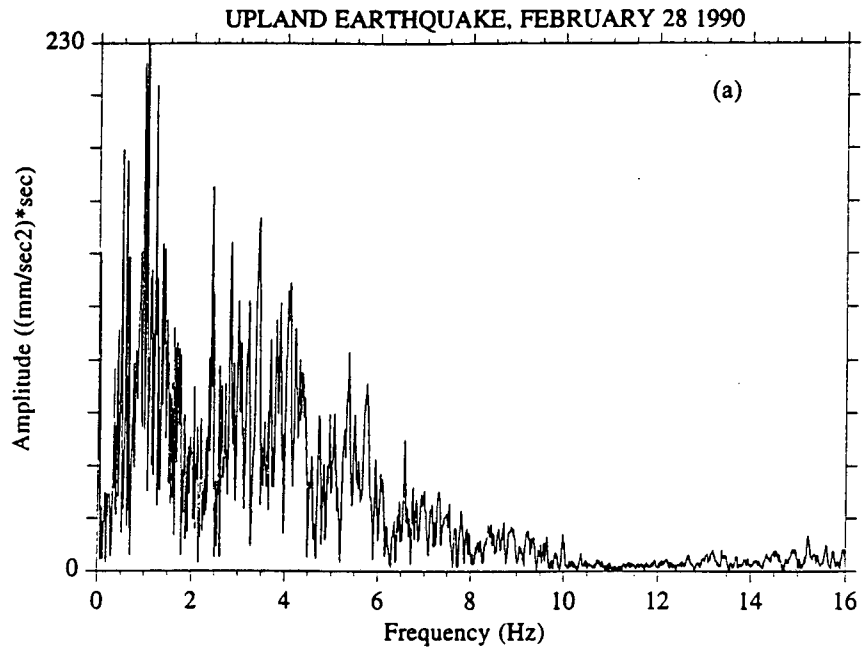
Fig. 3.2: Fourier Amplitude Spectra of Resultant Horizontal Ground Acceleration for the Upland Event (a), and the Oceanside Event (b)

28

Table 3.1: Earthquake Characteristics

Detail	Oceanside Event	Upland Event
Date, Place and Time	July 13th, 1986, at 13:47 UT, 50 km southwest of the city of Oceanside in San Diego county (32.97 N, 117.82 W)	February 28, 1990, at 23:43 UT, at 34.13 N, 117.702 W in Upland region in San Bernardino county
Focal Mechanism	Reverse faulting	Left lateral strike-slip faulting
Causative Fault	East-southeast-striking and south-dipping, San Diego Trough-Bahia Soledad fault zone	North east striking San Jose Fault
M_L	5.3	5.2
M_S	5.8	5.5
Seismicity : No. of earthquakes $M_L \geq 4$	1 (1932-1984)	2 (1981-1989)
Distance from Instrumentation site (SEMS)	74.0 km	74.4 km
Peak Ground Acceleration at SEMS	0.027 g	0.029 g
Predominant Frequency	3.5 Hz	1.0 Hz / 3.0 Hz
Hypocenter	9 km deep	5.2 km deep
Length of Rupture	7 - 9 km	4 km
Duration of Shaking	80 secs	90 secs

M_L - Body Wave Magnitude
M_S - Surface Wave Magnitude

and right-lateral strike-slip faults occur to the south (such as the Elsinore and Chino faults) in this region. The Upland event occurred on the San Jose fault, one of the few secondary left-lateral faults that exist in this region. The presence of these active left-lateral strike-slip faults has been understood to be a mechanism to transfer fault motion from the right-lateral strike slip on the north-west-trending faults to the reverse faults along the range fronts. Both the Oceanside and the Upland events were a part of general seismic activity over southern California during the period of the late 1980's. An abundance of aftershocks were recorded following these events (average of 100 aftershocks, $M_L = 3.0$). The pattern of the aftershocks, orientation of the stress and presence of a 14 km to 18 km long unbroken segment in the San Jose fault suggest that the stress has not been completely relieved or that there has been a recovery of the stress state after the Upland event and there exists a likelihood of occurrence of a damaging earthquake along the San Jose fault in the near future. In constrast, large temporal variations in stress orientation and magnitude during the Oceanside aftershock sequence indicate no recovery of stress along the causative fault for the Oceanside event [Hauksson et al. (1988), (1991)].

3.2 Digital Operations on Accelerograms

The horizontal components of the acceleration in the two orthogonal directions were combined together vectorally to obtain a resultant component in the major principal direction for each of the two events (Oceanside and Upland). Both the earthquakes were mild earthquakes with $M = 5.3$ and $M = 5.2$. Therefore, the resultant horizontal component of the accelerograms were scaled to obtain events of Richter magnitude 7.0, 7.5 and 8.0 using a scaling technique in the frequency domain. Digital operations performed on the accelerograms to obtain the scaled magnitude earthquake records are described below for the Upland event. Similar operations were also performed on the Oceanside event by Ochoa [1990].

3.2.1 Vectoral Combination of Accelerograms

A procedure similar to that of stress transformation in the principal directions proposed by Penzien and Watabi (1975) was employed for combining the measured horizontal components of the acceleration in the two orthogonal directions for each event.

The X and Y components in the two orthogonal directions for the Upland Event in the horizontal plane are shown in Fig. 3.3. The variances and covariances for the two records were calculated for the duration of the strong shaking (i.e. 25 secs - 40 secs) using

$$\mu_{ij} = <[a_i(t) - a_i][a_j(t) - a_j]>, \quad i, j = x, y, \tag{3.1}$$

where $a_i(t)$ and $a_j(t)$ are the acceleration-time histories in the orthogonal directions, a_i and a_j are the mean values found by averaging $a_i(t)$ and $a_j(t)$ over the entire duration of the motion.

For the Upland event, the following values were obtained:

$\mu_{xx} = 15.26$ milli-g's; $\mu_{yy} = 18.45$ milli-g's and $\mu_{xy} = -1.1717$ milli-g's.

The principal variances were then obtained by solving the characteristic equation resulting from

$$[\mu_{ij} - \mu I] \{n_x - n_y\} = 0, \tag{3.2}$$

where I is the identity matrix, n_x and n_y are the x and y components of the unit vector in the principal direction.

Solving the characteristic equation, the major principal variance is

$\mu_1 = 18.83$ milli-g's.

Using (3.2) and $n_x{}^2 + n_y{}^2 = 1$, the direction cosines of the unit vector in the major principal direction become $n_y = +0.9504$ and $n_x = -0.310$.

The accelerations were then combined using these direction cosines to obtain the resultant value in the principal stress direction in the following way:

$$a(t) = [n_x \quad n_y]^T \{a_i(t) \quad a_j(t)\}. \tag{3.3}$$

The combined acceleration-time history in the major principal direction for the Upland event is shown in Fig. 3.4.

3.2.2 Scaling of Accelerograms

The primary interest of geotechnical engineers in ground motion record lies in 1) the maximum amplitude of acceleration; 2) the predominant frequency or predominant period of the motion and 3) the duration of strong shaking. In most situations, due to a lack of representative numbers of earthquake records, the common approach in adopting accelerograms for design is to modify existing available records carefully to satisfy the above-mentioned characteristics of the desired earthquake records.

Peak acceleration, predominant frequency and shaking durations are selected based on a review by seismology experts of potential causative faults in the vicinity of the structure of interest, their distances from the structure, potential maximum Richter magnitudes for a return period compatible with the proposed design life of the structure, and potential lengths of fault rupture. Ordinarily, the peak acceleration is estimated by seismologists based on seismic wave transmission through rock to the foundation of the structure. If, as in the case of the SEMS site, the foundation of the structure is situated in soil resting on top of the rock, attenuation factors are applied to the peak acceleration on rock, either using measurements of ground acceleration relatives to acceleration of bedrock
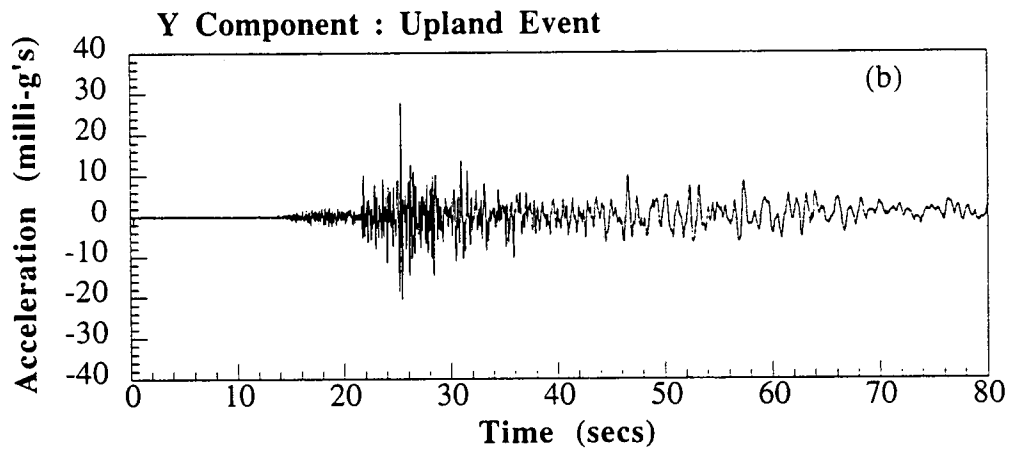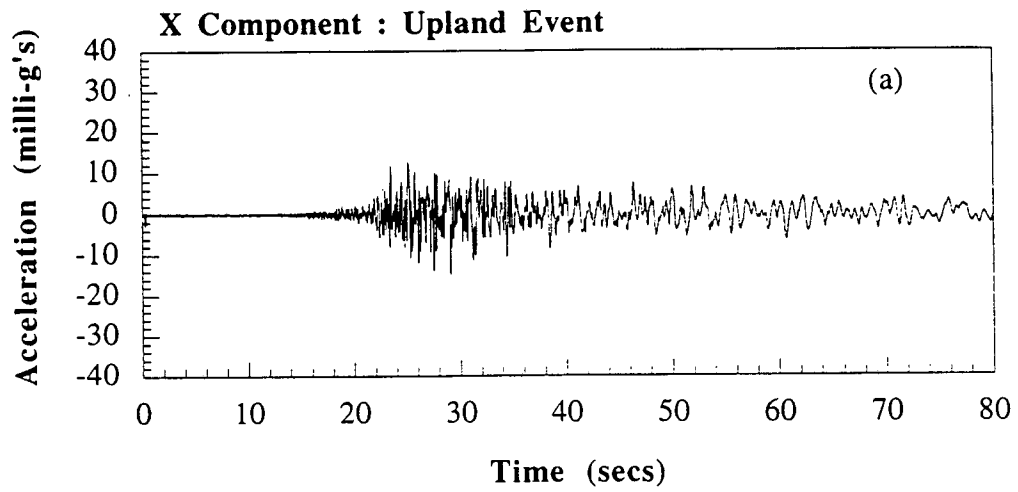
Fig. 3.3: Measured X (a) and Y (b) Acceleration Components in Two Orthogonal Directions for the Upland Event
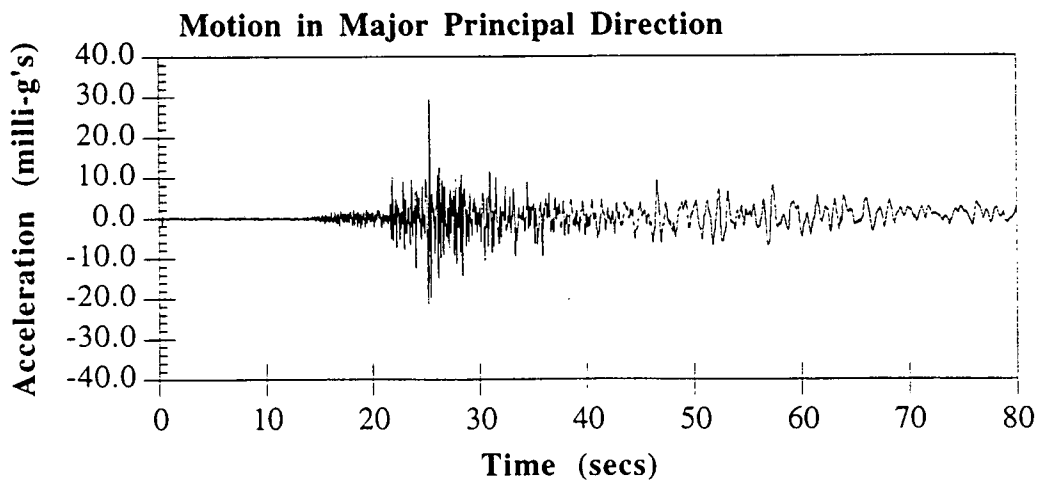
Fig. 3.4: Vectorally Combined X and Y Components of the Upland Event

33

at sites with similar geotechnical properties or through of simple soil models such as SHAKE or DESRA, which simulate the upward propagation of shear waves from bedrock to the surface of the overlying soil. The modification of earthquake records can then be performed in the time domain or the frequency domain [Seed and Idriss (1969)] to arrive at design accelerograms for specific projects. In addition, there are other complex methods of obtaining earthquake records, e.g., generation of artificial earthquakes obtained by mathematical simulation of fault rupture. However, these are not ordinarily used in design and hence have not been used here.

The vectorally combined horizontal acceleration-time histories of the two seismic events considered in this study were modified (scaled) to obtain higher magnitude events (Richter magnitude 7.0, 7.5 and 8.0). The scaling process was performed in the frequency domain. The phase difference of the signals were preserved during the scaling process so that the effect of signature (or different source mechanisms) could be studied.

The spectrum of the horizontal acceleration-time history for each of the two events was scaled to match a desired (target or envelope) Fourier amplitude spectrum, depending upon the magnitude of the desired earthquake record. The scaled spectrum was then transformed back into the time domain. The detailed procedure is explained below for the Upland event.

Selection of Target Fourier Amplitude Spectrum

The target or envelope Fourier amplitude spectrum in earthquake engineering commonly refers to the maximum response (acceleration, velocity or displacement) of a single-degree-of-freedom system as a function of system frequency and damping when subjected to a time-dependent excitation. From a physical point of view it represents the upper bound response of a site as a function of the assumed characteristics of the site and the strong ground motion. Trifunac (1979), based on the analysis of several earthquakes

34

with Richter magnitudes between 3.0 and 7.7, proposed a model for Fourier amplitude spectra (in the form of attenuation equations) directly relating spectral parameters to Modified Mercalli Intensity (MMI), distance, frequency, soil conditions and components (horizontal and vertical) of strong ground motion.

Trifunac's Model

Trifunac's model can be expressed as

$$\text{Log}_{10}[\text{ FS(T), p}] = a(T)p + b(T) I_{MM} + c(T) + d(T) s + e(T) v, \qquad (3.4)$$

where

FS(T), p =   Estimate of the Fourier spectra amplitude at the period of vibration, T, which is larger than the p fraction (confidence level) of all the data so far recorded under the same conditions,

a(T),.. e(T) =   Regression coefficients for parameters: p = confidence level; I_{MM} = level of intensity at the site in terms of Modified Mercalli Intensity (MMI); s = approximate site conditions (s = 0 for alluvial soil sites; s=2 for basement rock sites, and s = 1 for intermediate soil sites); v = type of motion (v = 0 for horizontal and 1 for vertical motion).

Using Trifunac's model with s = 0 and v = 0 for alluvial soils and horizontal ground motion, the target Fourier amplitude spectra shown in Fig. 3.5 were selected for obtaining the scaled horizontal motion records of Richter magnitudes 7.0, 7.5 and 8.0 for each of the two seismic events studied. In order to select the appropriate target Fourier amplitude spectrum for each of the selected magnitudes, the magnitudes were converted to the MMI scale using Fig. 3.6, in which R = epicentral distance.
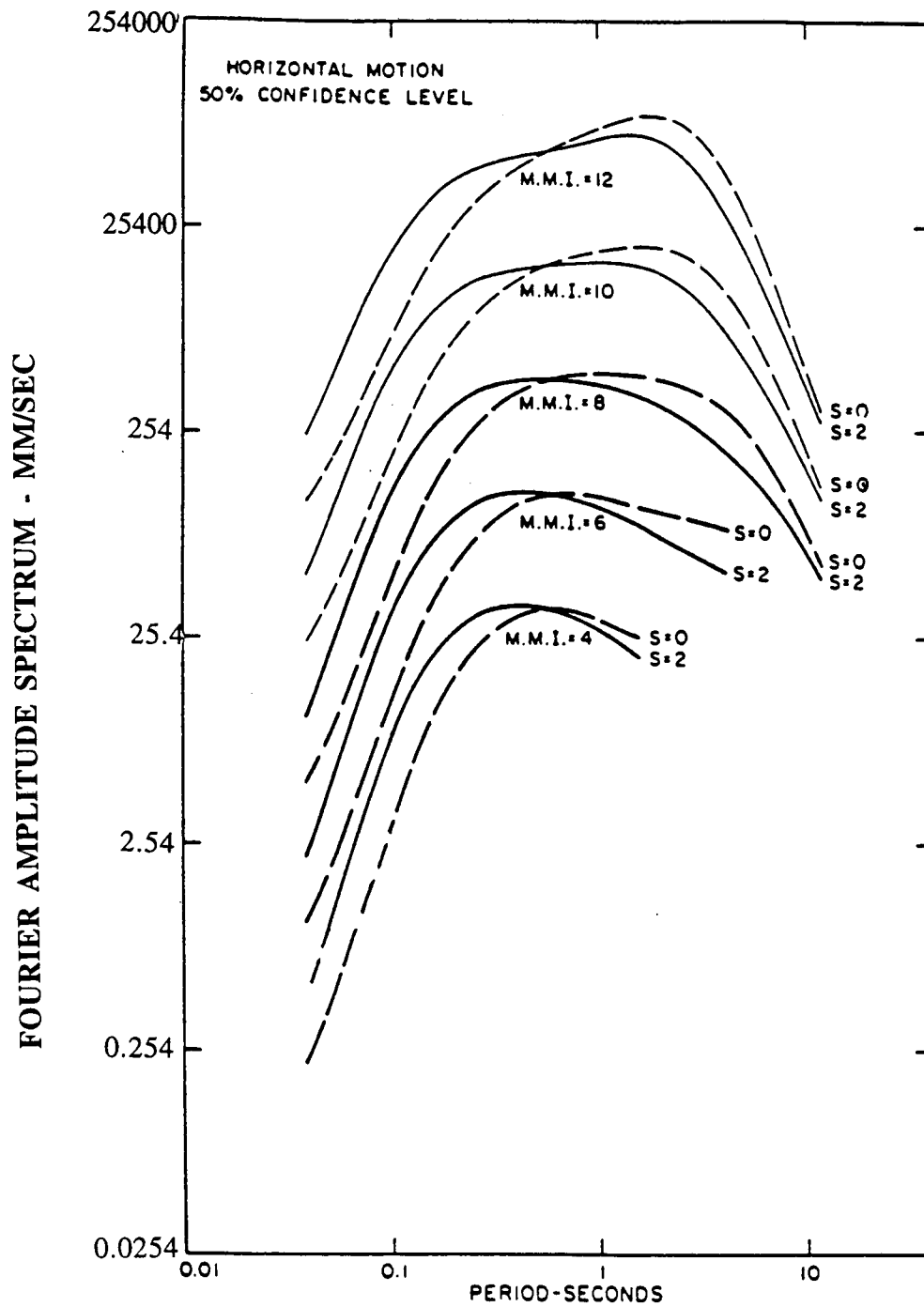
Fig. 3.5: Horizontal (v = 0) Fourier Amplitude Spectra for MMI = 4 - 12, for s = 0 and s = 2, and for p = 0.5 [After Trifunac (1979)]
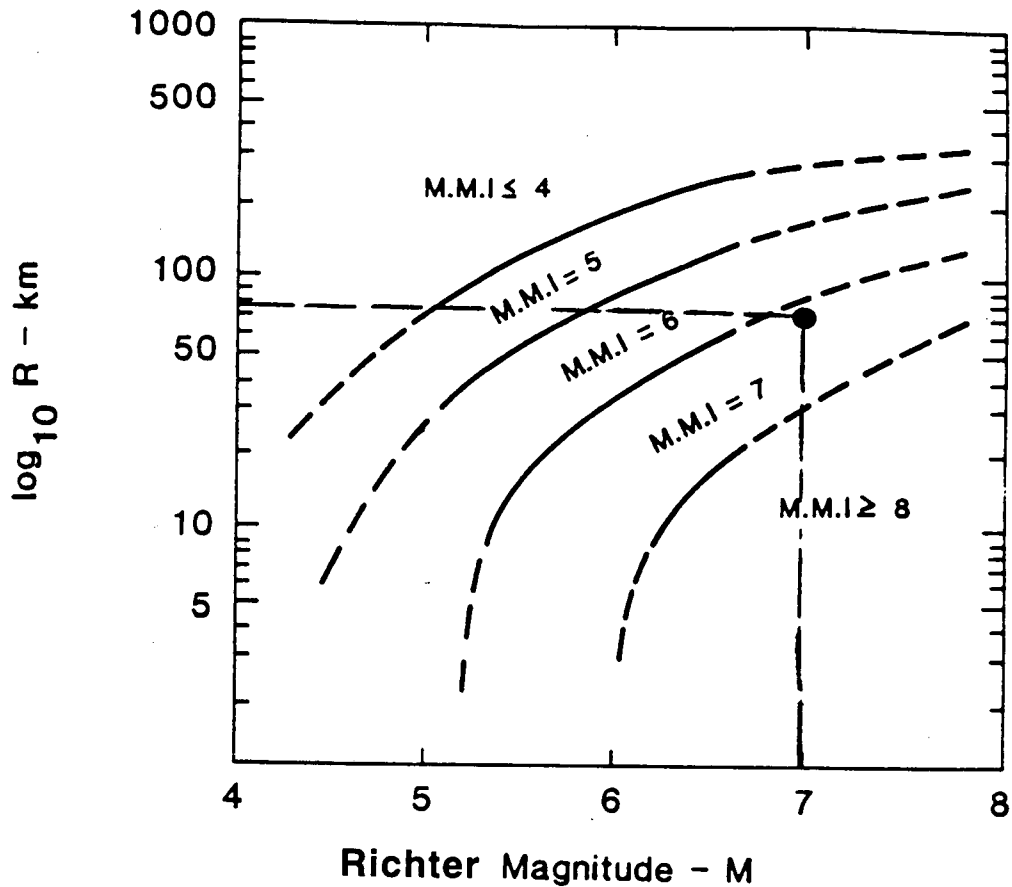
Fig. 3.6: Rate of Decay of MMI with Epicentral Distance, R, and Magnitude, M [After Trifunac (1979)]

Filtering of Acceleration Record

A recursive type of low-pass digital filter was used to eliminate higher frequency content (above 10 Hz) and noise from the predominant low frequency content of the unscaled acceleration record. This filter is characterized by the following equation:

$$Y_n = (1-A)X_n + AX_{n-1} \, , \qquad (3.5)$$

where, Y_n = Filtered value of acceleration,

X_n = Original, unfiltered value of acceleration,

37

A = Parameter indicating the degree of filtering (A = 0 corresponds to no filtering, A = 1 corresponds to maximum filtering, A = 0.7 was used in the present study); and

n = time step designator.

Matching the Spectrum of the Acceleration Record to the Target Spectrum

The frequency spectrum of the filtered, unscaled horizontal accelerogram was obtained by performing a FFT on the filtered accelerogram. This spectrum was then scaled by multiplying the Fourier amplitude (both the real and the imaginary components) of each point (representing the frequency) in the spectrum by a factor to match the desired target spectrum at each point interpolated from Fig. 3.5, depending upon the magnitude to which the scaling was desired. It was judged that frequencies lower than 0.1 Hz and higher than 10 Hz would not be scaled since their contribution to strong motion is minimal. The results of this operation for scaling to 7.0, 7.5 and 8.0 magnitude events are shown for the Upland event in Fig. 3.7.

The scaled horizontal component of the accelerograms were then transformed back into the time domain, preserving the phase difference between the frequencies. These time histories are shown in Fig. 3.8 for the Upland event. The phase difference before and after scaling for the magnitude 7.0 Upland event is shown in Fig. 3.9.

3.2.3 Extended Accelerograms

The duration of strong shaking during higher magnitude events, such as Richter 7.0, 7.5 and 8.0, usually ranges from 25 secs - 50 secs [Seed et al. (1975)]. To account for the increased length of the period of strong shaking in the higher magnitude events, the duration of strong shaking in the scaled accelerograms, i.e. the portion of the record from 25 - 40 secs (duration of strong shaking), was repeated with the tail portion of the record

38
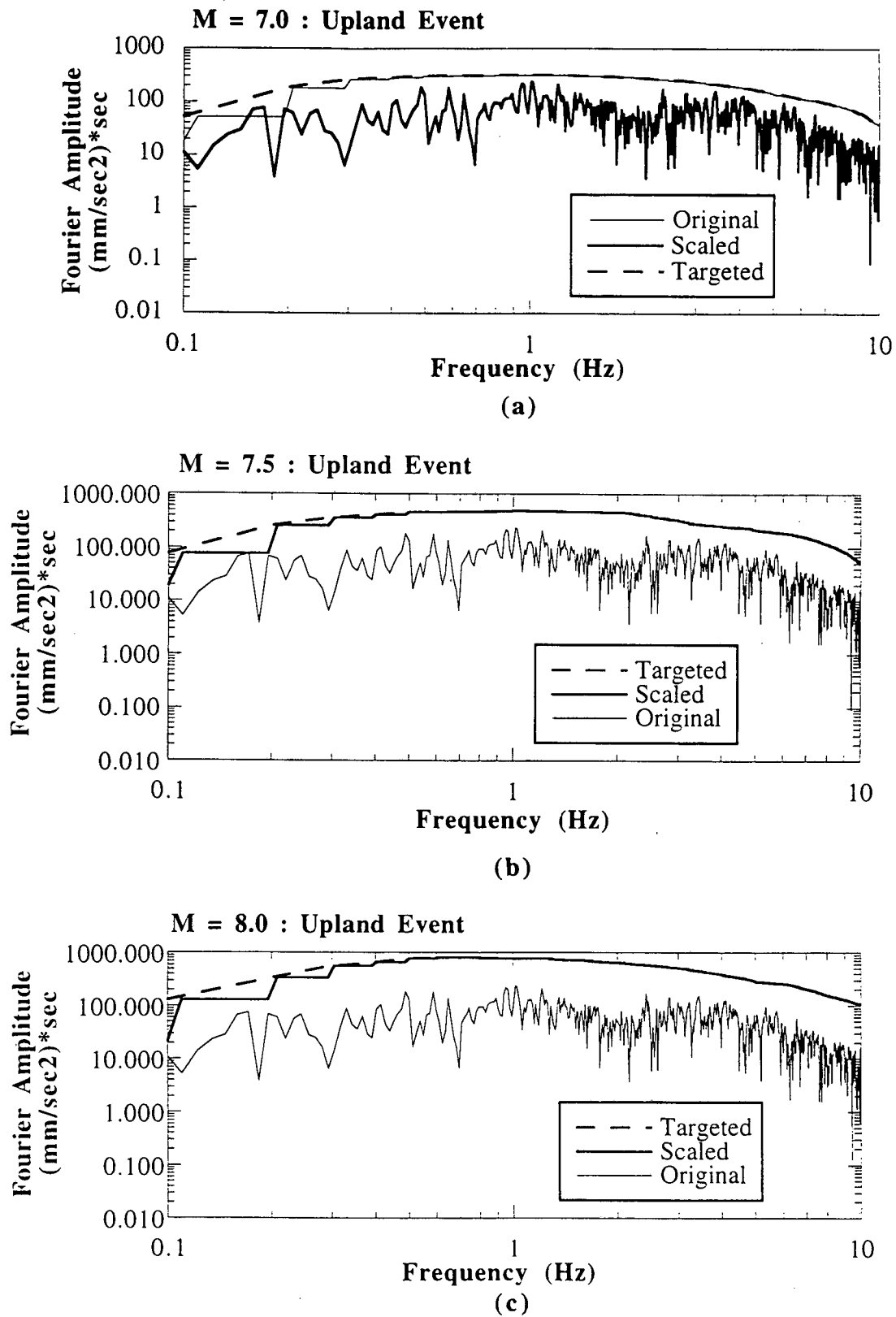
Fig. 3.7: Fourier Amplitude Spectra for the Scaled Magnitudes,
M = 7.0 (a), M = 7.5 (b), and M = 8.0 (c) of the Upland Event
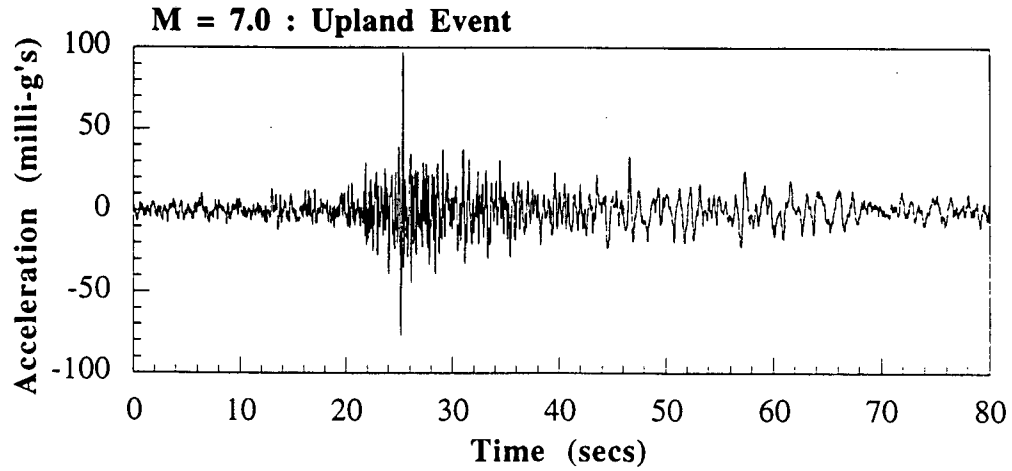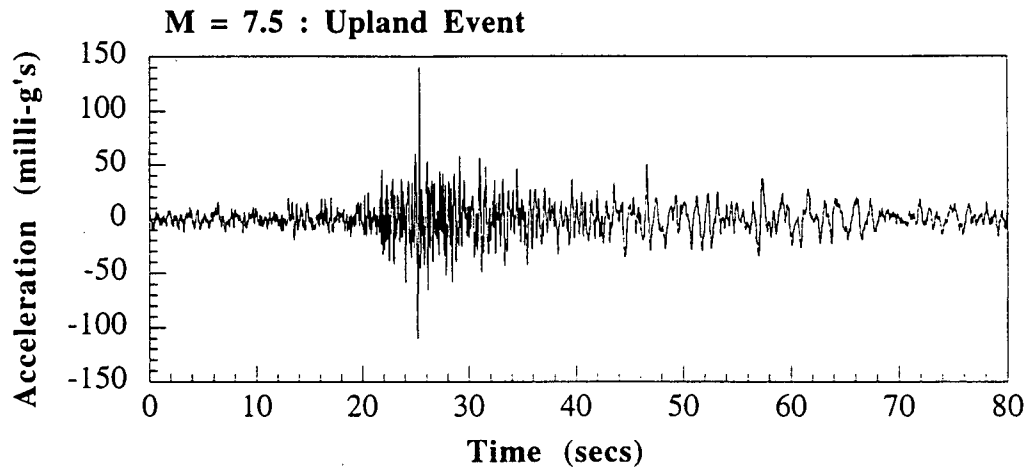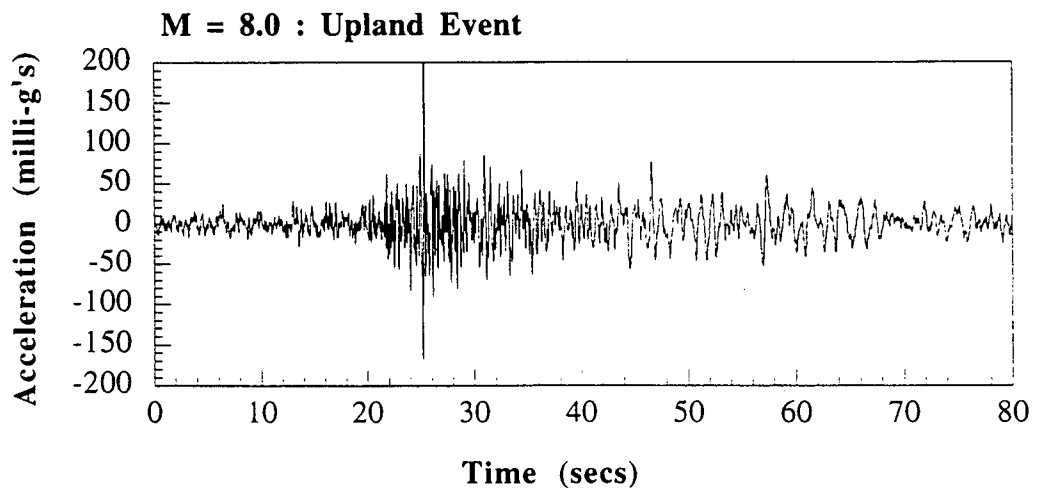
Fig. 3.8: Scaled, Vectorally Combined Horizontal Component of the Upland Event (a) M = 7.0, (b) M = 7.5, (c) M = 8.0

Unscaled Horizontal Component - Upland Event

(a)

M = 7.0 - Scaled Horizontal Component - Upland Event

(b)
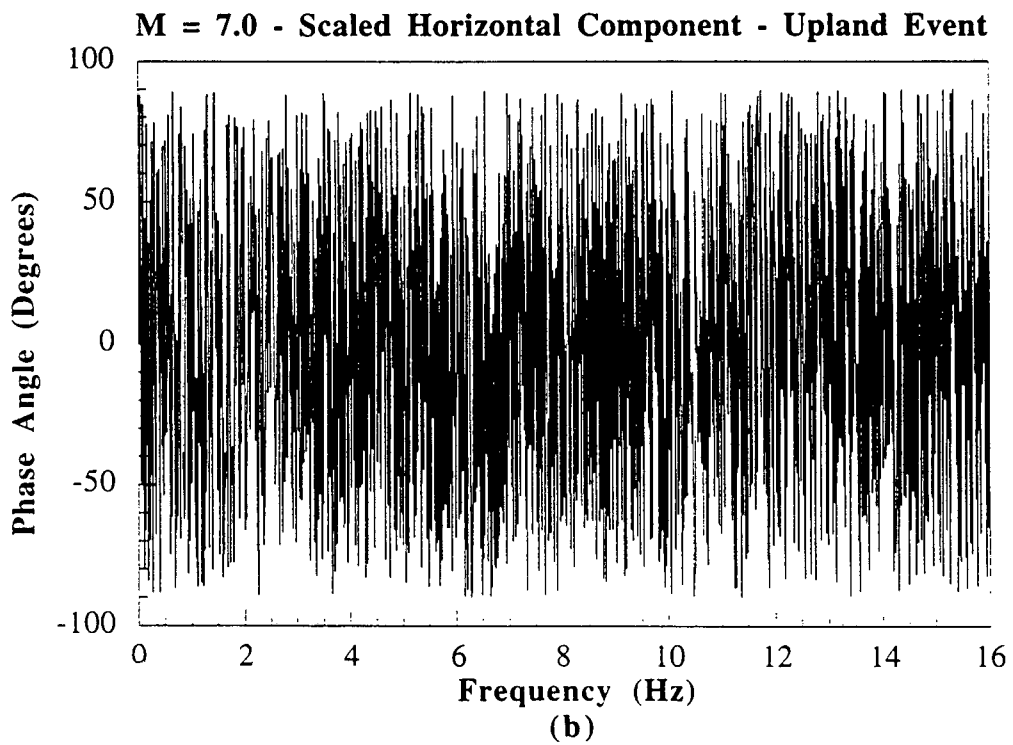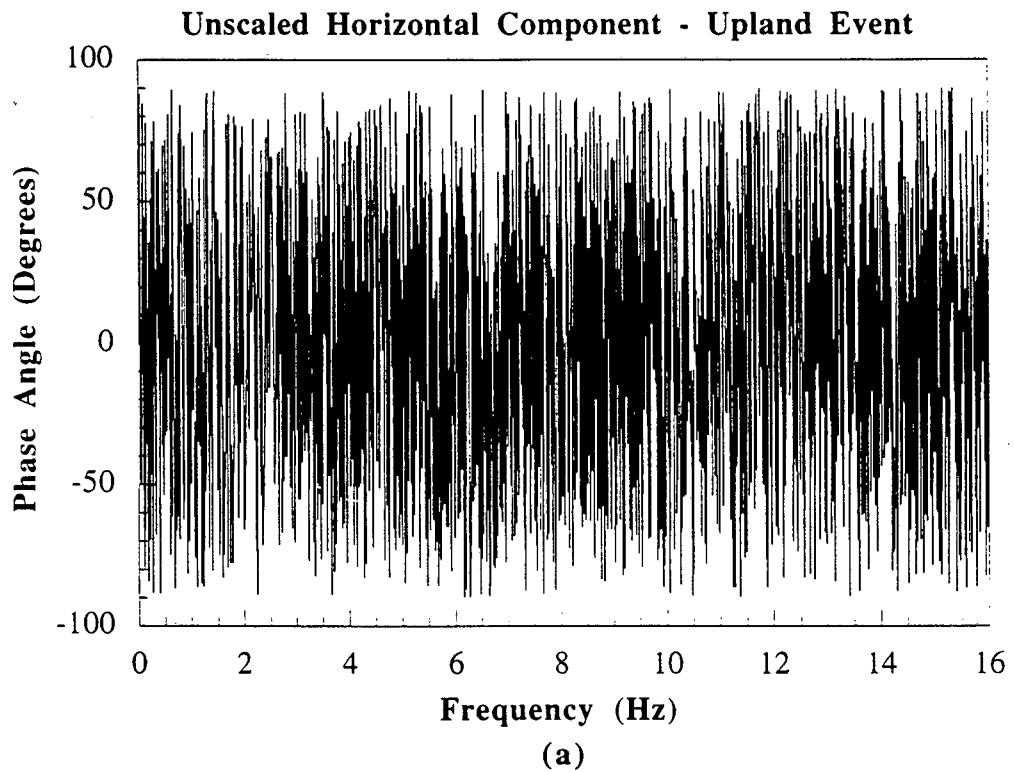
Fig. 3.9: Comparison of Phase Angles for the Unscaled (a) and Scaled (b) Upland Event

41

remaining unchanged to develop an extended accelerogram. Figs. 3.10 (a), 3.11 (a), and 3.12 (a) show the extended accelerograms for the three scaled magnitudes for the Upland event. The extended acceleration records for the Oceanside event have been attached in Appendix A.

3.2.4 Displacement-Time Records

The extended scaled accelerograms for each magnitude were then integrated once to obtain the velocity-time histories and twice to obtain the displacement-time histories. The integrated time records are sensitive to the number of points selected in the integration process. Hence, the number of points for the integration was selected such that the mean value of the acceleration and the mean value of velocity at the end of the window were zero. Sensitivity studies resulted in 7900, 7780, and 8180 data points for the magnitude 7.0, 7.5 and 8.0 records, respectively. Figs. 3.10(b), 3.11(b), 3.12(b) show the velocity-time histories for the Upland Event and Figs. 3.10(c) , 3.11(c), 3.12(c) show the displacement-time histories that resulted from integration of the velocity-time records. Displacement-time histories for the Oceanside event are attached in the Appendix A. In addition to scaling the magnitudes of the two events upwards, the displacement and time axes of the scaled events shown in Figs. 3.10 - 3.12 were scaled downwards by a factor of 0.19 to model the diffusion characteristics of pore water. This factor is discussed further in Chapter 4. These scaled displacement-time histories were used to control the base motion of a pressurized test chamber into which a model pile was driven, details of which are given in Chapter 4.

M = 7.0 : Upland Event

(a)

M = 7.0 : Upland Event

(b)

M = 7.0 : Upland Event

(c)
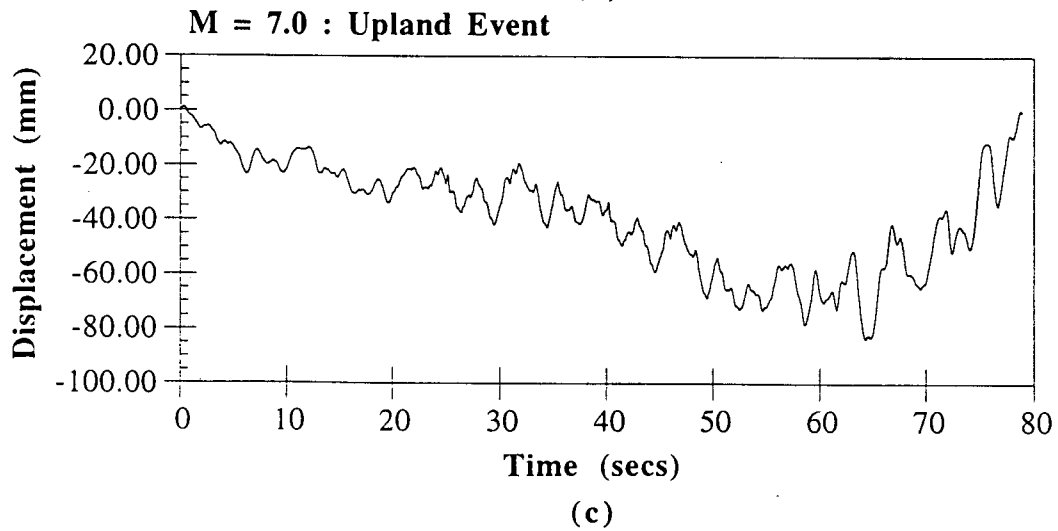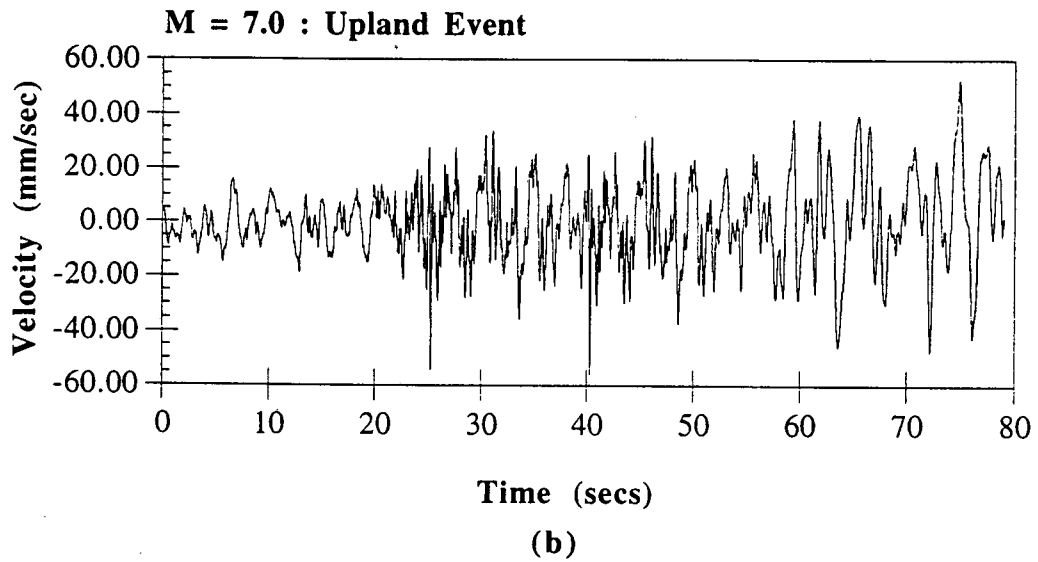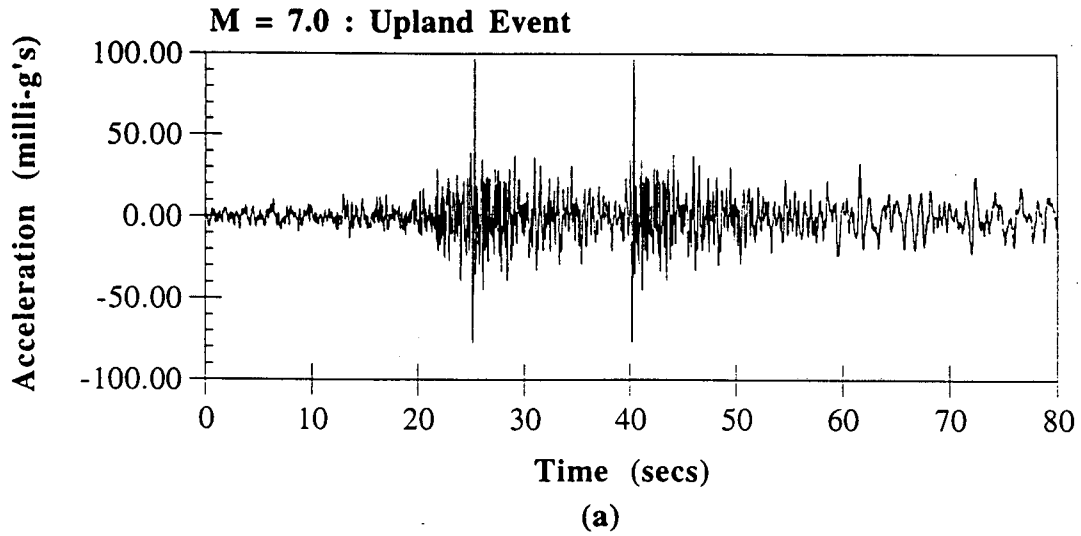
Fig. 3.10: Time Records of the Scaled M = 7.0, Upland Event:
(a) Extended Acceleration, (b) Velocity, and (c) Displacement
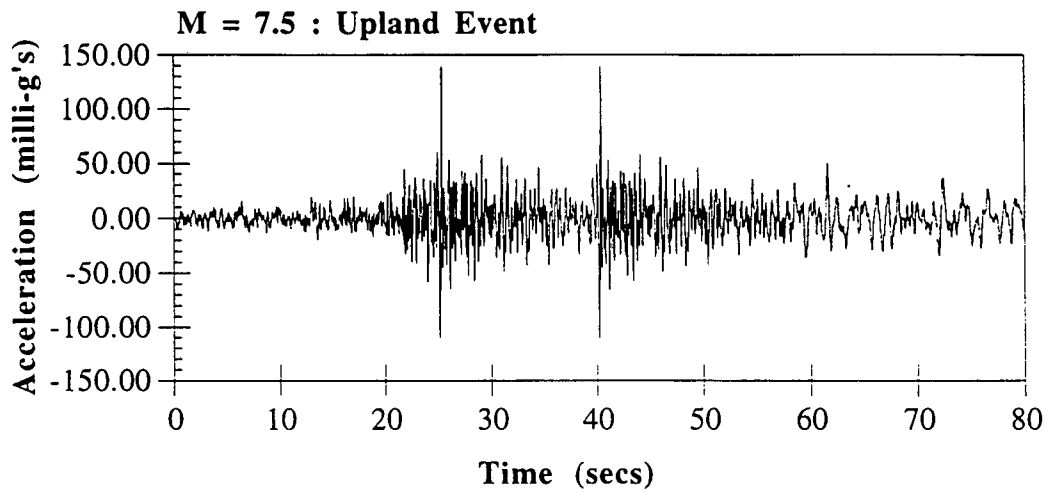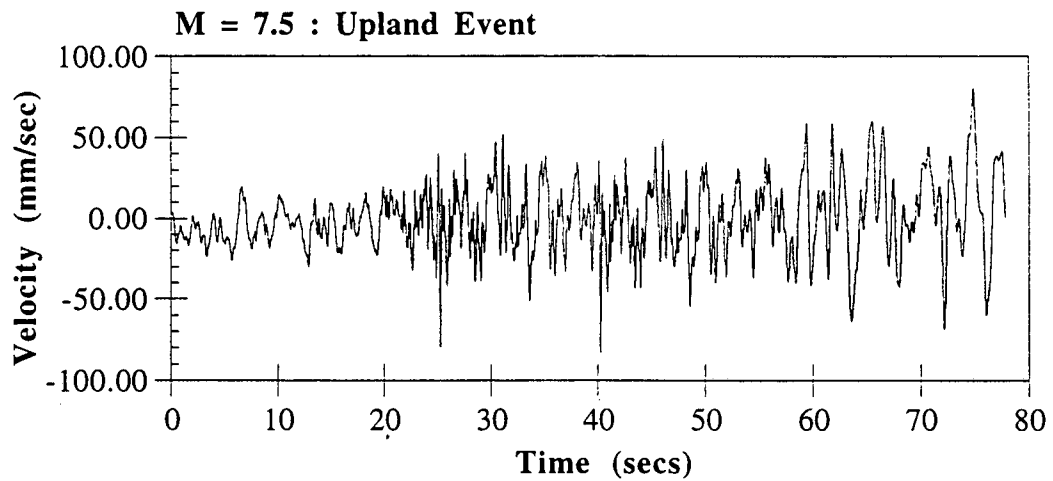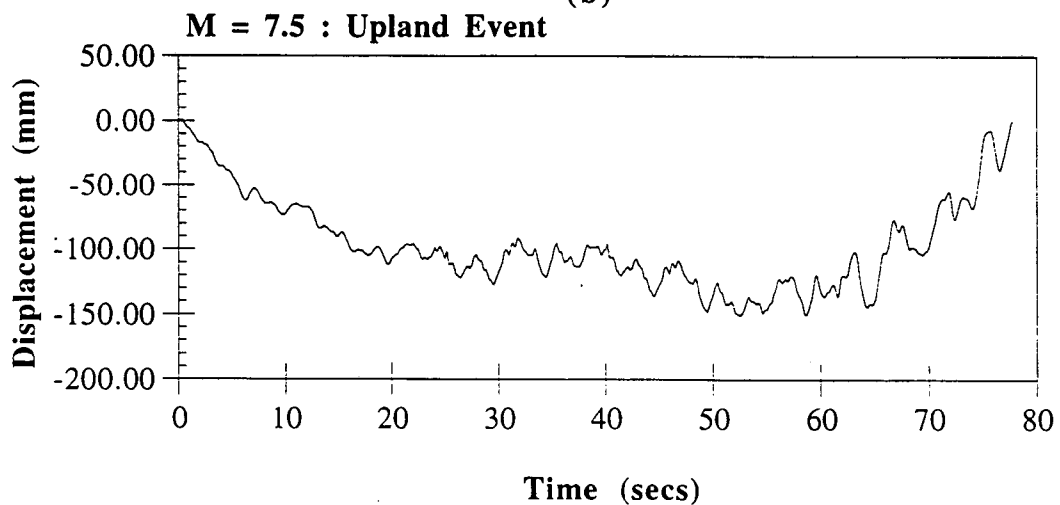
Fig. 3.11: Time Records for the Scaled M = 7.5, Upland Event:
(a) Extended Acceleration, (b) Velocity, and (c) Displacement
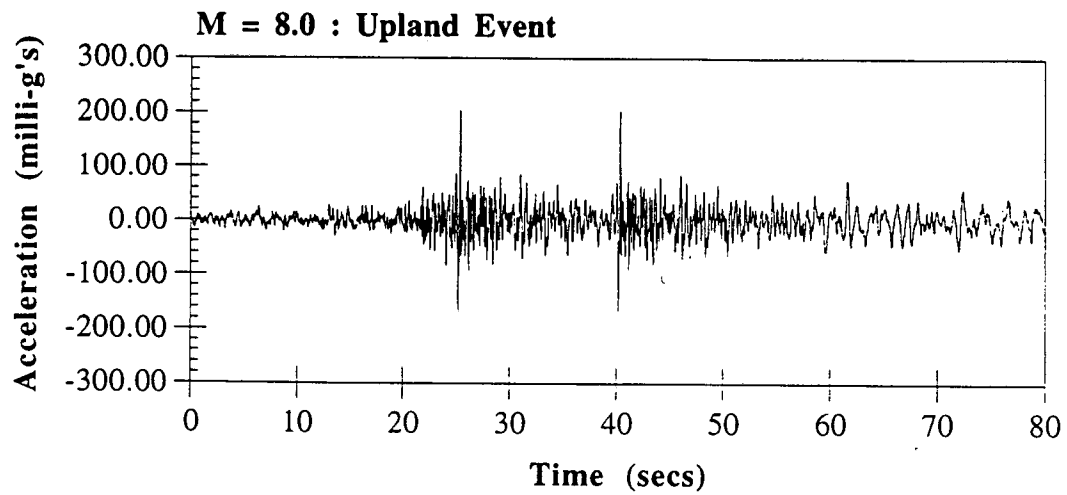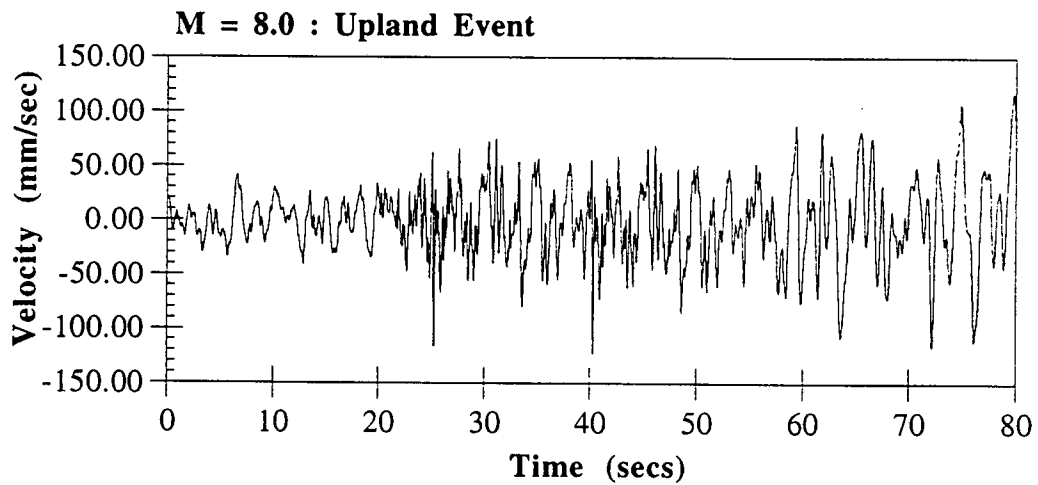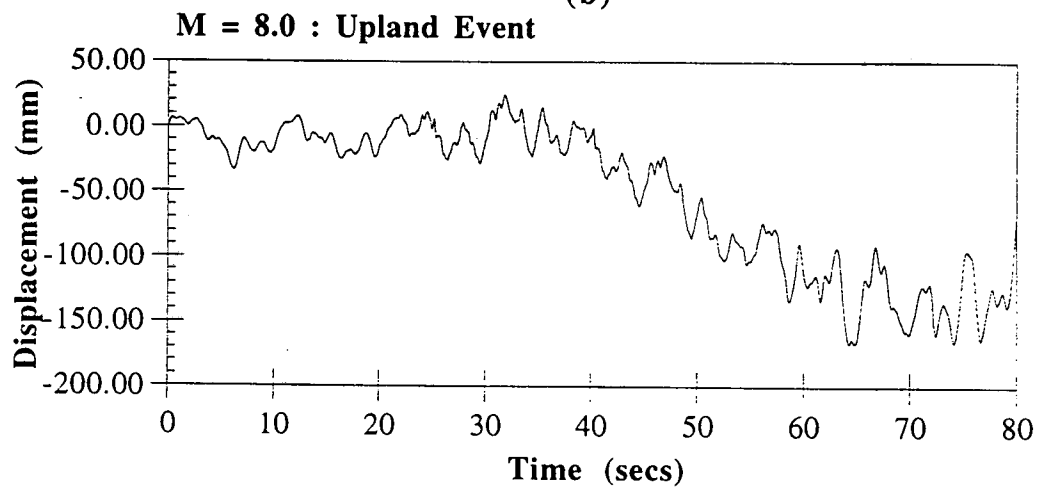
Fig. 3.12: Time Records for the Scaled M = 8.0, Upland Event:
(a) Extended Acceleration, (b) Velocity, and (c) Displacement

45

3.2.5 Validation

Peak Ground Motion

Based on regression analysis of ground motion data for the San Fernando and Parkfield earthquakes, Orphal et al. (1974) suggested equations for predicting peak ground motion for California earthquakes as a function of earthquake magnitude and focal distance. These equations were also found to be useful in predicting peak earthquake accelerations for a reasonably wide range of magnitudes, epicentral locations, focal depths and focal distances at numerous locations around the world.

The following predictive equations for peak ground motion were suggested :

$$\text{Acceleration (a)} = 6.6 \times 10^{-2} \, 10^{0.4M} R^{-1.39}, \tag{3.6}$$

where a is in g's, M is the Richter magnitude, and R is the focal distance in (km);

$$\text{Velocity (v)} = 7.26 \times 10^{-1} 10^{0.52M} R^{-1.34}, \tag{3.7}$$

where v is in cm/sec, M is the Richter magnitude, and R is the focal distance (km);

$$\text{Displacement (d)} = 4.71 \times 10^{-2} 10^{0.57M} R^{-1.18}, \tag{3.8}$$

where d is in cm, M is the Richter magnitude, and R is the focal distance (km).

Comparisons of the horizontal peak ground motion data for the scaled records for the Oceanside event and the Upland event with the values computed from the above predictive equations are shown in Fig. 3.13. The comparisons indicate that the peak values of the scaled records are realistic for typical Californian earthquakes.

Measured Vs. Target Spectra

To ensure that the displacement-time history applied to the servo-hydraulic machine that applied the scaled ground motion to the pressure chamber used in the experiments did indeed reproduce the intended acceleration-time history, records of acceleration-time histories were made by means of a low-g accelerometer mounted underneath the bottom of
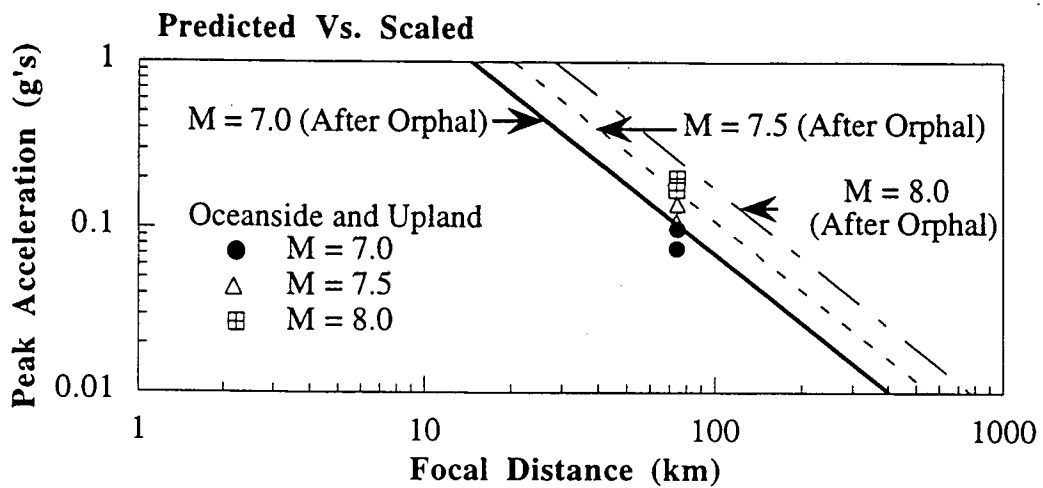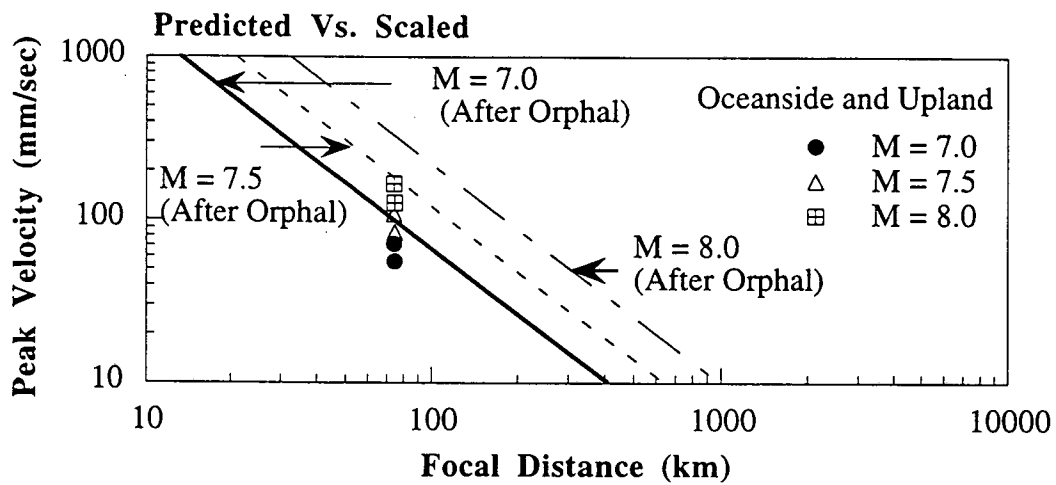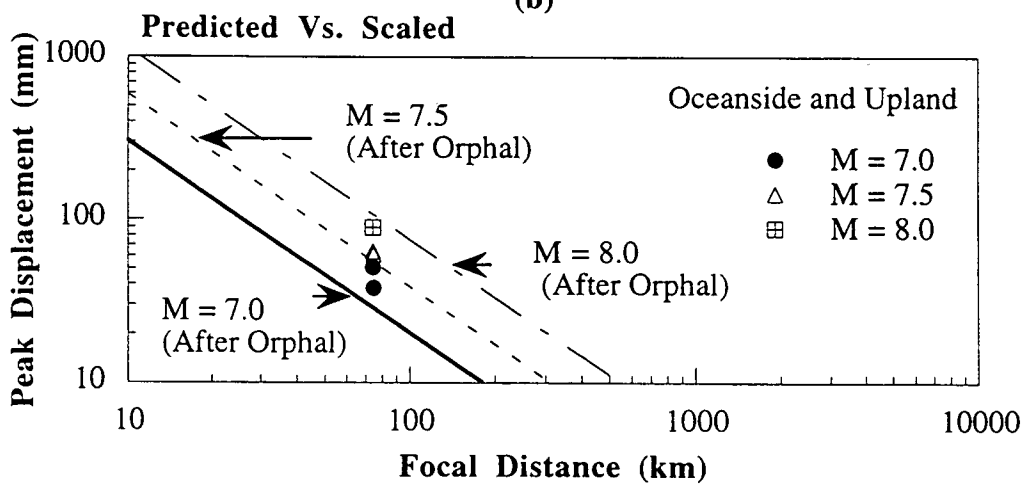
Fig. 3.13 : Comparison of Peak Ground Motions From the Scaled Records with the Predicted Values From Equations [Orphal et al., (1974)]

the rigid plate on which the chamber was seated during the applied motion. Fig. 3.14 shows the comparison of measured and target spectra for the different simulated magnitudes of the Upland event. The Fourier amplitude spectrum of the recorded response accelerogram was in good agreement with the original spectrum of the scaled accelerogram for all magnitudes at frequencies less than 4 Hz. Higher frequencies appeared to have been damped somewhat because of filtering caused by the servo-hydraulic system. This effect was not preventable with available testing equipment.
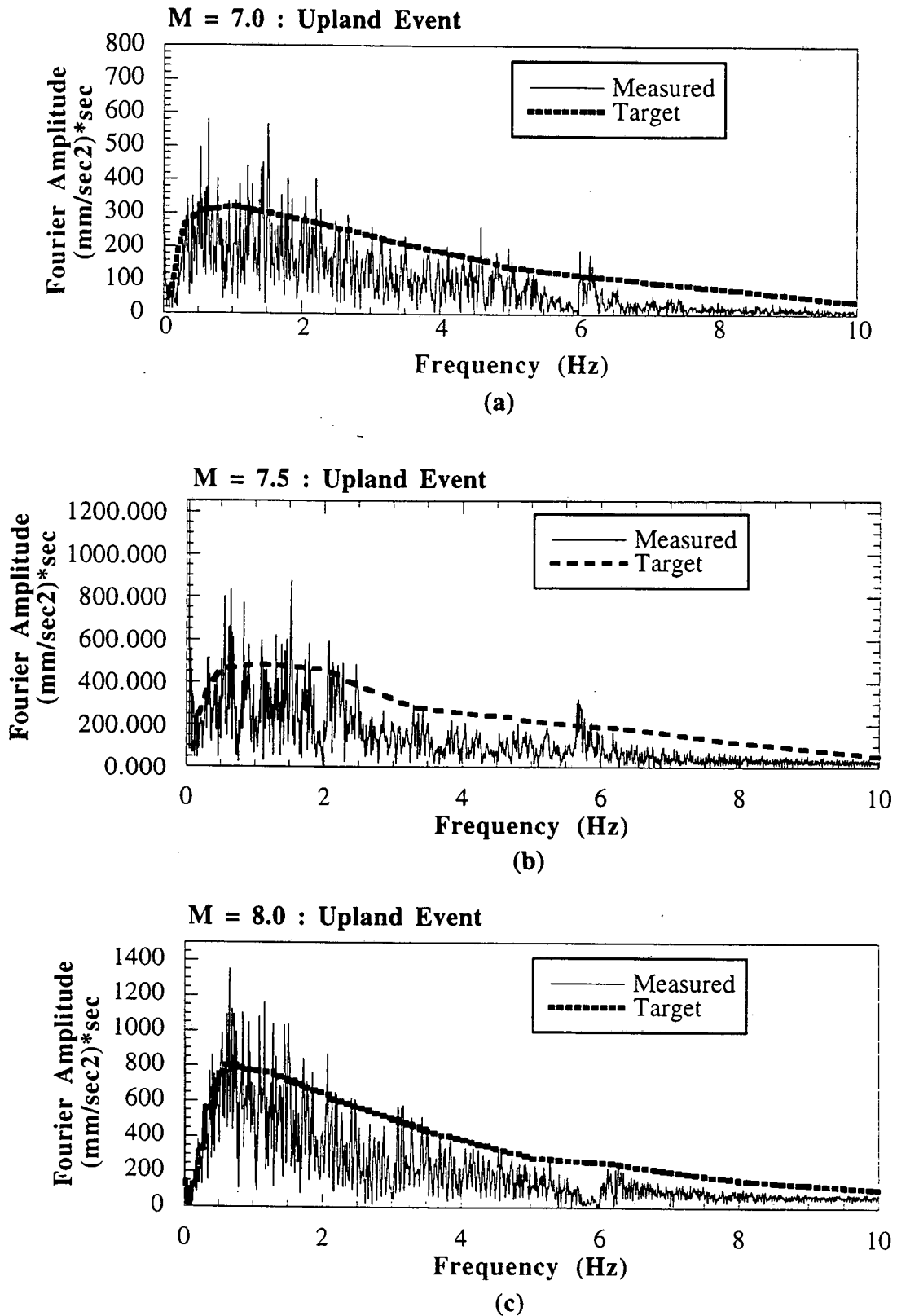
Fig. 3.14: Comparison of Measured and Target Acceleration Spectra for the Applied Horizontal Motion

Chapter 4
EXPERIMENTAL STUDY

4.1 Introduction

The performance of tension piles under ground excitation and seaquakes produced by earthquakes was studied by conducting model tests in a pressure chamber. The experimental controls, testing assembly and experimental protocol employed in the physical modeling of the process have been explained in the following sections.

The experiments were conducted on model piles. Similitude between the model pile conditions and prototype conditions were maintained as closely as possible. However, pressure chamber testing, while inexpensive and well-adapted to parametric studies, suffers from some limitations. The principal limitation is that the initial ambient effective stresses in the soil do not vary with depth, as occurs in the natural soil deposit. Therefore, a fundamental assumption is made that all effects involving effective stress in the soil scale according to the average stresses in the soil around the model and prototype, rather than the vertical gradient of stresses, which can be scaled in a centrifuge. Scaling issues will be addressed in Sec. 4.3.

4.2 Experimental Controls

4.2.1 Test Soil

The soil used for the experimental study consisted of fine, uniformly graded siliceous blasting sand mixed together with finely ground glass beads (grade 170/325) in the proportion of 3:1. Both of these materials were readily available commercially at CLEMTEX, Inc., located in Houston, Texas, and could be reused repeatedly for several tests without undergoing any change in mechanical properties [Ochoa (1990)]. The

selection of a very fine sand was necessary in order to scale the permeability of the prototype. It was judged that sand relative densities of practical interest for such a study would be in the range from 55% - 60%, which is representative of offshore California deposits and other continental shelf deposits outside of pro-delta regions. The test soil was deposited in the pressure chamber using the dry pluviatile (raining) technique, as this method of sample preparation had been shown in the past to have exhibited a greater degree of susceptibility to liquefy than other deposition methods, such as compaction or vibration [Vaid and Negussey (1984)].

The composition of this sand was slightly different from that of the sand used by Ochoa (1990) for shaking tests performed in a previous study. Since the results of the tests performed by Ochoa were to be used for comparison with the results from this study, it was considered important to ensure that the properties of the sand used were reasonably close. Laboratory tests were therefore conducted to characterize the sand for this purpose. The following tests were conducted: grain size distribution, permeability, triaxial shear, resonant column, direct interface shear and one-dimensional cyclic confined compression. Although these tests do not necessarily reflect the stress paths the soil elements would undergo in the chamber during the process of pile driving or during the shaking tests, they nevertheless provide valuable information about the volume change characteristics of the soil and mechanical properties such as strength, modulus and damping characteristics.

Grain Size Distribution

According to the Unified Soil Classification, the test sand, which was a mixture of fine sand and glass beads, was classified as "SP" (Very fine poorly graded sand). Its effective size, D_{10}, was equal to 0.107 mm, and the coefficient of uniformity, C_u, was 1.87. The grain size distribution is shown in Fig. 4.1.

Minimum and Maximum Densities

In order to control the actual dry density required for the attainment of a target relative density, maximum and minimum values of dry densities as defined by ASTM standards D 4253 and D4254 were obtained for the sand. The maximum and the minimum dry density values are 18.12 kN/m^3 and 15.51 kN/m^3, respectively.

Permeability

Results from variable-head permeability tests performed on 64-mm diameter X 102-mm length cylindrical saturated samples deposited by raining into the permeameter cell indicated an average coefficient of permeability in the order of 3 x 10^{-2} cm/sec for a relative density of 50%.
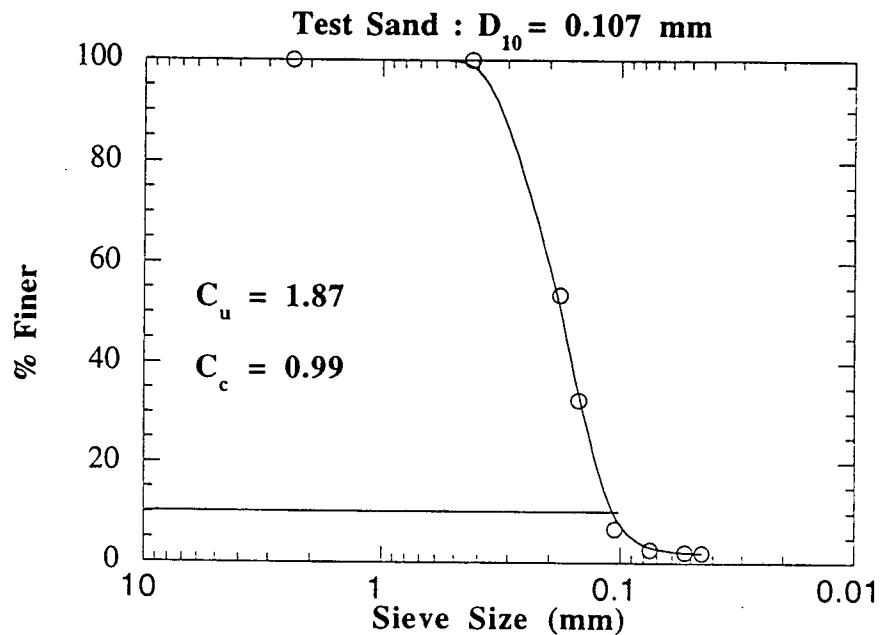
Fig. 4.1: Grain Size Distribution Curve for Test Sand

Triaxial Shear

Consolidated drained (CD) triaxial shear tests were performed on specimens with a relative density of 55% +/- 5% . Samples of length 68 mm and diameter 35 mm were prepared by raining the sand into split molds and then saturating them under gravity. The samples were then consolidated isotropically under a selected confining pressure and sheared monotonically by increasing the stress in the major principal direction at a controlled displacement rate of 0.076 mm/min. The tests were carried out at confining pressures of 69 kPa, 138 kPa, and 276 kPa. Volume strain during shear was calculated by measuring the amount of water flowing into or out of the specimen from a burette that communicated with the specimen. The results of the CD triaxial tests are plotted in Fig. 4.2. Part a of the figure shows the variation of deviatoric stress vs. axial (major principal) strain for different confining stresses, and Part b of the figure shows volumetric strain (the ratio of volume change of the specimen to its original volume) vs. axial strain, both expressed as a percentage. It can be seen from the results that under the medium-dense test condition, the test soil shows very little contractive behavior up to 75% of the peak deviator stress, the magnitude depending on the confining pressure, following which it dilates and continues to do so even after the sample has failed in shear. The drained shear strength parameters, c_d and ϕ_d, were obtained from the p-q envelope (a plot of maximum shear stress vs. the mean effective stress in the specimen) shown in Fig.4.3. The values of c_d = 0 and ϕ_d = 36.5 degrees were obtained.

Direct Interface Shear

The interface shear strength properties between the test sand and the pile material (steel) were investigated by conducting interface shear tests in a direct shear apparatus. A round steel plate of 63 mm diameter, made up of the same material as the pile, was placed

Test Sand - Rel. Density 55 +/- 5%

(a)

(b)
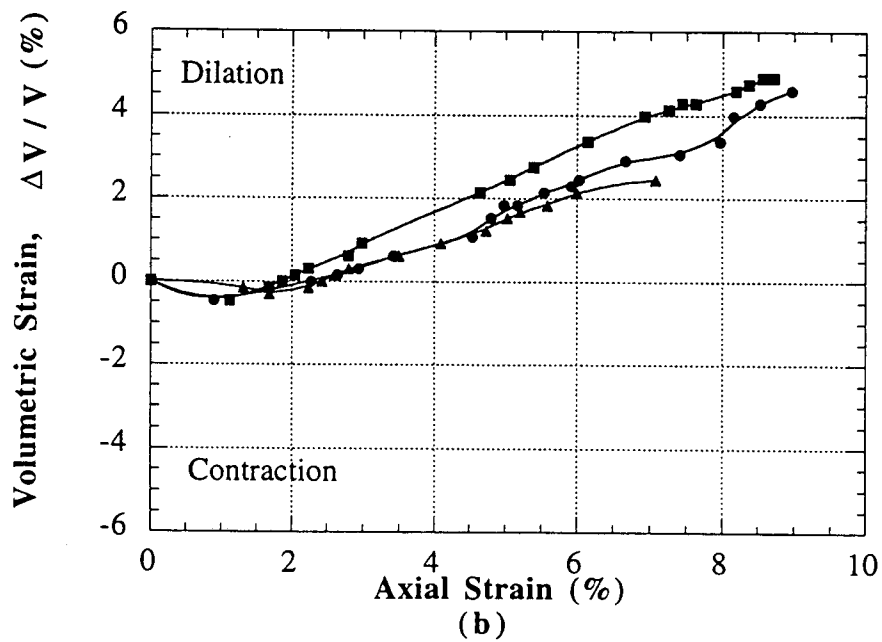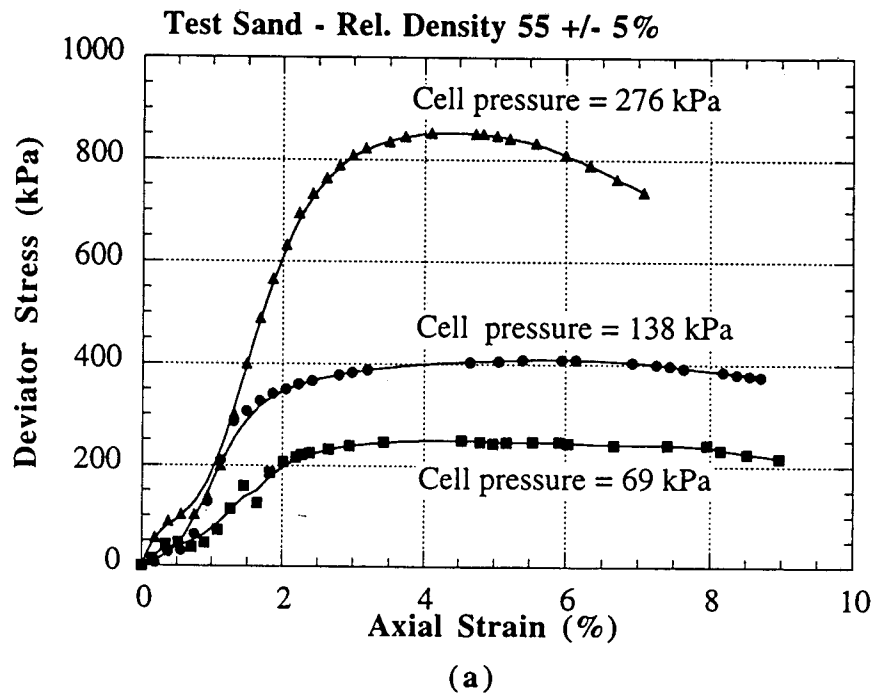
Fig. 4.2 : Consolidated Drained Triaxial Test -
(a) Deviator Stress Vs. Axial Strain
(b) Volumetric Strain Vs. Axial Strain
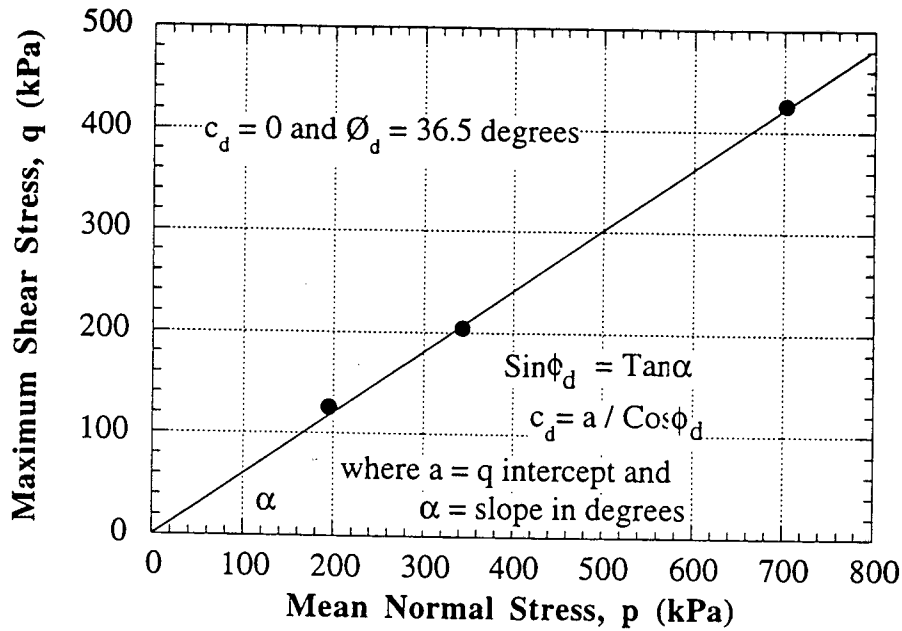
Fig. 4.3: **Consolidated Drained Triaxial Shear Test -**
p - q envelope

in the lower half of the circular direct shear box, and the test sand was deposited over this circular steel plate at a relative density of 55%. The sample was then sheared across the interface in the dry state under normal stresses of 79 kPa, 169 kPa and 259 kPa at a shearing rate of 0.08 mm/min. Fig. 4.4 shows shear stress vs. horizontal deformation and vertical deformation vs. horizontal deformation for the test sand. The plot suggests a tendency towards lesser contractive behavior with decreasing confining stress for the test sand. The interface friction angle, δ, obtained from the plot of shear stress vs. normal stress in Fig. 4.5 is about 27 degrees.

Resonant Column

A Drnevich "Long-Tor" resonant column test apparatus was used to obtain the shear- strain-dependent variation of shear modulus and hysteritic damping values for the

55
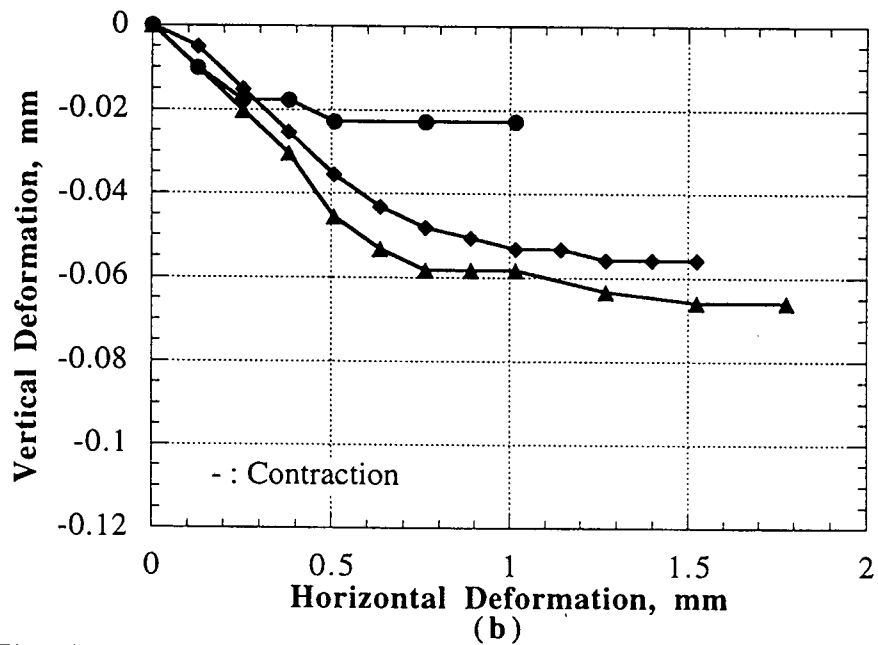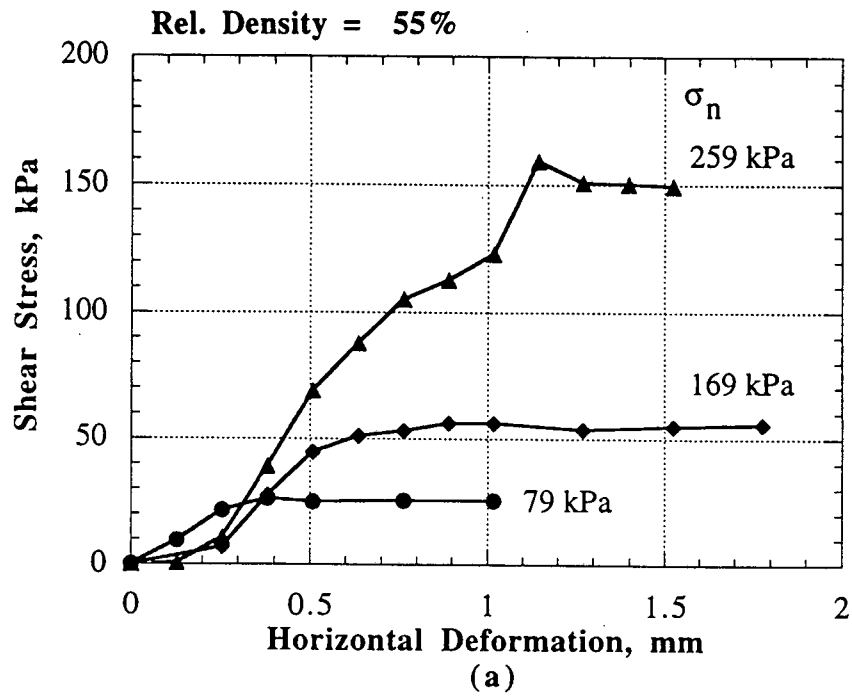
Fig. 4.4 : Direct Interface Shear Test - (a) Shear Stress Vs.
Horizontal Deformation; (b) Vertical Deformation
Vs. Horizontal Deformation
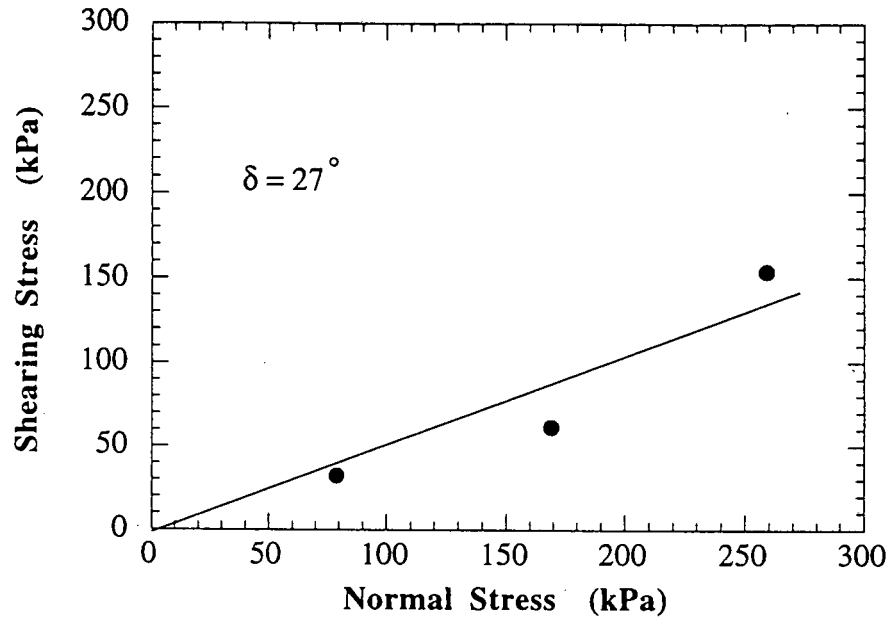
Fig. 4.5: Shear Stress at Failure Vs. Normal Stress for Direct Interface Shear Test

test sand at relative densities in the range of 50%-75%. This information was used for the SHAKE analyses described in Chapter 5. Two samples were tested at different relative densities, 50% and 75%, in a dry state at isotropic confining pressures of 17.24 kPa, 34.48 kPa, 68.96kPa, 137.93 kPa, and 275.8 kPa. The response of each specimen at resonance was determined by monitoring output from micro-accelerometers on the head of the specimen for different levels of the torque applied to the specimen head. The frequency at resonance was recorded at different levels of input torque.

For the Drnevich fixed-base resonant column apparatus [Drnevich (1994)], the shear modulus, G, was computed from the expression,

$$G = \rho \, (2 \pi L)^2 \left(\frac{f_t}{F_t}\right)^2, \tag{4.1}$$

57

where ρ = density of the specimen, L = length of the specimen, f_t = frequency at resonance and F_t = Frequency factor depending upon the geometric properties of the specimen and the active platen of the apparatus

The corresponding shear strain amplitude, γ, was obtained as follows :

$$\gamma = \frac{0.4\ (RCF \times RTO \times d)}{L}, \tag{4.2}$$

where RCF = rotational calibration factor (rads / volt), RTO = rotational transducer output (volts), d = diameter of the specimen and L = length of the specimen.

The damping ratio was computed from the free vibration decay of the motion of the micro-accelerometer recorded on the oscilloscope by stopping the forced vibration of the specimen. The slope of the natural logarithm of the amplitudes of each cycle of free vibration with the number of cycles is the logarithmic decrement, δ. The damping ratio, D_s was then calculated from δ using (4.3).

$$D_s = \sqrt{\frac{\delta^2}{4\pi^2 + \delta^2}}. \tag{4.3}$$

Illustrations of a typical free vibration decay curve and the corresponding logarithmic decrement are shown in Figs. 4.6 and 4.7, respectively.

Hardin and Drnevich (1972) have proposed a hyperbolic relationship for computing shear modulus at any strain level. Using

$$\frac{G}{G_{max}} = \frac{1}{\left(1 + \dfrac{m1\ \gamma}{\gamma_\rho}\right)}, \tag{4.4}$$

where G is the shear modulus at shear strain amplitude, γ, G_{max} is the maximum shear modulus at a reference strain, γ_ρ, and m1 is the shape parameter to represent the strain-dependent shear modulus, a relationship between the shear modulus normalized with maximum shear modulus vs. the normalized dynamic shear strain amplitude at different confining stresses have been computed and are shown in Fig. 4.8 and Fig. 4.9 for the test sand at 50% and 75% relative density, respectively. As seen from these figures, the shear modulus reduces with strain amplitude, a trend that has been reported for other siliceous sands as well [Saxena and Reddy (1989), Sherif (1977)].

According to Hardin and Drnevich's (1972) definition, reference strain, γ_ρ, corresponds to a strain below which the shear modulus has a maximum value and remains constant. For all practical purposes for shear strains less than about 5×10^{-4} %, shear modulus remains constant. The range of shear strains developed during the testing was from 7×10^{-4} (%) to 0.1%; therefore, $\gamma_\rho = 7 \times 10^{-4}$ was used for this study.

Shape parameter m1 can be related exponentially to effective confining stress σ_0 as shown in Fig. 4.10 by (4.5), in which p_a = atmospheric pressure.

$$m1 = 0.0231 \exp\left(\frac{0.5\,\sigma_0}{Pa}\right) \tag{4.5a}$$
$$\text{for 50% relative density and } 0.1 < \frac{\sigma_0}{Pa} < 1.4 \,.$$

$$m1 = 0.0173 \exp\left(\frac{0.5\,\sigma_0}{Pa}\right) \tag{4.5b}$$
$$\text{for 75% relative density and } 0.1 < \frac{\sigma_0}{Pa} < 2.75$$

The maximum shear modulus was found to be related approximately to the cube root of the effective confining pressure according to

$$G_{max}\,(kPa) = 28594(\sigma_0)^{0.32} \tag{4.6a}$$
$$\text{for 50% relative density and } 17.24 < \sigma_0 < 137.9 \,\,(kPa)\,;$$

Fig. 4.6: Typical Free Vibration Decay Curve

75% Rel. Density, σ = 68.76 kPa @ 0.02 % Strain Amplitude

Logarithmic Decrement = 0.084

Damping Ratio = 1.5 %
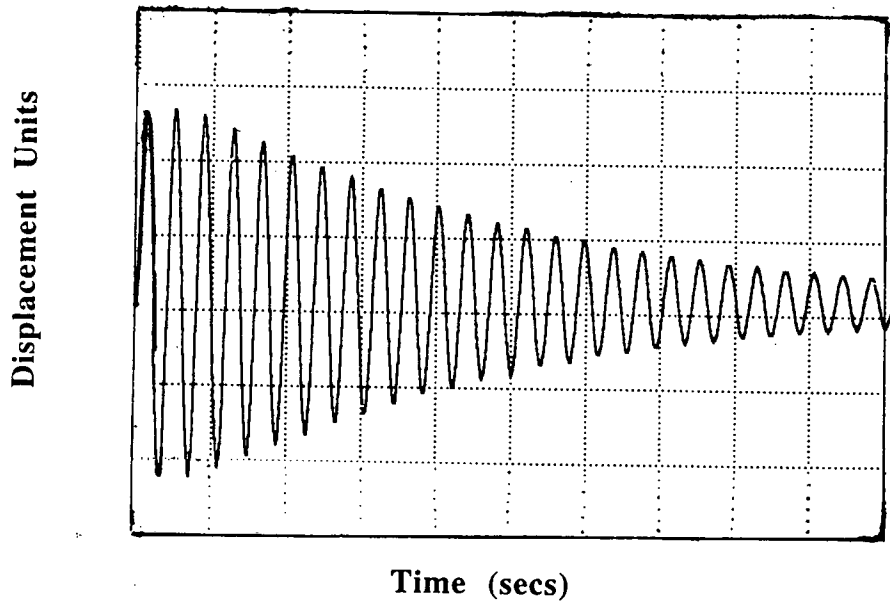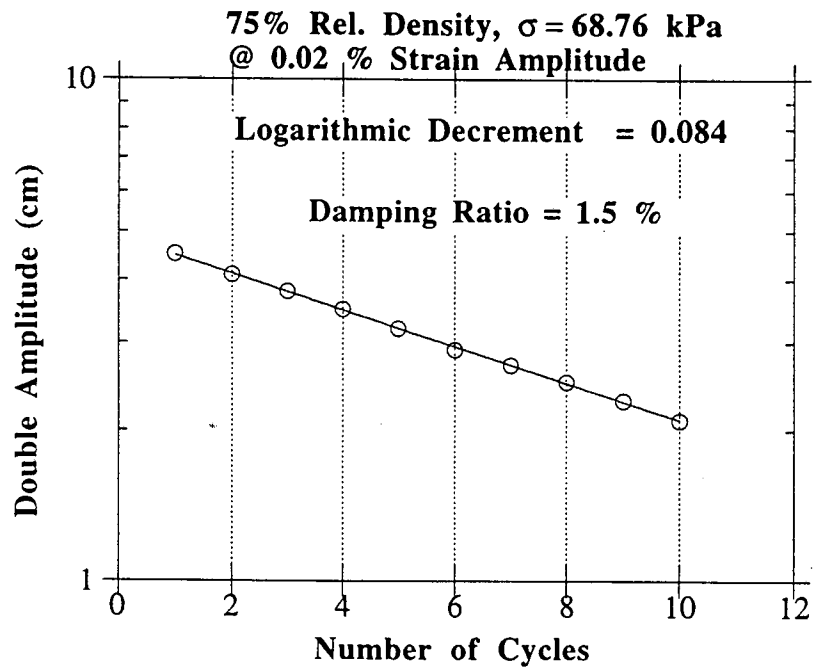
Fig. 4.7: Analysis of Free Vibration Decay

$$G / G_{max} = 1/ (1 + m1\gamma/ \gamma_\rho)$$

- 17.24 kPa
- 34.68 kPa
- 68.76 kPa
- 137.93 kPa

γ_ρ = Reference Strain = 0.0007 %
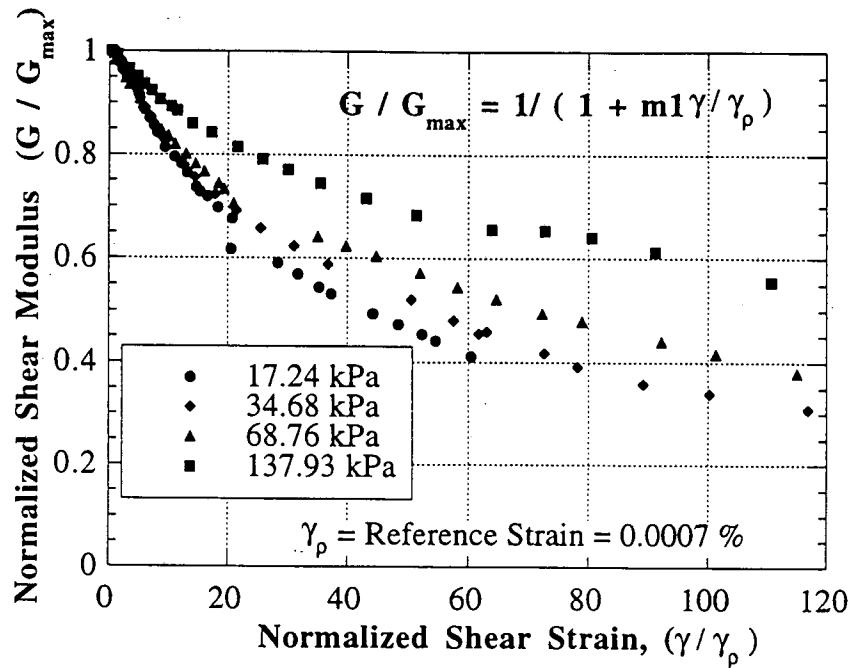
Fig. 4.8: Variation of Shear Modulus with Dynamic Shear Strain Amplitude - Rel.Density = 50%

$$G / G_{max} = 1/ (1+m1\gamma/ \gamma_\rho)$$

- 17.24 kPa
- 34.48 kPa
- 68.96 kPa
- 137.93 kPa
- 275.8 kPa

γ_ρ =Reference Strain = 0.0007 %
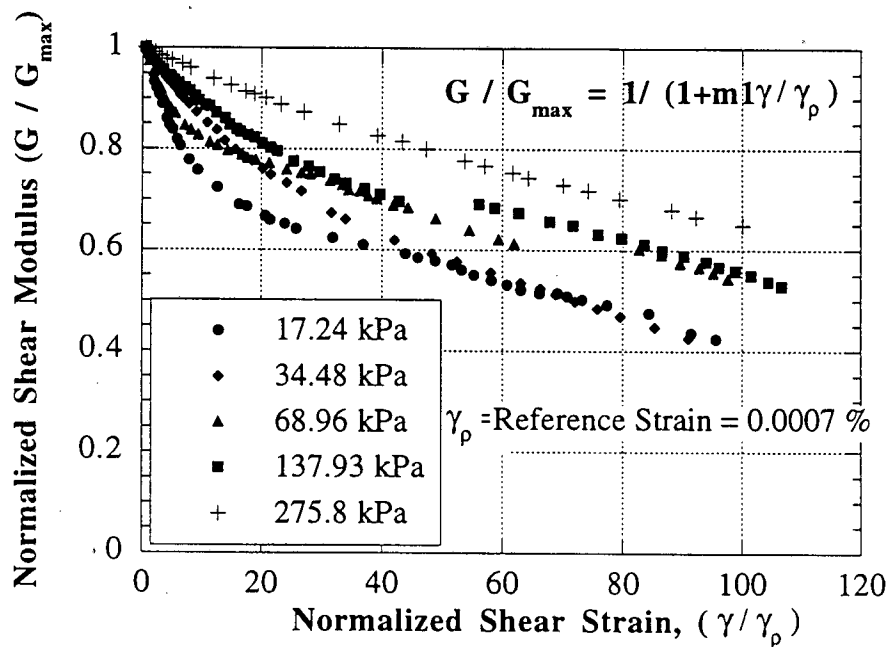
Fig. 4.9: Variation of Shear Modulus with Dynamic Shear Strain Amplitude - Rel. Density = 75%

$$G_{max} \text{ (kPa)} = 41173(\sigma_o)^{0.32} \qquad \qquad (4.6b)$$
$$\text{for 75\% relative density and } 17.24 < \sigma_o < 275.8 \text{ (kPa) ;}$$

as shown in Fig. 4.11.

Predicted values of shear modulus for different levels of shear strain amplitude using (4.4), (4.5) and (4.6) provide a reasonable approximation to experimental values, as seen in Fig. 4.12.

Fig. 4.13 shows the increase in damping values with increase in shear strain amplitude. Also, with increase in confining pressure, the damping values decrease at higher levels of shear strain amplitude, irrespective of the relative density of the sand. However, appreciable distinction in the damping values is not seen at lower levels of shear strain amplitude, especially for 50% relative density. A linear relationship between the logarithm of damping ratio and logarithm of shear strain amplitude has been proposed by several investigators [Sherif et al (1977), Saxena and Reddy (1989)]. Fig. 4.14 shows plots of variation of damping ratio in % with shear strain amplitude for different effective confining stresses. This relationship can be expressed as

$$D_S = C_1 \, \gamma^{0.55} , \qquad \qquad (4.7)$$

where D_S is the damping ratio, γ is the dynamic shear strain amplitude, and C_1 is a soil constant that is dependent upon the effective confining stress according to (4.8):

$$C_1 = 15.131 \left(\frac{\sigma_o}{P_a}\right)^{-0.3379} \text{ as per Fig. 4.15 .} \qquad \qquad (4.8)$$

One-Dimensional Cyclic Confined Compression

One-dimensional cyclic confined compression tests were separately executed in a consolidometer device. The inner diameter and the height of the ring were 63.5 mm and
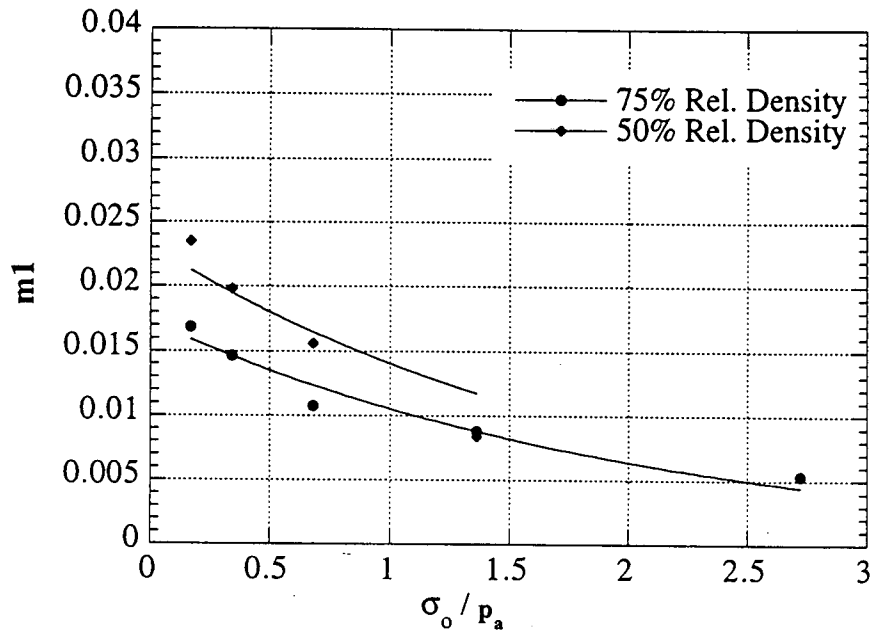
Fig. 4.10: Shape Parameter m1 Vs. Effective Confining Stress, σ_o
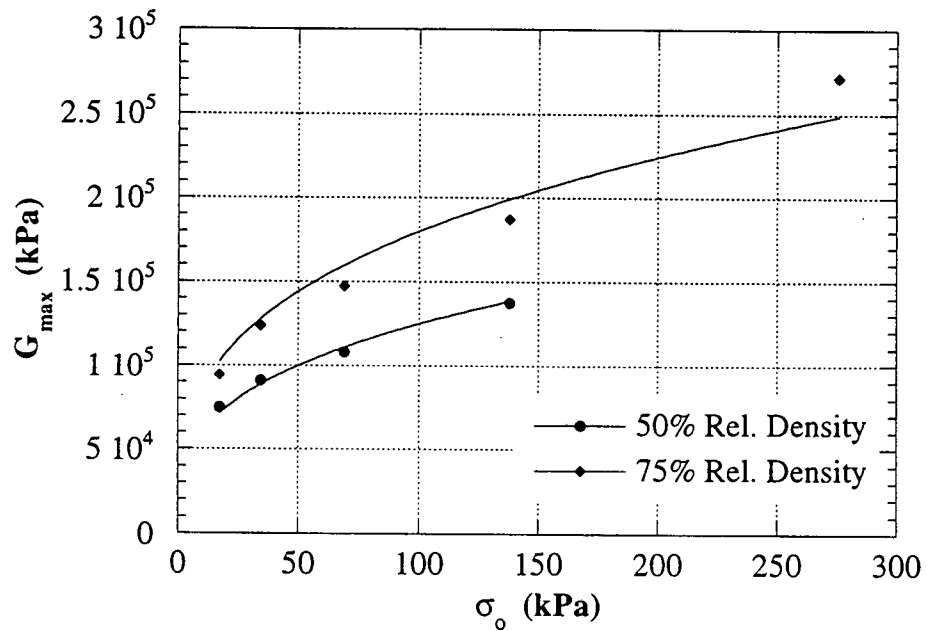
Fig. 4.11: G_{max} Vs. Effective Confining Stress σ_o

Test Sand: Rel. Density = 50%

(a)

Test Sand: Rel. Density = 75%

(b)
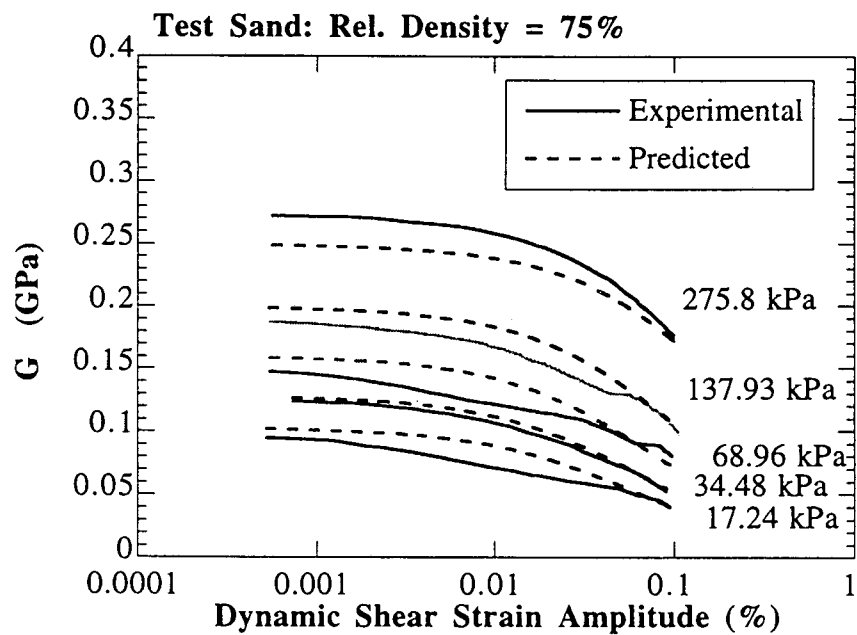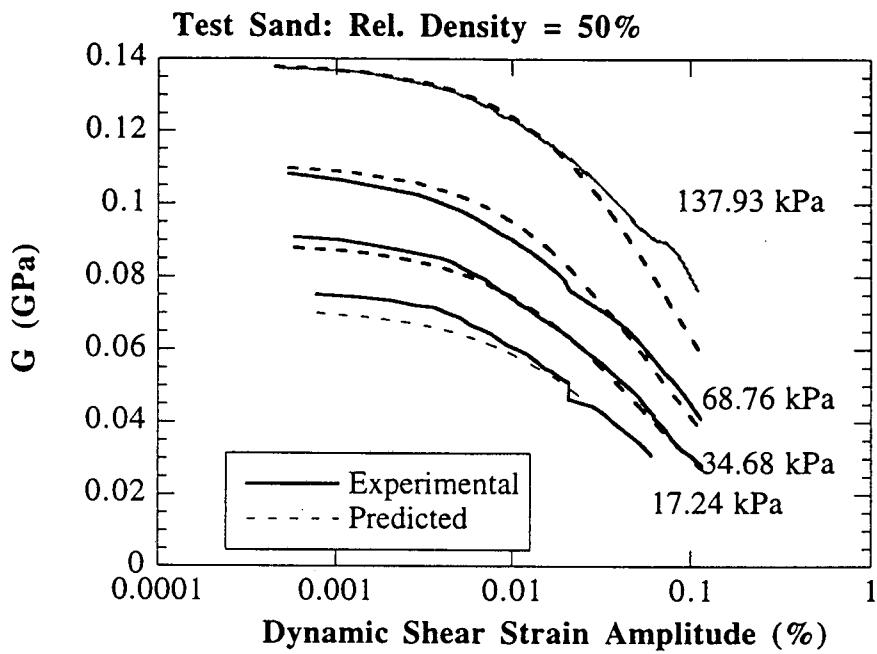
Fig. 4.12 : Experimental Vs. Predicted Values of G Using
Hyperbolic Stress-Strain Relationship (4.4)
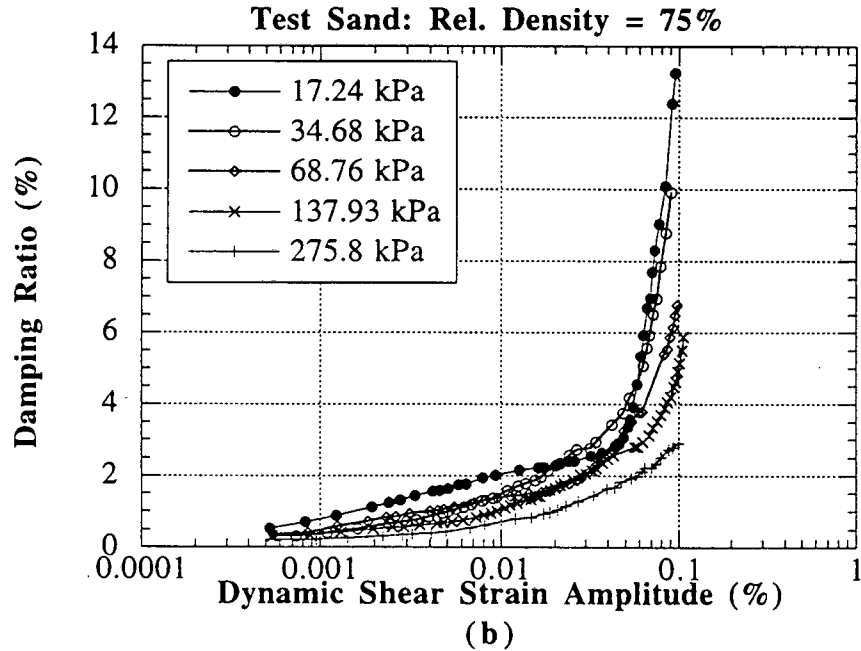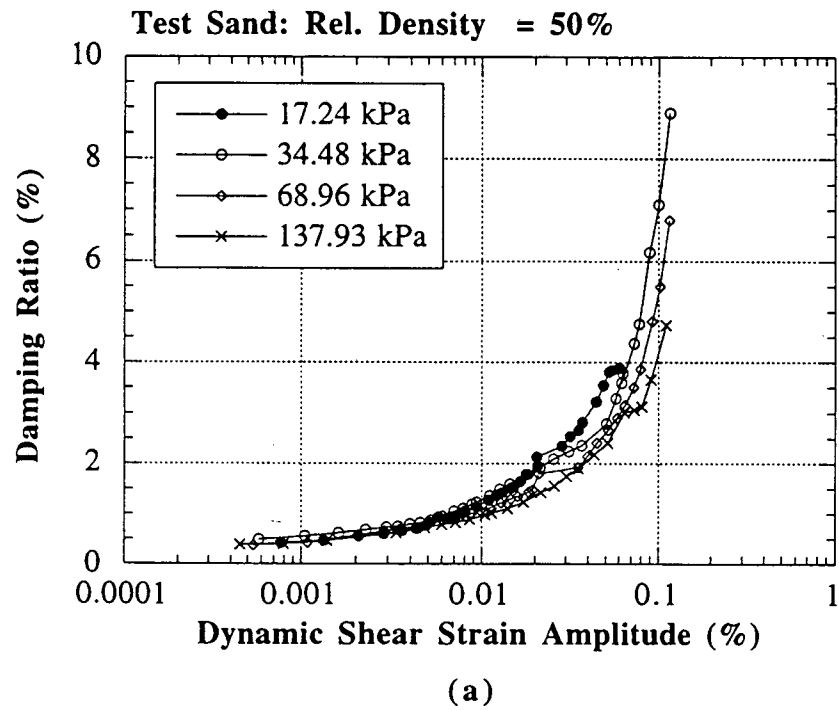
Fig. 4.13 : Damping Ratio Vs. Dynamic Shear Strain Amplitude
for Test Sand (a) Rel. Density 50%, (b) Rel. Density 75%
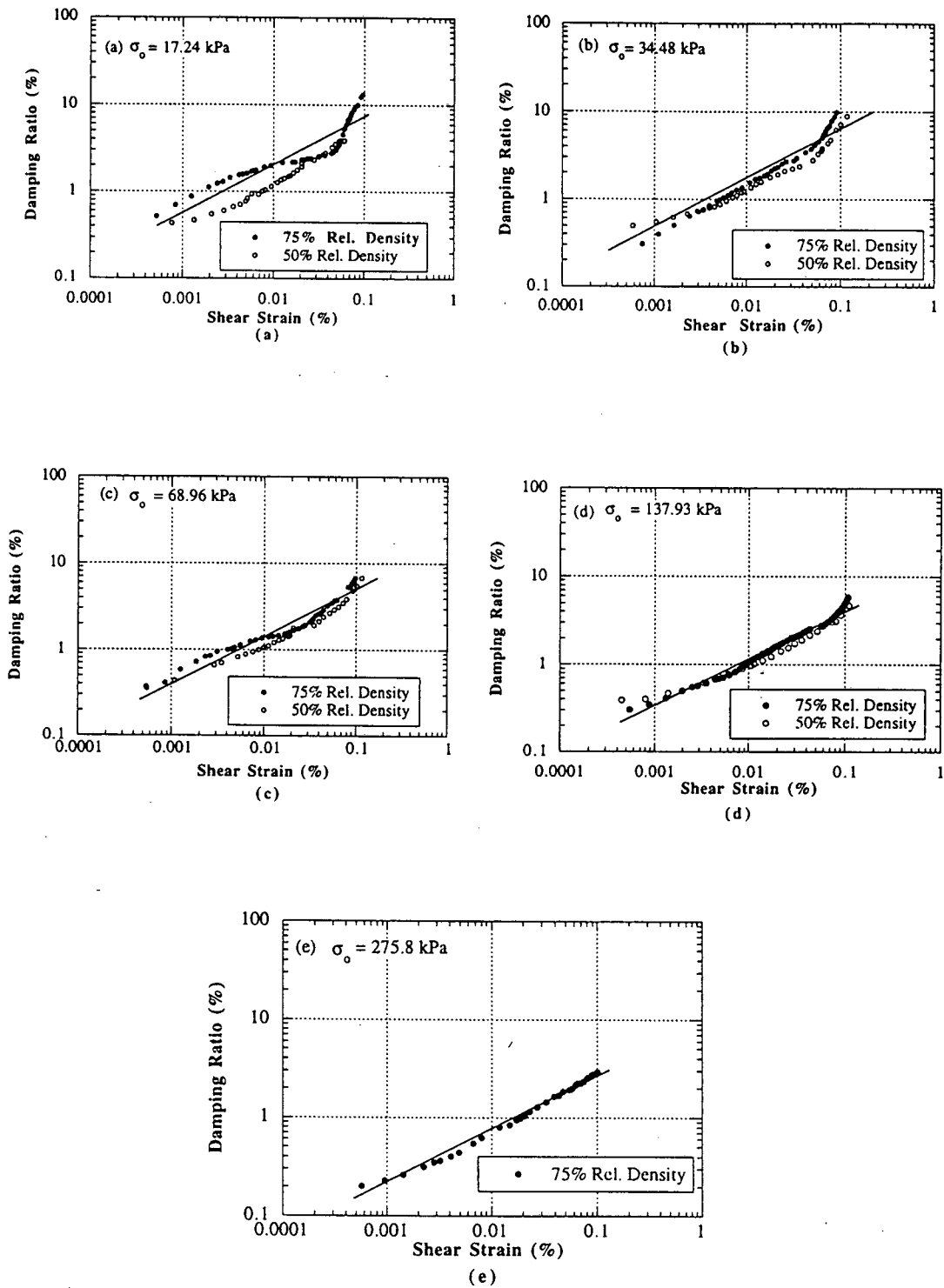
Fig. 4.14: Damping Ratio Vs. Dynamic Shear
Strain Amplitude for Various Confining Stresses

66

17.5 mm, respectively. The sample was deposited in the fixed ring oedometer at a relative density of 55% and saturated with deaired water using gravity saturation. Loading, unloading and reloading were repeated for four cycles by applying loads step by step. The vertical movements were measured at each loading step. The coefficient of volume compressibility was estimated from the vertical stress and strain relationships at each load step increment for the four loading and unloading cycles. See Fig. 4.16. The coefficient of permeability (obtained from laboratory tests) and the coefficient of volume compressibility were used to calculate the coefficient of consolidation.

Summary of Laboratory Results

Table 4.1 shows the summary of laboratory test results conducted on the test sand. The properties of sand used by Ochoa (1990) is also shown here for comparison. The test sand used in the previous study by Ochoa (1990) was slightly finer and had a lower permeability than the sand used in the current study. This was so because of a higher percentage of glass beads used in the sand in his study. The higher value of pile-soil friction angle of the test sand as compared to that used by Ochoa in his study also explains the higher static pile capacities obtained during the load tests. The use of a faster draining sand provides justification for the milder response of pile during the horizontal shaking tests discussed in Chapter 5.0 as compared to test results by Ochoa (1990). It is believed that using a slower draining sand is likely to reduce the differences in pile response due to signature of the earthquake.
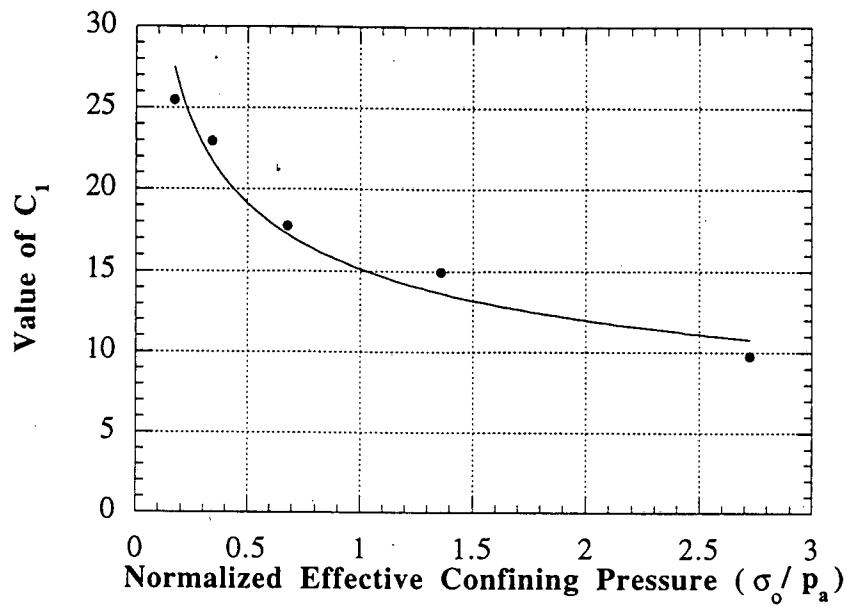
Fig. 4.15: Constant C_1 as a Function of Soil Confining Stress
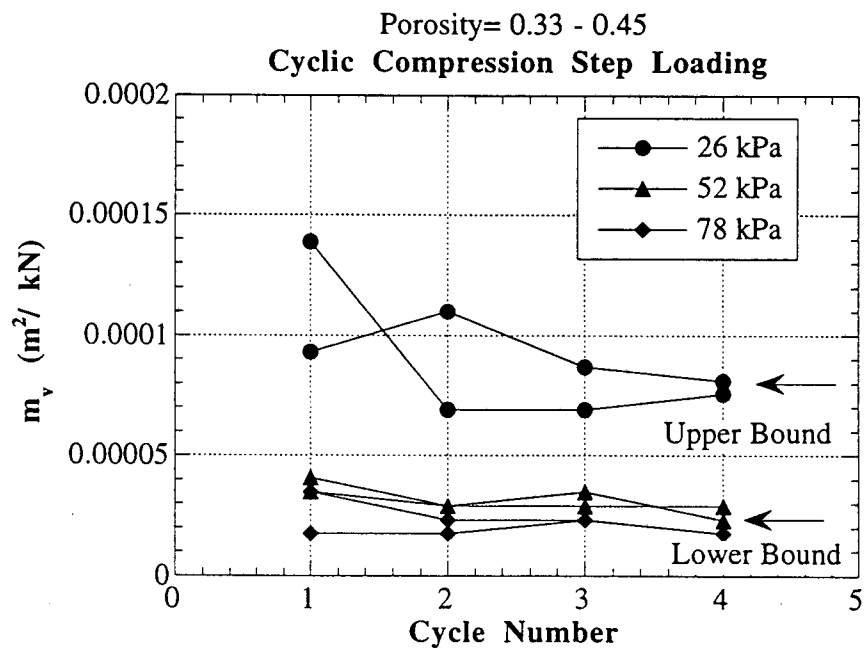
Fig. 4.16: Coefficient of Volume Compressibility

Table 4.1: Summary of Laboratory Results

Parameters	Value for Test Sand	Value for Sand Used by Ochoa (1990)
γ_{dry}	16.85 kN/m^3	Not Reported
$\gamma_{dry\,(max)}$	18.12 kN/m^3	19 kN/m^3
$\gamma_{dry\,(min)}$	15.51 kN/m^3	16 kN/m^3
D_{10}	0.107 mm	0.06 mm
Permeability	3 x 10^{-4} m/sec @ e = 0.54	1.21 x 10^{-5} m/sec
Angle of Internal Friction (ϕ_d)	36.5 degs	Not Reported
Pile-Soil Interface Friction Angle (δ)	27 degs	22 degs
Shear Modulus (G) @ 10^{-5} % strain at effective confining stress = 17.24 kPa	7 x 10^4 kPa	Not Reported

4.2.2 Model Pile

A reusable model test pile which was used in an earlier study conducted by Ochoa (1990) was reconditioned and used in this study. The pile chosen for the study was a closed-ended pipe pile, 25.4 mm in diameter with adjustable lengths of 432 mm and 610 mm, fabricated out of seamless steel tubing of 1.27 mm wall thickness. The larger length was used for the seaquake tests. This was necessary so that the effective penetration length of the pile in the soil could be maintained the same (356 mm) for the ground shaking and seaquake tests. The choice of the pile dimensions was such that the scale effect between the pile size and the maximum sand particle size (which was 0.4 mm in for the test sand) and the boundary effects of the pressure chamber were minimum. The size of the pressure chamber used had to be limited to the clearance within the frame of the closed-loop testing machine used to apply the seismic motion (Instron machine), which resulted in a 0.51-m-diameter test chamber.

Fig. 4.17 shows the longitudinal section of the pile. Originally, the pile had three levels of strain gages mounted on its inner wall to measure the load distribution along the

Cable to Pulley

Strain Gage

Threaded Joints

Pile Penetration into
the Soil = 356 mm

55.5 mm

108 mm
typ.

432 or
610 mm

Cable Plug

Sectional Longitudinal
View
(a)

Longitudinal View
(b)
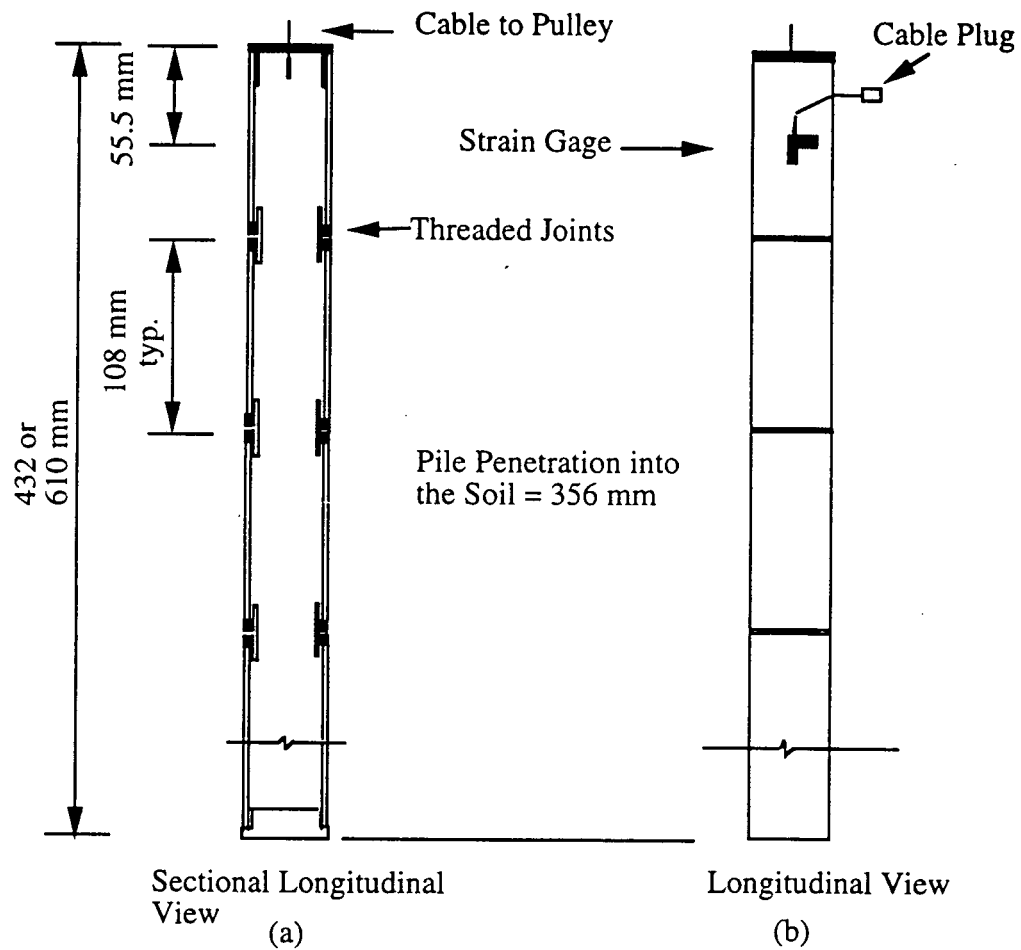
**Fig. 4.17: Schematic of the Model Pile (Assembled for
Earthquake Test)**

pile depth and hence the pile body was segmented to facilitate the placement of the strain

gages and then reassembled as a unit by screwing one segment into the threaded portion of

another. The last segment was available in two different lengths so that, depending upon

the type of test (ground excitation or seaquake) to be performed, the pile could be

configured to the desired length. For the present study, only one level of strain gages was

mounted at a depth of 50 mm from the top of the pile on the exterior surface of the pile

body. This level of strain gages consisted of two T rosettes (125 mm gage width) which

were epoxy-bonded to the outside wall of the pile body and connected together to form a

full bridge. The lead wires from these gages were connected to a plug that fed into a data

acquisition system. The pile instrumentation was placed permanently on the pile shaft prior to the first test and remained on the pile throughout the study. After every test, the pile was degreased and cleaned to ensure the consistency of the potential shear surface along the outside of the pile. The top end of the pile was threaded and accommodated a plug that had a cable hooked to it, the other end of which would be connected to a spring-mass system through a pulley for application of the bias tension load on the pile during the shaking tests. This mechanism is explained in a later section.

4.3 Model - Prototype Similitude

In order to be able to make meaningful physical interpretation of the test results and to scale the behavior of piles from model to prototype level, static and dynamic scaling factors for various soil and pile parameters must be established for the model testing conditions based on similitude criteria and dimensional analysis. The most important effects that require scaling for modeling an earthquake are 1) effective stresses in the soil, 2) inertial effects in the soil and pile, and 3) diffusion effects for the pore water. In a previous study, Ochoa (1990) established these factors for ground excitation tests based on effective stress similitude and dimensional analysis. For proper modeling of sea-seafloor interaction phenomena, both Froude and Mach similitude must be satisfied in addition to effective stress similitude [Yamamoto et al. (1983)]. The scaling factors for ground excitation ("earthquake") tests and for the sea-seabed interaction ("seaquake") tests in light of the above similitude criteria are presented below.

4.3.1 Similitude for Ground Excitation Tests

A geometric scaling factor was derived by establishing mean effective stress similitude between the model and the prototype, i.e., the initial effective stress in the soil at the depth of mean side shear stress transfer is equal in both the model and the prototype. The characteristics of the pressure chamber facilitated the application of known isotropic

71

effective stresses at the top and lateral boundaries. With the resulting uniform stress distribution in the model and a triangular stress distribution in the prototype as shown in Fig. 4.18, the mean effective stress at the mid-point of the model pile of length L_m must equal the mean effective stress at the depth of mean shear transfer of a prototype pile of length L_p.

Model Simulation   Prototype
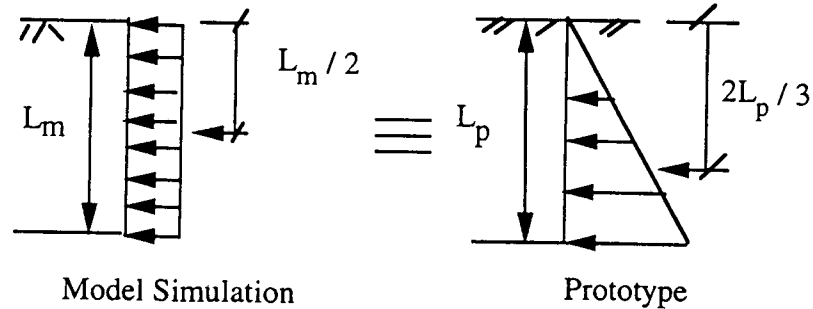
Fig. 4.18: Stress Distribution in the Model and the Prototype

The mean effective stress to be applied in the model to represent a prototype pile of length L_p can be calculated from the above triangular distribution as follows:

$$\langle \sigma'_{oav} \rangle = \frac{2L_p}{3}\gamma' \langle \frac{1 + 2K_{op}}{3} \rangle \tag{4.9}$$

where $\langle \sigma'_{oav} \rangle$ = mean effective stress at the point of mean shearing resistance, γ' = submerged unit weight of the prototype sand, K_{op} = coefficient of lateral earth pressure at rest for the prototype soil

Pile failure during an earthquake is likely to occur in side shearing resistance in the zone in which the effective soil stresses are the lowest (i.e., nearest the ground surface). Therefore, it was considered appropriate to simulate a 4.5 m prototype pile or top 4.5 m of a longer pile in the model.

Considering the following prototype parameters,

$2L_p / 3 = 3$ m (modeling a 4.5 m long pile)

$\gamma' = 55$ pcf, $\phi' = 39$ degs, OCR = 1.5, and $D_r = 55\%$ for a typical offshore sand site.

$K_{op} = (1 - \sin\phi')$ OCR$^{\sin\phi'}$ [after Mayne and Kulhawy (1982)]

and substituting, $\sigma'_{oav} = 17.24$ kPa.

The geometric scaling factor resulting from such similitude = $(L_m/2) / (2L_p/3)$, where L_m and L_p are as shown in Fig. 4.18. For the model pile of penetration, 406 mm representing a 4.5-m long prototype, this becomes $=(0.5)(0.406)/(0.67)(4.5) = 1/15$

Scaling factors for other basic soil and pile parameters summarized in Table 4.2 have been derived using dimensional analysis assuming the stress scaling factor is 1 (as illustrated above), that the prototype velocity is preserved in the model, that the prototype material and pore fluid are used in the model, i.e., density and viscosity are scaled by 1. It is also assumed that the permeability of the soil in model is 1/15 th of the permeability of the prototype, which means that the prototype sand is coarser than the model sand.

It is apparent from dimensional analysis that time (inertia) has to be scaled in the model by a factor less than 1. In other words, the duration of the shaking in the model has to be much shorter than for the prototype. Ideally, this factor should have been equal to the length scaling factor obtained from the effective stress similitude above. However, due to limitations of the response of the testing machine used in generating the shaking motion, a factor of 1/5.2 could only be achieved, which introduced an uncorrectable distortion in length scaling. Thus, a length scaling factor (n_d) different from static length scaling factor (n_s) is obtained for dynamic considerations (inertia and diffusion). For this reason the tests described here cannot be represented as having true similitude with a prototype. However,

73

the phenomena and trends that were observed in the tests are real physical phenomena and trends that are applicable to field problems.

The magnitude-scaled displacement-time histories obtained from the integration of the magnitude-scaled acceleration-time histories of the two seismic events were scaled again to model level by multiplying the ordinate and the abscissa of the record by 0.19 (according to Table 4.2). These records were supplied to the Instron testing machine to generate the seismic motion in the signature series tests.

4.3.2   Similitude for Seaquake Tests

Froude Similitude

The Froude number for the model and the prototype must be equal. That is,

$$\left\langle \frac{\omega_m^2 h_m}{g} \right\rangle = \left\langle \frac{\omega_p^2 h_p}{g} \right\rangle , \qquad (4.10)$$

where ω_m and ω_p are the angular frequencies of the model and the prototype water waves, respectively; h_m and h_p are the water depths in the model and prototype respectively; g is gravitational acceleration; and n_d is the dynamic scaling factor for length.

For a 1-g environment, g is the same in the model and the prototype; therefore, g is gravitational acceleration;

$$\left\langle \frac{\omega_m}{\omega_p} \right\rangle^2 = \left\langle \frac{h_p}{h_m} \right\rangle = \frac{1}{n_d} , \qquad (4.11)$$

where n_d is the dynamic scaling factor for length = 0.19.

Mach Similitude

For slow compressional waves which result from the seepage motion of the pore water relative to the moving solid skeletal frame of the soil, or diffusion waves, the mach number for the model and the prototype must be the same. That is,

$$\left\langle \frac{\omega\, k\, Kk_s}{\nu\, g} \right\rangle_m = \left\langle \frac{\omega\, k\, Kk_s}{\nu\, g} \right\rangle_p \quad , \tag{4.12}$$

where ω = angular frequency; k = wave number; K = the total bulk modulus of the soil; k_s = intrinsic permeability of the soil; ν = viscosity of the pore water; and g = acceleration due to gravity.

For a 1-g environment, g is the same in the model and in the prototype; therefore,

$$\left\langle \frac{\omega_m}{\omega_p} \right\rangle = \frac{1}{n_d} \quad , \tag{4.13}$$

Since, $k_m / k_p = 1/ n_d$; $k_{sm} = n_d{}^2 k_{sp}$; $K_m = K_p$; $\nu_m = \nu_p$; $\rho_m = \rho_p$

where n_d is the dynamic scaling factor for length (= 0.19) and ρ = fluid density

It is noted that there also exists an uncorrectable distortion between frequency scaling for effective stress (Mach similitude) and Froude similitude. As explained later, vertical ground motion of the seafloor produces a standing p wave in the water column with a primary frequency of about 1 Hz in a water depth of 300 m. This frequency translated into model frequencies of about 2.5 Hz for a 4.5 m long pile according to Froude scaling and 5.0 Hz according to Mach scaling. Simulated seaquakes were applied as sinusoidal compression waves to the water overlying the soil in the test chamber at frequencies of 2.5, 5.0 and 10.0 Hz with the same pressure amplitude as is predicted for the prototype. A summary of the testing parameters that were used in the model seaquake tests and the prototype depths represented by each of them based on approximate scaling factors presented in Table 4.2 is shown in Table 4.3.

Table 4.2: Scaling Factors

Scaling Factors	Model to Prototype Ratio
Static :	
Stress	1
Length	$n_S = 0.067$ (representing a 4.5 m long prototype)
Dynamic :	
Stress	1
Strain	1
Length	$n_d = 0.19$
Time (Inertial)	$n_d = 0.19 = 1/5.2$
Time (Diffusion)	$(n_d{}^2)(k_p/k_m) = (0.19{}^2)(5)$ $= 0.18$
Frequency - based on Froude similitude	$1 / \sqrt{n_d} = 2.3$
Frequency - based on Mach similitude	$1 / n_d = 5.2$
Acceleration	$1 / n_d = 5.2$
Velocity	1
Displacement	n_d
Fluid Viscosity	1

Table 4.3: Prototype Representation of the Model Tests for Seaquake Tests

Mean Ambient Effective Stress (kPa)	Frequency of the Applied Hydrodynamic Pressure (Hz)	Prototype Depth (m) (based on n_S)
17.24	2.5	4.5 (as derived)
34.48	5.0	9.0
55.17	10.0	14.5
103.45	10.0	27.0

4.4 Testing Assembly

4.4.1 Ground Excitation Tests (Signature Series)

Experimental simulation of the phenomenon was performed in a pressure chamber that was capable of applying vertical and lateral controlled stresses to a submerged mass of sand. A closed-loop hydraulic testing machine was used to apply the programmed seismic motion for the signature tests to the soil contained in the test chamber. The chamber size was 0.54 m. high and 0.51 m in diameter. This was the largest size that could be accommodated by the machine. The chamber was equipped with lateral rubber membranes around its wall and a bladder at its top for applying the lateral and the vertical stresses respectively, to the soil mass. In addition, the top plate used to cover the chamber had openings or ports for pile insertion and drainage. (See Fig. 4.19.)

The principle of operation of the pressure chamber / closed loop testing machine (Instron machine) is that the bottom of the pressure chamber is rotated by the Instron machine with a rotational motion that produces the desired scaled time history of motion in the tangential direction at the location of the toe of the pile (more precisely, a level just below the toe of the pile). This requires the pile to be placed off center, as shown in Fig. 4.19. In order to mimic linear motion as closely as possible the pressure chamber is equipped with a rigid cylindrical element at its center. The clearances between the model pile and both the external boundary and the boundary created by the presence of the central cylinder is 7 pile radii. In the direction perpendicular to the chamber radius, an essentially infinite clearance is achieved. No clear research exists that defines the boundary effects in such a case; however, in medium-dense sand of the type studied here some effects of the presence of the boundaries may exist in terms of modifying the effective stresses around the model pile produced due to the driving of the pile. These stress modifications are assumed to be insignificant relative to prototype conditions. Further details about the pressure chamber can be obtained from Ochoa (1990). The overall testing arrangement for

PILE PORT

TOP PLATE

19.1
19.1

190.5

1/2"-DIA.
ROD

TOP AIR
MEMBRANE

101.6 — 203.2

CONTAINMENT
CYLINDER

LATERAL
MEMBRANE

508

38.1

101.6

TEFLON
SHEET

PILE TOE
(PENETRATION
INTO SOIL = 381)

HOLLOW
CYLINDER

50.8

88.9   88.9'

203.2

SAND

19.1

BOTTOM PLATE

508

609.6

(DIRECTION OF SENSING FACE)

MINIATURE DYNAMIC
PORE WATER PRESSURE
TRANSDUCER
(LEADS OUT THROUGH
TOP DRAIN PORTS)

All Dimensions in mm
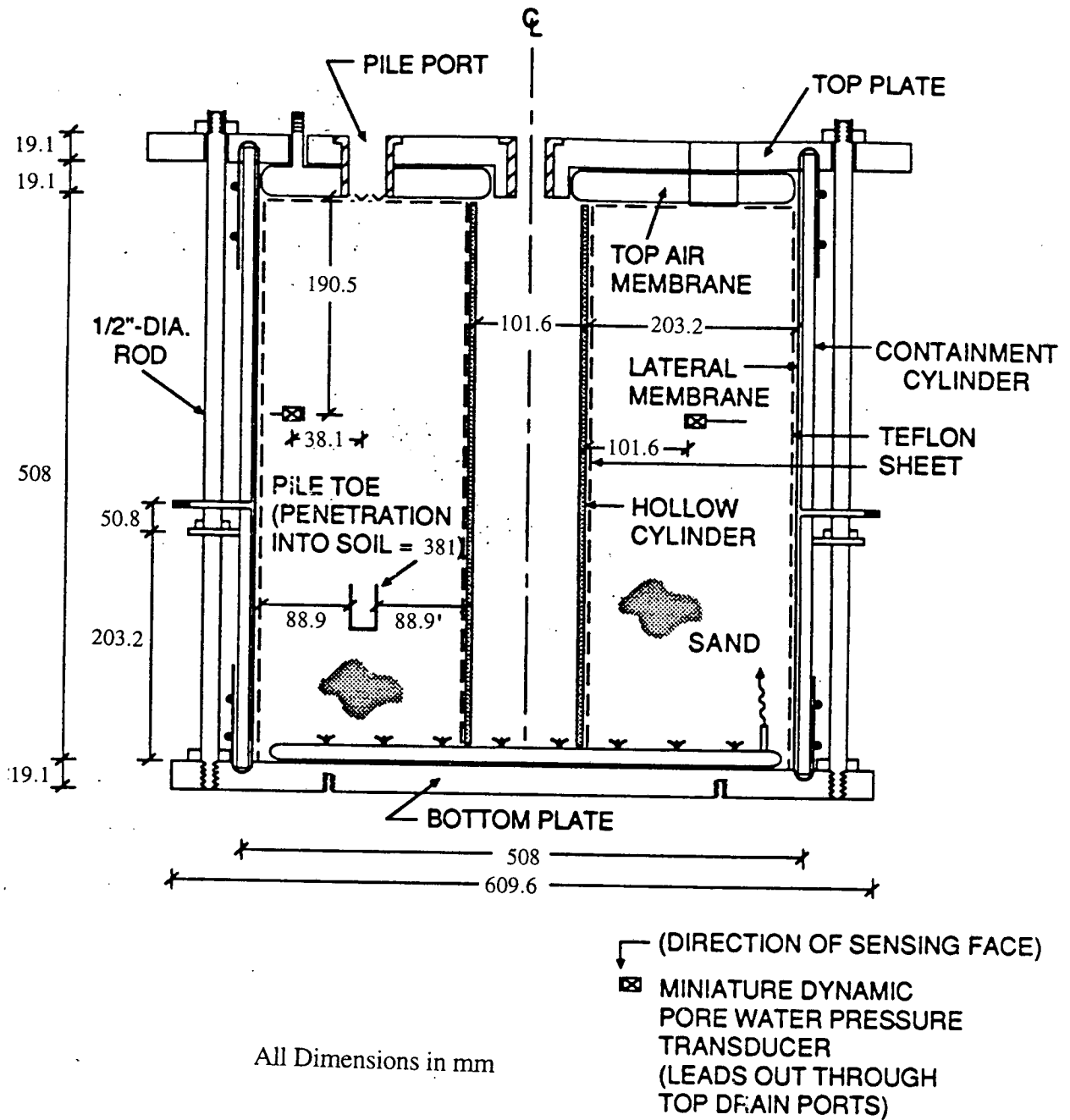
Fig. 4.19:   Schematic Elevation of the Test Chamber (Ground Excitation
Tests)

the ground excitation tests is shown in Fig. 4.20. The boundary conditions existing in the pressure chamber during the ground excitation tests are as follows :

Top : Controlled effective stress, with drainage at certain points.

Sides : Controlled total stress, no drainage; and

Base : No drainage, zero vertical strain; rigid surface no relative soil-chamber motion.

According to the classification system of Huang et al. (1991), this represents a "BC1" condition.

The condition of upward flow of water through the soil pores during simulated seismic activity (an important factor in development of liquefaction and cyclic mobility) was permitted.

The test sand was deposited using a dry raining technique into the pressure chamber, as illustrated in Fig. 4.21. Prior to the beginning of the raining process, a diffusion ring was placed at the bottom of the chamber for later saturation. The diffusion ring was connected to a hose at its outlet, the other end of which communicated with a deaired water reservoir at the top of the chamber. A rolled Teflon$^{®}$ sheet was placed around the sand column boundary in the chamber to provide lateral confinement to the sand, thus preventing changes in the density of the soil mass during deposition. The sand was allowed to fall from a prescribed height (about 100 mm) into the chamber, which was calibrated to the achievement of 55% ± 5% relative density. Sand was rained continuously, moving the funnel from the outside of the chamber to the inside in a circular pattern. Adjustments to the nozzle elevation were made to keep the drop height constant as the soil surface raised.

Raining was interrupted at the level where soil instruments were placed in the chamber, which was at about the mid-depth of the pile. The soil was flushed with carbon dioxide for about 10 minutes and then saturated with deaired water. (See Figs. 4.21 and

79
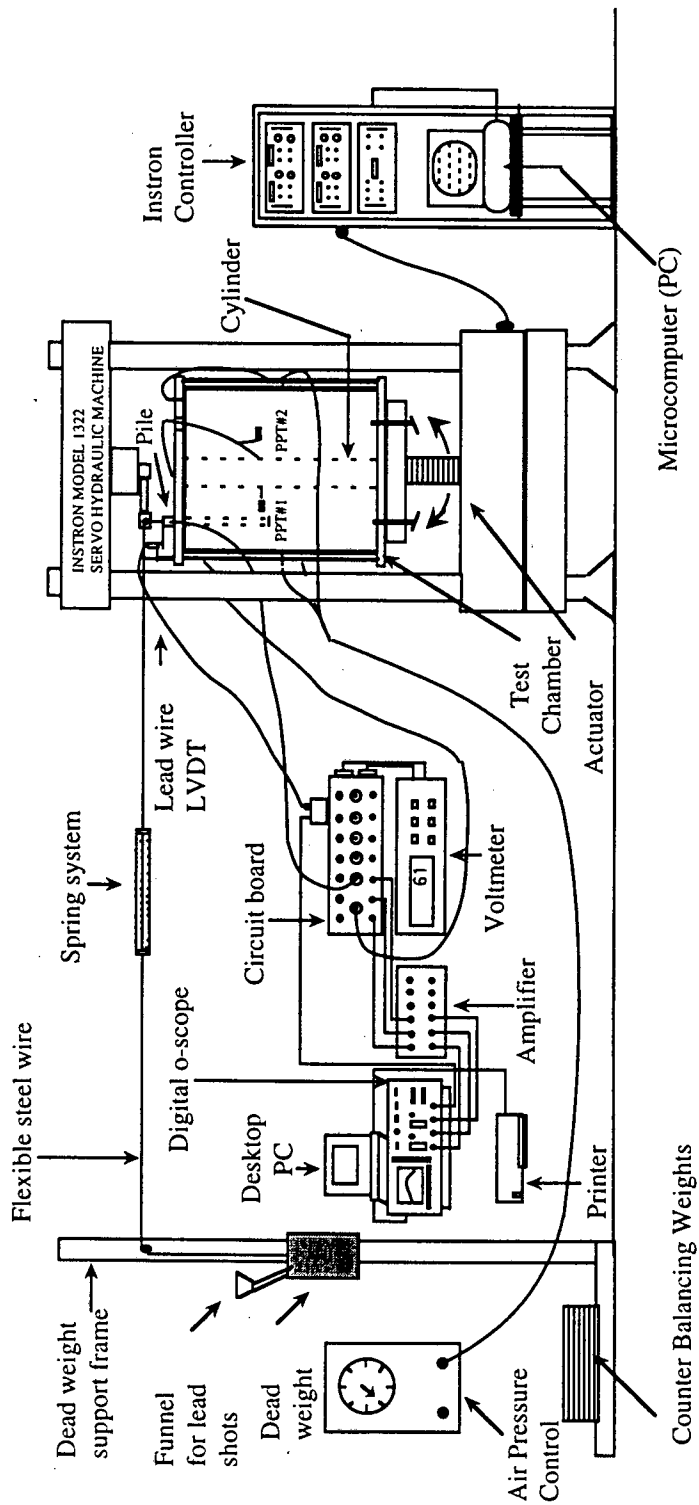
Fig. 4.20: Schematic of the Testing Assembly for the Ground Excitation Tests

80

4.22.) Miniature pore water pressure transducers were then placed in the soil mass at this level to sense the pore water pressure in the "near field," 1 diameter from the pile wall, and in the "far field," 14 diameters from the pile wall. Raining was then continued until the sand surface reached the top of the chamber, after which the remainder of the sand column was saturated. The entire process of saturation took about 24 hours. A rubber bladder (for applying the vertical stress) was then placed on top of the soil, following which a top plate was placed that was bolted to the allthreads fixed to the bottom plate of the chamber. To ensure that the soil sample was completely saturated, a "B" parameter check was performed on a completely charged chamber by closing all the ports in the chamber, applying a mean confining pressure of 17.24 kPa (working pressure) and recording the pore pressure developed in the sample. Fig C.1 shows the results for the B parameter check test. A "B" parameter close to 0.90 was obtained in each test, indicating essentially full saturation in the soil mass.

Under normal circumstances for the signature tests, the completely charged chamber was consolidated under an isotropic confining stress of 17.24 kPa by applying air pressure to the lateral rubber membranes and the bladder on the top. This represented a mean effective stress around a 4.5 m long prototype pile. (Sec. 4.3.) The volume of water expelled from the sample during consolidation was measured to calculate the volume change during consolidation. The results are presented in Chapter 5. The increase in relative density of the soil specimen ranged from 2 % to 4% during this step.

The model pile was then driven by impact using a hand-operated, single-acting drop hammer. A schematic of the hammer is shown in Fig. 4.23. To prevent damage to the pile head, a plywood cushion was placed on the pile head. The pile was marked along its length, and the number of blows required for every 25.4 mm of penetration was recorded. The pile was driven at a radius of 152 mm from the center of the chamber. (See Fig. 4.20.) The chamber was then placed and clamped onto the actuator of the machine. A flexible
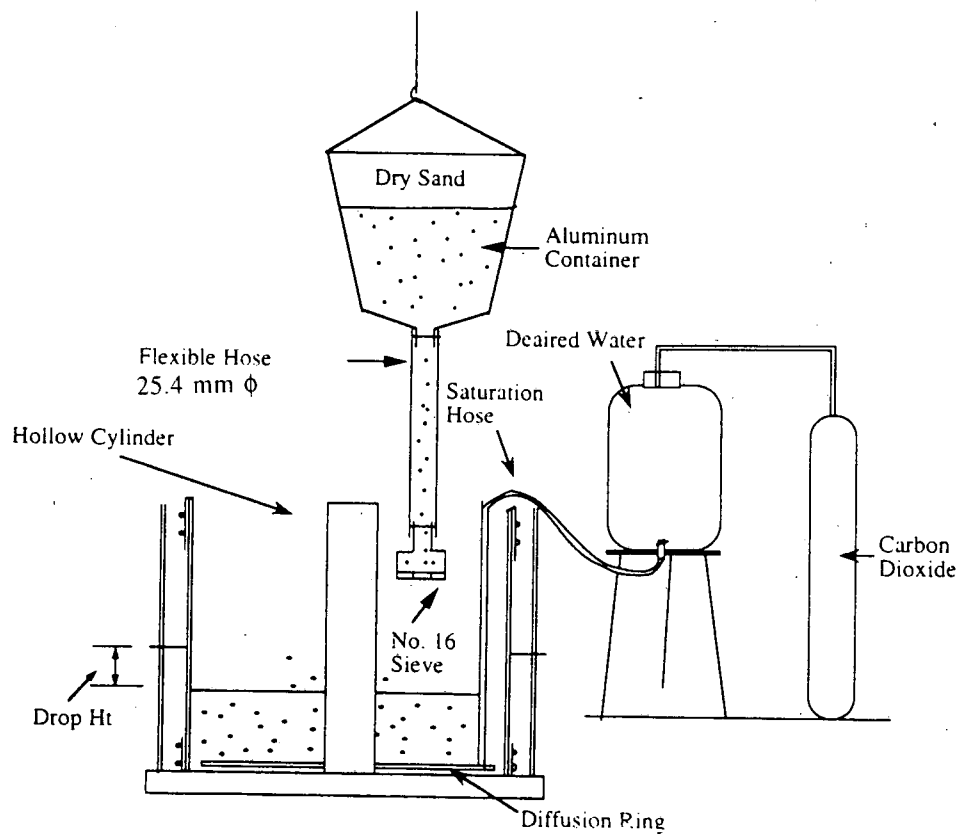
Fig. 4.21: Schematic of Sand Placement Arrangement
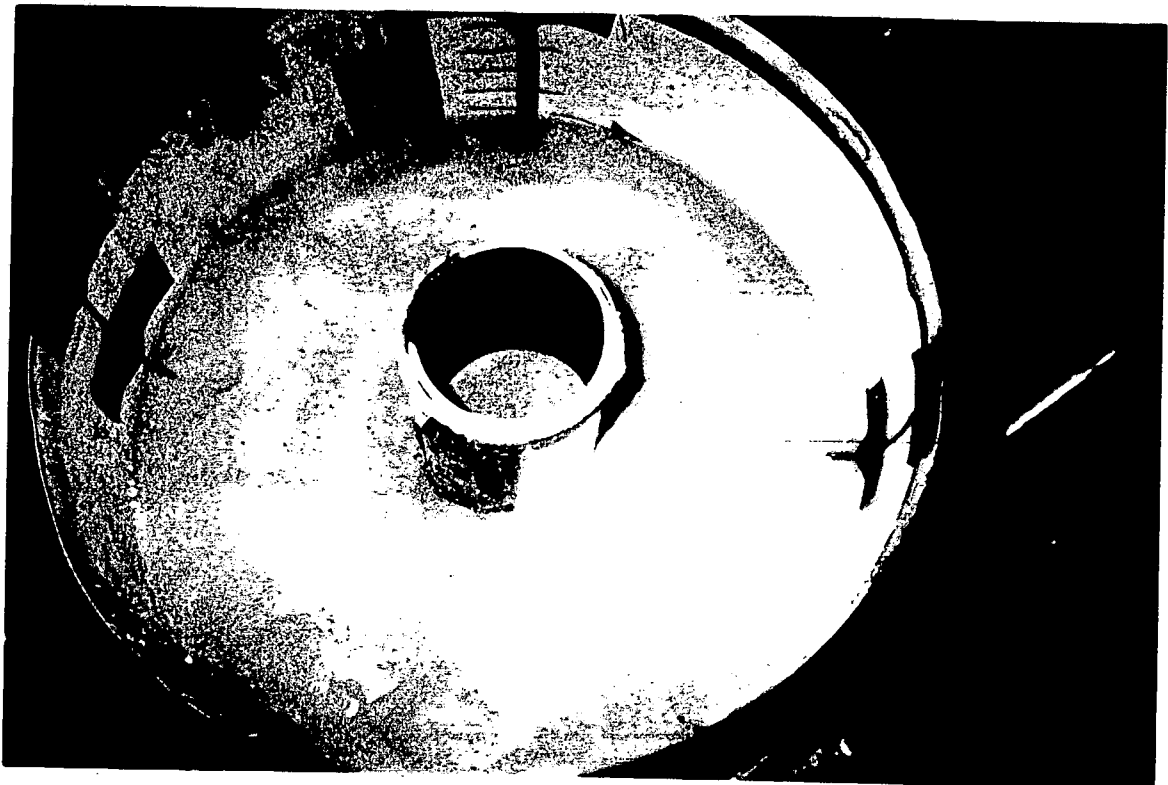
Fig. 4.22 : Pore Water Pressure Transducer Placement

high-strength cable, 1.59 mm thick was attached to a threaded steel plug inserted into the head of the pile, through which biased (static) tension load was applied continuously by means of a deadweight-and-spring system. The cable passed through frictionless pulleys, one supported by Instron's frame and the other supported by a loading frame. The other end of the cable was attached to a plastic container. The dead weight on the pile was then applied by pouring lead shot into the plastic container from a funnel at a controlled rate of 80 N / min. Stability of the loading frame was assured by presence of counter balancing weights placed on an extended arm welded to the base plate of loading frame (See Fig. 4.20.) The purpose of the weight-and-spring loading system was to simulate the presence of a simple superstructure of known natural frequency, such as a floating structure, that feeds axial load back into the pile during the seismic event as the pile's motion excites the structure. The spring constant was chosen so that the natural frequency of the simulated superstructure was about 2.0 sec at model scale, which was above the longest period in the wave train for the simulated seismic events. The load-deformation behavior of the spring is shown in Fig. D-1 in Appendix D.

In order to express the bias uplift load applied on the pile as a percentage of the static uplift capacity, a load test was conducted on the pile prior to applying bias loading during every shaking test. The pile was then restruck by a single blow of the hammer, following which the pile was loaded to the desired percentage of static uplift capacity using the measured static capacity as a reference.

The seismic motion for the signature tests was generated by applying the preprogrammed rotary motion to the base of the chamber through the actuator of the Instron machine. The rotary motion was such that the offcentered pile experienced a tangential displacement-time history equal to the desired linear displacement-time history obtained from the integration of the scaled acceleration record. The schematic in Fig. 4.24 shows the location of the pile and mechanism of applying the seismic motion. Ochoa (1990)

83
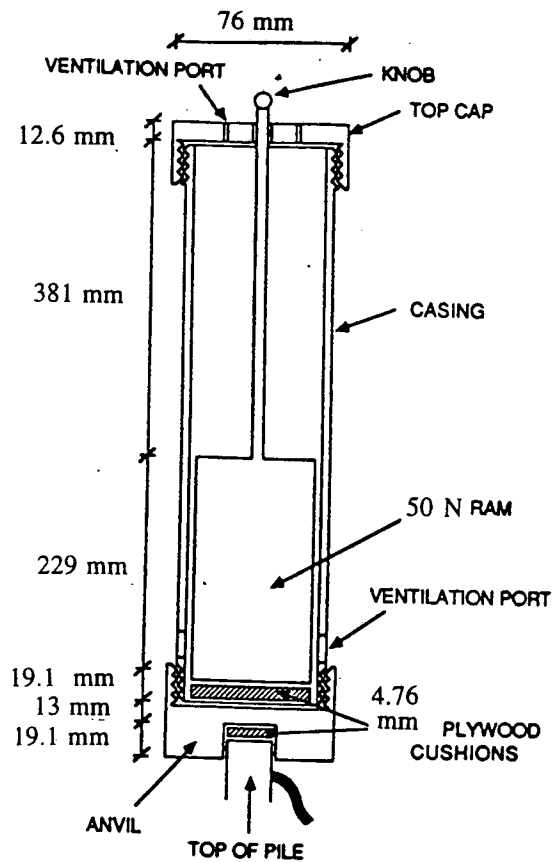
Fig. 4.23: Schematic of the Drop Hammer [After Ochoa (1990)]

76 mm

VENTILATION PORT — KNOB

TOP CAP

12.6 mm

381 mm

CASING

50 N RAM

229 mm

VENTILATION PORT

19.1 mm
13 mm
19.1 mm

4.76 mm

PLYWOOD CUSHIONS

ANVIL

TOP OF PILE

Test Chamber Boundary

Hollow Cylinder

Final Pile Position

Pile center at 152 mm radius from center

ϕ

Max. range of rotation of actuator = 108 degrees

Tangential Displ.
$S(t) = 152 * \phi(t)$

Initial Pile Position
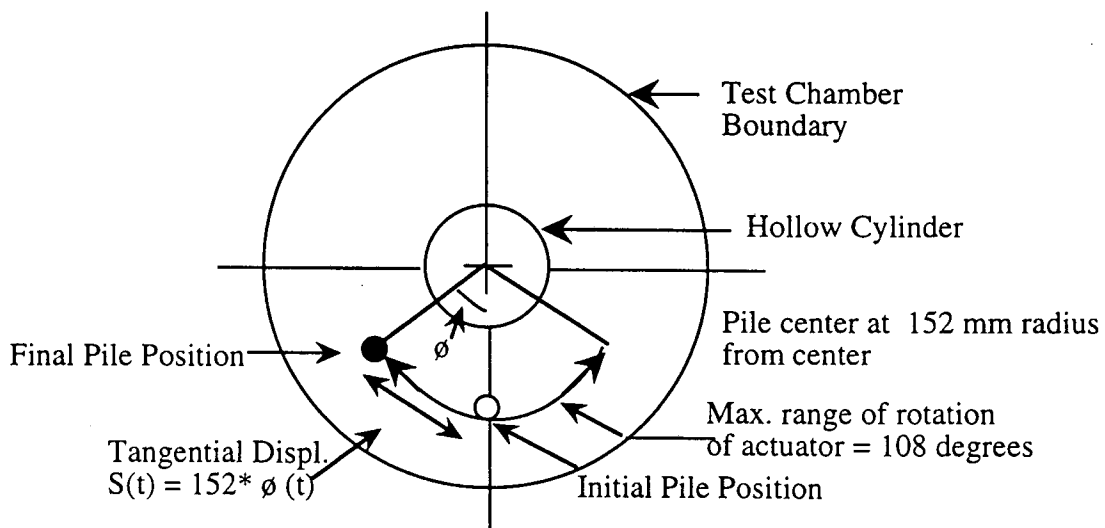
Fig. 4.24: Schematic Plan View of the Chamber Showing the Conversion of Rotational Motion to Horizontal Motion Applied at the Base of the Chamber

84

demonstrated through integration of the records of accelerometers buried in the sand within the chamber that the scaled amplitudes of the vertically propagating shear waves were approximately the amplitudes that would be predicted from SHAKE to occur in medium-dense sand deposits subjected to the magnitude-scaled Oceanside record.

The data acquired during the pile driving and ground shaking tests consisted of the pile-head load, vertical pile-head movement relative to the chamber, and the pore water pressure in the saturated soil mass. The relative movement between the pile and the chamber was recorded by means of an LVDT mounted on the chamber as shown in the schematic in Fig. 4.20. Pore pressures were recorded by means of pore water pressure transducers (PDCR 81 and Keller psi series 710-submersible pressure transducers). Prior to placement the transducers were deaired and saturated with water. Calibration constants for the pile-head strain-gage, pore-water transducers, soil pressure cells, and the LVDT are attached in Appendix B. The data signals from the instruments were amplified as required and were recorded by a digital oscilloscope which communicated with a desktop computer, where the signals were stored digitally. The amplification for the strain gage voltage readings was 1000, and that for the pore water pressure transducers was 100. Hard copies of the data signals were then obtained by printing them from the computer. The schematic of the data acquisition system for the signature tests is also shown in Fig. 4.20. After the completion of each test, the wet sand was taken out of the chamber and dried in an oven for about 24 hrs at 105° C for reuse in later tests.

Several seismic loading tests were performed on the model test pile by applying the displacement-time histories scaled for the event magnitude, geometry, and diffusion for the Upland and the Oceanside events to the base of the pressurized soil chamber while the pile was held under biased uplift load by the spring-mass system. Tests were conducted by varying the magnitude of the scaled earthquakes (7.0, 7.5, and 8.0) and the magnitude of the applied biased load (45% to 90% of the static capacity) on the pile for each of the two

events. For the piles that did not fail during the seismic events, static loading was performed to failure to define the post-shaking capacity of the pile.

4.4.2 Seaquake Tests

The seaquake tests were also conducted in the pressure chamber. The testing assembly was modified in order to develop a mechanism for the application of hydrodynamic pressure on the surface of the sand confined in the pressure chamber. The modified assembly was comprised of a compartment made up of two aluminum flanges with a rubber sleeve 76 mm wide and 7 mm thick attached to their ends, as shown in Fig. 4.25. The rubber sleeve was bonded to the two flanges by a high-bond-strength epoxy. This extension was then bolted to the top plate of the pressure chamber. The sinusoidal variation in the hydrodynamic pressure was developed by mechanically stroking water confined in this compartment by cyclic motion of the pressure chamber mounted on the actuator of the Instron testing machine, while the top compartment was held in place by two reaction beams attached to the loading frame of the Instron.

The test set-up was essentially the same as for the ground shaking tests. The sand was deposited at a relative density of 55% ± 5% by raining the same test into the chamber and saturating it with deaired water. Comparison of measurements of relative densities taken during the deposition process with the actual relative densities of the soil in the chamber is shown in Table 4.4. Both values were in close agreement. Unlike the set-up for the ground excitation tests, the sand was not placed around a cylinder at the center of the chamber. Raining was interrupted at the location where soil instruments were placed. Two miniature pore water pressure transducers (PDCR 81) were placed along the axis of the chamber in the soil at depths of 178 mm and 356mm from the bottom of the chamber to obtain the distribution of pore water pressure across the depth of the soil. A bed of coarse sand about 25 mm thick was placed on the top of the saturated bed of fine test sand so that
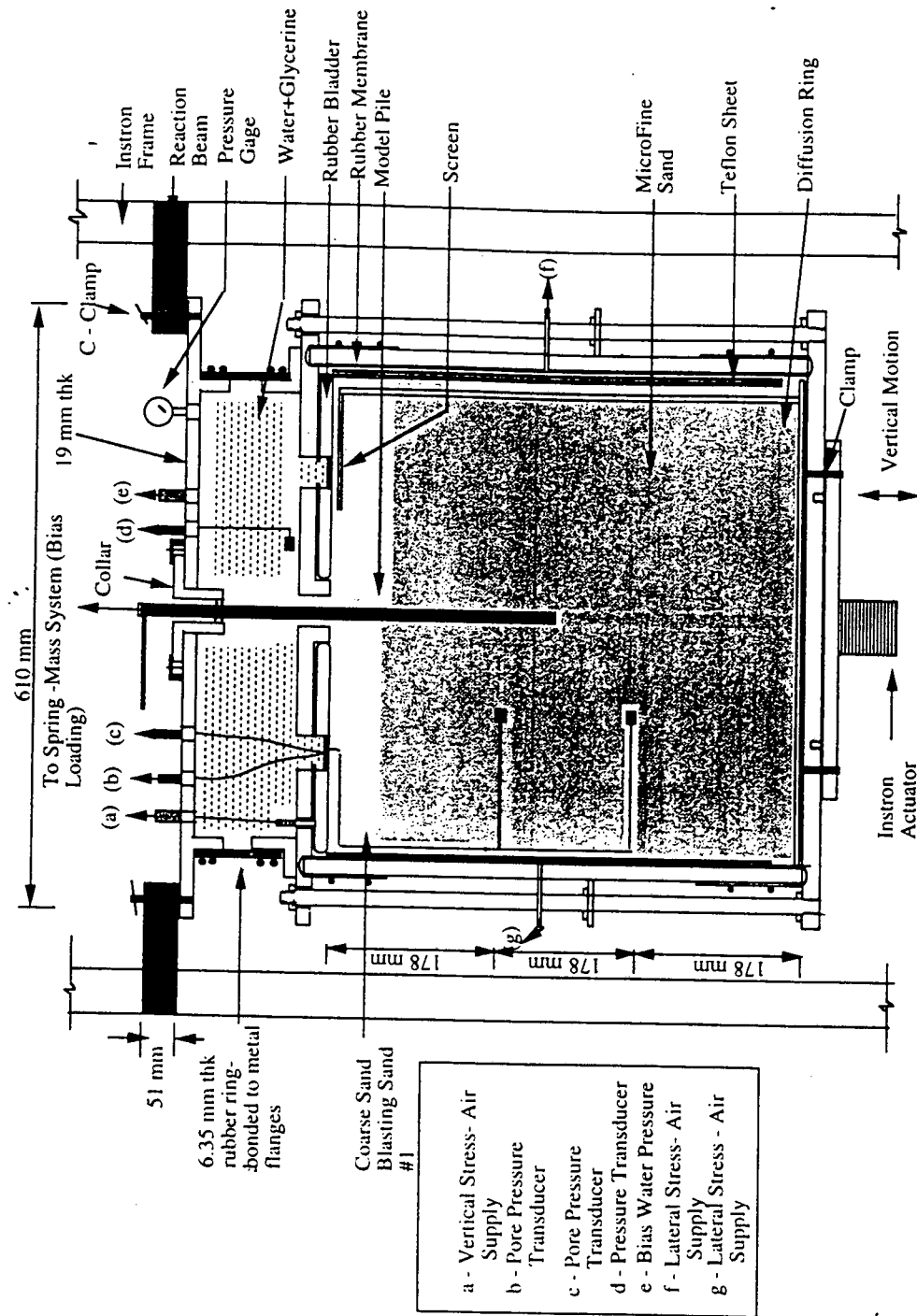
Fig. 4.25: Schematic Elevation of the Testing Assembly Used to Study Pile Response to Seaquakes

a - Vertical Stress- Air Supply
b - Pore Pressure Transducer
c - Pore Pressure Transducer
d - Pressure Transducer
e - Bias Water Pressure
f - Lateral Stress- Air Supply
g - Lateral Stress - Air Supply

Table 4.4: Relative Density Measurements

Test No.	Relative Density Measured During Deposition (%)	Relative Density Actually Measured by Weighing the Test Specimen
SSB#1	53.5	51
SSB#4	53	51
SSB#7	54	52.5
SSB#10	52	48

the applied hydrodynamic pressure could be transmitted uniformly to the top surface of the test sand. The top bladder for applying the vertical stress to the soil was then placed on top of the coarse sand and finally the top plate was bolted onto the chamber. The soil was then consolidated under one of two boundary conditions: 1) isotropic controlled stresses applied at the boundaries (BC1), or 2) one-dimensional vertical stress under zero lateral strain (BC3). The water compartment was then fixed on to the top plate such that the drainage holes on the top plate of the chamber were within the area occupied by the compartment. The applied hydrodynamic pressure was monitored by mounting a transducer (Keller PSI Inc.) on the top plate of the chamber as shown in Fig. 4.25. Watertight grommets were made in the top flange of the compartment through which the cables for the transducers, air supply hose to the vertical bladder and water supply to the unit were passed to be hooked to the data acquisition system, air supply and water supply panels, respectively.

The pressure chamber assembly was mounted on the base plate of the actuator of the Instron. The top flange of the water compartment was set flush against two reaction beams 51 mm thick affixed to the loading frame of the Instron and clamped. The compartment was then filled completely with a mixture of deaired water and glycerine

through a port provided at the top of the unit. The procedure for applying the hydrodynamic pressure consisted of initially applying a prescribed hydrostatic pressure to the water confined in the compartment. This was accomplished by applying air pressure from a pressure panel to the water-glycerine column in an accumulator that communicated with the water compartment of the testing assembly. Prior to the application of the hydrostatic pressure, the actuator of the Instron was raised to a mean position about 6% of the maximum movement (51mm) of the actuator above its lowest position. Once the desired hydrostatic pressure was applied to the water, the inlet valve of the compartment was closed. The pressure chamber was then oscillated with a stroke of 4% of the maximum actuator displacement. The cyclic vertical motion of the actuator generated a hydrodynamic pressure on the surface of the coarse sand at the top of the chamber. Measurements of the actual hydrodynamic pressure applied and the pore water pressures generated in the soil mass at the two instrumented locations were taken during the tests. The duration of a test was about 20 secs. Drainage is a critical issue in these tests. The surface of the sea floor is free to drain at all times during hydrodynamic loading. However, for the laboratory conditions, the mechanism for applying the hydrodynamic pressure being a closed system, drainage at top (simulated sea floor) was only possible during the unloading cycle of the applied hydrodynamic pressure. This is likely to be a good one-dimensional idealization of the prototype seafloor conditions, where drainage should not occur during the loading part of the cycle.

Several tests were conducted to investigate sea-seabed interaction during seaquakes for typical water depths during M = 8.0 simulated earthquakes without a model pile present. The schematic of the testing assembly for the sea-seabed interaction tests is shown in Fig. 4.26. The range of amplitudes of hydrodynamic pressures developed varied from 13.8 kPa to 55 kPa. Tests were conducted at varying frequencies (2.5 Hz, 5.0 Hz, 10 Hz)
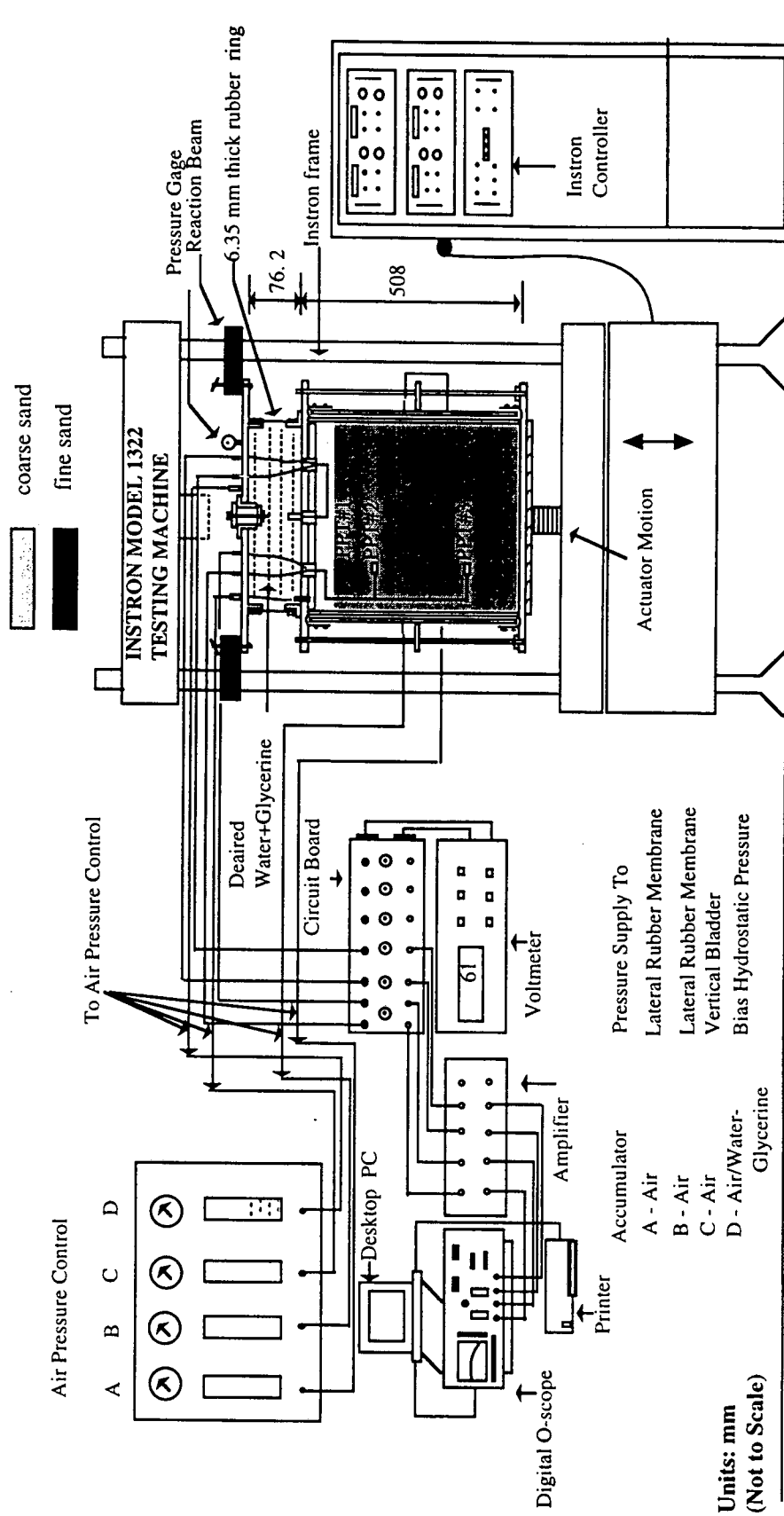
Fig. 4.26: Schematic of the Testing Assembly for Sea-Seabed Interaction Tests

90

and different effective stress conditions to scale variable depths (4.5m, 9m, 18m) in the prototype pile. Tests were conducted with different boundary conditions in the chamber, as shown in Fig. 4.27. Tests with application of only vertical overburden on the soil and rigid lateral boundaries simulated the one-dimensional zero lateral strain conditions that are assumed to exist in the field during seaquakes, and tests with both vertical and lateral effective stresses were used to compare the results with the ground shaking tests. The zero-lateral-strain (one-dimensional) test condition can be justified when simulating foundation response at a deep soil site, 75 km from the earthquake epicenter (SEMS site) because the p wave arrives at the site first, producing vertical motion in the sea floor, which is the phenomenon being simulated. Later, s-waves arrive to produce the ground shaking that was simulated as described in the previous section, at which time soil motion no longer approximates one-dimensional motion.

Additional tests were conducted to study the pile-sea-seabed interaction during seaquakes. The sand deposition, transducer placement procedures and the mechanism of development of the hydrodynamic pressure on the surface of the sand column were exactly the same as the previous tests without the pile. A collar to accommodate the pile was introduced through an opening made at the center of the top flange of the overpressure generation unit and was pinned to the surface of the flange. The collar had a 25.4 mm hole in the center for pile insertion, which was plugged during the sea-seabed interaction tests. O-rings were inserted into grooves inside this hole to prevent leakage of water from around the pile during the application of seaquake pressure. The water compartment attached to the pressure chamber made it necessary to increase the length of the model pile to 610 mm in order to ensure that the effective penetration depth of the pile into the soil was the same for both the ground shaking and seaquake tests. After the consolidation of the test sand at the desired effective stress and the attachment of the water compartment to the top plate, the model pile was driven by impact through the collar into the confined soil. The pile was marked along its depth, and the number of blows required per 25.4 mm of penetration of

Controlled Hydrodynamic Pressure
(Drainage only during unloading)

Controlled TotalStress
(through flexible bladder)

A - Test I
  Rigid Wall
  (Zero Lateral Strain)
A - Test II
  Controlled Total Stress

A

Rigid
Boundary,
No
Drainage
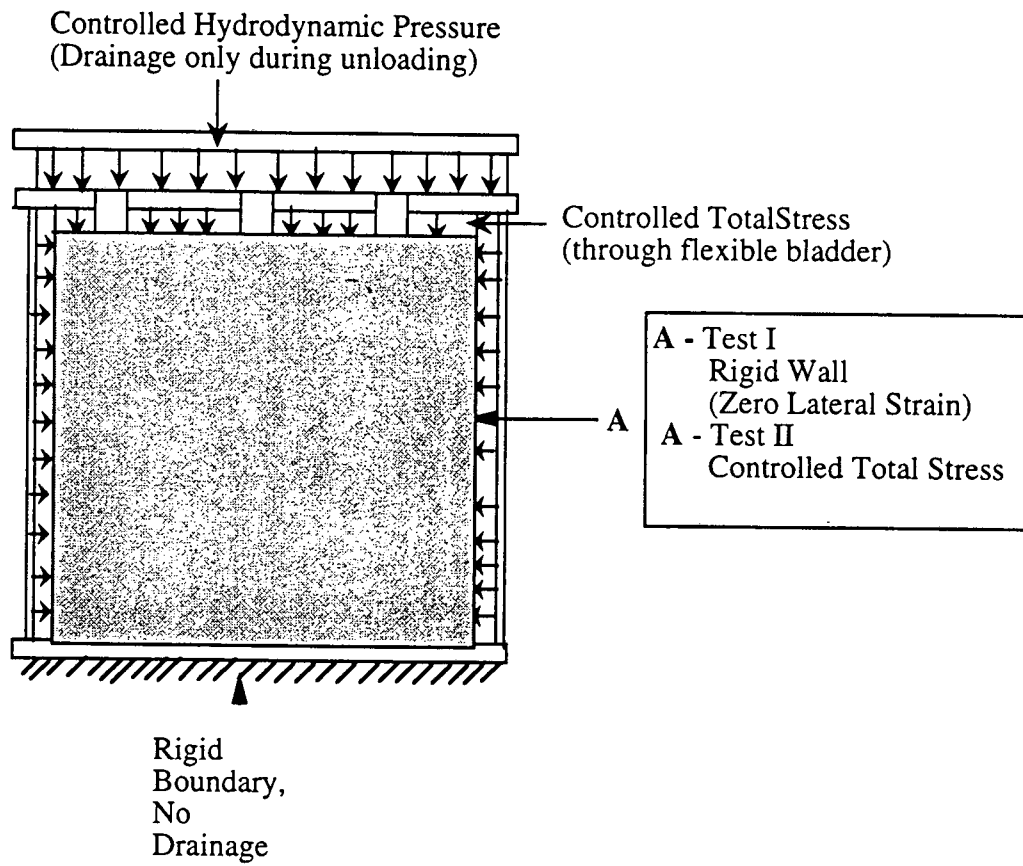
Fig. 4. 27: Chamber Boundary Conditions for Seaquake Tests

pile was recorded for the last 100 mm. The pile driving process is illustrated in Fig. 4.28. The chamber assembly was then mounted on the base plate of the actuator of the Instron testing machine and configured as shown in Fig. 4.29.

The bias load on the pile was applied through a spring-mass system. The mechanism of application of the bias load was similar to that used in the ground shaking tests. Data acquired during the application of the simulated seaquake consisted of the pile-head load, pile-head movement, applied hydrodynamic pressure and the pore water pressure measured at the mid-depth of the pile about 25.4 mm from its face. An LVDT with a range of ± 25.4 mm and an accuracy of 0.025 mm was mounted on a stand fixed to the chamber to measure the relative movement between the pile head and the chamber during the tests, as seen in Fig. 4.29.

The data signals from the instruments were amplified as required and were recorded by a digital oscilloscope that communicated with a desktop computer, where the signals were stored. The amplification for the strain gage voltage readings was 1000 and that for the pore water pressure transducers was 100. Hard copies of the data signals were then obtained by printing them from the computer. The overall testing assembly for the pile-sea-seabed interaction tests is shown in Fig. 4.30.

The pile performance during $M = 8.0$ earthquakes due to seaquake-induced pressure on the seabed in typical water depths was studied experimentally for various bias tension loads expressed as a percentage of the pile's static capacity and mean effective stress conditions. The duration of the tests was about 20 secs. Piles that did not fail during the application of the seaquake were further loaded statically until failure. Based on the test results, the failure mechanism and conditions for pile stability during seaquakes were established.
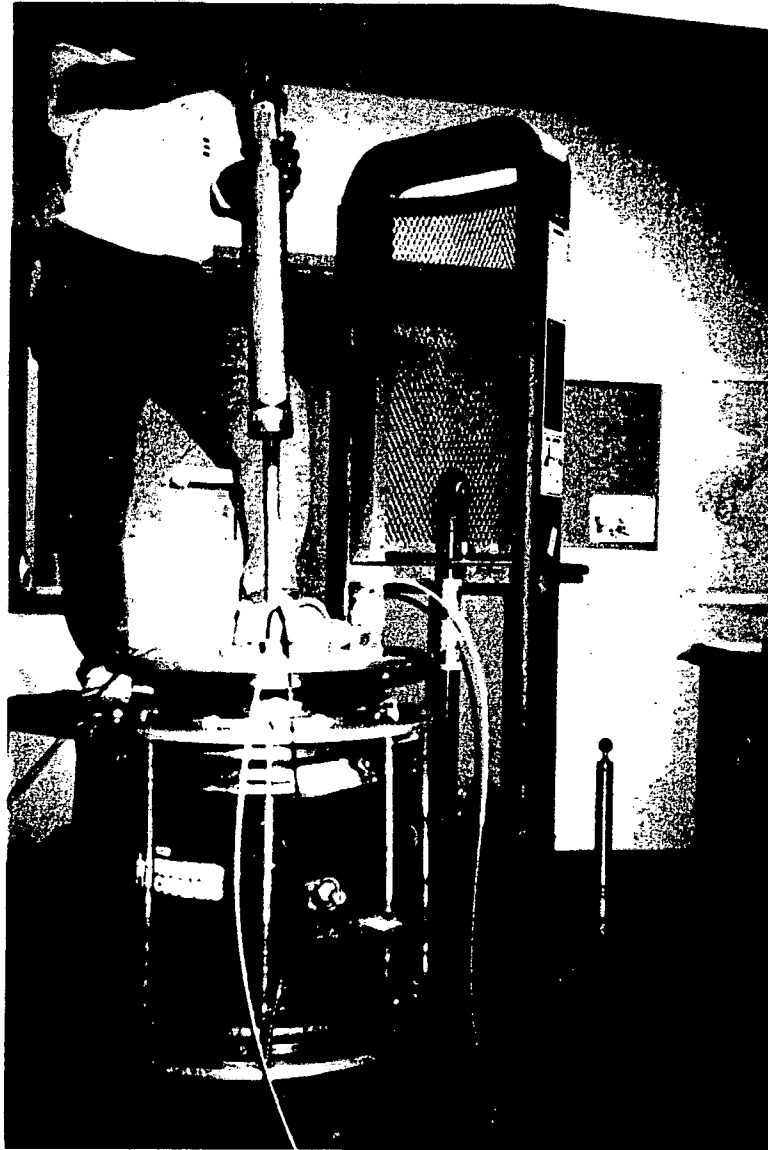
Fig. 4.28: Pile Driving Process for the Seaquake Tests
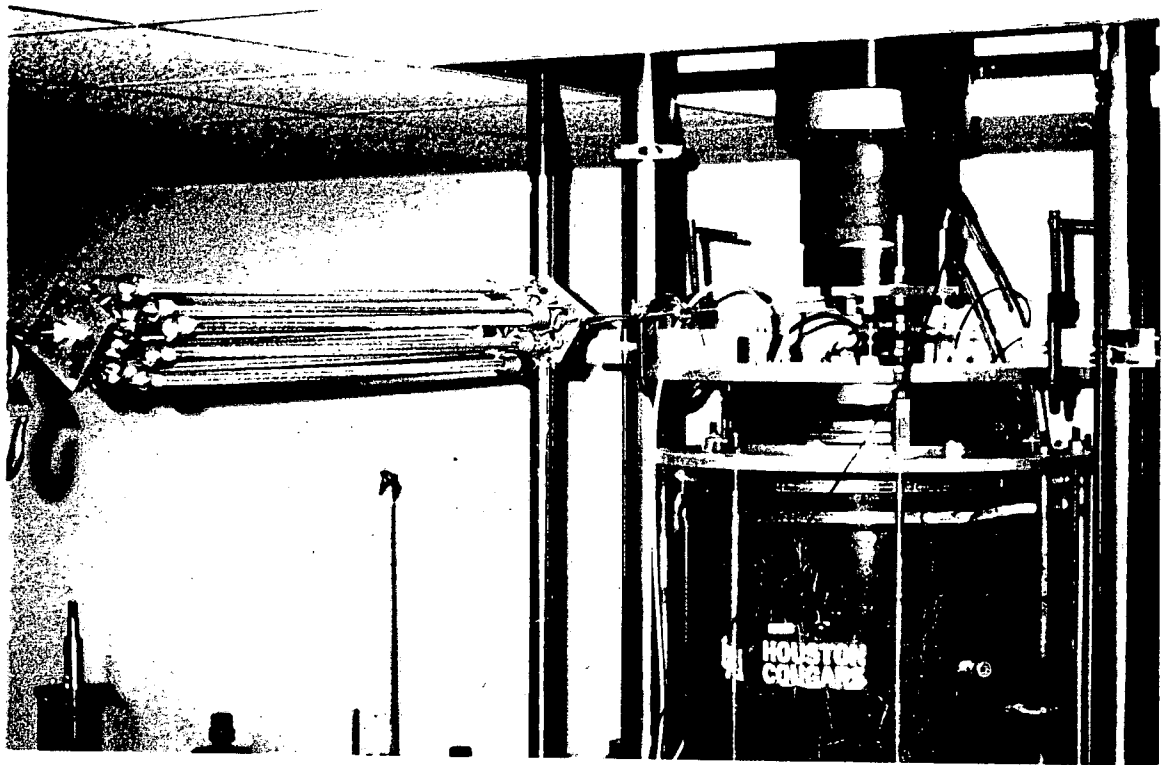
Fig. 4.29: Display of the Water Compartment for the Seaquake Tests
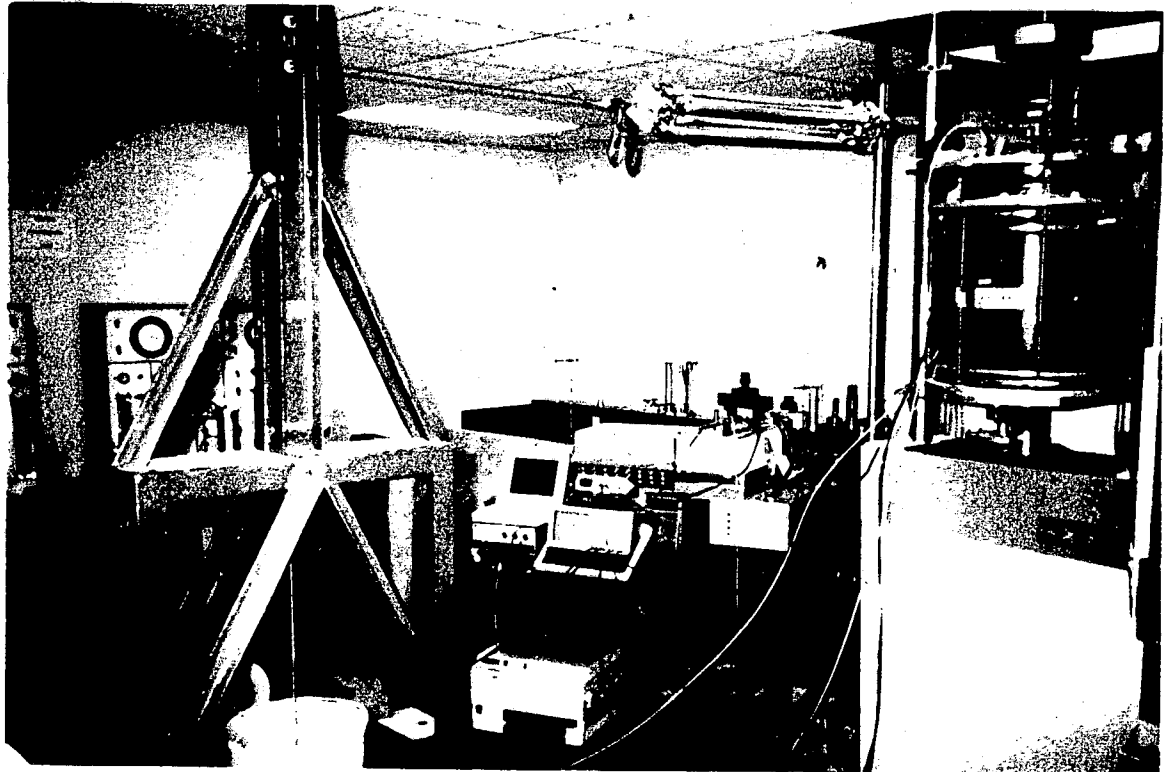
Fig. 4.30: Testing Arrangement for Study of Pile Response During Seaquakes

4.5 Testing Protocol

4.5.1 Signature Series

Ground excitation tests were conducted with scaled magnitudes of the simulated Upland and Oceanside events to compare the effects of signature of the two events on pile performance at the SEMS site. The following testing sequence was followed.

i) The test sand was deposited into the chamber at 55% ± 3% relative density. The sand was saturated with deaired water.

ii) The sand was allowed to consolidate under an isotropic confining stress of 17.24 kPa (simulating top 4.5 m of the prototype modeled). Volume change during consolidation was measured.

iii) The model pile was driven by impact into the chamber. Records of pore water pressure in the near field and the far field were obtained during the process of driving.

iv) A static uplift load-controlled test was conducted on the pile and the pile capacity at a prescribed failure displacement was measured.

v) The pile was restruck by a single blow of the hammer and then loaded in tension to the desired percentage of the static uplift capacity obtained in step (iv) using the spring-mass system.

vi) The pressure chamber along with the loaded pile was then subjected to the desired shaking event using the Instron testing machine.

vii) Records of pile-head load, pile-head movement, and the pore-water pressure development in the near field and the far field were made during the shaking event.

viii) Following the shaking event, the post-shaking capacity of the pile was evaluated by loading the pile to failure in uplift.

4.5.2   Seaquake Tests

Two series of tests were conducted. The first series of tests was conducted in the absence of the pile to investigate the sea-seabed interaction during seaquakes, and the second series studied the pile response to the sea-seabed interaction during seaquakes. The procedures for the test soil deposition and placement of soil instruments were essentially identical to those for the ground excitation tests, except for differences in the locations of the instruments, which have been pointed out earlier. The following procedures were adopted during the testing :

Sea-Seabed Interaction Tests

(i)   The test sand was deposited into the chamber at 55% ± 5% relative density. The sand was saturated with deaired water.

(ii) The sand was allowed to consolidate under the applied boundary stresses, and volume change during consolidation was measured.

(iii) The pressure chamber was seated on the base plate of the actuator of the Instron machine and configured to apply the hydrostatic water pressure.

(iv) The desired hydrostatic pressure bias was applied through an air supply panel.

(v) Records of the applied pressure and the pore water pressure in the soil mass at selected locations in the chamber were measured during the application of biased hydrostatic pressure.

(vi) The air supply inlet valve was shut, and the actuator was set to a cyclic sinusoidal motion in a stroke-controlled mode at the prescribed frequency.

(vii) Records of the applied hydrodynamic pressure and pore water pressures in the soil mass at two locations were made during the tests.

Pile-Sea-Seabed Interaction Tests

(i) The test sand was deposited into the chamber at 55% ± 5% relative density. The sand was saturated with deaired water.

(ii) The sand was allowed to consolidate under the applied boundary stresses and volume change during consolidation measured.

(iii) The model pile was driven by impact into the chamber. Records of pore water pressure at the $1/3^{rd}$ and $2/3^{th}$ depth locations were obtained during the process of driving.

(iv) The chamber was mounted on the base plate of the actuator of the Instron testing machine.

(v) A static, load-controlled uplift test was conducted on the pile, and the pile capacity at a prescribed failure displacement was measured.

(vi) The pile was restruck by a single blow of the hammer and then loaded in tension to the desired percentage of the static uplift capacity obtained in step (v) using the spring-mass system.

(v) The chamber was configured to apply the hydrostatic pressure.

(vi) Steps (iv), (v) , and (vi) for "Sea-Seabed Interaction Tests" were performed.

(vii) Records of the pile-head load, pile-head movement, applied hydrodynamic pressure and the pore water pressure developed adjacent to the pile in the mid-depth of the chamber were measured during the test.

(viii) Following the seaquake, the post shaking capacity of the pile was evaluated by loading the pile to failure in uplift.

Chapter 5

EFFECTS OF SIMULATED HORIZONTAL GROUND SHAKING ON AXIAL PILE RESPONSE

5.1 Introduction

This chapter describes the analysis of test data relevant to the understanding of the mechanism of axial response of biased loaded tension piles during horizontal ground shaking events. The following issues have been investigated: (i) Pile behavior under static uplift loads, (ii) Pore water pressures induced during impact driving (an indirect indication of the susceptibility of the test sand to pore water pressure generated during dynamic loading), (iii) Pile performance during horizontal ground shaking from simulated seismic events of different magnitudes (M = 7.0, M = 7.5, and M = 8.0) and signatures 75 km distant, (iv) Post-shaking pile static capacities, (v) Effect of event signature on the condition of pile extraction, and (vi) Implications of test results on pile design.

5.2 Static Uplift Pile Capacity

5.2.1 Testing Program Summary

Preliminary load-controlled static uplift capacity tests were conducted on the model pile driven into the chamber with the intent of investigating the mechanism of load transfer under static uplift loading and establishing a definition of static failure load. All the static capacity tests were load-controlled which was also the manner of application of biased tension loads on the model pile during the shaking tests. A majority of the tests were conducted with the model pile driven into saturated sands deposited at about 55% relative density and confined under a mean ambient effective stress of 17.24 kPa which was the soil condition during the shaking tests, although some tests were performed at higher effective chamber pressure. Additional tests (S#5, S#6, and S#7) were conducted to

estimate the restrike static capacity of a failed pile when redriven by a single blow of a hammer. A summary of the tests is provided in Table 5.1.

5.2.2   f-w   Relationships

Unit shaft shearing resistance versus pile-head movement relationships were derived experimentally for tests S#1, S#2, S#3, S#6, and S#10. Such information is useful in visually interpreting the development of load transfer at the pile-soil interface. Unit load transfer relationships can be used to synthesize the static axial behavior of piles of dimensions different from those employed in this study, provided the effective stresses in the system are equivalent to those in the chamber. Development of the f-w relationships required the determination of load distribution along the pile length. This was accomplished by measuring calibrated output of loads from three levels of strain gages mounted at the pile-head, mid-section and the near-toe locations, respectively, on selected tests. Figs. E.1 - E.4 in Appendix E show the load distribution for these selected static tests. It should be noted that the toe load in tests S1, S2 and S10 is not zero at pullout implying development of suction at the pile toe as it lifts off the soil. In these plots negative values of load indicate tension, while positive values indicate compression. The weight of the pile is not explicitly included in the results since its effect was zeroed during the initial readings. The strain gage readings represent the effect of the external forces acting on the pile during static load tests. The measured loads are based on zero readings taken before the pile was driven, and the unit load transfer curves that were developed from these load distributions contain the effects of any residual stresses that were developed during the pile installation.

The f-w relations were developed for two sections (between gage points), the top section (0 - 178 mm sand penetration) and the bottom section (178 - 356 mm). Unit shaft load transfer, f, was computed from the following expression,

Table 5.1: Summary of Load-Controlled Static Uplift Tests

| Test No. | Soil Parameters | | Blow Count per 25.4 mm during the final phase of driving | Reference Static Capacity (kN) | Static Capacity after Redrive (kN) |
	Measured Relative Density (%)	Initial Mean Effective Stress (kPa)			
S#1	53	17.24	4.0	0.50	
S#2	48	17.24	3.0	0.52	
S#3	48	17.24	3.6	0.61	
S#4	50	17.24	3.6	0.62	
S#5	49	17.24	4.0	0.58	0.55
S#6	50	17.24	3.0	0.44	0.48
S#7	58	17.24	3.6	0.60	0.64
S#8	50	17.24	3.3	0.55	
S#9	52	34.48	6.6	1.10	
S#10	55	34.48	5.0	0.94	

$$f = \frac{\Delta Q}{\pi dz}, \qquad\qquad (5.1)$$

where

DQ = load difference in the pile between gage points,

d = pile diameter, and

z = length difference between gage points.

The parameter w is the pile-head displacement for the corresponding applied load, measured by means of the LVDT mounted to the pile-head. Pile elongation was negligible. The process was repeated for each load to develop sets of points defining the f-w relations. The unit shear transfer and the movements from these relations were then normalized by the effective horizontal chamber pressure, σ'_h, and the pile diamteter, d, respectively. The normalized f-w relationships for selected static tests for the both top and the bottom sections will be given in 5.2.3.

101

5.2.3 OBSERVATIONS AND INTERPRETATIONS

The following observations and interpretations are made:

(i) The piles demonstrated a "ratcheting" behavior under continued uplift loading for both effective stress conditions. Only tests S#2, S#3, S#8, S#9, and S#10 show this kind of behavior in Figs 5.1 and 5.2 as the uplift loading was stopped after the first slip in all the other tests. Successive slipping after the initial slip of the pile was accompanied by a slight gain in capacity. Lehane et al. (1993) studied the mechanisms of shaft friction in medium-dense siliceous sand from instrumented pile uplift and compression load tests. Their investigation revealed that changes occur in the radial effective stress close to the pile during pile loading due to volume strains concentrated in a narrow band of soil close to the interface in addition to changes caused during impact driving. Initial radial effecitve stress reduction along the shaft during uplift loading occurs as a consequence of principal stress rotations relative to that applied during consolidation (a rotation of 90 degrees of the major principal direction), leading to a more contractive response. Following an initial reduction, a marked increase in the radial effective stress occurs as the pile approaches failure, possibly due to dilation, whereby the soil grains close to the shaft move radially to permit slip to occur. The first slip in these static capacity tests can therefore be considered to be the point of complete mobilization of static unit shaft friction associated with increased pile loading and reduction in effective stress, and the gain in capacity in successive slips can be attributed to the dilation of the soil close to the pile-soil interface under very large deformation.

(ii) For each of the static uplift capacity tests, the first slip occurred within a pile-head movement of 0.5% of the pile diameter (0.15 mm).

(iii) The static capacities of the restruck piles were within ± 8% of their measured static capacities prior to restrike, and failure occurred at about the same pile-head movement as that measured during the first test. See Fig.5.3.
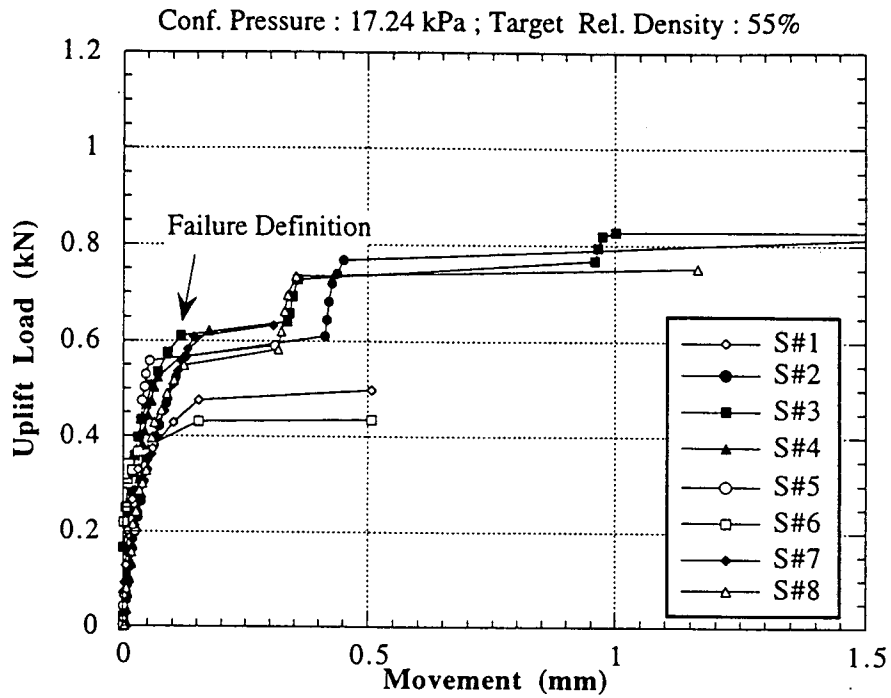
Fig. 5.1: Static Load-Movement Curves in Medium-Dense Saturated Sand Under a Mean Effective Stress of 17.24 kPa
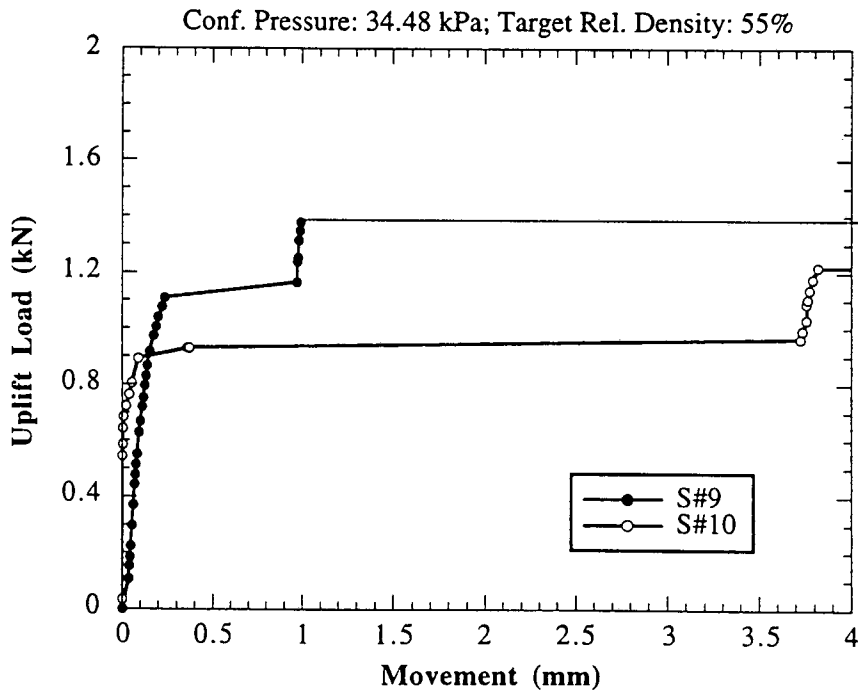
Fig. 5.2: Static Load-Movement Curves in Medium-Dense Saturated Sand Under Mean Effective Stress of 34.48 kPa
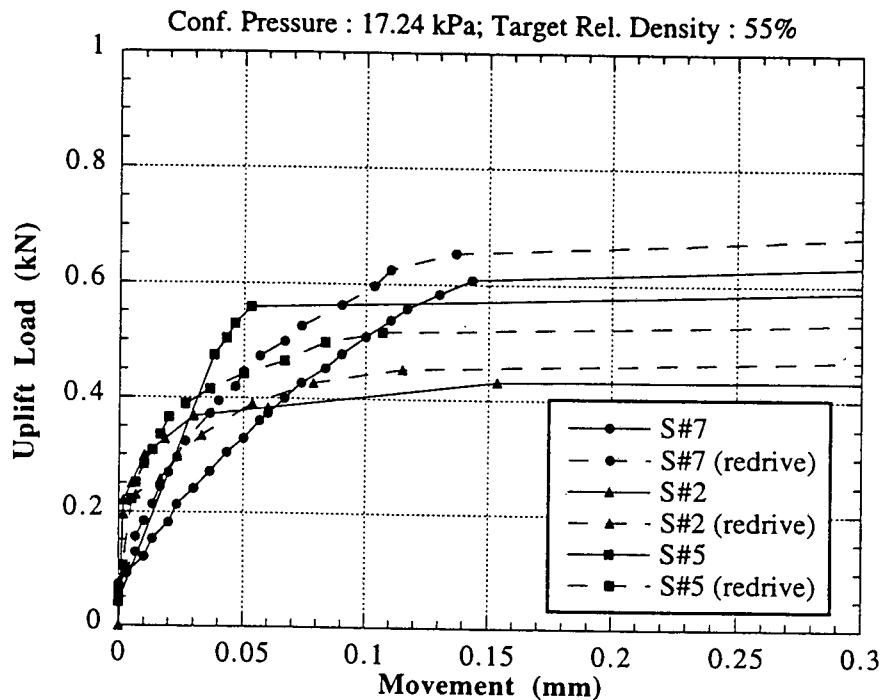
Fig. 5.3 : Comparison of Restrike Uplift Behavior of the Pile
with the Reference Uplift Behavior

(iv) The mean static capacity of the piles for an effective stress condition of 17.24 kPa was 0.55 kN, and the corresponding mean static capacity for an effective stress condition of 34.48 kPa was approximately 1.02 kN.

(v) Greater maximum values of unit shaft resistance occurred in the lower half of the pile (depths greater than seven diameters). The average ultimate f values normalized by the mean effective chamber pressure for both effective stress conditions was 0.84 in the top half of the pile and 1.33 in the bottom half of the pile, as shown in Fig.5.4. These data suggest that a surface effect existed during uplift loading, whereby the flexible, pressurized surface of the sand within the chamber permitted development of shear planes at an angle to the interface, which possessed a lower shear strength than the interface plane, permitting failure to occur at a lower interface shearing stress.

104
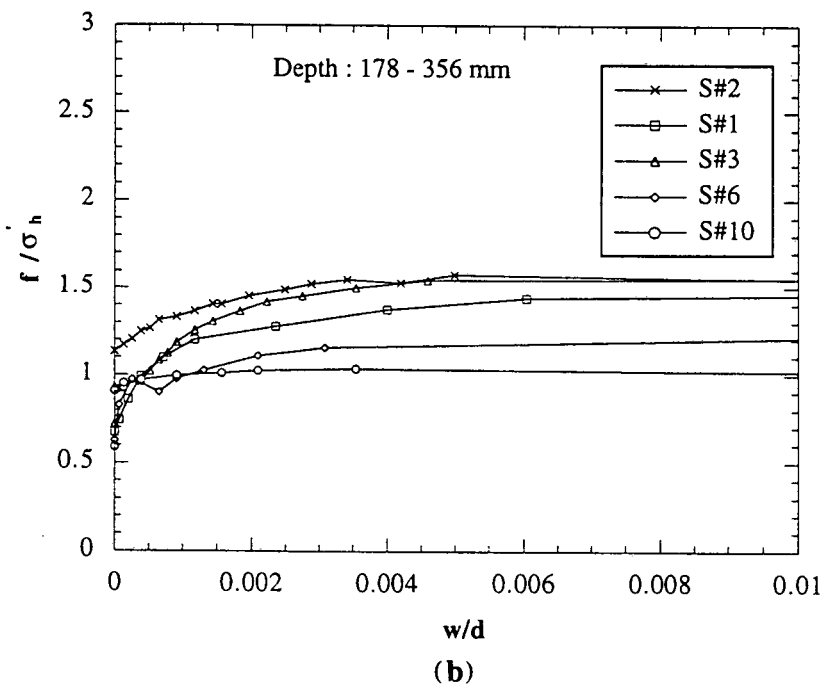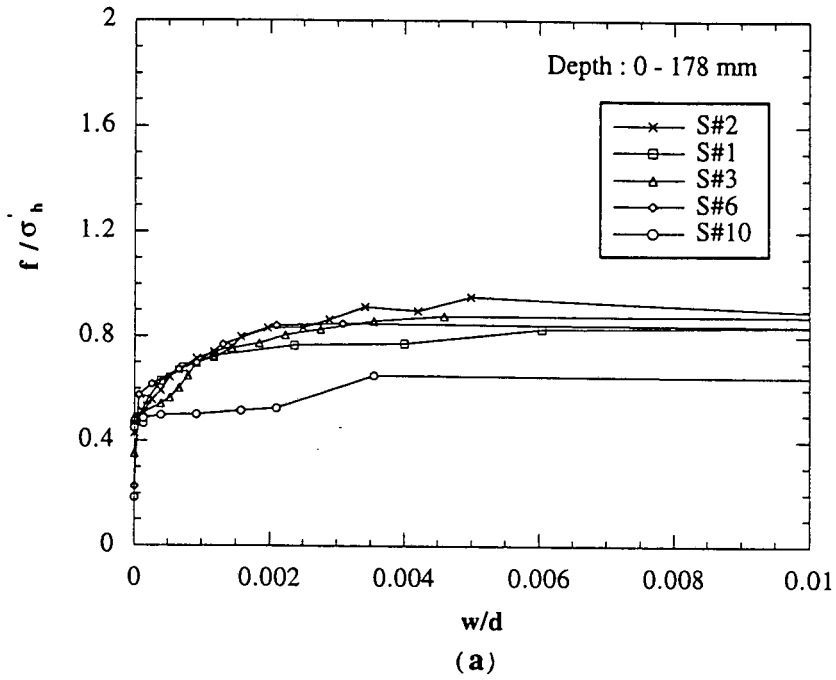
Fig. 5.4: f-w Relationships for Selected Tests: (a) Upper Half
of Pile; (b) Lower Half of Pile

105

(vi) Much of the unit shaft friction (typically 35% - 60%) was already developed in the form of residual stresses before the pile was subjected to uplift loading.

(vii) The insertion of the pile into the chamber produced an increase in the horizontal effective stress in the chamber at the pile-soil interface. Assuming that $f_{max} = \sigma'_h \tan\delta$, where σ'_h = radial effective stress at the pile-soil interface, and δ = angle of interface shear (27°), the average radial effective stress at the pile-soil interface can be computed to be $1.09 / \tan 27° = 2.0$ times the simulated radial in-situ (lateral effective chamber) pressure. The insertion of the pile, therefore, must have increased the effective stress in the soil immediately surrounding the pile, as is predicted by the expanding cavity models [Vesic (1972)]. Based on extensive tension tests performed on model piles placed by different driving methods in a calibration chamber, Levacher et al. (1984) suggested a "placement method coefficient" of 2 for driven piles to account for increase in radial effective stress during placement, which appears to be in agreement with the value obtained here.

5.3 Pile Performance During Simulated Seismic Events

5.3.1 Testing Program Summary

Seismic loading tests were performed on the model test pile by applying the displacement-time histories scaled for event magnitude, geometry, and diffusion for the Upland and the Oceanside events to the base of the pressurized soil chamber while the pile was held under biased uplift load by the spring-mass system. Several tests were conducted in medium-dense saturated sand at a relative density of 55±5% and a mean effective chamber stress of 17.24 kPa by varying the magnitude of the scaled earthquakes (7.0, 7.5, and 8.0) and the magnitude of the applied biased load (45% to 90% of the static capacity) on the pile for each of the two events. For piles that did not fail during the seismic events, static loading was performed to failure to define the post-shaking capacity of the pile. The

106

results of horizontal shaking tests with the Oceanside event and the Upland event are summarized in Tables 5.2 and 5.3, respectively. Results from previous tests conducted with the Oceanside event by Ochoa [1990] have also been included in Table 5.2 for comparison purposes.

5.3.2 Pore Water Pressure Response During Impact Driving

Measurements of induced pore water pressure generated in the soil mass by impact driving of piles for the shaking tests were made by means of miniature pore water pressure transducers embedded in the soil mass at the level of the mid-depth of the chamber, one in the "near field," 1 diameter from the pile wall and the other in the "far field," 14 diameters from the pile wall. Variations in the initial relative densities of the soil, volume changes during consolidation and during pile driving resulted in a range of blow counts (2.5 blows to 5 blows), measured during the final phase of driving during the shaking tests (about 3 pile diameters depth). Pore water pressure measured for typical tests such as UP#19, UP#8, UP#4 and UP#5, representing tests with different blow counts, are shown in Figs. 5.5 and 5.6. Data for other tests have been attached in Appendix F. The pile driving process generally took about 60 secs for completion. A residual build up of excess pore water pressure was observed both in the near field and the far field, in addition to the instantaneous pore water pressure response of the pile to each blow of the hammer, possibly due to the boundary effects of the proximity to the chamber wall. This reasoning was verified by pore water pressure measurements during the driving process for the seaquake tests, where the pile was driven in the center of the chamber further from the boundary. These results are presented in Chapter 6. The positive pore water pressure increased as the pile toe approached the level of the instruments, and the peak values were in the order of 20% - 40% of the effective chamber pressure in the near field and 10% - 18% of the effective chamber pressure in the far field. Once the pile toe passed the level of the instruments further increase in positive pore water pressure was arrested.

107

Table 5.2: Summary of the Results of Horizontal Shaking Tests Conducted for the Oceanside Event

Test* No.	Event Magnitude	Meas. Relative Density (%)	Vol. Decrease During Consolidation (cc)	Blow Count per 25.4 mm During Final Phase of Driving	Reference Static Capacity (kN)	Applied Bias Load Expressed as a Percentage of Static Capacity	Post Shaking Capacity (kN) / Loss (-) or Gain (+) in Capacity (%)	Pile-Head Movement During Shaking (mm)	Condition of Pile Extraction
OS#1	7.0	58	350	3	0.49	46	0.47 (-4)	0.06	Stability
OS#2	7.0	55	-	3	0.46	65	0.47 (+2)	0.05	Stability
OS#3	8.0	55	500	4	0.68	60	0.59 (-13)	0.30	Mobility
OS#4	8.0	62	370	6	0.87	64	0.77 (-12)	0.23	Mobility
OS#5	8.0	53	325	3	0.43	77	(-23)	pull out	Failure
OS#6	8.0	55	-	3	0.53	92	-	pull out	Failure
OS#7a	8.0	54	375	3	0.52	69	0.41 (-21)	0.33	Mobility
R1b	7.0	-	-	4	0.44	76	0.42 (-4.5)	0.15	Stability
R2b	7.0	-	-	4.3	0.49	89	0.46 (-6.1)	1.14	Mobility
S1b	7.5	-	-	5.0	0.61	63	0.57 (-6.5)	0.04	Stability
S2b	7.5	-	-	5.0	0.61	62	0.56 (-8)	0.00	Stability
S3b	7.5	-	-	4.3	0.49	77	0.45 (-8)	0.25	Mobility
S4b	7.5	-	-	4.2	0.47	91	(-9)	pull out	Failure
U1b	8.0	-	-	3.5	0.35	45	0.32 (-8)	0.05	Stability
U2b	8.0	-	-	4.3	0.51	64	0.43 (-16)	0.25	Mobility
U3b	8.0	-	-	4.0	0.44	78	(-22)	pull out	Failure

* All tests conducted in saturated sand deposited at 55% target relative density and 17.24 kPa mean ambient effective stress
a Test in which the only controlled vertical stress was applied to the pressure chamber (Mean Effective Stress = 17.24)
b Tests conducted by Ochoa (1990)
c Initial volume of soil = 93200 cc

Table 5.3: Summary of the Results of the Horizontal Shaking Tests Conducted for the Upland Event

Test* No.	Event Magnitude	Meas. Relative Density (%)	Vol. Decrease During Consolidation (cc)	Blow Count per 25.4 mm During Final Phase of Driving	Measured Reference Static Capacity (kN)	Applied Bias Load Expressed as a Percentage of Static Capacity	Post Shaking Capacity (kN) / Loss (-) or Gain (+) in Capacity (%)	Pile-Head Movement During Shaking (mm)	Condition of Pile Extraction
UP#1	7.0	55	570	3	0.56	50	0.55 (-2)	0.006	Stability
UP#2	7.0	53	600	4	0.59	63	0.575 (-2.5)	0.06	Stability
UP#3	7.0	62	600	5	0.86	73	0.84 (2.3)	0.06	Stability
UP#4	7.0	56	570	4	0.62	75	0.59 (-4.8)	0.17	Mobility
UP#5	7.0	60	600	5	0.87	78	0.82 (-5.7)	0.29	Mobility
UP#6	7.0	57	370	3	0.51	80	0.50 (-2.0)	0.19	Mobility
UP#7	7.0	52	570	3.25	0.52	85	0.48 (-7.7)	0.30	Mobility
UP#8	7.5	55	340	3.5	0.48	60	0.45 (-6.3)	0.10	Stability
UP#9	7.5	51	700	3.0	0.52	75	0.51 (-2)	0.15	Mobility
UP#10	7.5	50	700	2.5	0.35	75	0.29 (-17.1)	0.18	Mobility
UP#11	7.5	48	570	3	0.45	80	0.39 (-13.3)	0.53	Mobility
UP#12	7.5	62	600	4	0.71	81	0.66 (-7)	0.38	Mobility
UP#13	7.5	54	625	3.5	0.44	85	0.39 (-11)	0.41	Mobility
UP#14	7.5	50	325	3	0.46	89	-	pull out	Failure
UP#15	8.0	60	425	5	0.89	45	0.83 (-6.7)	0.09	Stability
UP#16	8.0	53	400	4.5	0.64	61	0.56 (-12.5)	0.99	Mobility
UP#17	8.0	50	470	2.5	0.36	71	0.29 (-19.0)	0.38	Mobility
UP#18	8.0	53	530	3	0.46	78	-	pull out	Failure
UP#19	8.0	55	460	3	0.48	75	-	pull out	Failure

* All tests conducted in saturated sand deposited at 55% target relative density and 17.24 kPa mean ambient effective stress
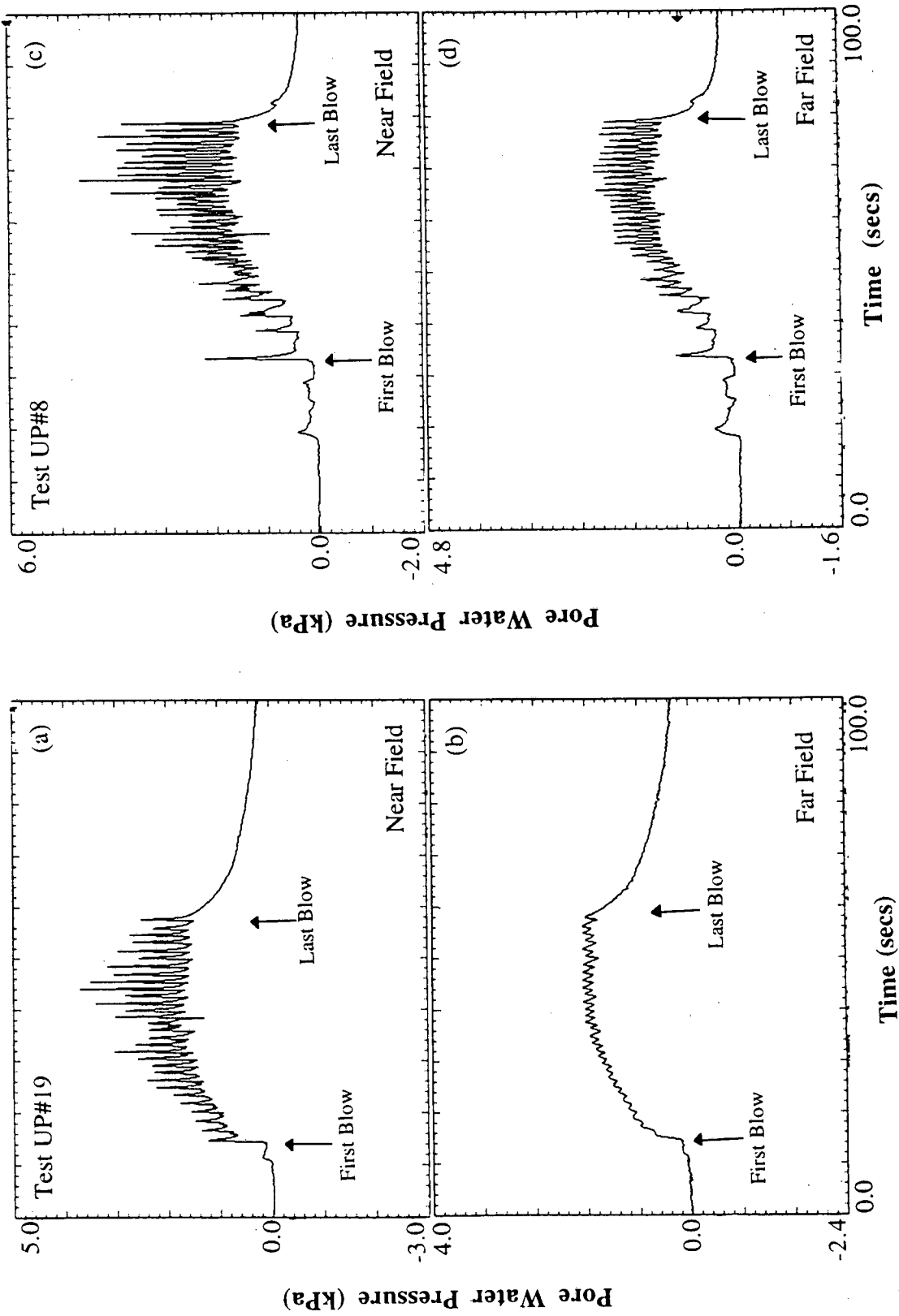
Fig. 5.5: Pore Water Pressure Measured During Impact Driving; Tests UP#19 and UP#18

110
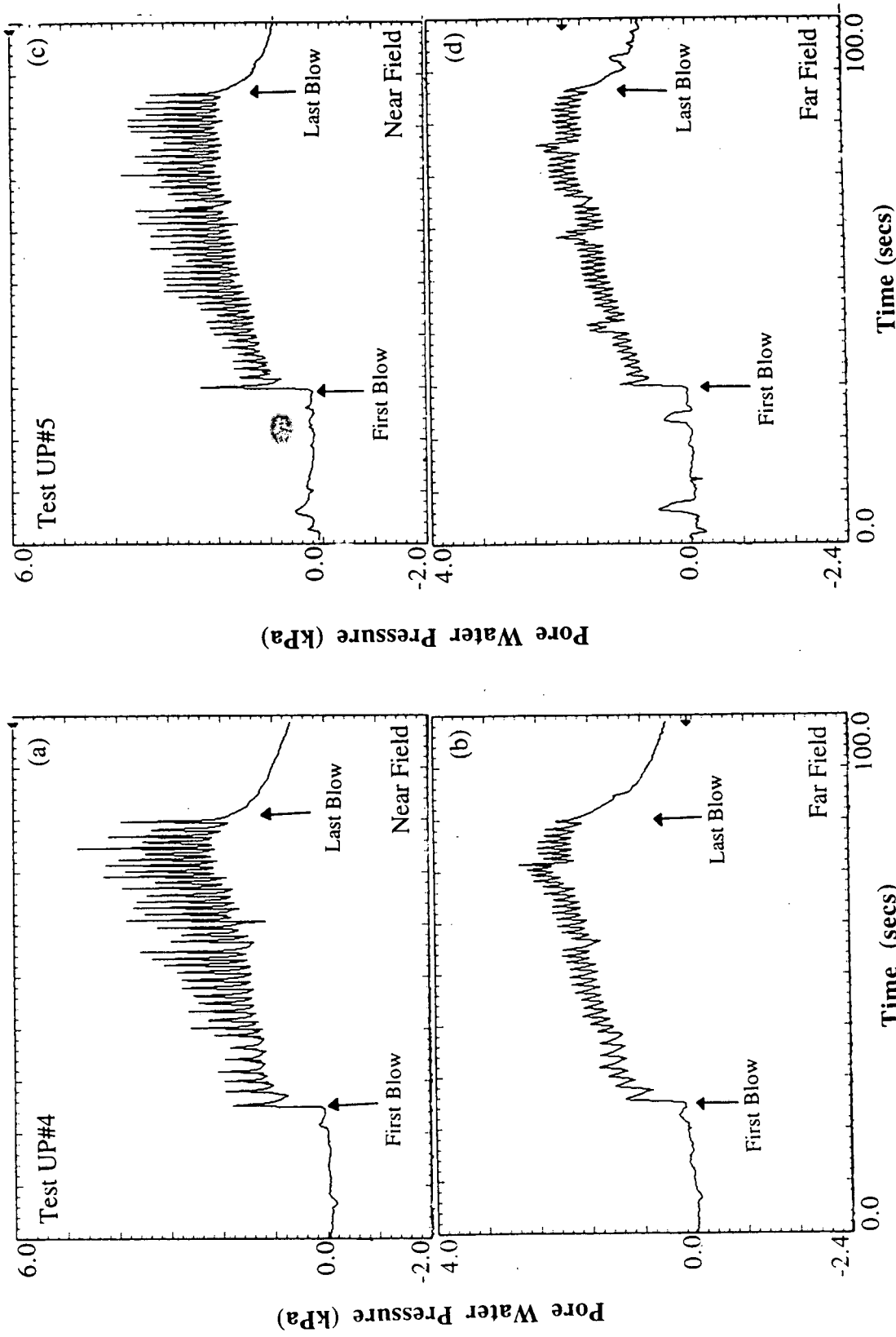
Fig. 5.6: Pore Water Pressure Measured During Impact Driving: Tests UP#4 and UP#5

111

5.3.3 Pile Response Mechanisms

Time history measurements of pile-head axial load, pile-head axial movement and the near field and far field pore water pressure were made during the horizontal shaking tests. Data from typical tests which have been summarized in Tables 5.2 and 5.3, are discussed below to describe the mechanism of pile response under various levels of static biased tension loads during different magnitudes of the simulated seismic events (Upland and Oceanside). Data for the remaining tests are presented in Appendix G.

Magnitude = 7.0 - Stablity and Mobility Conditions

Test UP#1 - Bias Load = 50% of Uplift Static Capacity - Upland Event (Fig. 5.7)
Test UP#4 - Bias Load = 75% of Uplift Static Capacity - Upland Event (Fig.5.8)
Test R2 - Bias Load = 90% of Uplift Static Capacity - Oceanside Event (Fig. 5.9)

Time history measurements of the axial pile-head load, movement and pore water pressure response during horizontal ground shaking with M = 7.0 for the simulated Upland event (Test UP#1 and Test UP#4) are shown in Figs 5.7 and 5.8, respectively. It is noted that despite the imposed horizontal motion in the soil, some near random axial load variation occurred at the pile-head with positive and negative load excursions from the applied bias load. This effect has been explained by Ochoa [1990] as being produced by a lag between the translatory motion of the pile-head and the translatory motion of the pulley arm supporting the tension cable above the pile-head, which caused the direction of loading to oscillate near-randomly between the vertical and about 20 degrees from the vertical. Such action produced both decreases and increases in the axial component of head load. The decreases were apparently due mostly to the effect of the axial component of an inclined tensile load, while the increases were apparently associated with slight stretching of the spring in the simulated superstructure associated with small increases in distance between

112

Fig. 5.7: Time History Measurements During Shaking Test UP#1
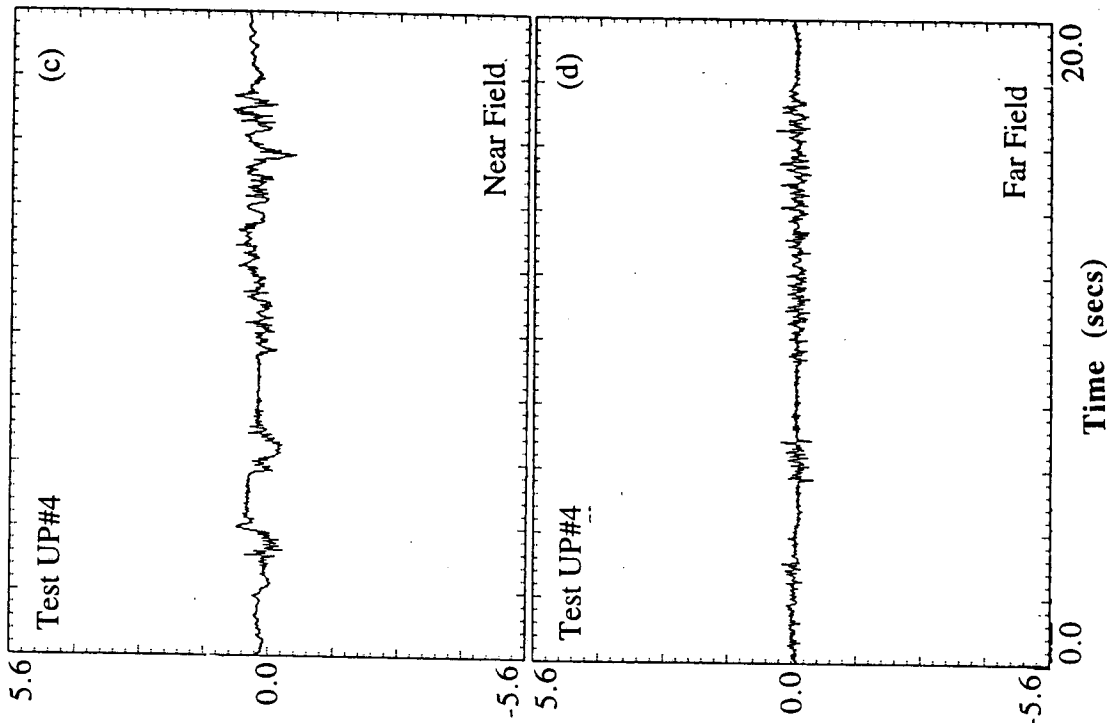
113

Fig. 5.8: Time History Measurements During Shaking Test UP#4

114

(Note: 1 in. = 25.4 mm; 1 psi = 6.9 kPa, 1 lb = 0.005 kN)

Fig. 5.9: Time History Measurements During Shaking Test R2 [After Ochoa (1990)]

115

the pulley and pile-head as the chamber moved and the pulley support lagged the chamber motion. The increase in the peak tension load was about 7% of the static uplift capacity of the pile.

Such type of axial load variations on a bias tension-loaded pile are likely to occur in real structures, although the amplitude of axial load variation will be dependent on the details of the superstructure-foundation interaction. This type of dynamic load excursion was common for all horizontal shaking tests.

The pore water pressure buildup in the far field during the M = 7.0 simulated Upland event was in the order of 0.21 kPa - 0.34 kPa (1.2 - 2% of the pre-drive effective chamber pressure), mainly oscillatory with very little buildup of residual pore water pressure. The near field pore water pressure close to the surface of the pile was twice as large as in the far field. It appears that higher pore pressures were generated in the near field as a result of relative movement of the pile with respect to the soil and vice versa.

The horizontal shaking resulted in an upward movement of the pile in the direction of the applied bias tension load. The upward motion resulted from the combined effect of degradation of strength due to positive pore water generation and overloading due to the superstructure feedback. In all the three tests, complete failure or pile extraction with complete loss in pile capacity did not occur during shaking. In test UP#1, where the applied bias loading was about 50% of the static uplift capacity, very small upward movement was observed during the shaking (less than the movement required to cause static failure, i.e., 0.15 mm). In contrast, in test UP#4, where the applied bias loading was 75% of the static uplift capacity an upward movement of 0.17 mm (corresponding to prototype movement of 0.17 x 5.2 = 0.88 mm) occurred. In other words, the pile-head movement increased with increase in the magnitude of bias loading for the same magnitude of the event. It appeared that there existed a threshold uplift static bias load below which the piles remained in a stable condition during the seismic event with very little (less than the

static failure movement) or no movement under sustained loading. Similar behavioral trends were also observed for other magnitude earthquakes for both the Upland and Oceanside events (See Tables 5.2 and 5.3.) Test UP#4 represented a "mobility" condition where the pile movement exceeded the static failure movement without a drop in the pile load-carrying capacity during the event. This is an important serviceability consideration for prototype piles that are designed as rigid and elastic, where a movement of such an order can affect the serviceability of the superstructure that these piles support.

The observed pile behavior is consistent with observations made during undrained cyclic loading of saturated sands [Seed and Idriss (1971)]. These studies show that there exists a threshold or critical level of repeated stress below which only limited strains are developed in a triaxial specimen with an increasing number of cycles. Beyond this critical level, accumulation of large strains occurs with an increasing number of cycles of loading, ultimately leading to failure of the specimen. An increase in the initial static shear stress bias also accelerates the failure of the specimen.

The pile-head load and movement response and the soil pore water pressure response for Test R2 are shown in Fig. 5.9. The test was performed under 90% bias tension load and the simulated Oceanside event with M = 7.0. Despite the difference in signature of the Oceanside event, the circumstances leading to an excessive upward movement condition, in terms of pile and soil response were similar to test UP#4 for the Upland event.

Magnitude = 7.5 - Stability and Mobility Conditions

Test UP#8 - Bias Load = 60% of the Uplift Static Capacity - Upland Event (Fig. 5.10)
Test UP#13 - Bias Load = 85% of the Uplift Static Capacity - Upland Event (Fig. 5.11)

The following comments can be made regarding pile and soil response during the M = 7.5 simulated seismic events. Peak excursions in the pile-head load were about 7 - 8 %

117

of the static uplift capacity, similar to those observed during M = 7.0 simulated events. The time history measurements of pile-head movement, near field pore water pressure and far field pore water pressure for Test UP#8 are shown in Figs 5.10 (b), (c), and (d), respectively. Similar measurements for Test UP#13 are shown in Figs 5.11 (b), (c), and (d). These figures suggest that the excess pore water pressures in the soil mass (far field) for the M = 7.5 simulated Upland event were about three times those developed for the M = 7.0 events, primarily because of higher shear strains induced in the soil during the M = 7.5 shaking event. The near field pore water pressure close to the pile was about 1.05 kPa (6% of the predrive ambient effective stress), which was marginally higher than the far field pore water pressure of about 0.86 kPa (5% of the predrive ambient effective stress). Higher pore water pressures can be expected close to the pile at lower levels of bias loading (< 60%), where the soil response is initially more contractive. This phenomenon was verified during direct-interface shear tests conducted at the same relative density, given in Chapter 4. Axial pile movement occurred in the form of successive slips in response to load changes at the pile-head and mainly to instantaneous rises in pore water pressure, corresponding to severe displacement peaks in the train of displacements to which the soil was subjected. The first severe peak occurred at about 4 - 5 secs (unscaled time), or 21 - 26 secs scaled time, after the start of the simulated seismic event, corresponding to the point of peak ground velocity of the simulated Upland event, as shown in Fig. 3.11 in Chapter 3.

Positive pore pressures reached 6% of the initial ambient effective stress, which implies a maximum reduction in pile capacity of 6%. Since the combined static bias and dynamic axial head load did not exceed about 94% of the pile's static capacity, failure did not occur during tests UP#8, UP#13. In test UP#8, the pile remained stable with a net movement of 0.10 mm (less than static failure movement of 0.15 mm), corresponding to a scaled prototype movement of 0.52 mm, whereas pile movement exceeded the
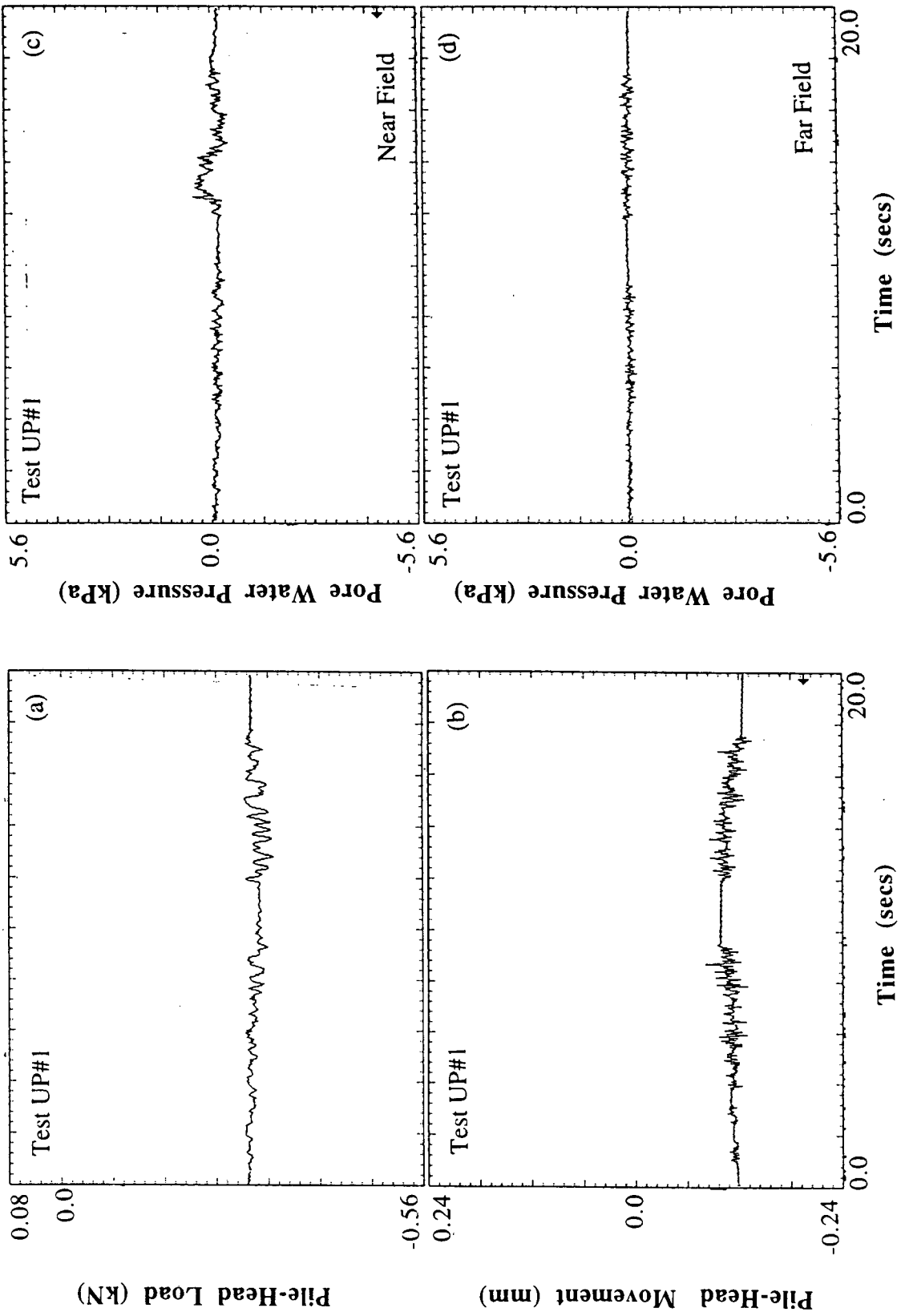
Fig. 5.10: Time History Measurements During Shaking Test UP#8

119
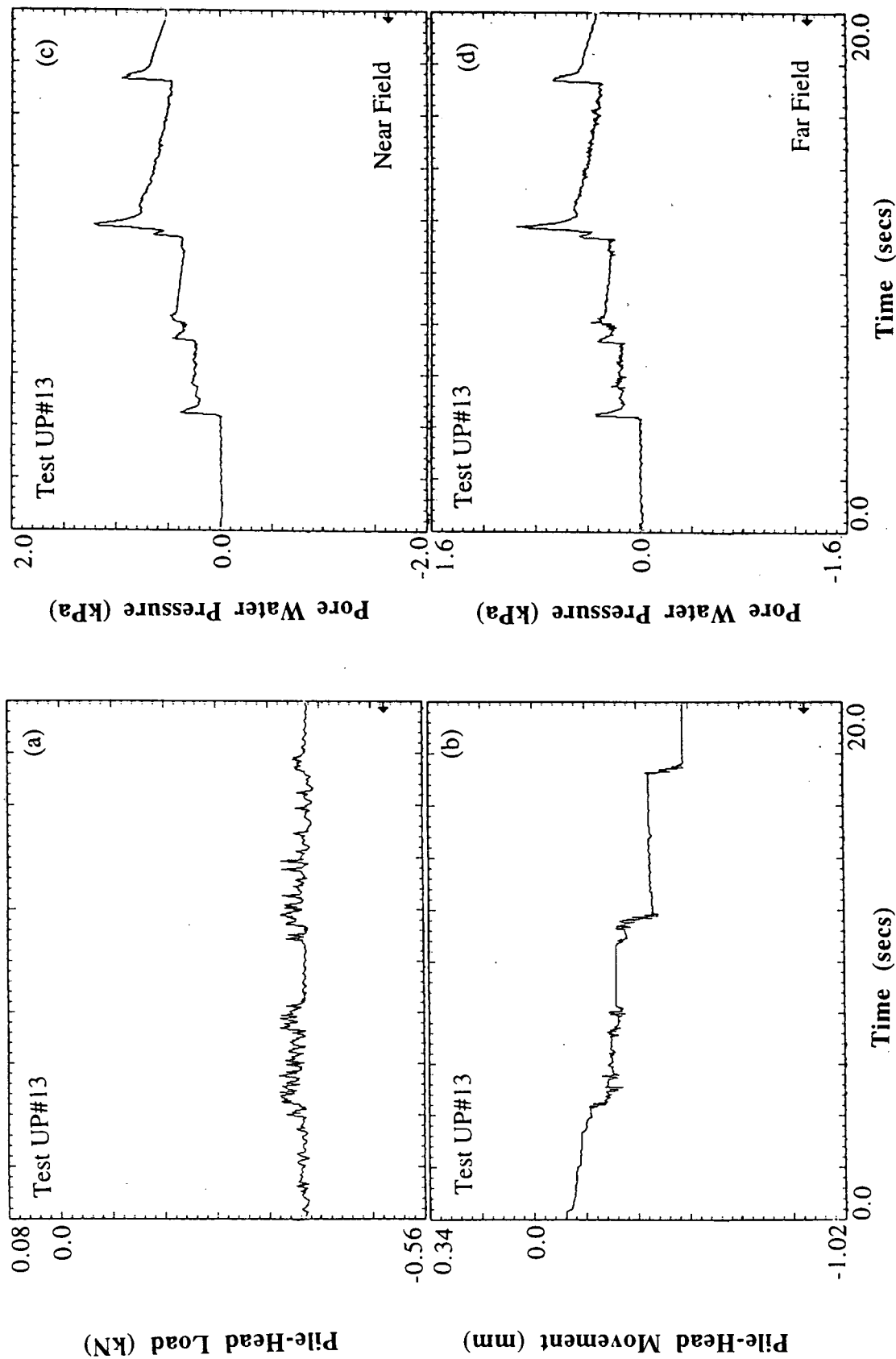
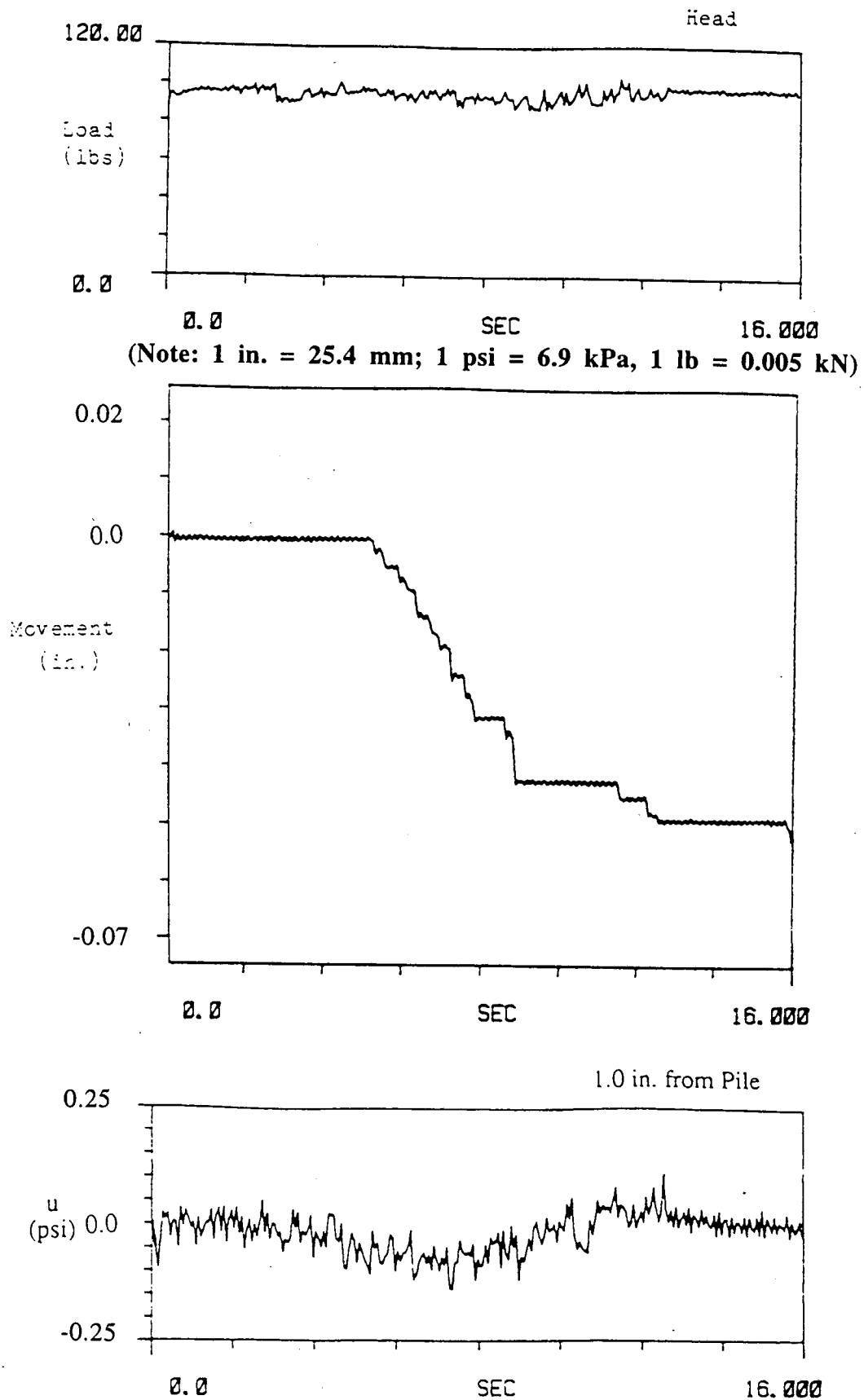Fig. 5.11: Time History Measurements During Shaking Test UP#13

static movement of 0.15 mm (i.e. 0.41 mm unscaled movement) in Test UP#13. This implies that the threshold bias load condition for stability for the piles during M = 7.5 lay somewhere between 60% bias loading and 85% bias loading

Magnitude = 7.5 - Failure Condition

Test UP#14 - Bias Load = 89% of Uplift Static Capacity - Upland Event (Fig. 5.12)

Some comments regarding Test UP#14 are in order. First, initiation of failure started at about 4 secs (scaled time) at which point a surge in pile-head load (8% of the static uplift capacity of the pile) caused a movement of 0.39 mm. Second, failure (excessive pile movement associated with significant reduction of load on the pile) took place about 8 sec (unscaled (model) time), or 42 secs, scaled (prototype) time, after the start of the simulated seismic event. It must be noted at this point that in Test UP#13 discussed above, although excessive pile movement occurred at a slightly lower bias loading (85%), permanent loss in capacity did not occur in that test during the shaking event. Third, generation of positive pore water pressure did not occur prior to pullout in UP#14. That is, no degradation of unit shaft resistance occurred during the event, but the soil-pile-structure interaction produced enough additional instantaneous load at the pile head to exceed the pile's static capacity, following which failure occurred. Fourth, negative pore water pressure (suction) was triggered by the pile while being pulled out. Similar trends in pile displacement and generation of negative pore water pressure were observed in a study conducted on small scales piles embedded in clay and subjected to tensile cyclic loading in a centrifuge [Lambson (1988)]. A time lag of a fraction of a second existed between the development of suction in the far field and the near field, possibly because of flow of water to fill the void generated at the pile toe as the pile was being pulled out. Once the pile movement was arrested as the pile head hit the cross beam, suction decreased and positive pore pressures were established. The failure mechanism, therefore, for this event was primarily as a result of overloading of the pile, and pore water pressure did not have any
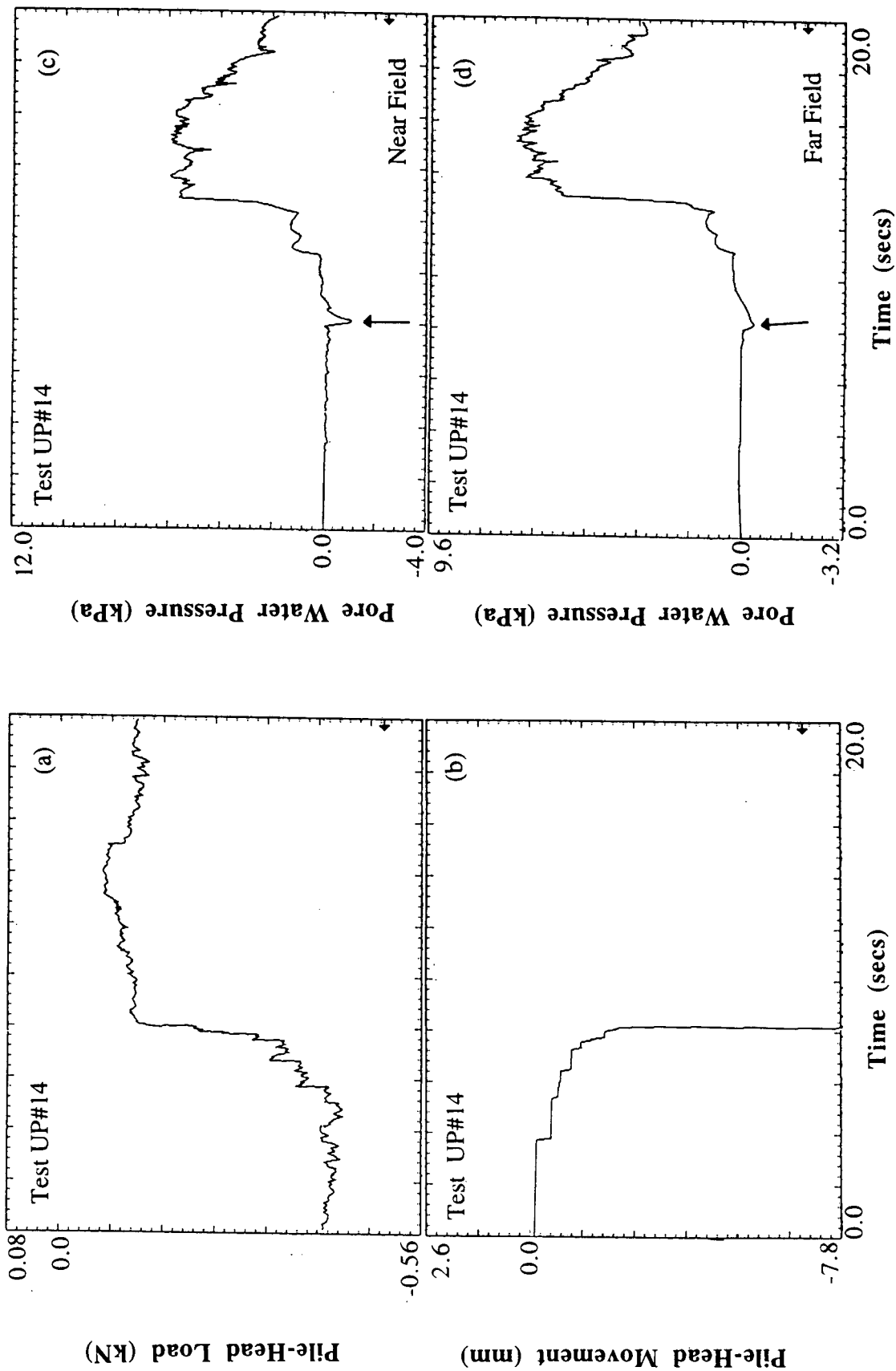
Fig. 5.12: Time History Measurements During Shaking Test UP#14

122

consequential effect on the soil strength. Test S4 conducted with the M = 7.5 simulated Oceanside event also demonstrated similar pile behavior. Therefore, in general, these failure conditions and the mechanism can be postulated as typical for M = 7.5 offshore California-type seismic events.

Magnitude = 8.0 - Stability and Mobility Conditions

Test UP#15 - Bias Load = 45% of the Uplift Static Capacity - Upland Event (Fig. 5.13)
Test UP#16 - Bias Load = 61% of Uplift Static Capacity - Upland Event (Fig. 5.14)
Test OS#3 - Bias Load = 60% of Uplift Static Capacity - Oceanside Event (Fig. 5.15)

Time history measurements of pile-head bias tension load during the M = 8.0 simulated seismic events (Upland and Oceanside) are shown in Figs 5.13, 5.14 and 5.15. Similar trends to those observed during M = 7.0 and M = 7.5 events are seen, except that the dynamic load excursions on the pile head were larger, ranging from 10 - 12% of the static uplift capacity due to increased movement of the chamber associated with a larger earthquake and increased lag between the pile head and loading pulley. Pile movement in Test UP#15 was substantially smaller than in Test UP#16, which was conducted at a relatively higher level of bias loading (about 0.09 mm, which is 0.47 mm in the prototype). Such a movement is interpreted as representing a "stable" condition.

The effect of signature of an event on the pile response can be clearly understood by comparing tests UP#16 and OS#3, both conducted at about 60% bias loading. In both cases, the piles sustained the applied load with significant movements exceeding the stability criterion established earlier, and the pile extraction condition was classified as in between stability and failure (referred to as "mobility").

A comparison of UP#16 with UP#8 shows that for the same bias loading, greater pile-head movement occurred due to an increase in the magnitude of the simulated seismic

123
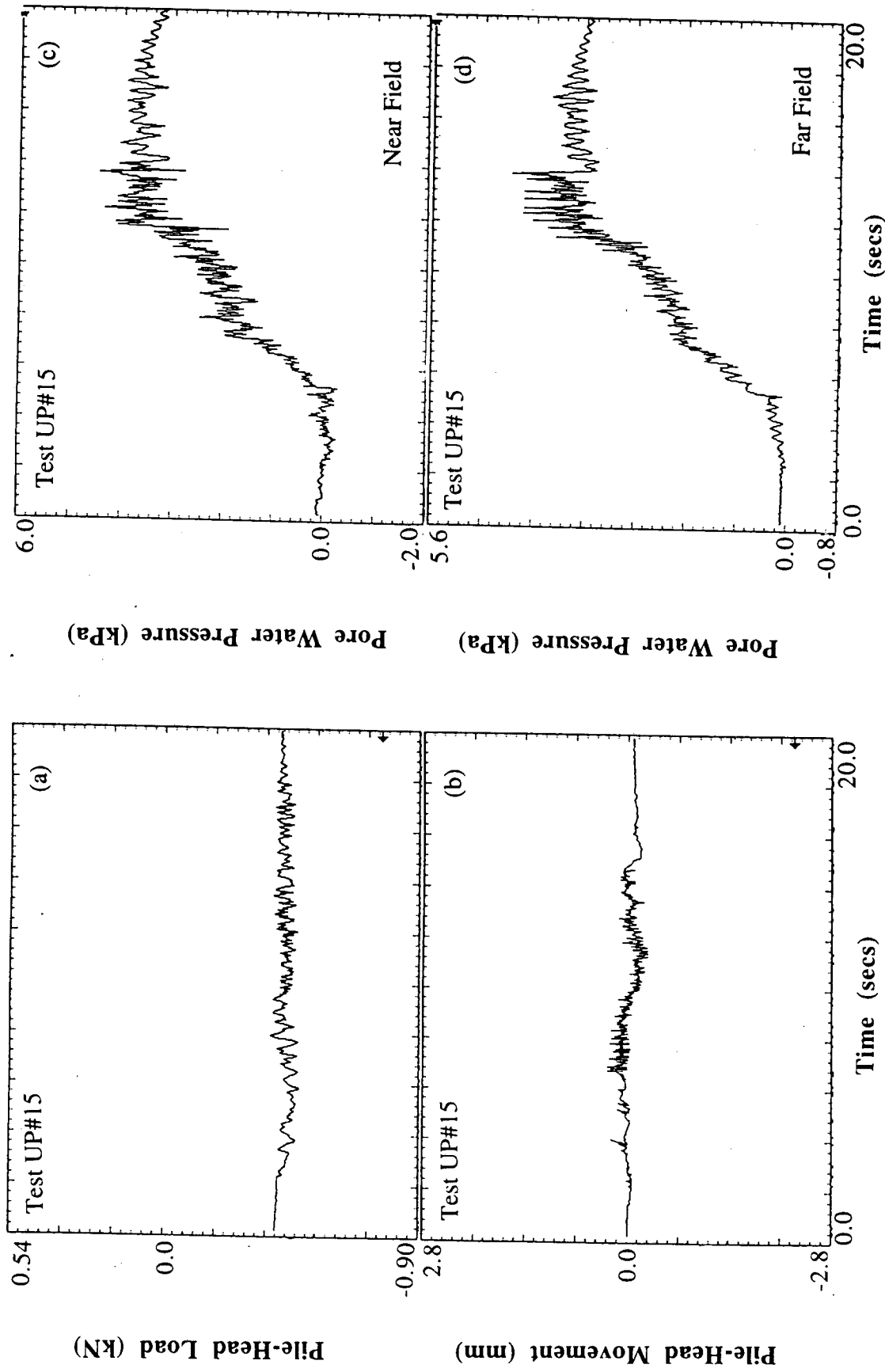
Fig. 5.13: Time History Measurements During Shaking Test UP#15
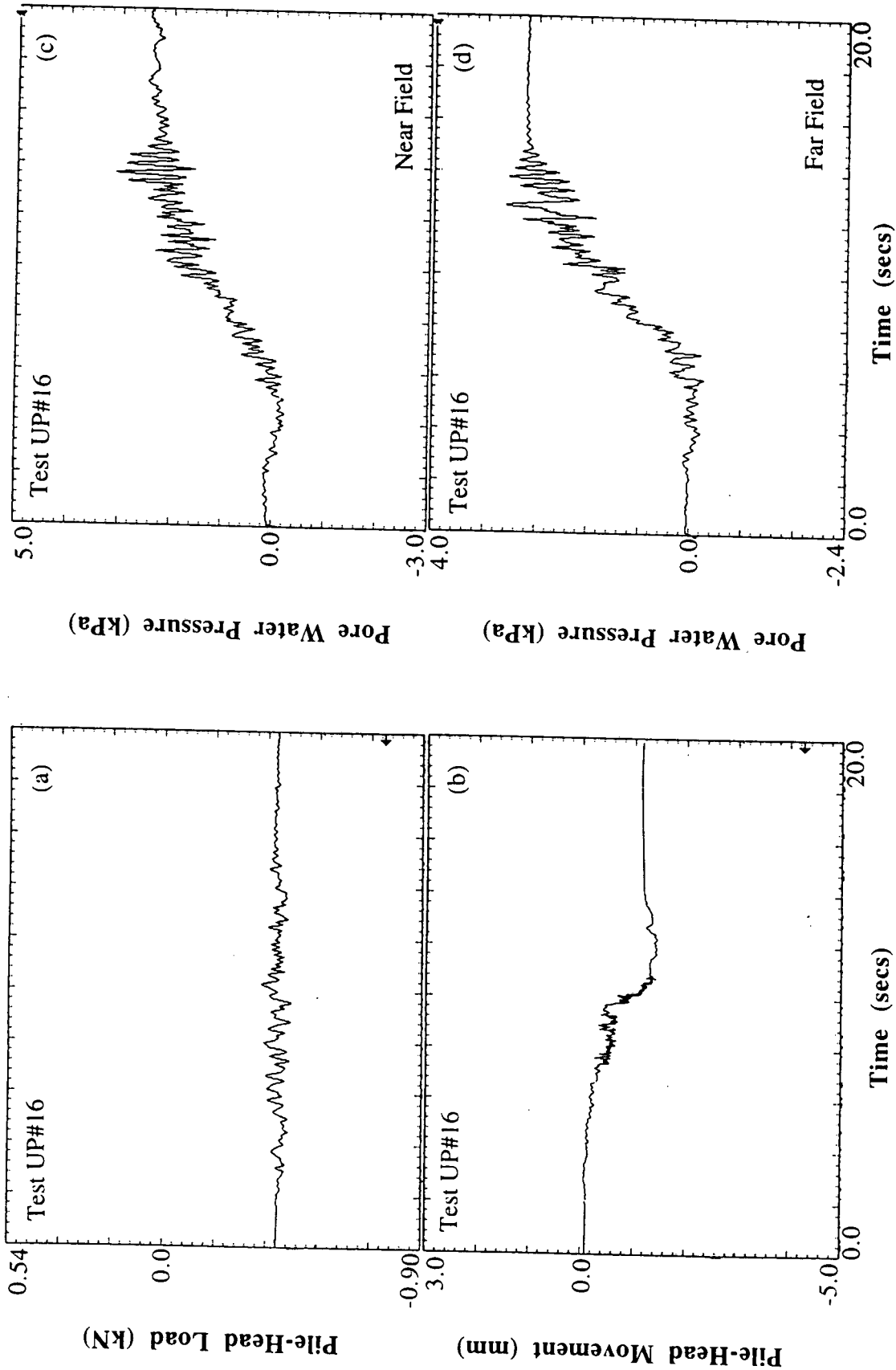
Fig. 5.14: Time History Measurements During Shaking Test UP#16

125
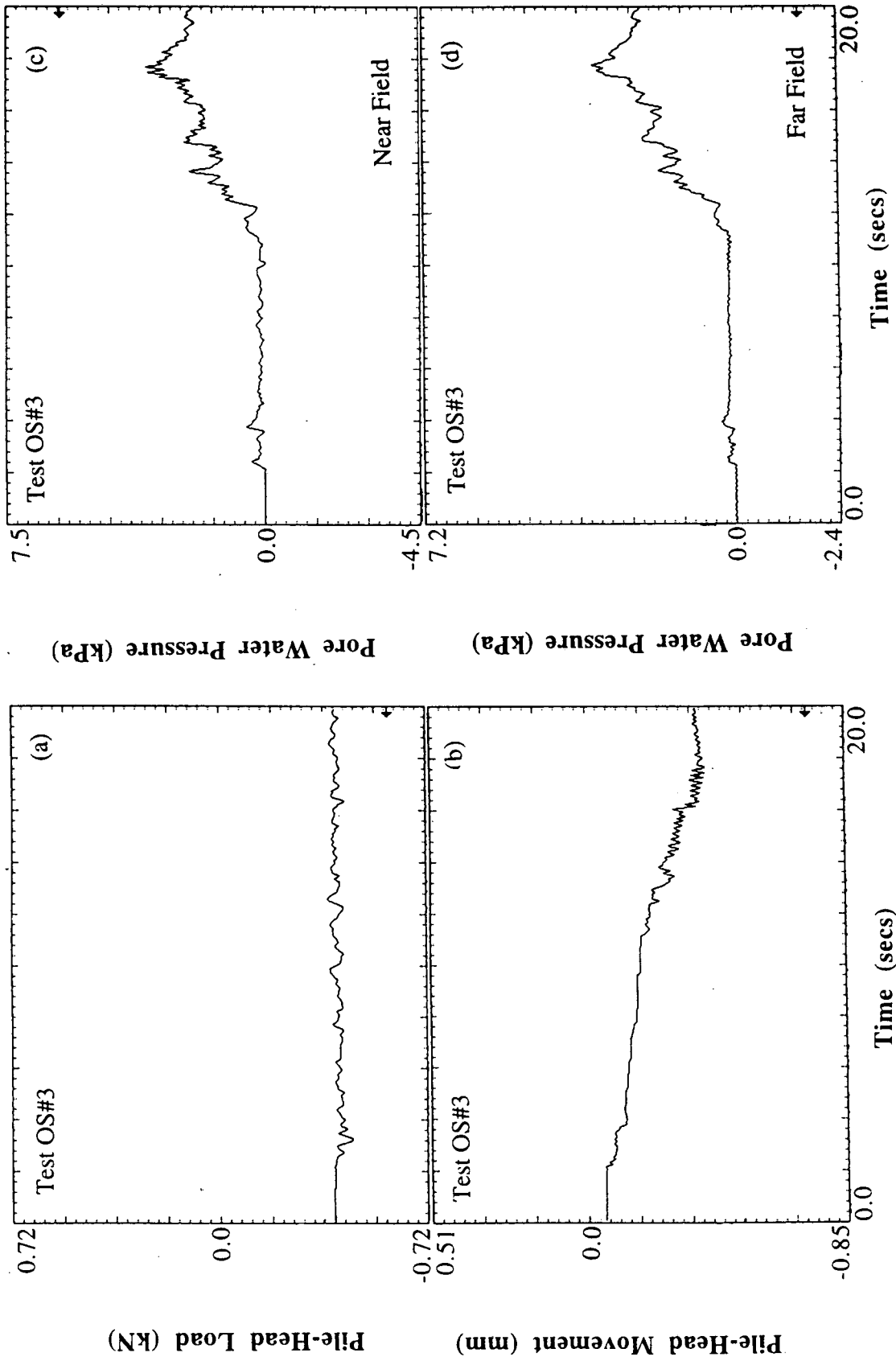
Fig. 5.15: Time History Measurements During Shaking Test OS#3

126

event. Hence, it is logical to expect a lower threshold of bias loading for stability conditions for higher magnitude events.

Significant residual buildup of pore water pressures in both the near and far fields was observed, unlike the M = 7.0 and M = 7.5 events, especially just prior to the completion of the simulated events (both Upland as well as Oceanside). In test UP#15 and UP#16, no residual buildup of pore water pressure was initiated until about 6 sec after the start of the shaking event, following which the pore pressure rapidly peaked up to a maximum in about 8 secs. Most of the pile-head movement occurred during the period of buildup of pore water pressure. Positive pore pressures reached about 20 - 25% of the initial ambient effective stress for the Upland and the Oceanside event, which implies a maximum reduction in the pile capacity of 25%. Therefore, failure did not occur in each of these tests since the combined static bias and the dynamic axial head load did not exceed 75% of the pile's static capacity in each of these cases.

Magnitude = 8.0 - Failure Condition

Test UP#19 - Bias Load = 75% of Uplift Static Capacity - Upland Event (Figs 5.16, 5.18)
Test OS#5 - Bias Load = 77% of Uplift Static Capacity - Oceanside Event (Figs 5.17, 5.19)

Typical time-history measurements in which the pile was completely pulled out of the chamber are shown in Figs 5.16 and 5.17 for the Upland and the Oceanside events, respectively. First, the conditions leading to failure were similar for both types of events. The magnitude of excess pore water pressures was essentially equal to that measured in Test UP#15 and Test OS#3 for the corresponding events, although they increased somewhat more rapidly in these tests than in Test UP#15 and Test OS#3, possibly due to the effect of initial shear strain in the sand due to the presence of higher bias load. The peak pore water pressure of 4 kPa was 23% of the initial effective stress in the soil for test

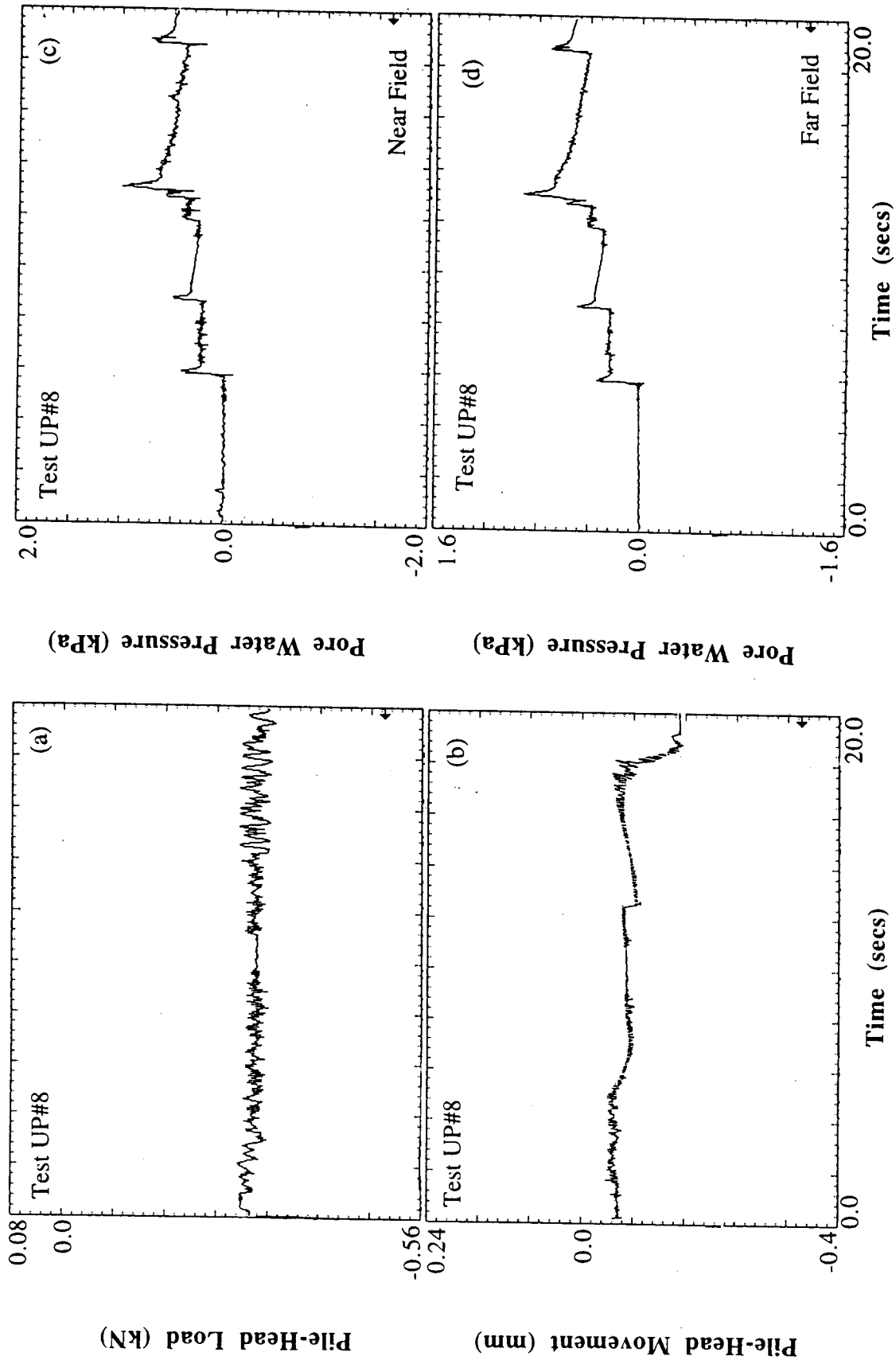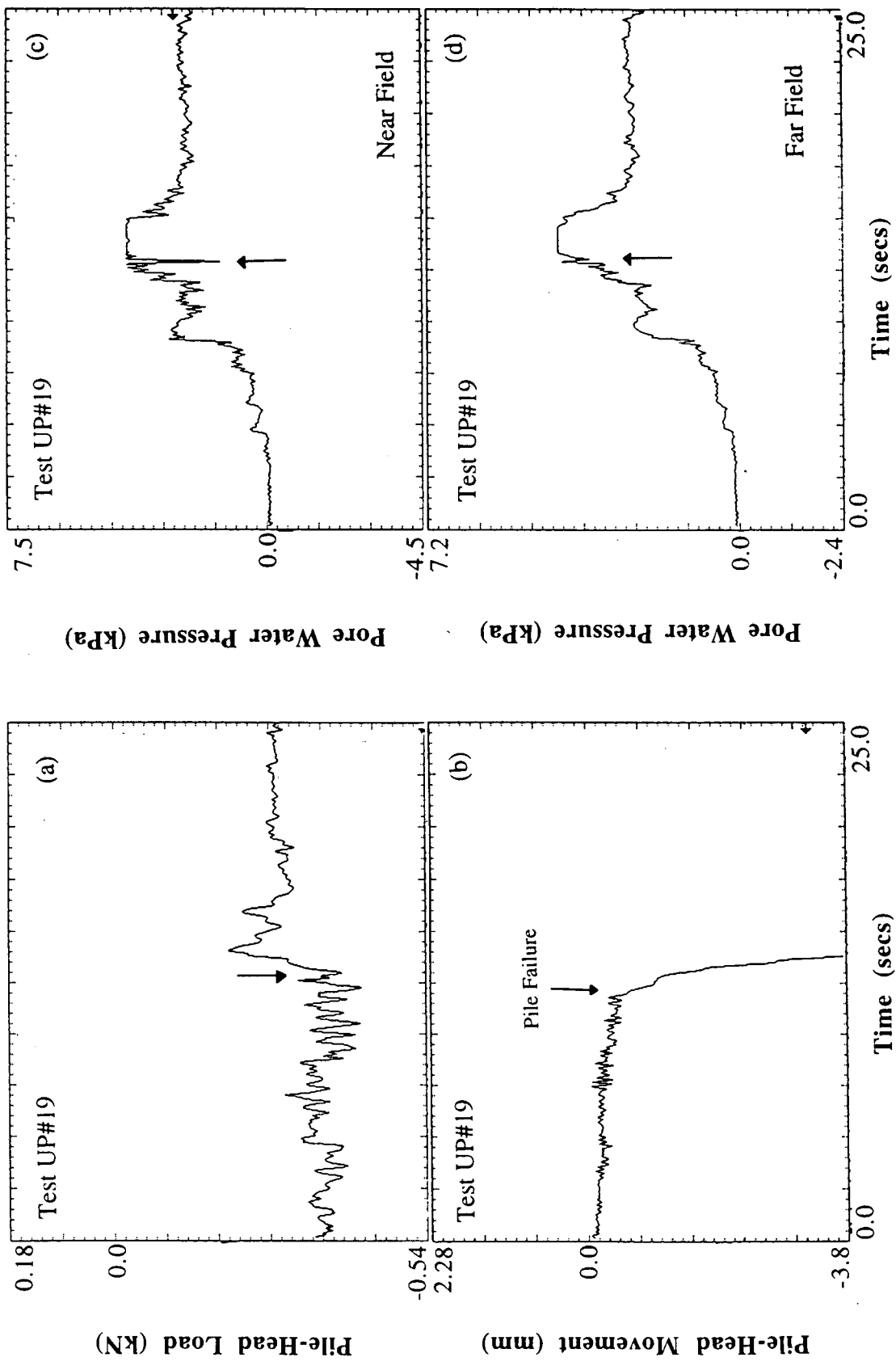Fig. 5.16: Time History Measurements During Shaking Test UP#19

128
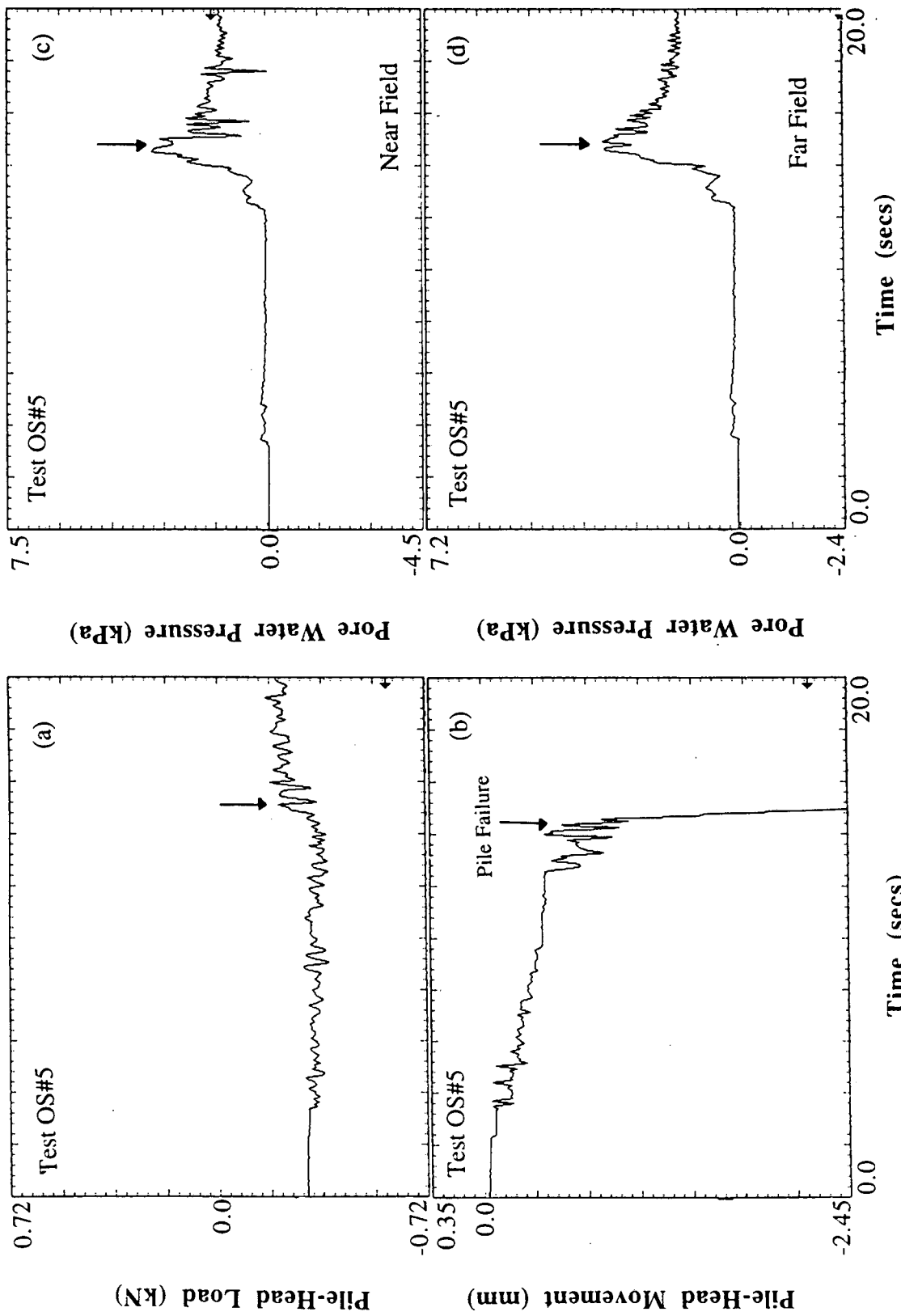
Fig. 5.17: Time History Measurements During Shaking Test OS#5

129
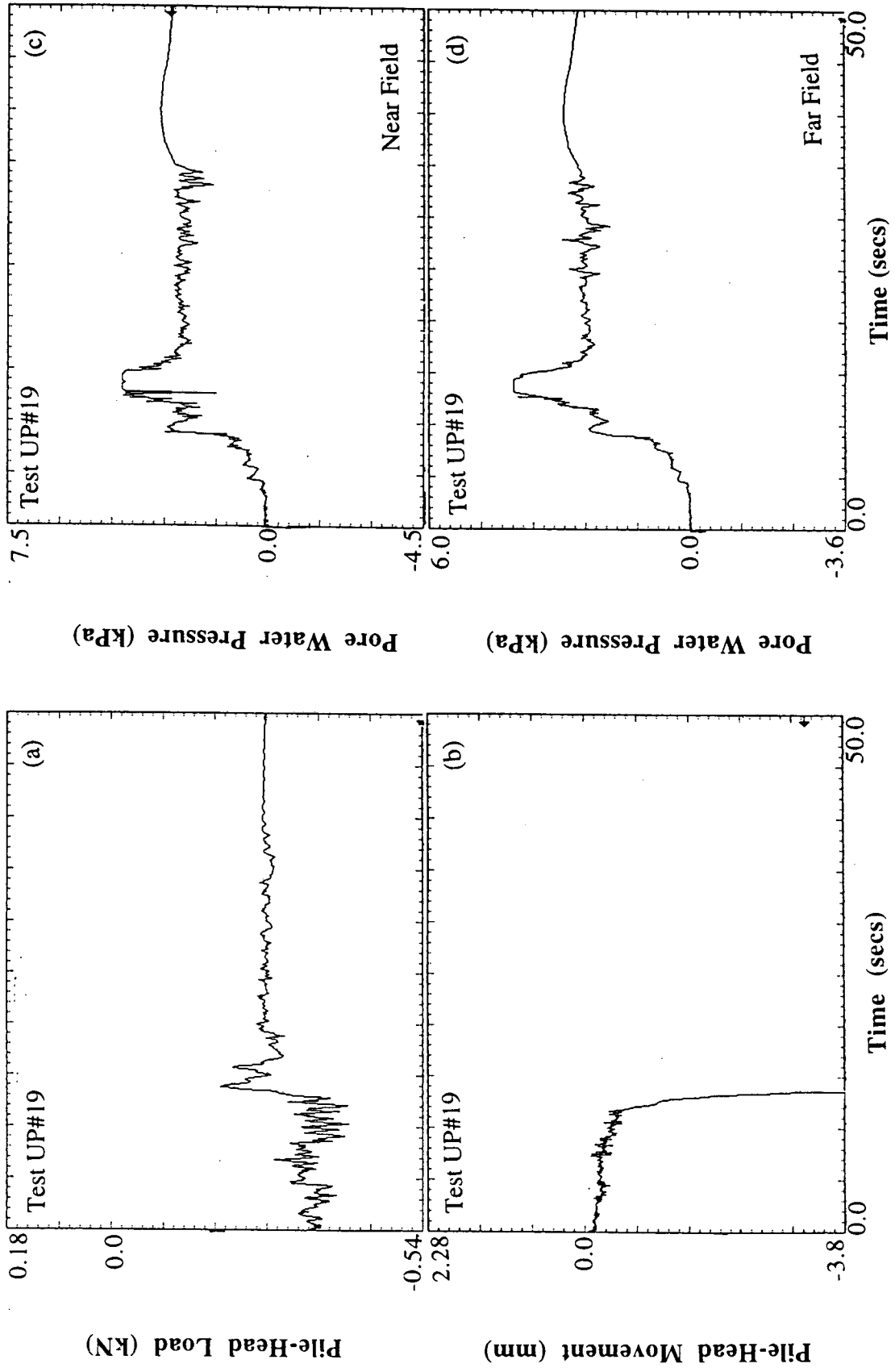
Fig. 5.18: Extended Time Record Measured During Shaking Test UP#19

130
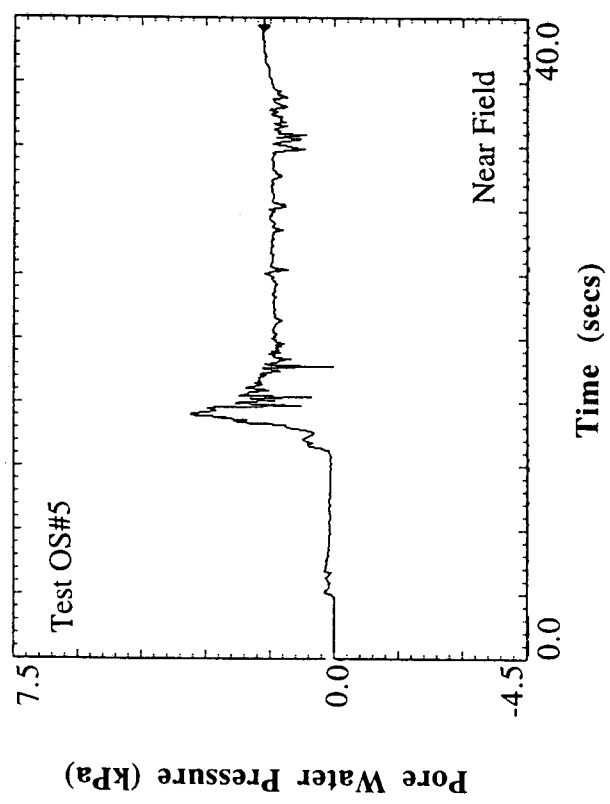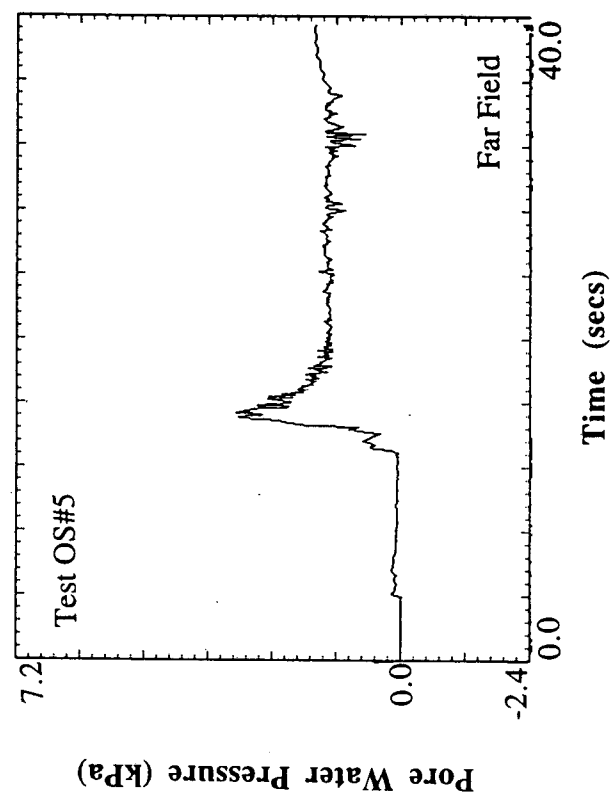
Fig. 5.19: Extended Time-Record of Pore Water Pressure Measured During Shaking Test OS#5

131

UP#19, and the corresponding value for test OS#5 was about 3.5 kPa, or about 20% of the initial effective stress in the soil. It is likely that the induced pore water pressure at the pile interface was even higher. In both cases, the degradation in strength due to buildup of pore pressures coupled with the load excursions due to feedback from the spring-mass system was enough to cause complete and catastropic failure. Extraction occurred at approximately 13.5 secs, corresponding to a prototype time of 71 secs for the Upland event, and 15 secs, corresponding to a prototype time of 78 secs for the Oceanside event. Second, local liquefaction took place immediately after extraction of the piles around the drainage ports which served as points of stress relief (as displayed in Fig. 5.20). Third, for liquefaction to have developed, the magnitude of excess pore water pressure must be equal to the applied confining pressure at some point in the chamber. Since the magnitude of the pore water pressures at locations of the pore pressure transducers (mid-depth of the chamber) was about 1/4 th of the applied confining pressure, it is believed that liquefaction may have started in another location of the chamber, possibly near the toes of the piles.

The sudden pullout of the pile was accompanied by drop in the pore water pressure close to the pile, possibly as a result of dilation of the soil. Furthermore, as the pile was pulled out induced flow of loose soil and water into the cavity left by the pile at the toe may have occurred. It is believed that this action may have triggered liquefaction at or near the toe of the pile. Ochoa (1990) observed a drastic reduction in load transfer in the bottom half of the pile just prior to failure during horizontal shaking accompanied by a corresponding momentary increase in load transfer in the top half of the pile, suggesting a rapid progressive failure originating at the bottom of the pile. The situation modelled in this test may be more severe for the case of piles driven as a group, in which the interaction of the nearby piles may significantly speed up the buildup of pore water pressures in the surrounding soil to a level large enough to promote greater degradation of skin friction than occurs with a single pile.
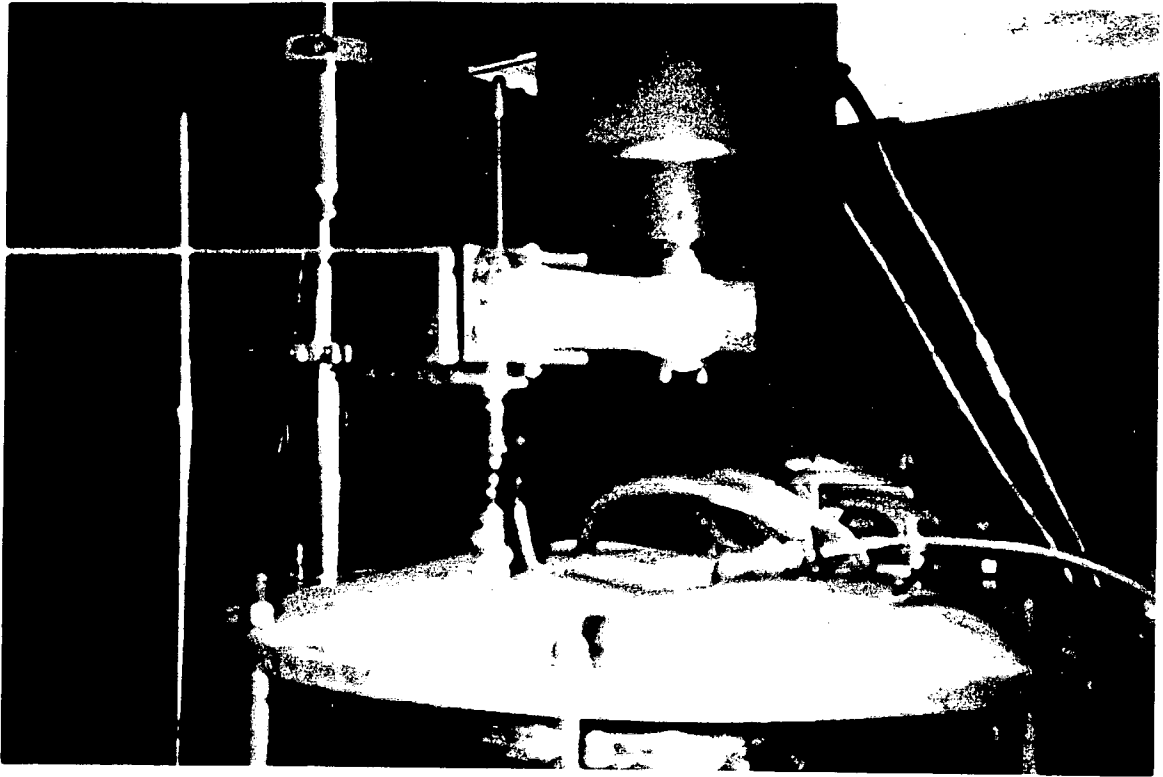
Fig. 5.20: Evidence of Post-Shaking Liquefaction During Test UP#19

As the pile was being extracted, positive positive pore water pressures were re-established very rapidly once the pile movement was arrested. This condition can be understood as a direct effect in response to the local liquefaction at the pile toe. At both the near field and far field locations, however, only about one-half of the excess pore water pressure generated at the time of pile failure had dissipated about $1^1/_2$ minutes (scaled) after the shaking event, as evident from Figs 5.18 and 5.19.

5.4 Post-Shaking Pile Capacties

Load-movement curves plotted in the same sequence as occurred during testing (i.e., first, load application during reference static capacity tests, then application of bias load after restrike, following by shaking test, and last, application of post-shaking static load to failure if the piles did not fail during shaking) are shown for representative tests in Figs. 5.21 and 5.22: Tests UP#6, UP#7, UP#11, and OS#1. The load-movement curves for other tests have been included in Appendix H. The bold-lined curves in Figs 5.21 and 5.22 represent load-movement relationships during reference static load tests, and dashed-lined curves represent the same during the shaking tests. The post-test loss of static capacities were determined by comparing post-shaking measured capacities with the reference static capacities. The trends of loss of static capacity following the shaking event for all tests are shown in Fig. 5.23 and summarized in Tables 5.2 and 5.3.

The following observations can be made :

It is evident from Figs 5.21 and 5.22 that larger pile movements during shaking tests were associated with large magnitude events and large applied bias loads.

For both the Upland and the Oceanside events, the capacity of the soil to sustain static uplift loads after the seismic event was not affected significantly by the action of M = 7.0 events, while reductions in capacity occurred in stronger events. (See Fig. 5.23.) For

134
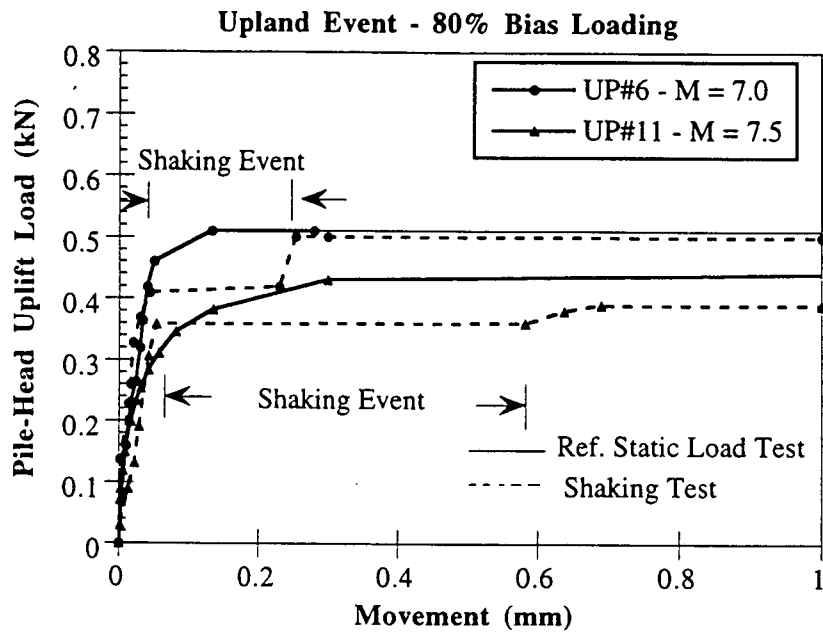
Fig. 5.21: Load Movement Curves, Tests UP#6, and UP#11
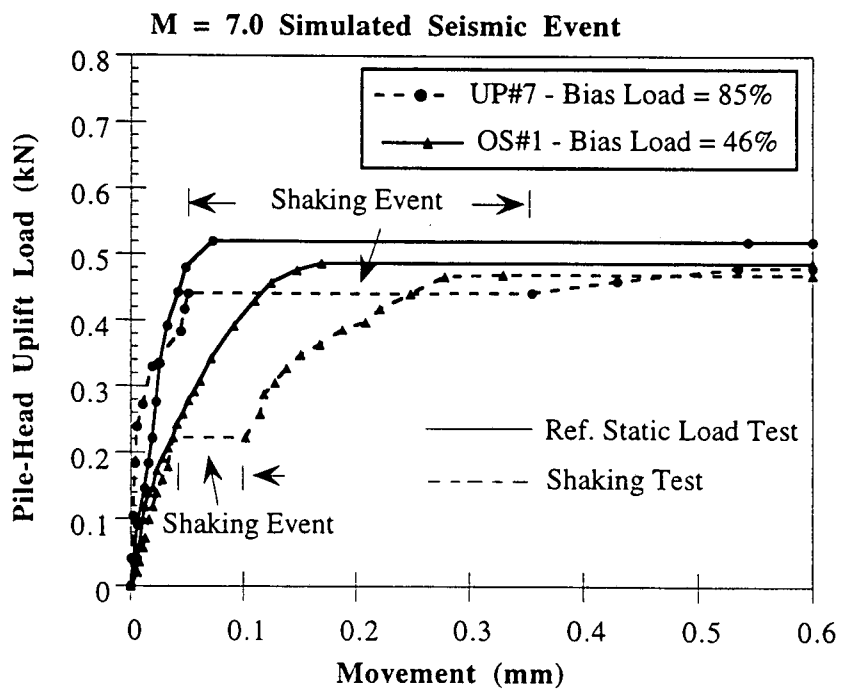
Fig. 5.22: Load-Movement Curves, Tests OS#1, and UP#7

135
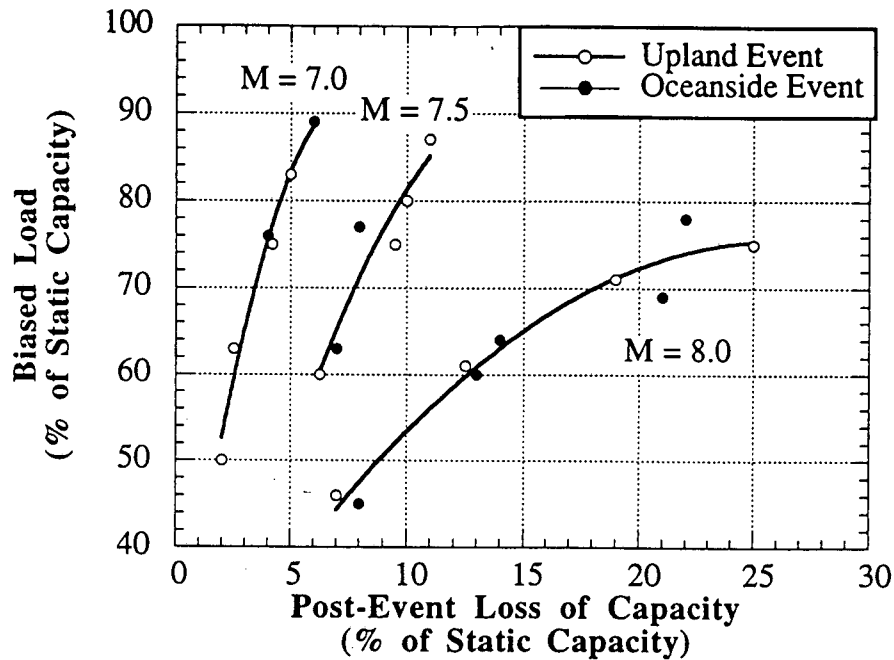
Fig. 5.23: Average Loss of Static Capacity Following the Shaking Event (4.5 m - long prototype)

piles in sand, degradation of skin friction has also been found by others [Poulos(1984)] in tests with direct loading of the pile under a slow rate of cyclic loading.

5.5 Interpretation

Based on the experimental results, contour plots were developed for stability conditions (sustained load and small pile movement), mobility conditions (sustained load associated with substantial pile movement) and failure conditions (extraction) for closed-ended piles driven in medium-dense saturated sand, loaded with a biased tension load during California-type seismic events that occurred 74 km from the earthquake epicenter. Regimes for stability, mobility, and failure condition of the pile are shown in Fig. 5.24. A movement of 0.15 mm (scaled movement = 2.3 mm using a static scaling factor of 15) was established as an upper bound to pile stability. Piles that moved less than this amount

vertically were classified as stable, and those that moved in excess of 0.15 mm but were not completely extracted were considered to represent a "mobility" condition between stability and failure. Using the above criteria, contour lines were drawn separating stability, mobility, and failure for both the Upland and the Oceanside events. It can be concluded from Fig. 5.24 that the signature of California-type events of similar magnitudes, epicentral distances and duration of shaking had relatively little effect on the pile behavior during shaking.

The similarity in behavior of pile extraction for the two events can be linked to the shear strains induced in the soil mass by these events. A mathematical analysis of the strains developed in the free field in the vertical plane by the horizontal component of ground motions from simulated Upland seismic events was computed using the program SHAKE [Schnabel et al. (1972)] for the range of assumed soil characteristics at the SEMS site (See Fig. 5.25.) The time window for input motion was between 20 to 60 secs, which included the period of strong shaking of the magnitude-scaled events of the Upland earthquake shown in Figs. 3.10 - 3.12. The input motion was applied at the top of layer 3 (3 m below ground level); which was the depth of the SEMS unit. Computed shear strain-time histories at the level of applied motion are shown in Fig. 5.26 for different magnitudes of the simulated Upland event. Similar computations of shear strain-time history have also been reported for the M = 8.0 Oceanside event by Ochoa (1990), as shown in Fig. 5.27. For both earthquakes, maximum peak shear strain of about 0.02% was computed for the M = 8.0 simulated event, despite the differences in time histories, which may indicate why the extraction behavior of the piles was similar.
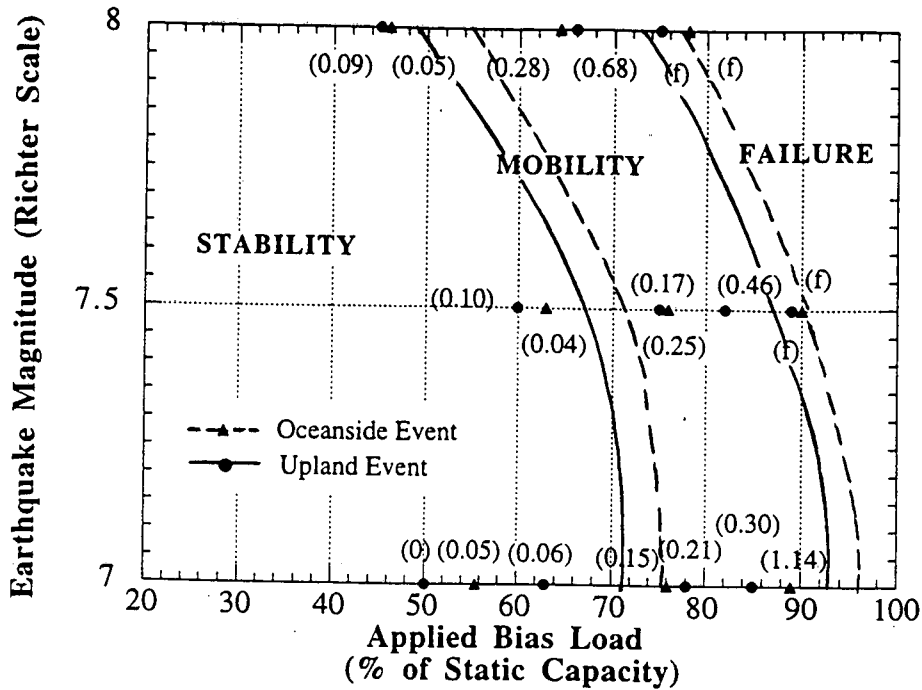
Fig. 5.24: Regimes for Stability, Mobility, and Failure Conditions of the Pile (4.5 m - long Prototype), $\sigma_c = 17.24$ kPa; $D_r = 55\%$
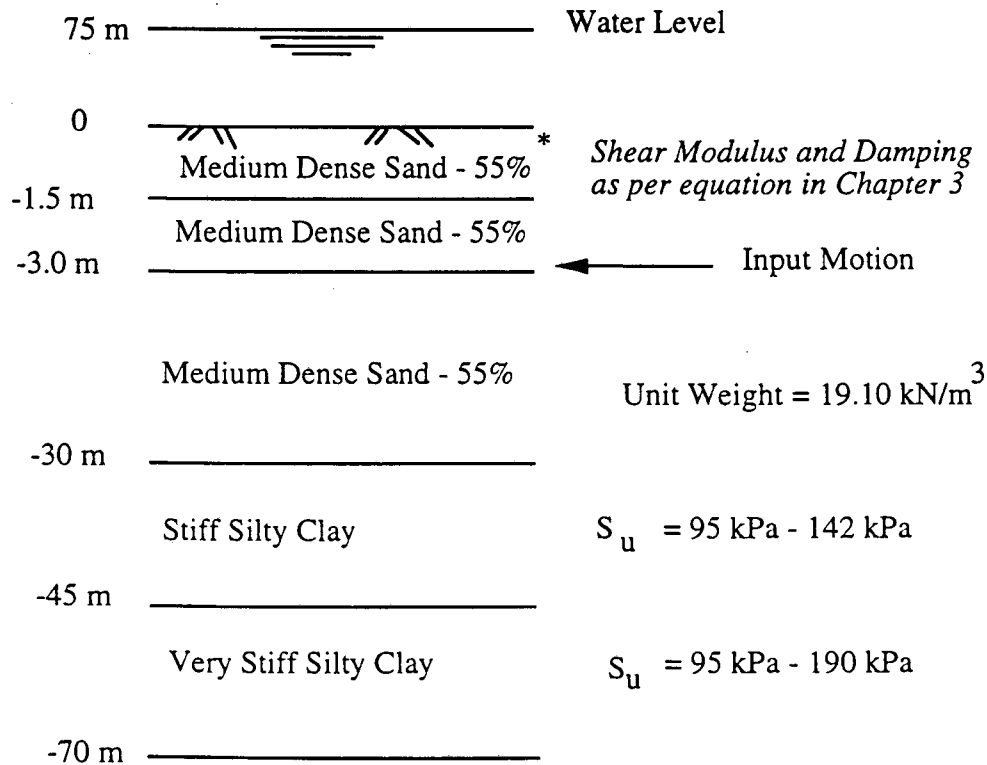
Fig. 5.25: Soil Profile for SHAKE Analysis
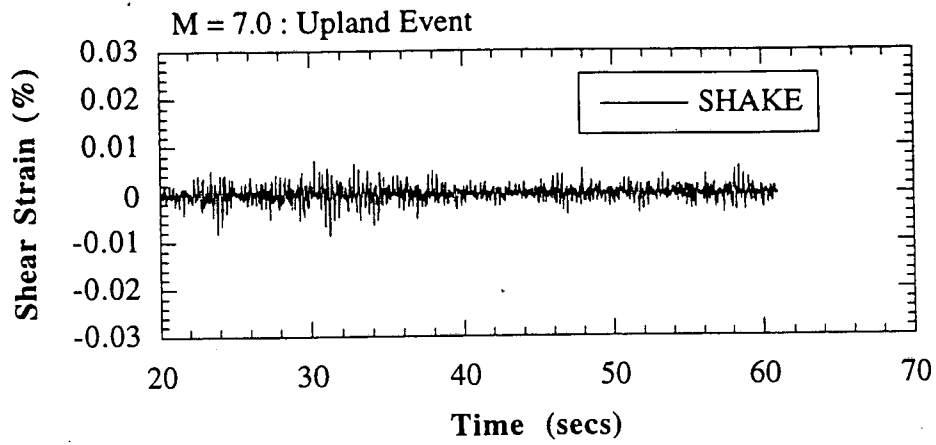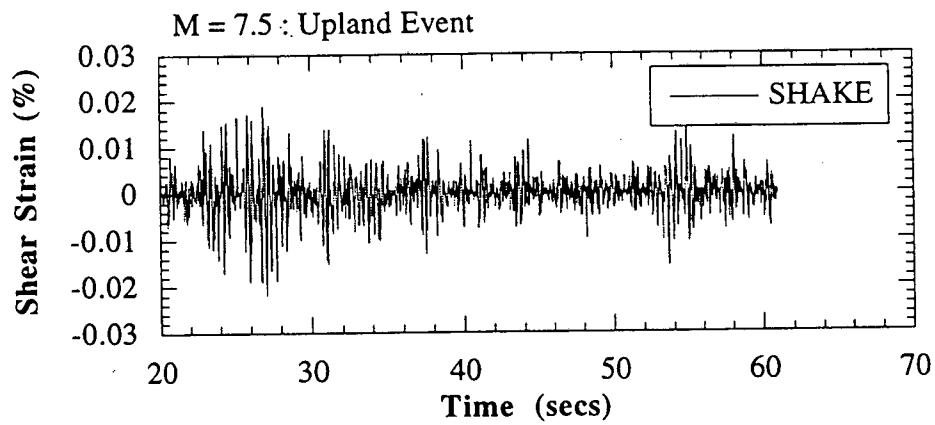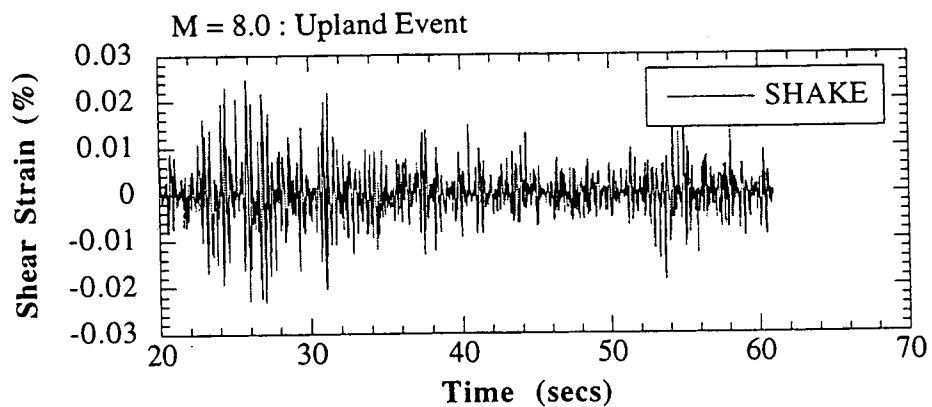
Fig. 5.26: Shear Strains in the Soil Mass Computed at 3 m Depth
Using SHAKE for the Upland Event

139
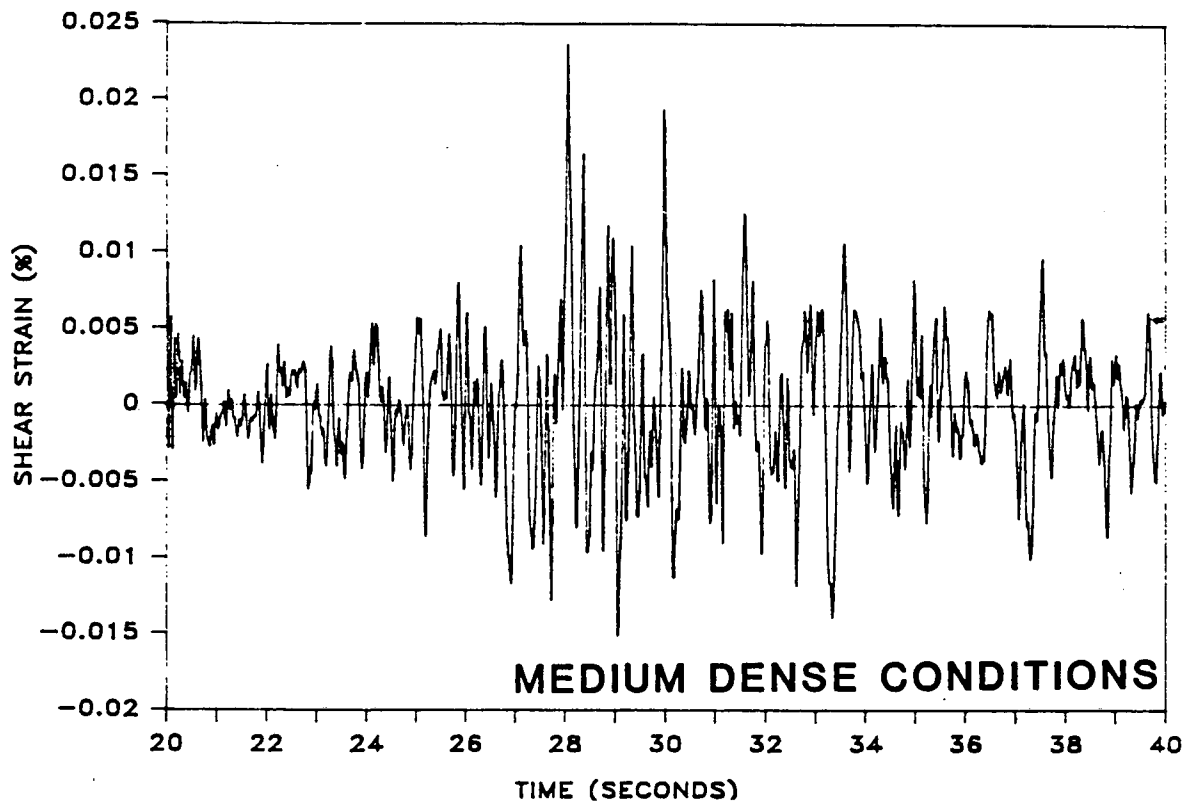
Fig. 5.27: Shear Strains in the Soil Mass at 3 m Depth Computed Using
SHAKE for the M = 8.0 Scaled Oceanside Event (Ochoa, 1990)

5.6 Design Implications

Fig. 5.24 can be used to develop preliminary design criteria for displacement piles in medium-dense, submerged sand, where the piles are rigid and the superstructure is nonductile (cannot redistribute loads among piles). The ratios of maximum biased loads for stable conditions to static uplift capacities (ϕ) can be viewed as seismic resistance factors for California-type earthquakes approximately 74 km distant from a site. Fig. 5.24 can be used to determine ϕ for pile penetrations of about 4.5 m. Similar tests were conducted with initial isotropic effectives of 34.5 kPa, or scaled pile penetrations of about 9 m [Ochoa (1990)]. Values of 1-ϕ (resistance loss factor) are plotted vs. pile length in Fig. 5.28. Values of 1-ϕ for piles longer than 9 m were computed assuming no degradation of resistance below a depth of 9 m due to pore pressure buildup.

Fig. 5.28 must be considered preliminary and incomplete because several effects have not been modeled. Wave and inertial loadings on the superstructure may influence the pile loading, and hence soil response, differently than the simple feedback loading modeled here. In the absence of information on these effects, a load factor should be applied to the sum of the static biased load and the peak dynamic excursion in load applied to the pile by the superstructure. In addition, sea-seabed interaction effects may produce greater pore pressures in the soil, causing further loss of pile capacity. Such effects have not been considered in this chapter; hence, Fig. 5.28 would need to be applied with considerable caution [Kobayashi et al. (1992)]. A detailed discussion of sea-seabed interaction effects appears in Chapter 8.

141
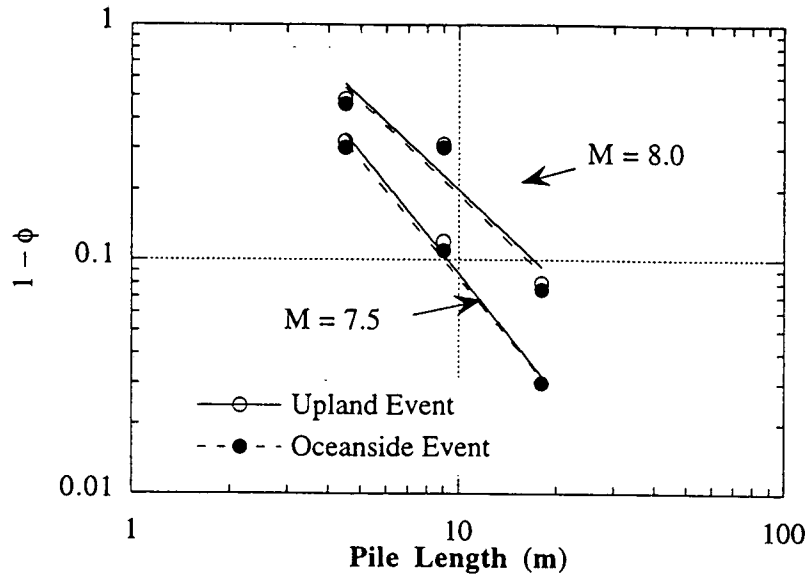
Fig. 5.28: Seismic resistance factor, ø, as a function of pile length

5.7 Summary

(a) Greater maximum unit static shaft resistance developed in the bottom half of the pile than in the upper half. Much of the unit shaft friction (about 35 - 60%) was mobilized in the form of residual stresses before subjecting the pile to uplift load.

(b) Insertion of the pile produced an increase in the effective stress at the pile-soil interface by a factor of about 2.

(c) For both events, for any given magnitude of the earthquake, there existed a threshold uplift static bias load below which the piles remained in a stable condition during the seismic event with little or no movement under sustained loading. For M = 8.0, this was about 1/2 of the static uplift capacity.

(d)   The larger the magnitude of the earthquake and the larger the bias loading on the pile, the larger were the pile-head movements during shaking.

(e)   The excursions in pile-head load measured during shaking for both the events ranged from 7% to 12% of the static capacity, with the higher value for M = 8.0 earthquakes.

(f)   The pore pressures developed in the soil mass during M = 7.0 and M = 7.5 earthquakes for both events were not more than 4- 6% of the ambient mean effective stress. Extraction was observed only for high bias load (90% of uplift capacity) for M = 7.5, primarily as a result of superstructure feedback.

(g)   Pile failure during M = 8.0 events was catastrophic and occurred at a relatively low level of bias loading (75%) as compared to M = 7.0 and M = 7.5 events. Failure of the pile during an event of M = 8.0 occurred due to sufficient degradation of skin friction produced by buildup of pore water pressure in the soil, as a consequence of shearing strains in the soil generated by sudden repetitive pull-outs of the pile (in response to the superstructure feedback), and additional shearing strains in soil generated by the horizontal component of the seismic event.

(h)   Significant reductions in the static frictional uplift capacity of the soil occurred after M = 7.5 and M = 8.0 events.

(i)   Based on the observation of pile response for different combinations of simulated earthquake magnitudes (7.0, 7.5,and 8.0) of the two events and bias tension loading on the pile ratioed to the static capacity, contours for the regions of stability, mobility, and failure conditions of the pile were established.

(j)   The signature of simulated seismic events of similar magnitudes but different origins and paths of transmissions to the site had relatively little influence on the condition of pile extraction for piles driven in saturated medium-dense sand.

Chapter 6

DEGRADATION FACTORS FOR SHAFT RESISTANCE

6.1 Introduction

The experimental results were modeled using the program "PAR." [PMB (1994)]. PAR is a powerful finite difference analysis tool for dynamic analysis of pile foundations. The purpose of using PAR was to develop a means of using the results of the scaled horizontal ground shaking tests to analyze prototype piles. A key observation in these experiments was the degradation of side shear resistance during shaking. In general, a degradation factor was developed to degrade the static unit axial resistance of the soil in PAR to provide a match in axial movements computed in the PAR simulation of a prototype-sized pile with scaled, measured pile-head movements. Loading rate effects and the effect due to pile tip suction during the cyclic loading on the pile were assumed to be insignificant and neglected in these analyses.

6.2 PAR: Pile-Soil Numerical Model

The approximate mathematical model adopted by PAR [PMB (1994)] for dynamic soil-pile interaction analysis is illustrated in Fig. 6.1. PAR, industry standard software, makes the analysis by dividing the pile lengthwise into a number of small discrete elements, and interconnecting the elements at points called "nodes." Conceptually, the response of the system can be divided into the response of the pile and the corresponding response of the soil. PAR models the internal axial loads, shears and moments induced in the pile by interconnecting the nodes with a continuous linear beam - column that extends the length of the pile. The response of the soil at each node is modeled in the axial and lateral directions by nonlinear springs that model the load-deflection characteristics, by dashpots that model
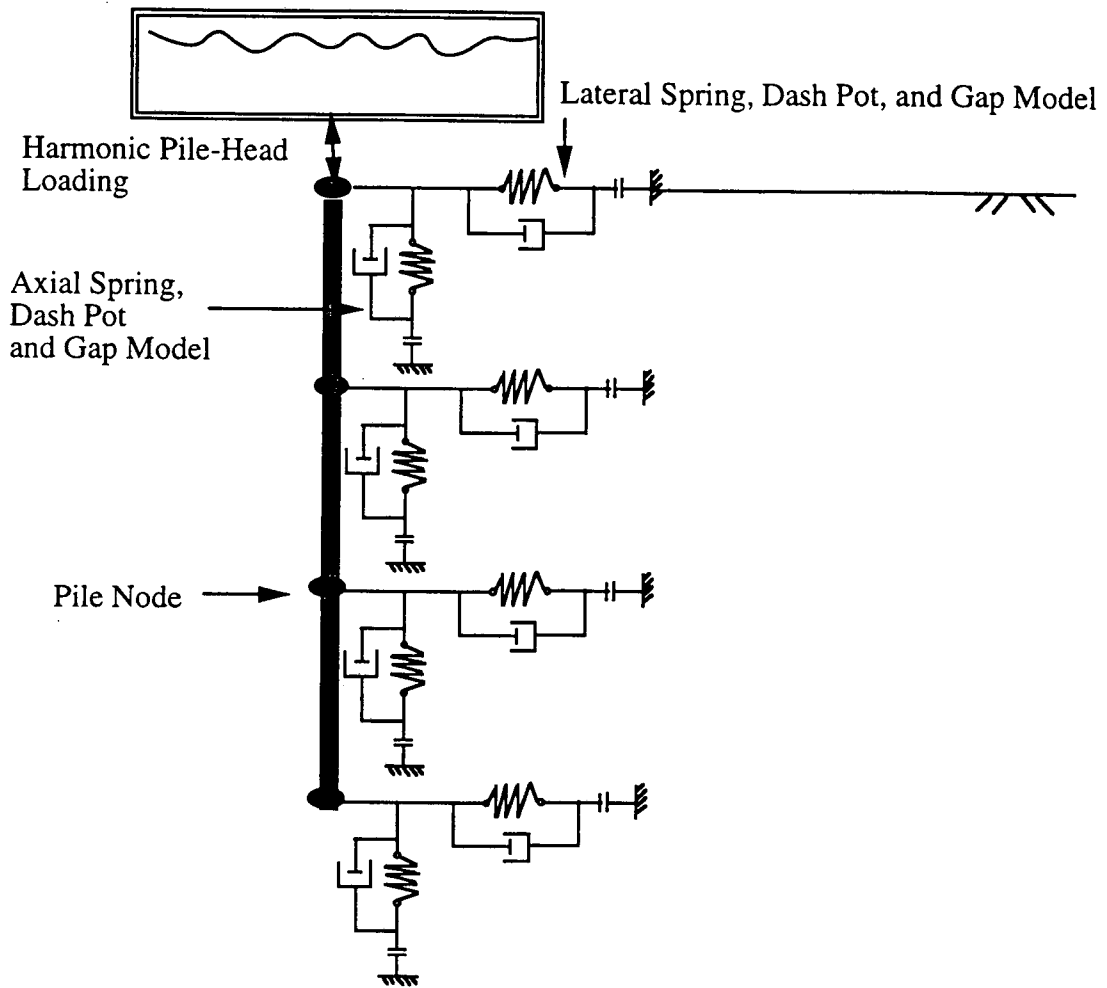
Fig. 6.1: Approximate Mathematical Model for Dynamic Soil-Pile Interaction Analysis (PMB, 1994)

the energy dissipated through radiation, and by gap elements that disconnect the spring and the dashpot if there is no contact between the pile and the soil at a given node.

PAR has the capability to analyze piles subjected to static or dynamic loading. The input to the program consists of the following: (i) Loading condition: The response of the pile can be analyzed for imposed forces or displacements at the top of the pile or the base of the pile. These imposed loads can range from simple (monotonic) load or deflection patterns to irregular load-time histories. (ii) Soil Properties: Unit lateral load and unit axial load transfer curves that degrade with loading cycles or include strain hardening characteristics. (iii) Pile Characteristics: The pile characteristics include the node locations, element properties, nodal masses, soil springs, material properties, section properties.

The forces in the springs and the internal axial loads, shears and moments induced in the pile are unknown but can be easily expressed in terms of the axial, lateral and rotational displacements of the nodes. At each node a set of equilibrium equations can thus be written, and the finite element method reduces the original complex pile-soil interaction problem to one of solving a set of simultaneous equations with displacements at each node as unknowns.

Once the analysis has been performed, results such as deformed shapes, load-deflection curves, and shear and moment diagrams can be displayed varying with time and/or varying along the length of the pile.

6.3 Degradation Factors for Soil Strength and Stiffness

For axial pile response analysis to horizontal ground shaking, it was assumed that the soil strength and stiffness degradation phenomenon occurs primarily through lateral loading of the soil and that the degradation in axial soil response was exactly equal to that occurring laterally. The underlying assumption in the above hypothesis is that the principal

146

degradation phenomenon is the pore water pressure buildup. The above hypothesis was tested using the experimental results from Chapter 5.

Finn and Martin (1979) proposed an effective stress model to degrade the lateral soil strength (p values in p-y curves) during horizontal ground shaking. According to the proposed model, the API p -y curves are to be degraded as a function of the generated pore water pressure during the earthquake in the free field as follows:

(i) For small deflections in the elastic range, the initial soil modulus is assumed proportional to $(\sigma'_v)^{1/2}$. That is, the initial soil modulus defining the slope of the p-y curve at the origin is reduced by a factor $[(\sigma'_{vo} - \Delta u) / \sigma'_{vo}]^{1/2}$., where σ'_{vo} is the initial vertical effective stress and Δu is the pore water pressure increase at time t.

(ii) For deflections in the yielding range, soil strength characteristics dominate lateral resistance, and the p-y curve is degraded in proportion to σ'_v, that is, the p value is reduced by a factor $[(\sigma'_{vo} - \Delta u) / \sigma'_{vo}]$ if significant pore pressure dissipation can occur. If the loading is essentially undrained as in the present study, the strength degrades as $(\sigma'_v)^{1/2}$.

(iii) The p-y curves between these two regions are drawn as described in the 1979 API procedure [Finn and Martin (1979)].

Alternatively, p-y curves can be modified for pore pressure buildup effects by reducing the p values on the static API curve by the degradation factor , $(1-r)^{1/2}$, in which;

r = the pore water pressure ratio, $\Delta u / \sigma'_{vo}$,

σ'_{vo} = the initial effective vertical stress, and

Δu = induced excess pore water pressure during the seismic event.

The analysis for axial pile response was then conducted by degrading the axial unit resistance curve (f-w) by the same degradation factor as that used for the lateral unit resistance curve (p-y).

6.4   Analysis Approach

The pile response analysis was conducted for a prototype pile 4.5 m long, shown in Fig. 6.2. which was scaled from the model pile used in this study. Refer to Chapter 4 for scaling factors. The following approach was used for the analysis

(1) The pile was divided into six segments.

(2) The static p-y curves were constructed at each node along the pile according to the current API criteria [API (1993)]. Details of construction are explained in Appendix I.

(3) The static f-w curves were constructed for the prototype by appropriately scaling the pile-head load movement relationship obtained during the model tests. (See Appendix I.)

(4) Degradation factors to be used in the analysis were computed for each individual test using the method proposed by Finn and Martin (1979). This degradation factor was applied to both the p values from the static p-y and the f values from the f-w curves. The estimated degradation factors for the shaking tests are shown in Table. 6.1.

(5) The pile was analyzed using PAR. Gap effects, radiation damping and strain rate effects were not considered. This step was subdivided into the following:

5-1 - The load transfer curves generated in Steps (2) and (3) were input. Both the virgin curves and the fully degraded curves (degraded using the degradation factor derived in Step (4)) were input to the program.

5-2 - A static analysis was first conducted to determine the pile-head displacement under the bias load only. The virgin p-y and f-w curves were used in this case. Table 6.2 shows the input data for the static analysis of the prototype pile.

5-3 - Following the static analysis, dynamic analyses were performed to determine the effect of the seismic event. The degraded p-y curves and f-w curves were used in this case. The dynamic loading was applied directly to the pile-head in the form of an
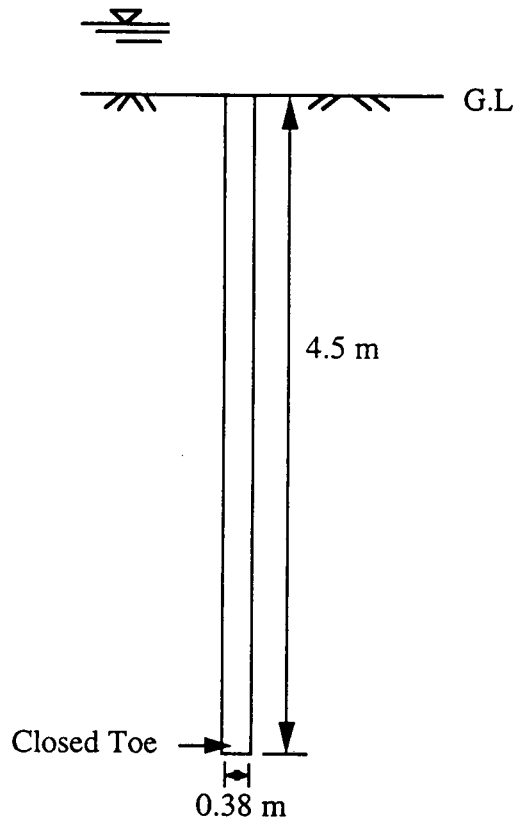
Fig. 6.2: Prototype Pile for PAR Analysis

equivalent sine curve. Table 6.3 shows the input data for the dynamic analysis of the prototype pile.

5-4 - The displacement computed after the simulated seismic event was then compared to the displacement scaled from the model test. If the calculated and the scaled measured displacements were equal, then the degradation factor for the f-w curve was accepted as correct; otherwise, the degradation factor for the f-w curve only was varied until the measured and calculated displacements matched. No further degradation was made in the p-y curves.

Table 6.1: Estimated Degradation Factors for the Model Shaking Tests

Test	PWP u (kPa)	PWP Ratio $r = u / \sigma_c$	D.F. $\rho = (1-r)^{1/2}$
R1	1.52	0.088	0.96
R2	0.83	0.048	0.97
S1	0.74	0.043	0.98
S3	1.2	0.069	0.96
S4	0.41	0.024	0.99
U1	1.30	0.2	0.89
U2	0.86	0.141	0.93
U3	3.45	0.223	0.88
OS#1	1.24	0.072	0.96
OS#2	0.69	0.040	0.98
OS#3	3.45	0.200	0.89
OS#4	3.79	0.220	0.88
OS#5	3.45	0.200	0.89
OS#6	3.45	0.200	0.89
OS#7	3.62	0.21	0.89
UP#1	0.69	0.04	0.98
UP#2	0.69	0.04	0.98
UP#3	0.69	0.04	0.98
UP#4	0.69	0.04	0.98
UP#5	0.69	0.04	0.98
UP#6	0.69	0.04	0.98
UP#7	0.69	0.04	0.98
UP#8	1.03	0.06	0.97
UP#9	1.03	0.06	0.97
UP#10	1.09	0.063	0.97
UP#11	1.09	0.063	0.97
UP#12	1.09	0.063	0.97
UP#13	1.09	0.063	0.97
UP#14	1.09	0.063	0.97
UP#15	4.48	0.26	0.86
UP#16	2.93	0.17	0.91
UP#17	4.14	0.24	0.87
UP#18	4.14	0.24	0.87
UP#19	4.14	0.24	0.87

PWP = Pore water pressure

D.F. = Degradation factor

σ_c = Ambient effective isotropic confining pressure.

Table 6.2: Input Data for Static Analysis (D_r = 55%, and σ_c = 17.24 kPa)

Test	Static Capacity (Model) kN	Static Capacity (Prototype)* kN	Bias Load (Model) kN	Bias Load (Prototype) kN	Percentage of Inferred Static Capacity
R1	0.44	99	0.33	75	76
R2	0.49	110.25	0.42	94.5	86
S1	0.61	137.25	0.39	87.75	64
S3	0.49	110.45	0.38	85.50	77
S4	0.47	105.75	0.43	96.75	91
U1	0.35	78.75	0.16	36.00	46
U2	0.51	114.75	0.33	74	64
U3	0.44	99.00	0.34	77	78
OS#1	0.49	110.25	0.23	50.72	46
OS#2	0.46	103.50	0.30	67.27	65
OS#3	0.68	153.00	0.41	91.80	60
OS#4	0.87	196.00	0.56	125.28	64
OS#5	0.43	96.75	0.33	74.50	77
OS#6	0.53	119.25	0.49	109.71	92
OS#7	0.52	117.00	0.36	80.73	69
UP#1	0.56	126.00	0.28	63.00	50
UP#2	0.59	132.75	0.37	83.63	63
UP#3	0.86	193.50	0.63	141.25	73
UP#4	0.62	139.5	0.47	104.63	75
UP#5	0.87	195.75	0.68	152.68	78
UP#6	0.51	114.75	0.41	91.80	80
UP#7	0.52	117.00	0.44	99.45	85
UP#8	0.48	108.00	0.29	64.80	60
UP#9	0.52	117.0	0.39	87.75	75
UP#10	0.35	78.75	0.26	59.06	75
UP#11	0.45	101.25	0.36	81.00	80
UP#12	0.71	159.75	0.58	129.40	81
UP#13	0.44	99.00	0.37	84.15	85
UP#14	0.46	103.50	0.41	92.12	89
UP#15	0.89	200.25	0.40	90.11	45
UP#16	0.64	144.00	0.39	87.84	61
UP#17	0.36	81.00	0.26	57.51	71
UP#18	0.46	103.50	0.36	80.73	78
UP#19	0.48	108.00	0.36	81.00	75

D_r = Relative density

σ_c = Ambient effective isotropic confining pressure

* = Prototype static capacity scaled from the model capacity using the static scaling factor of $(n_s)^2$ = 225

Table 6.3: Input Data for Dynamic Analysis of the Prototype Pile Subjected to Harmonic Pile-Head Loading

Test	Earthquake Magnitude	Duration (sec)	Amplitude of Sine Force (kN)	No. of Significant Cycles	Period (sec)	Frequency (Hz)
R1	7.0	25.00	1.02	10	2.500	0.4000
R2	7.0	25.00	1.27	10	2.500	0.4000
S1	7.5	35.00	0.80	15	2.333	0.4286
S3	7.5	35.00	1.93	15	2.333	0.4286
S4	7.5	35.00	0.70	15	2.333	0.4286
U1	8.0	50.00	3.12	21	2.381	0.4200
U2	8.0	50.00	1.85	21	2.381	0.4200
U3	8.0	50.00	2.45	21	2.381	0.4200
OS#1	7.0	25.00	0.86	10	2.500	0.4000
OS#2	7.0	25.00	0.87	10	2.500	0.4000
OS#3	8.0	50.00	1.84	21	2.381	0.4200
OS#4	8.0	50.00	2.35	21	2.381	0.4200
OS#5	8.0	50.00	1.40	21	2.381	0.4200
OS#6	8.0	50.00	1.43	21	2.381	0.4200
OS#7	8.0	50.00	1.69	21	2.381	0.4200
UP#1	7.0	25.00	1.06	10	2.500	0.4000
UP#2	7.0	25.00	1.12	10	2.500	0.4000
UP#3	7.0	25.00	1.16	10	2.500	0.4000
UP#4	7.0	25.00	1.17	10	2.500	0.4000
UP#5	7.0	25.00	1.65	10	2.500	0.4000
UP#6	7.0	25.00	0.97	10	2.500	0.4000
UP#7	7.0	25.00	0.98	10	2.500	0.4000
UP#8	7.5	35.00	1.08	15	2.333	0.4286
UP#9	7.5	35.00	1.17	15	2.333	0.4286
UP#10	7.5	35.00	0.85	15	2.333	0.4286
UP#11	7.5	35.00	1.10	15	2.333	0.4286
UP#12	7.5	35.00	1.73	15	2.333	0.4286
UP#13	7.5	35.00	1.07	15	2.333	0.4286
UP#14	7.5	35.00	1.12	15	2.333	0.4286
UP#15	8.0	50.00	2.40	21	2.381	0.4200
UP#16	8.0	50.00	1.73	21	2.381	0.4200
UP#17	8.0	50.00	1.07	21	2.381	0.4200
UP#18	8.0	50.00	1.37	21	2.381	0.4200
UP#19	8.0	50.00	1.56	21	2.381	04200

6.4.1 Pile-Head Loading

PAR allows direct dynamic loading of the pile-head through a harmonic pile-head loading function. Therefore, the pile loading in the vertical direction in the horizontal ground shaking tests was represented by a sinusoidal approximation of the load-time history (feedback from the simulated superstructure in the physical experiments) and applied in PAR. In other words, the measured force-time history at the pile-head during the model shaking tests were utilized to determine axial dynamic loading. The maximum measured axial force amplitude was multiplied by a dynamic scaling factor ($n_d^2 = 49$ for Ochoa's tests and $n_d^2 = 27.04$ for the other tests) to obtain the maximum force amplitude in the prototype.

The excursions in the pile-head loading occur due to the relative movement between the superstructure and the pile supporting it. In absence of any field data available for prototype analysis, the excursions in the pile-head load measured during the model tests were scaled and applied as uniform load cycles of average amplitude. In the case of an irregular dynamic loading pattern, Seed et al. (1975) proposed a rational method to determine the number of cycles of an equivalent uniform stress amplitude to be applied during the duration of the loading. This procedure ensured that the cumulative effect of corresponding cycles of various stress levels in the irregular loading patterns on the pore water pressure magnitude was approximately the same as that of the equivalent uniform stress cycles. The equivalent stress amplitude used in this case was 0.65 times the peak stress amplitude. This procedure required conducting cyclic triaxial strength tests to determine the number of cycles required for liquefaction for each stress level. In the absence of specific laboratory strength data for a particular earthquake record, Seed suggested a representative number of uniform equivalent stress cycles from studies of different magnitude earthquakes for typical time durations, which were used here.

Therefore, the irregular force-time history was then represented by an equivalent number of uniform sinusoidal stress cycles: 10, 15, and 21 cycles were used for earthquake magnitudes of 7.0, 7.5, and 8.0, respectively. These uniform load cycles had an amplitude of 0.65 of the maximum load amplitude, as per liquefaction analysis [Seed et al. (1975)]. Assuming the duration of strong shaking to be 50 seconds in a Magnitude 8.0 earthquake, the duration for earthquake magnitudes of 7.5 and 7.0 were then taken to be 35 and 25 seconds, respectively. Table 6.4 summarizes the characteristics of the applied harmonic loading for events of different simulated magnitudes.

Table 6.4: Number of Uniform Stress Cycles and Duration for Different Earthquake Magnitudes, per Seed et al. (1975)

Magnitude of Earthquake	No. of Uniform Stress Cycles at 0.65 t_{max}	Duration of Strong Shaking (sec)
7.0	10	25
7.5	15	35
8.0	21	50

6.5 Results and Discussion

Table 6.5 shows the measured and calculated degradation factors for the Oceanside and the Upland event tests. In all the tests, the degradation factors computed based on the matching of test data were lower than that estimated from the pore water measured during lateral loading of the soil, suggesting that the degradation of the axial soil resistance was much more severe than the lateral soil resistance. Thus the hypothesis that pore water pressure generation close to the pile is solely responsible for degradation of the stiffness and the strength of the soil may not be true. There appears to be degradation in the pile-soil interface friction angle or earth pressure coefficient also.

The actual degradation factors in tests in which failure occurred at relatively high bias loading of about 90% are not known because failure occurred during the earthquake

Table 6.5: Degradation Factors Calculated From the Dynamic Analysis using PAR

Test	$(\delta_s)^p$ (mm)	$(\delta_{de})^p$ (mm)	ρ_e	$(\delta_{dc})^p$ (mm)	ρ_c	$(\delta_c)^m$ during shaking (mm)	$(\delta_m)^m$ during shaking (mm)
R1	1.07	1.30	0.96	2.15	0.82	0.15	0.15
R2	1.26	1.77	0.97	16.00	0.71	2.83	1.14
S1	0.79	0.92	0.98	1.11	0.92	0.04	0.04
S3	0.98	1.19	0.96	3.05	0.795	0.29	0.25
S4	1.11	2.36	0.99	109.4	0.94	failure	failure
U1	0.39	0.71	0.89	0.74	0.85	0.05	0.05
U2	1.15	1.71	0.93	3.04	0.74	0.27	0.25
U3	1.38	2.28	0.88	16.82	0.65	failure	failure
OS#1	0.61	0.66	0.96	0.86	0.80	0.07	0.06
OS#2	0.39	0.45	0.98	0.65	0.86	0.05	0.05
OS#3	0.59	0.84	0.89	1.83	0.78	0.24	0.30
OS#4	0.93	1.36	0.88	2.25	0.73	0.25	0.23
OS#5	1.04	1.37	0.89	719.32	0.78	failure	failure
OS#6	1.86	2.01	0.89	124.64	0.85	failure	failure
OS#7	0.58	0.95	0.89	3.48	0.75	0.56	0.33
UP#1	0.32	0.36	0.98	-	-	0.007	0.006
UP#2	1.59	1.68	0.98	1.88	0.89	0.06	0.06
UP#3	1.29	1.37	0.98	1.61	0.92	0.06	0.06
UP#4	0.82	0.94	0.98	1.70	0.83	0.17	0.17
UP#5	1.64	2.07	0.98	3.11	0.795	0.28	0.29
UP#6	0.62	0.68	0.98	1.59	0.85	0.19	0.19
UP#7	0.70	0.73	0.98	2.26	0.86	0.30	0.30
UP#8	0.65	0.76	0.97	1.15	0.78	0.10	0.10
UP#9	1.34	1.61	0.97	2.08	0.78	0.14	0.15
UP#11	1.52	2.03	0.97	4.24	0.77	0.52	0.53
UP#12	1.44	1.54	0.97	5.10	0.74	0.70	0.38
UP#13	1.41	1.88	0.97	4.00	0.75	0.49	0.41
UP#14	1.31	1.51	0.97	300.0	0.91	failure	failure
UP#15	0.64	0.80	0.86	1.07	0.90	0.08	0.09
UP#16	1.09	1.16	0.91	6.10	0.62	0.96	0.99
UP#17	1.64	2.23	0.87	3.05	0.745	0.27	0.38
UP#18	1.26	2.10	0.87	21.79	0.68	failure	failure
UP#19	1.14	2.36	0.87	12.19	0.71	failure	failure

$(\delta_s)^p$ = Static prototype pile-head displacement under bias load

$(\delta_{de})^p$ = Computed prototype pile-head displacement after the dynamic analysis with degradation factors estimated from pore water pressure buildup set equal in both curves

ρ_e = Estimated degradation factors; ρ_c = Matched degradation factors

$(\delta_{dc})^p$ = Computed prototype pile-head displacement with reduced degradation factors in the f-w curves to match the measured displacement of the model pile

$(\delta_c)^m$ = Calculated model pile-head displacement during shaking from prototype value using (n_d = 7 for Ochoa's tests and n_d = 5.2 for other tests)

$(\delta_m)^m$ = Measured model pile-head displacement during shaking

shaking, which prevented using displacement matching for calculating the degradation factor.

The value of the degradation factor was a function of the magnitude of the simulated seismic event and the magnitude of the bias loading on the pile. Fig. 6.3 shows the relation between the earthquake magnitude and the degradation factors for all events. It can be noticed from the figure that the degree of degradation increases with the magnitude of the earthquake.

Fig. 6.4 shows the relation between the amount of bias load relative to the pile capacity, expressed in percentage, and the degradation factors. This figure gives a clearer picture for degradation in f-w curves because it accounts for the applied bias load for different earthquake magnitudes. Again, it can be seen that the difference between the effects of earthquake magnitudes 7.0 and 7.5 is not significant, while for an earthquake magnitude of 8.0, the degradation is more severe. Fig. 6.4 appears to be a reasonable preliminary criterion for analysis of prototype piles for axial loading for California-type seismic events exclusive of the effects of seaquakes.
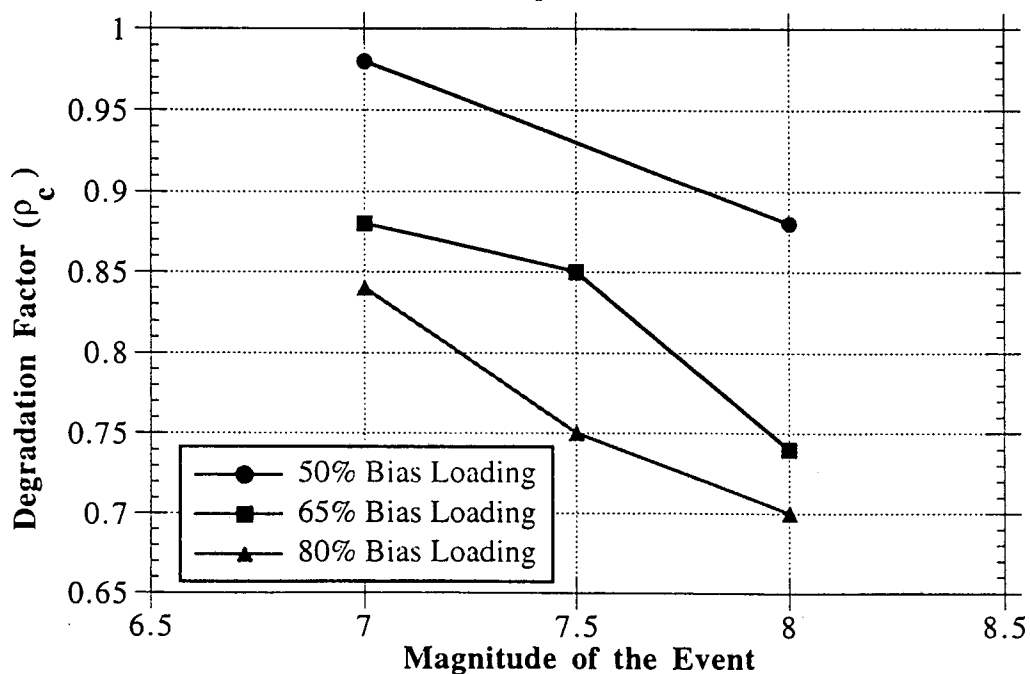
Fig. 6.3: Relation between Earthquake Magnitude (M) and Degradation Factor (ρ_c)

156
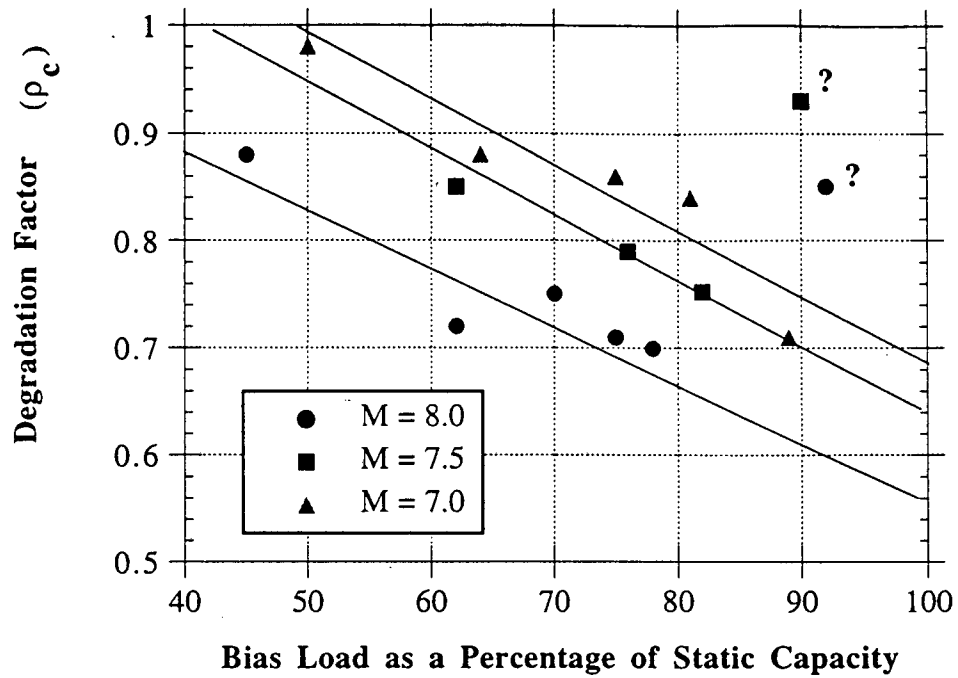
Fig. 6.4: Relation between Bias Load the Degradation Factors for Different Earthquake Magnitudes

In practice Fig. 6.4 would be used as indicated in (6.1).

$$f(w) = r_c \, f(w, \text{backbone}), \qquad\qquad (6.1)$$

where $f(w)$ is a value on a degraded f-w curve at any value of w, r_c is the degradation factor from Fig. 6.4 and $f(w, \text{backbone})$ is the value of f at the same value of w as is associated with $f(w)$ on the undegraded backbone curve.

Chapter 7
THEORETICAL EXAMINATION OF HYDRODYNAMIC SEABED PRESSURE AND OSCILLATORY WATER PRESSURE RESPONSE

7.1 Introduction

The effects of seaquakes on pile capacity were studied experimentally by applying oscillatory pressures to a reservoir of water atop the test chamber. These tests are described in Chapter 8. This chapter provides a theoretical basis for the selection of applied pressure amplitudes and for interpreting patterns of observed water pressure attenuation in the soil mass.

7.2 Theoretical Computation of Hydrodynamic Pressure Caused by Seaquakes

The vertical motion of the seabed during an earthquake produces compressional waves that propagate through seawater and impose large loads on the structures in the sea and the seabed. This phenomenon is referred to as a "seaquake."

The total induced water pressure on the seafloor is obtained by adding the dynamic pressure generated in the seawater due to seafloor excitation to the existing hydrostatic pressure field. Therefore, the total water pressure can be expressed as follows :

$$P = \rho \frac{\partial \Phi}{\partial t} + \rho g h \qquad (7.1)$$

where ρ = density of the seawater, Φ is the seawater velocity potential evaluated on the seafloor, h is the depth of water below the surface of the sea, and g is the acceleration due to gravity.

7.2.1 Analytical Method

Analysis of the underwater propagation of the compressional wave requires solving the governing wave equation in the flow field for the velocity potential under a given set of boundary conditions. The seawater is assumed to be inviscid, compressible and irrotational fluid. The hydrodynamic pressure developed on the seabed and beneath the hull of a TLP has been evaluated in two dimensions for a wave source of length L_s and unit width on the seafloor by Kobayashi et al. (1992). A physical model of a TLP with its hull moored in tension by tendons from a template on the seabed is shown in Fig. 7.1. The hull is assumed to be fixed and its motion is neglected. The wave reflection or scattering due to the presence of the hull is disregarded. The formulation of the velocity potential for the above problem has been provided by Kobayashi et al. (1992).

7.2.2 Governing Wave Equation

The propagation of a wave in an elastic seabed is expressed by the following equation,

$$\frac{\partial^2 q}{\partial t^2} = \frac{\lambda + \mu}{\rho} \nabla \Delta + \frac{\mu}{\rho} \nabla^2 q \ , \tag{7.2}$$

where, q is the displacement vector,

$$\nabla = i\frac{\partial}{\partial x} + j\frac{\partial}{\partial y} + k\frac{\partial}{\partial z},$$

i, j, k are the unit vectors in the x, y, and z directions,

Δ = dilatation ($\Delta = \nabla q$),

$$\nabla^2 = \frac{\partial^2}{\partial x^2} + \frac{\partial^2}{\partial y^2} + \frac{\partial^2}{\partial z^2},$$

λ, μ = Lame's constants, ρ = seawater density, t = time.

The first term on the right hand side of (7.2) represents the p-wave component, and the second term represents the s-wave component.

159
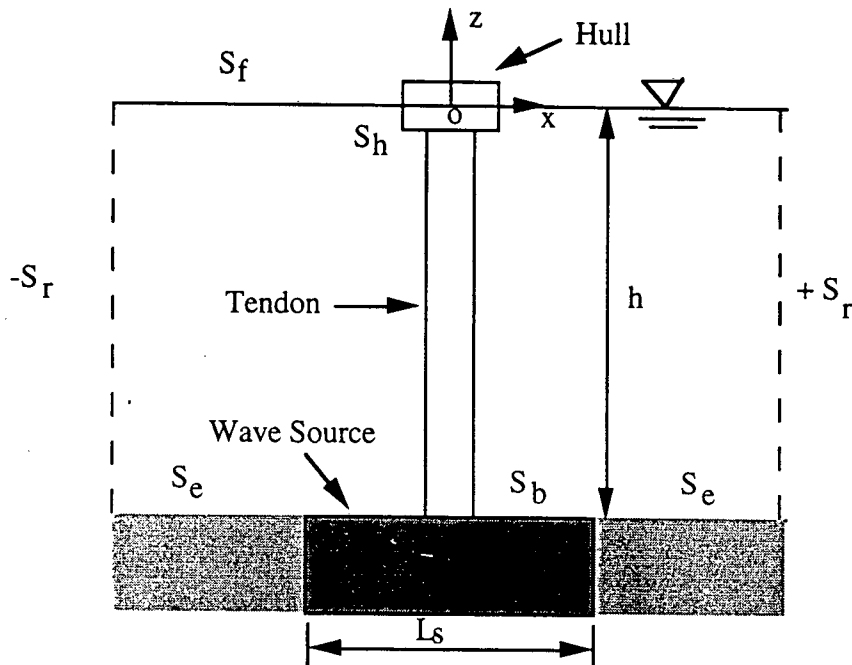
S_r - Surface of the far field boundary

S_b - Surface of seabed undergoing vertical excitation

S_e - Surface of seabed not undergoing vertical excitation

S_f - Surface of the freewater

S_h - Surface of the hull submerged in water

Fig. 7.1. Physical Representation of the Analytical Model

However, shear waves do not propagate or exist in the seawater ($\mu = 0$) and ground motion composed both of p and s waves, propagates through the seawater as compressional waves. Replacing displacement in the above equation with dilatation, (7.2) takes the following form

$$\frac{\partial^2 \Delta}{\partial t^2} = \frac{\lambda}{\rho} \nabla^2 \Delta .$$

(7.3)

The particle velocity vector in the flow field can be written as

$$v = \frac{\partial q}{\partial t} = \nabla \Phi,$$

(7.4)

where Φ is the velocity potential in the flow field.

Combining (7.2), (7.3), and (7.4)

$$\frac{\partial^2 \Phi}{\partial t^2} = c^2 \nabla^2 \Phi, \tag{7.5}$$

where c is the underwater acoustic speed or the wave velocity of a compressional wave in water. $c = (\lambda / \rho)^{1/2} = (B_w / \rho)^{1/2}$, where B_w is the bulk modulus of water. The propagation of waves in seawater depends on the compressibility of the seawater. If the seawater is assumed to be incompressible, or its compressibility is very small, then the propagation of the dynamic water pressure caused by the vibration of seabed does not occur.

7.2.3 Seawater Velocity Potential

The seawater velocity potential is a function of both space and time. Therefore, it is given by

$$\Phi(x,z,t) = \phi(x,z)\, e^{i\Omega t}, \tag{7.6}$$

where ϕ is the seawater velocity potential amplitude, Ω is the displacement excitation frequency, t is the time, e is the exponential, and $i = \sqrt{-1}$.

The displacement excitation function (w) of the seabed can be expressed as

$$w = We^{i\Omega t}, \tag{7.7}$$

where, W is the displacement amplitude, Ω is the frequency of excitation and t is time.

For a wave to propagate, the velocity potential must satisfy the governing wave equation, yielding the equation shown below.

161

$$\left(\frac{\partial^2}{\partial x^2} + \frac{\partial^2}{\partial z^2} + \frac{\Omega^2}{c^2}\right)\phi(x,z) = 0 , \qquad (7.8)$$

where c is the acoustic speed in water = 1430 m/sec.

The boundary conditions on $\phi(x,z)$ are

$$\frac{\partial \phi}{\partial z} = 0 \text{ on } S_h \text{ (neglecting motion of the hull).} \qquad (7.9)$$

$$\phi = 0 \text{ on } S_f \text{ (disregarding the generation of surface waves).} \qquad (7.10)$$

$$\frac{\partial \phi}{\partial z} = 0 \text{ on } S_e \text{ (nontransmission condition of the wave into the seabed).} \qquad (7.11)$$

$$\frac{\partial \phi}{\partial z} = v_b \text{ on } S_b \text{(portion of seabed under vertical excitation).} \qquad (7.12)$$

where v_b is the velocity amplitude of vertical vibration of the seabed.

In addition, in order to ensure that the progressive waves disappear in the far field, Sommerfield's radiation condition equation is applied.

$$\lim_{|x| \to \infty} |x|^{1/2}\left(\frac{\partial \phi}{\partial x} - ik\phi\right) = 0 \quad \text{(at infinity),} \qquad (7.13)$$

where $k = \Omega / c$ is the wave number.

A Green's function, $G(x,z, x_0, z_0)$ is defined for analysis of hydrodynamic pressure near the sea surface, disregarding the hull. The Green's function physically represents the potential at a point $F(x,z)$ due to a unit potential at a point $S(x_0, z_0)$. Points F and S are known as the field and source points, respectively.

The Green's function is required to satisfy the wave equation at all points except at the source. This condition is represented by (7.14).

$$\left(\frac{\partial^2}{\partial x^2} + \frac{\partial^2}{\partial z^2} + \frac{\Omega^2}{c^2}\right)G = \delta(x - x_0)(z - z_0) , \qquad (7.14)$$

162

where δ denotes a delta function. The boundary conditions imposed on G are

$$G = 0, \text{ on } S_f .\tag{7.15}$$

$$\frac{\partial G}{\partial z} = 0, \text{ on } S_e .\tag{7.16}$$

$$\frac{\partial G}{\partial z} = 0, \text{ on } S_b .\tag{7.17}$$

Sommerfield's radiation condition is also applied here as in the case of the velocity potential.

$$\lim_{|x| \to \infty} |x|^{1/2}(\frac{\partial G}{\partial x} - i\lambda_n G) = 0 \quad \text{(at infinity)} ,\tag{7.18}$$

where $\lambda_n = \dfrac{\Omega^2}{c^2} - \left\langle (2n\text{-}1)\dfrac{\pi}{2h}\right\rangle^2 .$

Applying Green's second identity to f and G over the surface $S = S_f + S_h + S_b + S_e + S_r$,

$$\int_V \left[G\left\langle\left\langle \frac{\partial^2}{\partial x^2} + \frac{\partial^2}{\partial z^2} + \frac{\Omega^2}{c^2}\right\rangle\phi\right\rangle - \phi\left\langle\left\langle \frac{\partial^2}{\partial x^2} + \frac{\partial^2}{\partial z^2} + \frac{\Omega^2}{c^2}\right\rangle G\right\rangle\right] dV = \int_S \left[G\frac{\partial\phi}{\partial n} - \phi\frac{\partial G}{\partial n}\right] dS.$$
$$\tag{7.19}$$

Using equations 7.8, 7.14,

$$-\int_v \left[\phi\left\langle\delta(x\text{ - }x_o)(z\text{ - }z_o)\right\rangle\right]dV = \int_{S_f} \left[G\frac{\partial\phi}{\partial n} - \phi\frac{\partial G}{\partial n}\right]dS + \int_{S_r} \left[G\frac{\partial\phi}{\partial n} - \phi\frac{\partial G}{\partial n}\right] dS$$

$$+ \int_{S_e} \left[G\frac{\partial \phi}{\partial n} - \phi\frac{\partial G}{\partial n} \right] dS + \int_{S_b} \left[G\frac{\partial \phi}{\partial n} - \phi\frac{\partial G}{\partial n} \right] dS + \int_{S_h} \left[G\frac{\partial \phi}{\partial n} - \phi\frac{\partial G}{\partial n} \right] dS. \qquad (7.20)$$

Substituting the boundary conditions of (7.9) - (7.12), and (7.15) - (7.17), the following equation is obtained.

$$\phi(x,z) = -\frac{1}{2} \int_{S_b} G\, v_b\, dS = -\frac{1}{2} i\Omega W \int_{-L_s/2}^{+L_s/2} G\, dS, \qquad (7.21)$$

where, v_b = amplitude of $\partial w/\partial t = i\Omega W$, where W = displacement amplitude.

A Green's function that satisfies the above governing equation and the boundary conditions suggested by Kobayashi et al. (1992) is given by

$$G(x,z,x_o,z_o) = \sum_{n=1}^{s} \frac{i}{\lambda_n^2 h} Sin(k_n z)Sin(k_n z_o)e^{i\lambda_n|x - x_o|}$$

$$+ \sum_{n=s+1}^{\infty} \frac{i}{\lambda'^2_n h} Sin(k_n z)Sin(k_n z_o)e^{-\lambda'_n|x - x_o|}, \qquad (7.22)$$

where x, z are the coordinates of field points, x_o and z_o are the coordinates of the wave source point, and k_n (n = 1,2 ...), l_n (n=1,2...,s), l'_n (n=s+1, s+2,...) are constants defined by

$$k_n = (2n-1)\frac{\pi}{2h}, \qquad (7.23)$$

$$\lambda_n^2 = \frac{\omega^2}{c^2} - \left\langle (2n-1)\frac{\pi}{2h} \right\rangle^2, \qquad (7.24)$$

$$\lambda'^2_n = \left\langle (2n-1)\frac{\pi}{2h} \right\rangle^2 - \frac{\omega^2}{c^2}. \qquad (7.25)$$

s is the maximum integer which makes the right side of (7.24) positive.

Substituting (7.22) into (7.21), the velocity potential at any observation point in the region $|x| \leq 0.5L_s$ is given by

$$\phi(x,z) = i\Omega W(\sum_{n=1}^{s} (-1)^n \frac{2i}{\lambda_n^2 h} Sin(k_n z)(e^{i\frac{\lambda_n L_s}{2}} Cos\lambda_n x \; -1)$$

$$+ \sum_{n=s+1}^{\infty} (-1)^n \frac{2}{\lambda_n'^2 h} Sin k_n z (1- e^{\frac{\lambda_n' L_s}{2}} Cosh\lambda_n' x)) \; . \tag{7.26}$$

For a one-dimensional case, the length of the seabed undergoing excitation is infinity, i.e., L_s tends to infinity.

Alternatively, an independent solution is available for a one-dimensional case. The governing wave equation for the seawater, i.e., (7.8), reduces to the form

$$\frac{\partial^2 \phi(z)}{\partial z^2} + k^2 \phi(z) = 0 \; . \tag{7.27}$$

A suitable form for ϕ that satisfies the above equation and boundary conditions given by (7.10) - (7.12) has been given by Williams and Mau (1988) as

$$\phi(z) = \frac{i\Omega W}{k} \frac{Sin \; kz}{Cos \; kh} \; . \tag{7.28}$$

In either case, the dynamic pressure amplitude generated in seawater is expressed by the following equation.

$$P_s = -\rho \frac{\partial \Phi}{\partial t} = -\rho \phi i\Omega e^{i\Omega t} \; . \tag{7.29}$$

The idealized sinusoidal hydrodynamic pressure induced on the seabed due to the effect of seaquakes were computed for typical $M = 8.0$ California-type seismic events, viz., the Oceanside and Upland events using $c = 1430$ m/sec and $\rho = 1000$ kg/m^3 in (7.29). The vertical displacement-time histories for these events are shown in Figs. 7.2 and 7.3, respectively. The time windows displayed in Figs. 7.2 and 7.3 were used to estimate equivalent harmonic uniform displacement-time histories to represent the irregular vertical displacement-time histories for the two events. Two predominant frequencies could be

165

OCEANSIDE EVENT

Time Window Used for Seaquake-Induced
Pressure Computation
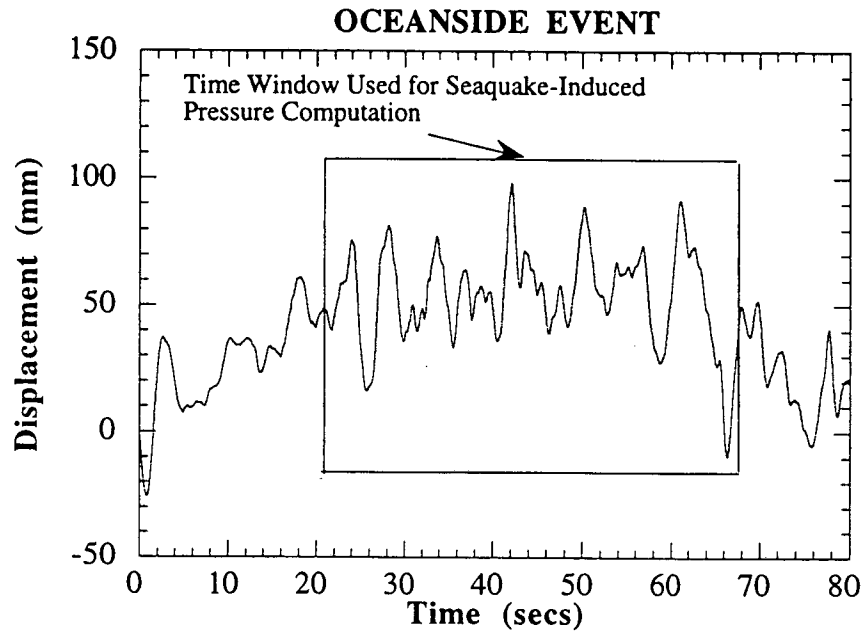
Fig. 7.2: Displacement-Time Record of the Vertical
Component of Scaled M = 8.0 Oceanside Event

UPLAND EVENT

Time Window Used for Seaquake-Induced
Pressure Computation
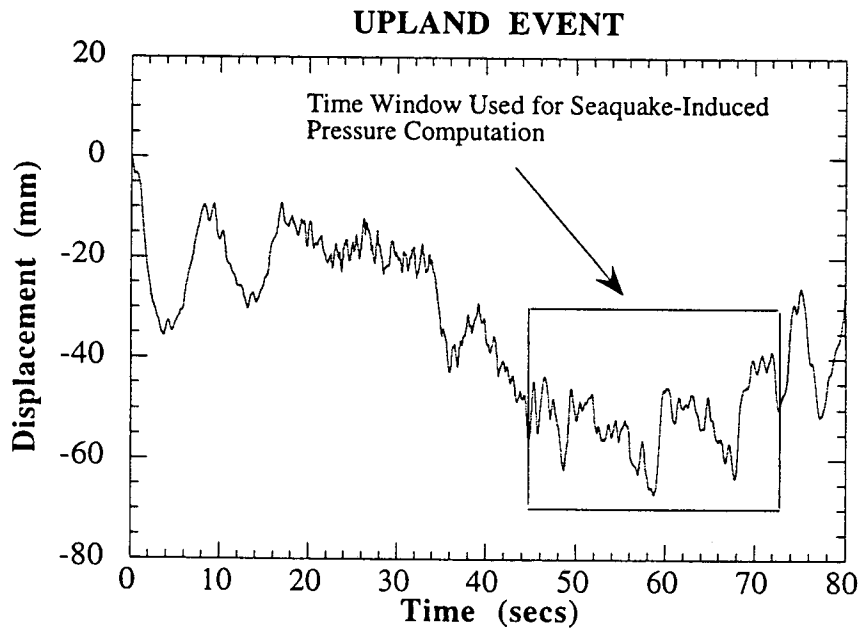
Fig. 7.3: Displacement-Time Record of the Vertical
Component of Scaled M = 8.0 Upland Event

166

observed for the two events. Table 7.1 shows the parameters selected to be used in (7.26) and (7.28) for the two events and the computed amplitudes of the idealized sinusoidal pressures induced on the seabed due to the seaquake using the solutions provided by Kobayashi et al. and Williams and Mau for typical water depths. Typically, for both events, the high-frequency, low-amplitude component of the signal contributed significantly to the generation of the hydrodynamic pressure on the seabed. Computations of the hydrodynamic pressure amplitudes using both solutions were in close agreement for all water depths for both events. In the case of the Upland event, the mathematical solution for seaquake pressure tends to infinity at water depths beyond 300 m for the higher frequency component, resulting in extremely large values of seaquake pressures on the seabed. The low-amplitude, high-frequency and the high-amplitude, low-frequency components of each of the two seismic events (Upland and Oceanside) were combined to obtain a mean value as indicated in Table 7.1.

7.3 Oscillatory Pore Water Pressure Response

The dominant factors controlling the development of liquefaction or densification conditions in seabed are the seaquake associated bottom pressure, the oscillatory pore water pressure in the seabed and the vertical effective stress at calm. When the seaquake associated bottom pressure and the vertical effective stress at calm are given, the only factor to be known is the oscillatory pore water pressure. It is reasonable to assume the problem of oscillatory pore water pressures excited in the seabed to be one-dimensional. Several researchers have solved this one-dimensional vertical problem of oscillatory flow from the perspective of surface wave loading of the seabed [Barends (1978), Zen and Yamazaki (1990)]. A finite difference solution of the oscillatory excess pore water pressure developed by Zen and Yamazaki is summarized below.

167

Table 7.1: **Computed Amplitudes of Idealized Sinusoidal Pressure Induced on the Seabed During Seaquakes for Typical Water Depths**

Parameter	Oceanside Event M = 8.0, Vertical Comp.		Upland Event M = 8.0, Vertical Comp.	
	Low-Frequency high-amplitude signal	High-Frequency low-amplitude signal	Low-Frequency high-amplitude signal	High-Frequency low-amplitude signal
Ω (Hz) (Figs. 7.2 and 7.3)	0.12	1	0.14	1.2
Mean Ω (Hz)	0.6		0.7	
W (mm) (Figs. 7.2 and 7.3)	18.5	1.25	10.1	0.61
h (m) (Fig. 7.1)	Hydrodynamic Pressure, kPa (Kobayashi et al, 1992)	Hydrodynamic Pressure, kPa (Kobayashi et al., 1992)	Hydrodynamic Pressure, kPa (Kobayashi et al., 1992)	Hydrodynamic Pressure, kPa (Kobayashi et al., 1992)
100	0.88	4.30	0.63	3.17
150	1.33	7.30	0.95	5.67
200	1.77	11.70	1.28	10.34
225	2.00	15.00	1.42	14.96
250	2.22	19.77	1.59	24.46
275	2.45	27.36	1.75	56.13
300	2.67	41.63	1.92	tends to infinity
h (m) (Fig. 7.1)	Hydrodynamic Pressure, kPa (Williams and Mau, 1988)	Hydrodynamic Pressure, kPa (Williams and Mau, 1988)	Hydrodynamic Pressure, kPa (Williams and Mau, 1988)	Hydrodynamic Pressure, kPa (Williams and Mau, 1988)
100	1.08	5.30	0.78	3.80
150	1.63	8.69	1.17	6.64
200	2.18	13.57	1.56	11.60
225	2.46	17.05	1.76	16.70
250	2.73	21.96	1.95	25.63
275	3.00	29.55	2.16	55.00
300	3.30	43.37	2.36	tends to infinity

Consider a soil element at depth, z, in the seabed. Assuming the flow of pore water in the soil is one-dimensional and governed by the steady state form of Darcy's Law, (7.30) is derived from the conservation of mass of pore water and is given as

$$\frac{k}{\gamma_w} \frac{\partial^2 P_m}{\partial z^2} = -m_v \frac{\partial \sigma_v'}{\partial t} + n m_w \frac{\partial P_m}{\partial t} \qquad (7.30)$$

where, k is the coefficient of permeability, m_v is the coefficient of volume compressibility, n is the porosity, m_w is the compressibility of the pore water including air, γ_w is the unit weight of the pore wate, t is the time, σ_v' is the vertical effective stress under one-dimensional plane-strain condition, and P_m is the oscillatory pore water pressure induced in the seabed.

The vertical effective stress can be expressed by the following equation

$$\sigma_v' = \sigma_{vo}' + P_d - P_m, \qquad (7.31)$$

where σ_{vo}' is the initial vertical effective stress at calm, P_d is the seaquake-associated pressure on the surface of the seabed, and P_m is the oscillatory pore pressure induced in the seabed. Then, the oscillatory excess pore pressure, u_e is defined by

$$u_e = P_m - P_d \ . \qquad (7.32)$$

Differentiating (7.31) and introducing it in (7.30), we get

$$\frac{k}{\gamma_w m_v} \frac{\partial^2 P_m}{\partial z^2} = (1 + \frac{n m_w}{m_v}) \frac{\partial P_m}{\partial t} - \frac{\partial P_d}{\partial t} \ . \qquad (7.33)$$

Substituting

$$c_v = \frac{k}{\gamma_w m_v} \qquad (7.34)$$

and

$$\alpha = 1 + \frac{n m_v}{m_v} \qquad (7.35)$$

into (7.33), we get the governing equation on the oscillatory pore pressure in the seabed in the following form.

$$c_v \frac{\partial^2 P_m}{\partial z^2} = \alpha \frac{\partial P_m}{\partial t} - \frac{\partial P_d}{\partial t} \quad . \tag{7.36}$$

The boundary conditions for the above equation can be written as

$$P_m = P_d \text{ at } z = 0 \quad , \tag{7.37}$$

i.e., the oscillatory pore water pressure excited in the seabed is equal to the seaquake-associated pressure on the surface of the seabed.

If the porous seabed is of finite thickness, L, and the underlying soil is assumed impermeable, no water flows normal to the horizontal boundary giving rise to (7.38).

$$\frac{\partial P_m}{\partial z} = 0 \text{ at } z = L \quad . \tag{7.38}$$

Initial conditions can be written as

$$P_m = 0 \text{ at } t = 0 \quad .$$

The solution for seaquake-induced pressure on the seabed was found to be

$$P_d = \frac{\rho \Omega^2 W}{k} \tan (kh) \operatorname{Sin} \left(\frac{2\pi t}{T}\right) \quad , \tag{7.39}$$

where Ω is the displacement excitation frequency of the seabed, W is the displacement amplitude, k = wave number = Ω / c, h=water depth, c = acoustic speed in water, T is the displacement excitation period and t = prototype time.

Alternatively,

$$P_d = p_d \operatorname{Sin}\left(\frac{2\pi t}{T}\right) \quad . \tag{7.40}$$

Simplifying, using

$$\overline{P} = \frac{P_m}{p_d} \quad , \tag{7.41}$$

$$\overline{Z} = \frac{z}{L} \quad , \tag{7.42}$$

170

$$\overline{T} = \frac{t}{T} \; , \tag{7.43}$$

$$C = \frac{c_v T}{L^2} \; , \tag{7.44}$$

(7.36) can be written in nondimensional form

$$C\frac{\partial^2 \overline{P}}{\partial \overline{Z}^2} = \alpha\frac{\partial \overline{P}}{\partial \overline{T}} - 2\pi Cos(2\pi\overline{T}) \; . \tag{7.45}$$

The revised boundary conditions then become

$$\overline{P} = Sin(2\pi\overline{T}) \text{ at } \overline{Z} = 0 \; , \tag{7.46}$$

$$\frac{\partial \overline{P}}{\partial \overline{Z}} = 0 \text{ at } \overline{Z} = L \; . \tag{7.47}$$

The revised initial condition then becomes

$$\overline{P} = 0 \text{ at } \overline{T} = 0 \; . \tag{7.48}$$

C is considered to represent the drainage effect of the excess pore pressure and is referred to as the coefficient of drainage. Higher the coefficient of drainage, the excess pore pressure will dissipate more quickly from the permeable seabed.

α is the coefficient of wave propagation and under undrained conditions, (7.36) reduces to the form

$$\frac{1}{\alpha} = \frac{\dfrac{\partial P_m}{\partial t}}{\dfrac{\partial P_d}{\partial t}} \; , \tag{7.49}$$

where $1/\alpha$ is equivalent to the Skempton B coefficient.

171

7.3.1 Finite Difference Solution

(7.45) can be solved using finite difference analysis. The normalized oscillatory pore water pressure, $\overline{P}$ is a function of $\overline{Z}$ and $\overline{T}$. Using a superscript-subscript notation, where $\overline{P}(\overline{Z}) = \overline{P}_i$ and $\overline{P}(\overline{T}) = \overline{P}^k$ then $\overline{P}_i^k =$ normalized oscillatory pore water pressure at normalized depth, $\overline{Z}$ and time, $\overline{T}$.

The Finite difference analogs for the PDE are as follows

$$\frac{\partial^2 \overline{P}}{\partial \overline{Z}^2} = \frac{\overline{P}_{i-1}^k - 2\overline{P}_i^k + \overline{P}_{i+1}^k}{\Delta \overline{Z}^2} \quad , \tag{7.50}$$

$$\frac{\partial \overline{P}}{\partial \overline{T}} = \frac{\overline{P}_i^{k+1} - \overline{P}_i^k}{\Delta \overline{T}} \quad , \tag{7.51}$$

$$\overline{T} = (k+1) \Delta \overline{T} \quad . \tag{7.52}$$

Substituting (7.50), (7.51) and (7.52) in (7.45),

$$C\left(\frac{\overline{P}_{i-1}^k - 2\overline{P}_i^k + \overline{P}_{i+1}^k}{\Delta \overline{Z}^2}\right) = \alpha\left(\frac{\overline{P}_i^{k+1} - \overline{P}_i^k}{\Delta \overline{T}}\right) - 2\pi \, Cos(2\pi(k+1)\Delta \overline{T}) \quad . \tag{7.53}$$

Rearranging,

$$\overline{P}_i^{k+1} = \overline{P}_i^k + \left(C\left(\frac{\overline{P}_{i-1}^k - 2\overline{P}_i^k + \overline{P}_{i+1}^k}{\Delta \overline{Z}^2}\right) + 2\pi \, Cos(2\pi(k+1) \Delta \overline{T}\right)\frac{\Delta \overline{T}}{\alpha} \quad . \tag{7.54}$$

Thus, (7.54) gives the solution of (7.53).

Considering oscillatory water pressure loading on the surface of the sand in the test chamber, and using $\Delta \overline{Z} = 0.1$ and $\Delta \overline{T} = 0.001$ as mesh intervals in space and time respectively for the computations, 12 nodes are generated as shown in Fig. 7.4 below. One additional node i.e., node # 12 is generated to satisfy the boundary condition at the bottom boundary. The mesh intervals have been chosen so as to give stable and convergent solutions.
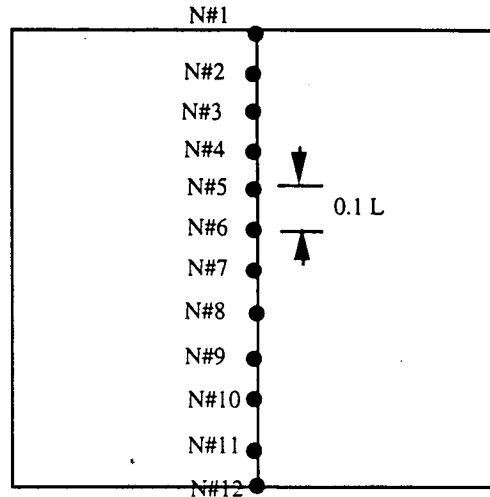
N#1
N#2
N#3
N#4
N#5
0.1 L
N#6
N#7
N#8
N#9
N#10
N#11
N#12

Fig. 7.4: **Node Generation for Finite Difference Analysis for Tests Conducted in the Chamber**

Boundary Conditions :

At top boundary:

$$\overline{P}_1^{k+1} = Sin(2\pi(k+1)\Delta\overline{T}) \ . \tag{7.55}$$

At bottom boundary:

$$\overline{P}_{11}^{k+1} = \overline{P}_{12}^{k+1} \ . \tag{7.56}$$

Initial Condition (t = 0):

$$\overline{P}_1^0 = \overline{P}_2^0 = \ .... \ = \overline{P}_{12}^0 = 0 \ . \tag{7.57}$$

7.3.2 Pore Fluid Compressibility

It can be seen from (7.45) that the parameters most influencing the development of oscillatory pore water pressure in the seabed are C and α. C is a function of length of the permeable seabed which in this case is the chamber height, the period of the applied hydrodynamic pressure, the soil permeability and the volume compressibility of the pore water which is dependent on the degree of saturation. For 100% saturation and the undrained condition $\alpha = 1$.

Okusa (1985) presented the one-dimensional compressibility of the pore water, m_w by the following equation

$$m_w = m_{wo}S_r + \frac{1 - S_r}{p_{mg}} \; , \tag{7.58}$$

where, m_{wo} is the one-dimensional compressibility of water at the fully saturated state, S_r, degree of saturation, and p_{mg} is the sum of the hydrostatic pressure and the wave-associated dynamic pressure.

Assuming $m_{wo} = 0$ for a fully saturated case, (7.58) becomes,

$$m_w = \frac{1 - S_r}{p_{mg}} \tag{7.59}$$

An approximate estimate of degree of saturation for the present study is made based on the Skempton B parameter and the one-dimensional volume compressibility of the soil. Experimentally, B = 0.90 and average m_v of the soil = 0.00005 m^2/ kN. The degree of saturation, $S_r = 0.995$ according to Fredlund (1976) for the conditions. Measurements of degree of saturation were not made for the individual seaquake tests. Therefore, $S_r = 0.995$ was used in the computation of the compressibility of the pore fluid. This information will be used to interpret the results in Chapter 8.

It is significant to note that this analytical model predicts a significant attenuation in the pore water pressure wave and a measurable phase shift after short distances.

Chapter 8
EFFECTS OF SEAQUAKES ON AXIAL PILE RESPONSE

8.1 Introduction

This chapter describes the results of the model-scale laboratory tests conducted on piles loaded in biased tension to investigate the coupled effect of vertical motion of the seabed and the induced seaquake on the performance of these piles. The following aspects of the problem have been addressed: (i) the prototype representation of the scaled model parameters used in the experiments; (ii) explanation of the mechanism of pore water pressure response during seaquake loading of the seabed (sea-seabed interaction tests without the pile) and the effects of various seaquake wave parameters and soil parameters on this mechanism based on the experiments; (iii) the axial pile response during seaquakes and its comparison with the effects of horizontal ground shaking and (iv) implications of test results to pile design.

8.2 Prototype Representation of the Model Parameters Selected

As described in Chapter 4, the mechanism of generation of the sinusoidal seaquake pressure during the seaquake tests consisted of stroking water confined in a compartment mounted on top of the soil chamber by cyclic vertical motion of the soil chamber, mounted on the actuator of a servo-hydraulic testing machine, against a fixed piston. The amplitudes of the controlled sinusoidal pressures in the model tests ranged from 14 to 50 kPa, representing seaquake pressures developed on the seabed in water depths of 225 - 300 m during typical M = 8.0 seismic events.

A discussion of model-prototype similitude is included in Chapter 4 with derivation of scaling factors for a 4.5-m-long pile or for the top 4.5m of a longer pile. For simulating longer piles, these scaling factors need to be modified in order to simulate the diffusion characteristics of the pore water. This is in recognition of the fact that for a longer pile, the

path of travel for the pore water to the drainage surface is also longer. Dynamic scaling factors have been derived for the basic soil parameters in Table 8.1 based on dimensional analysis assuming that acceleration is scaled by n_d (velocity is preserved in the model), model length is scaled by $1/n_d$, and that the prototype materials are used in the model. This means that density, viscosity and particle size are scaled by a factor of 1. n_d represents the dynamic length scaling factor. Table 8.2 shows the computed and selected dynamic scaling factors for basic soil parameters for different lengths of the pile simulated in the chamber. The selected values for the model seaquake tests conducted with the pile were a compromise between the inconsistencies in the scaling factors for the different soil parameters, also taking into account the limitations of the testing machine. Table 8.3 shows the model parameters that were actually used in the chamber for simulating different pile lengths based on the selected approximate scaling factors for the following prototype conditions.

Frequency of excitation = 0.6 Hz (mean value per Table 7.1 in Chapter 7)

Displacement amplitude of excitation :

Low amplitude high frequency signal = 18.1 mm (upper bound per Table 7.1)

High amplitude low frequency signal = 0.61 mm (lower bound per Table 7.1)

Duration of excitation = 80 secs (typical)

The amplitudes of the cyclic vertical displacement of the chamber in the model tests shown in column 1 of Table 8.3 were such that they were average values of the upper and lower bounds of the scaled displacements computed from prototype values This ensured that the range of soil velocities in the chamber would similar to those in the prototype. The experiments can therefore be considered a parametric study rather than a precise scale-model study.

Table 8.1: Model Test Scaling Factors [Ochoa (1990)]

Parameter	Symbol	Dimensionless Group	Similarity Requirements: Model / Prototype
STATIC			
Length	L		$N_l = 1/n_s$
DYNAMIC			
Length	L		$N_l = 1/n_d$
Velocity	v		$N_v = 1$
Time (In inertial terms)	t_1		$N_t = 1/n_d$
Frequency (Froude Similitude)	f	$4\pi^2 L/g$	$N_f = \sqrt{n_d}$
Frequency (Mach Similitude)	f	$4\pi^2 \sigma k_s/L\eta g$	$N_f = n_d$
Acceleration	a		$N_a = n_d$
Soil Density[a]	ρ		$N_\rho = 1$
Liquid Density[a]	ρ_λ		$N_{\rho_\lambda} = 1$
Particle Size	d	d/L	$N_d = 1/n_d$
Mass	m		$N_m = 1/n_d^3$
Force	F	F/ma	$N_F = N_m N_a = 1/n_d^2$
Viscosity	η		$N_\eta = 1$
Permeability	k	$k\eta/d^2\rho_\lambda a$	$N_k = N_d^2 N_{\rho_\lambda} N_a N_\eta^{-1} = 1/n_d$ ($N_k = 1$ for 1-g cond.)
Stress	σ	$\sigma L^2/F$	$N_\sigma = N_F N_L^{-2} = 1$
Strain	ε		$N_\varepsilon = 1$
Coefficient of Consolidation[a]	c_v	$c_v \rho g m_v/k$	$N_{c_v} = N_k N_\rho^{-1} N_{m_v}^{-1} = 1/n_d$
Time[a,b] (in diffusion terms)	t_2	$t c_v/L^2$	$N_t = N_L^2 N_{c_v}^{-1} = 1/n_d$

(a) Model and prototype soil and pore fluid are the same

(b) From differential equation, $\partial u/\partial t = c_v (\partial^2 u/\partial L^2)$, $N_\sigma/N_t = N_{c_v}(N_\sigma/N_L^2) = N_t = N_L^2 N_{c_v}^{-1}$

(c) k_s = intrinsic permeability of the soil

177

Table 8.2: Computed and Selected Values of Scaling Factors for Different Pile Lengths

Scaling Factor Symbol	4.5 m		9.0 m		14.5 m		27.0 m	
	Comp.	Selected	Comp.	Selected	Comp.	Selected	Comp.	Selected *
N_L (dynamic)	1/5.2	1/4	1/10	1/8	1/16	1/14	1/31	1/14
N_L** (static)	1/15	1/15	1/30	1/30	1/48	1/48	1/90	1/90
N_v	1	1	1		1	1	1	
N_t (inertial)	1/5.2	1/4	1/10	1/8	1/16	1/14	1/31	1/14
N_f (Mach)	5.2	-	10	-	16	-	31	-
N_f (Froude)	2.3	-	4	-	6	-	14	-
N_f (RMS)	4.0	4.0	8.0	8.0	12	14	24	14
N_a	5.2	4.0	10.0	8.0	16	14	31	14
N_r	1	1	1	1	1	1	1	1
N_{rl}	1	1	1	1	1	1	1	1
N_d	1/5.2	1/4.0	1	1	1	1	1	1
N_m	$1/(5.2)^3$	$1/(4.0)^3$	$1/(10)^3$	$1/(8.0)^3$	$1/(16)^3$	$1/(14)^3$	$1/(31)^3$	$1/(14)^3$
N_F	$1/(5.2)^2$	$1/(4.0)^2$	$1/(10)^2$	$1/(8.0)^2$	$1/(16)^2$	$1/(14)^2$	$1/(31)^3$	$1/(14)^2$
N_h	1	1	1	1	1	1	1	1
N_k	1/5.2	1/5.2	1/10	1/5.2	1/16	1/5.2	1/31	1/5.2
N_s	1	1	1	1	1	1	1	1
N_e	1	1	1	1	1	1	1	1
Nc_v	1/5.2	1/5.2	1/10	1/5.2	1/16	1/5.2	1/5.2	1/5.2
N_t diffusion	1/5.2	1/4	1/10	1/8	1/16	1/14	1/31	1/14

** - static scaling factor based on effective stress similitude (derivation shown in Chapter 4.0 for a 4.5 m long pile); * - Parameters selected due to limitations of the testing machine

Table 8.3: Model Parameters Used in Tests to Represent Different Pile Depths Based on Approximate Scaling Factors Selected

Amplitude of Chamber Vertical Excitation (mm)*	Frequency of Vertical Excitation (Hz)	Duration of Shaking (secs)	Initial Effective Chamber Stress (Isotropic) (kPa)	Prototype Depth (m) Based On Static Scaling
2.03	2.5	20	17.24	4.5
2.03	5.0	10	34.48	9.0
1.02	10.0	6	55.17	14.5
1.02	10.0	6	103.45	27.0

* These displacements are unscaled chamber displacements and were such that the scaled seabed displacements were within the upper and lower bound values shown in Table 7.1.

8.3 Sea-Seabed Interaction Test Results and Discussion

8.3.1 Summary of Testing Program

Several tests were conducted in the absence of the pile to understand the mechanism of development of pore water pressure in the soil during seaquakes and the influence of parameters such as the predominant frequency of the vertical excitation, number of cycles of loading, the initial effective stress in the soil, and the boundary condition of the imposed stresses on the phenomenon of propagation of seaquake-induced pore water pressure during simulated seismic events. The summary of the testing program is shown in Table 8.4. Tests SSB#1, SSB#2, SSB#4, SSB#5, SSB#6, SSB#7, SSB#8, and SSB#9 were conducted with the application of only vertical overburden with rigid lateral boundaries that simulated the one-dimensional zero lateral strain conditions. On the other hand, Tests SSB#3 and SSB#10 were conducted with equal vertical and lateral effective stresses at the boundary (identical to the ground shaking tests). Model tests were conducted at frequencies of 2.5, 5.0 and 10.0 Hz, which represented approximate prototype frequencies of about 0.6 Hz (mean value for M = 8.0 simulated event), 1.2 Hz, and 2.5 Hz (scaling factor = 4).

Columns 1 and 2 in Table 8.4 show the applied initial effective stresses at the top and the lateral boundary of the chamber, respectively, for the two boundary conditions. σ'_v refers to the applied vertical effective stress. σ'_h refers to the applied lateral effective stress. An interpretation of the mean effective stress in the chamber, σ'_m, is made for tests conducted with a rigid lateral boundary for the sake of comparison of results with the tests conducted with isotropic stress condition, viz., SSB#3 and SSB#10. The computations for σ'_m for tests with rigid lateral boundary condition are presented in Appendix J and are summarized in the footnotes of Table 8.4.

179

Table 8.4: Summary of the Seaquake Tests

Test No.	Applied Vertical Effective Stress, kPa σ'_v	Initial Lateral Effective Stress, kPa σ'_h	Applied Biased Hydrostatic Pressure, p_s (kPa) amplitude	Applied Hydrody-namic Pressure, p_d (kPa) amplitude	Duration of Seaquake (secs)	Freq. of Hydrody-namic Pressure (Hz)
SSB#1	0	RIGID	42.83	38.27	20	2.5
SSB#2[a]	41.38	RIGID	43.00	42.04	20	2.5
SSB#3	17.24	17.24	31.03	30.34	25	2.5
SSB#4[b]	124.14	RIGID	37.24	33.52	9	2.5
SSB#5[b]	124.14	RIGID	39.62	20.28	20	2.5
SSB#6[b]	124.14	RIGID	37.24	14.23	20	10.0
SSB#7[b]	124.14	RIGID	39.31	30.62	20	5.0
SSB#8[b]	124.14	RIGID	53.79	49.65	20	2.5
SSB#9	0	RIGID	41.38	39.72	50	2.5
SSB#10	27.59	27.59	29.11	16.14	20	2.5

a - Mean effective stress in the chamber, $\sigma'_m = 20$ kPa

b - Mean effective stress in the chamber, $\sigma'_m = 56$ kPa

8.3.2 Mechanism of Pore Water Pressure Response

The seaquake tests consisted of imposing a periodic water pressure on the surface of the sand bed. The periodic water pressure was superimposed over a hydrostatic bias pressure applied on the sand surface. The hydrostatic pressure was gradually applied on the surface of the sand in stages. Measurements of the hydrostatic pressure applied on the sand surface were made, and the corresponding pore water pressures were measured at 1/3 and 2/3 of the depth of the sand bed (168 mm and 336 mm) in the chamber. A typical record is shown in Fig. 8.1. Figure 8.2 shows a typical example of the seaquake-associated seabed pressure and the oscillatory pore pressures recorded at the 1/3rd and 2/3rd depths in the chamber. Snapshot measurements of these pressures after approximately 35 cycles of loading in Fig. 8.3 clearly show that the amplitude of the seaquake-associated bottom pressure, p_d, attenuates from 20.28 kPa to about 13.79 kPa with depth. Additionally, the peak value of the pore water pressure generated in the soil
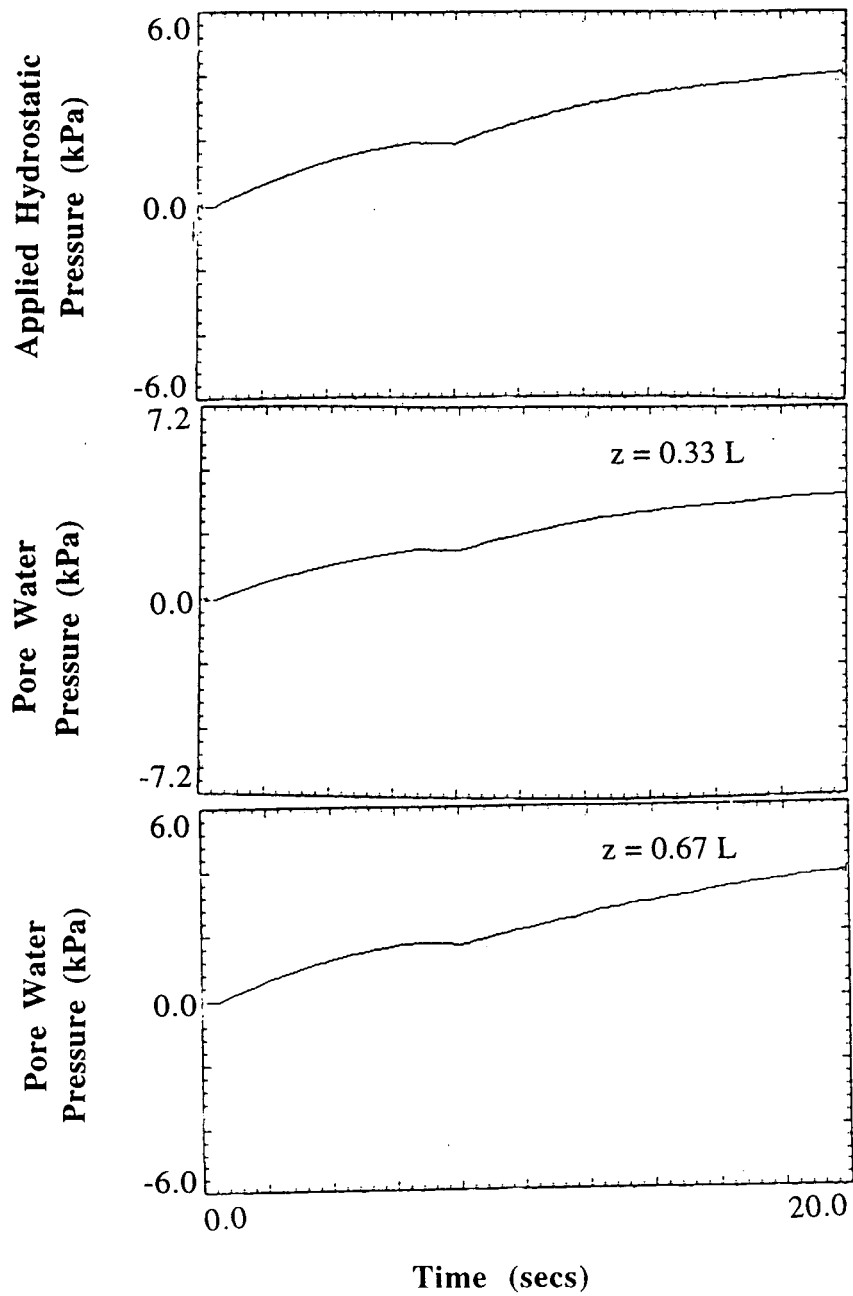
180

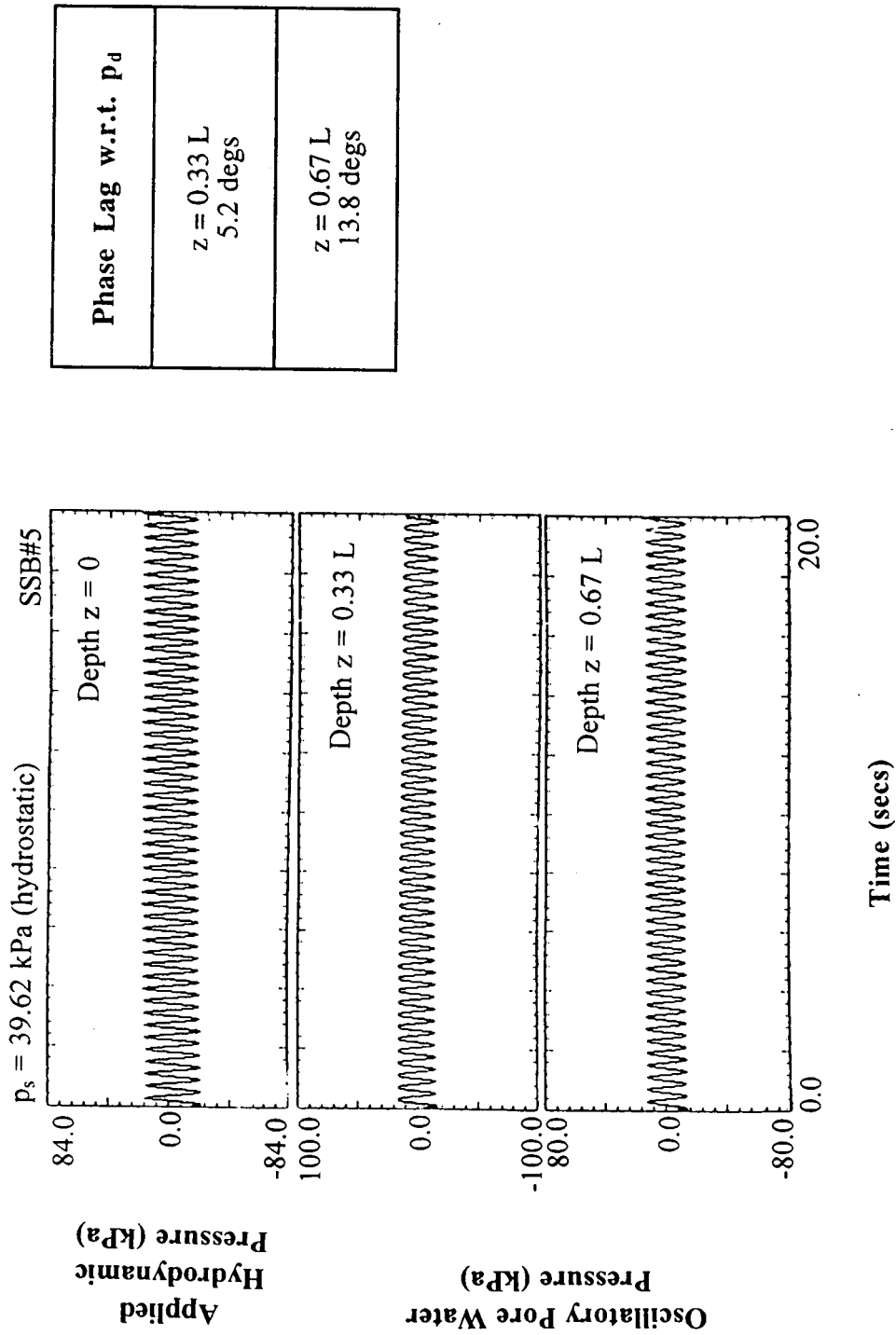**Fig. 8.1 : Pore Water Pressures Measured in the Soil Mass During Application of Hydrostatic Pressure**

181

Phase Lag w.r.t. p_d

z = 0.33 L 5.2 degs	
z = 0.67 L 13.8 degs	

SSB#5

Depth z = 0

p_s = 39.62 kPa (hydrostatic)

Depth z = 0.33 L

Depth z = 0.67 L

84.0
0.0
-84.0

100.0
0.0
-100.0

80.0
0.0
-80.0

0.0

20.0

Time (secs)

Applied Hydrodynamic Pressure (kPa)

Oscillatory Pore Water Pressure (kPa)

Fig. 8.2: Pore Water Pressure Response During Seaquakes - SSB#5 (Rigid Lateral Boundary, σ'_v = 124.14 kPa)

mass shifts to the right, indicating a phase lag between the applied hydrodynamic pressure and the oscillatory pore water pressure. Illustration of phase lag between the applied hydrodynamic presure and the measured pore water pressure at $z = 0.67$ L in the soil mass for test SSB#5 is shown in Fig. 8.4. Results for representative tests are shown here and similar measurements taken for other tests are included in Appendix K. The effects of various parameters on the phenomenon of propagation of seaquake-induced pore water pressure during the simulated seismic events of M = 8.0 are discussed below.

8.3.2.1   Effect of Number of Cycles of Seaquake Loading

The pore water pressure response measured in the soil mass during seaquake loading for a duration of 50 sec is shown in Fig. 8.5 for a test condition with 2.5 Hz excitation frequency and a rigid lateral boundary condition. The comparision of the measurements of the applied seaquake-associated hydrodynamic pressure and the pore water pressures in the soil mass taken after 10 and 100 cycles of loading is made in Fig. 8.6. Figure 8.7 shows the effect of number of cycles of seaquake loading on the variation of pressure ratio for different tests, i.e., oscillatory pore water pressure amplitude, p_m normalized by the amplitude of the seabed pressure, p_d. It is clear from the measurements that the number of cycles of loading had very little influence on the degree of attenuation. It should be noted that the phase lag in Fig. 8.6 is about 0.02 secs which is not clearly obvious because of the time scale used

The experimental results were verified for tests SSB#5, SSB#6 and SSB#7 using (7.45) to predict the pore water pressure response in the soil column due to seaquake-associated seabed pressure. All the three tests were conducted under σ'_v of 124.14 kPa with rigid lateral boundary. The following properties of the soil were used.

$k = 3 \times 10^{-4}$ m/sec, n = 0.39 and $m_v = 0.00002$ m^2/ kN
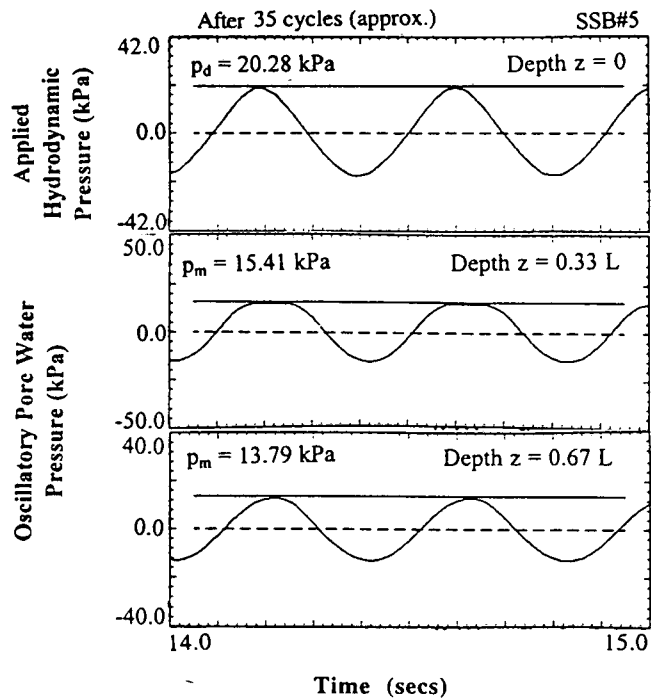
Fig. 8.3: Seaquake-Associated Seabed Pressure and Oscillatory Water Pressure in the Soil Mass - SSB#5 (Rigid Lateral Boundary, σ'_v = 124.14 kPa)
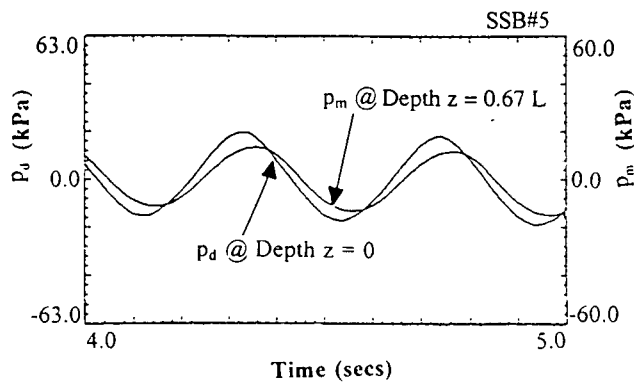

Fig. 8.4: Illustration of Phase Lag Between Seaquake Associated Seabed Pressure and Measured Pore Water Pressure at z = 0.67L in the Soil Mass - SSB#5 (Rigid Lateral Boundary, σ'_v = 124.14 kPa)
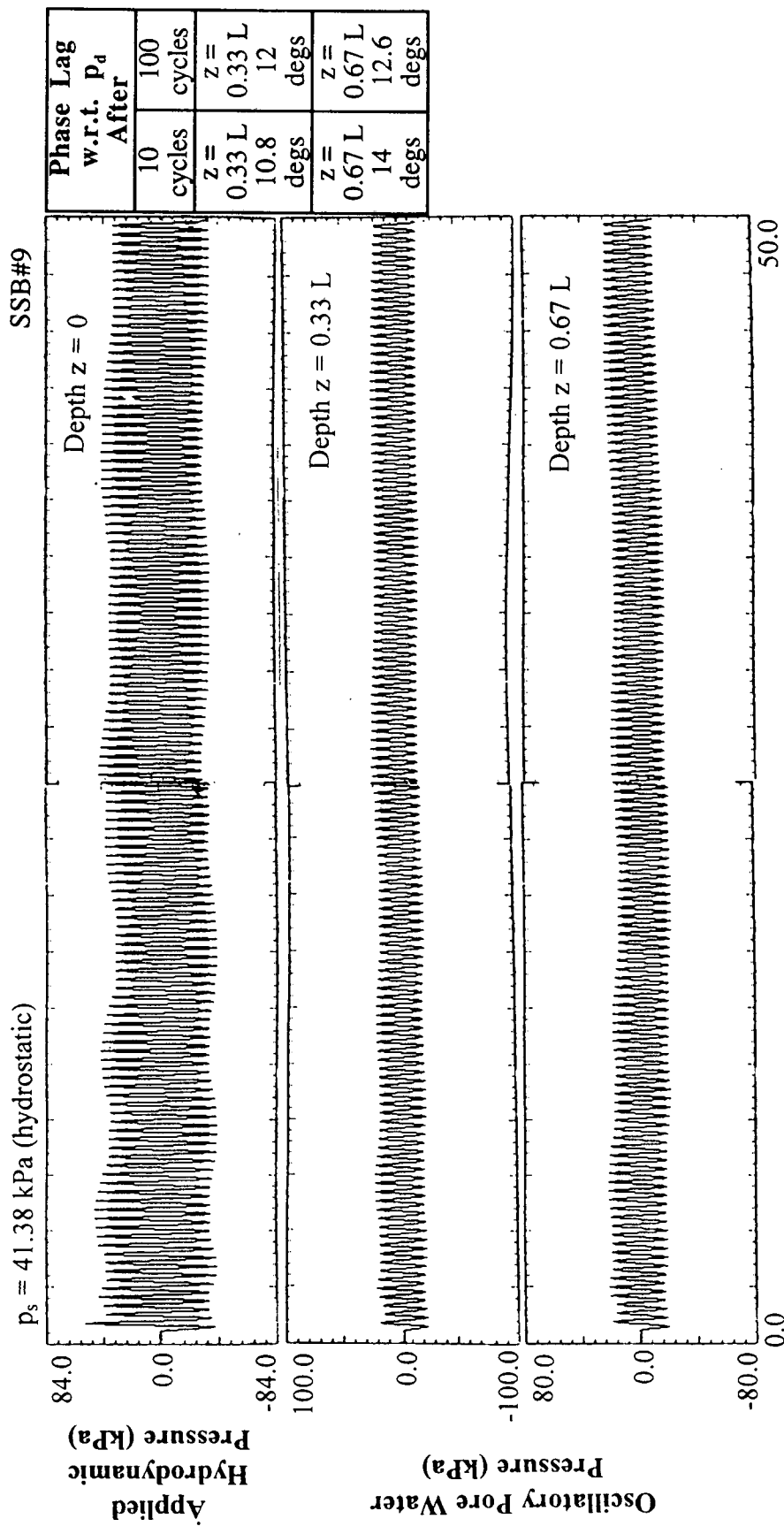
184

Phase Lag w.r.t. p_d After	
10 cycles	100 cycles
z = 0.33 L 10.8 degs	z = 0.33 L 12 degs
z = 0.67 L 14 degs	z = 0.67 L 12.6 degs

SSB#9

p_s = 41.38 kPa (hydrostatic)

Depth z = 0

Depth z = 0.33 L

Depth z = 0.67 L

Applied Hydrodynamic Pressure (kPa)

84.0
0.0
-84.0

Oscillatory Pore Water Pressure (kPa)

100.0
0.0
-100.0

80.0
0.0
-80.0

Time (secs)

0.0
50.0

Fig. 8.5: Pore Water Pressure Response During Seaquakes - SSB#9
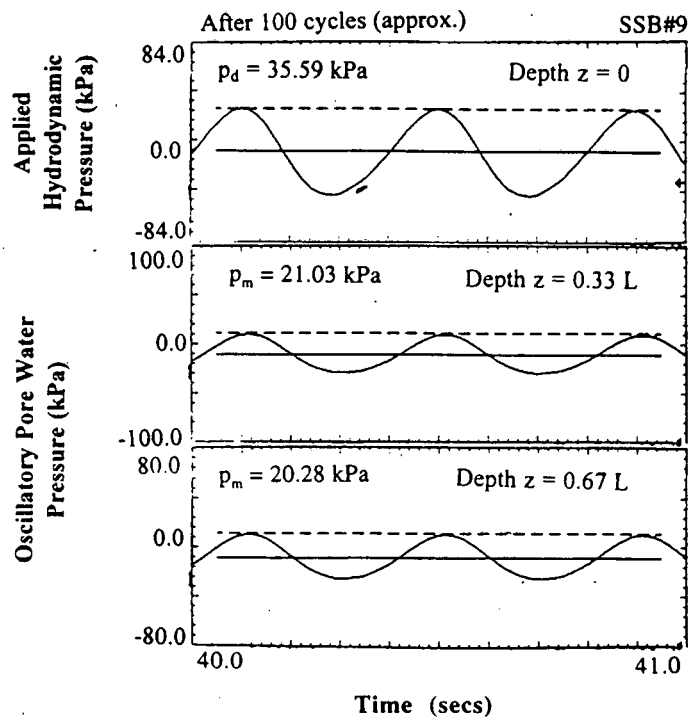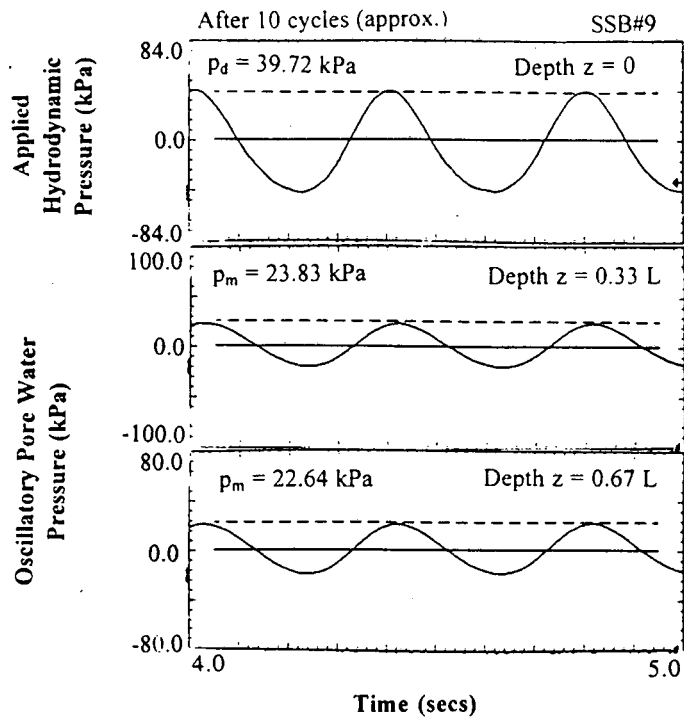
Fig. 8.6: Variation of Seaquake Associated Seabed Pressure with Number of Cycles of Loading (a) After 10 cycles and (b) After 100 cycles, SSB#9
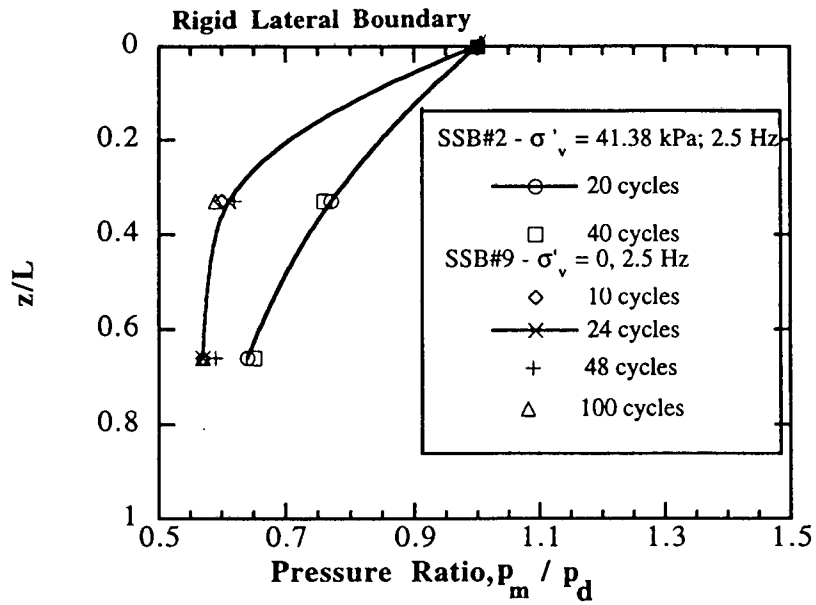
Fig. 8.7: Variation of Pressure Ratio with Number of Cycles of Seaquake Loading for a Rigid Boundary Test Condition

The values of C and α used in the calculations are shown in Table 8.5, and the predicted peak pore water pressure ratios in the soil mass at depths of L/3 and 2L/3 and their phase lags with the applied hydrodynamic pressures are tabulated in Table 8.6. Corresponding measured values are also shown. Typical pore water pressure response predicted for test SSB#5 is shown in Fig. 8.8.

Qualitatively, the predicted peak pore water pressure responses were in close agreement with the measured ratios, i.e., with increase in frequency, the seaquake associated hydrodynamic pressure is propagated into the soil with greater attenuation. An absolute match was not observed between the predicted and the measured results. This may be due to a combination of factors, viz., the error associated with the approximation in the degree of saturation, and the assumptions in the theory, such as elastic response of the soil and neglect of the shear stress along the wall of the chamber during seaquake loading. It is especially significant to note that the phase lag in pore pressure appears not to be

187

associated with p-wave propagation in the pore water, which will lead to almost infinitesimal phase angles for these tests.

Table 8.5: C and α Values

Test No.*	Applied Vertical Effective Stress (kPa) σ'_v	Hydrodynamic Pressure Frequency (Hz)	Lateral Boundary Condition	C	α
SSB#5	124.14	2.5	RIGID	2.3	2.5
SSB#6	124.14	10.0	RIGID	0.58	2.5
SSB#7	124.14	5.0	RIGID	1.15	2.5

*Applied lateral effective stress, $\sigma'_h = 0$

Table 8.6: Predicted Vs. Measured Values of Pore Water Pressure Response

Test No.	Predicted Values				Measured Values			
	0.33L		0.67L		0.33L		0.67L	
	P_m / P_d	Phase Lag (degs)	P_m / P_d	Phase Lag (degs)	P_m / P_d	Phase Lag	P_m / P_d	Phase Lag (degs)
SSB#5	0.70	15.84	0.50	25.2	0.71	5.2	0.69	13.8
SSB#6	0.52	20.16	0.37	3.96	0.32	28.0	0.29	11.5
SSB#7	0.60	18.00	0.40	13.68	0.51	27.0	0.48	27.0

8.3.2.2 Effect of Applied Effective Stress in the Soil

Figures 8.9 and 8.10 demonstrate the variation of pressure ratio as a function of applied vertical effective stress, σ'_v for a rigid lateral boundary condition and as a function of isotropically applied effective stress, ($\sigma'_v = \sigma'_h$) for a controlled stress lateral boundary, respectively. Typically, the pressure at $z/L = 0.67$ ranged from 60% to 80% of the applied hydrodynamic pressure on the seabed for the rigid lateral boundary tests and was about 90% for the flexible lateral boundary (Figs. 8.11 through 8.15). The pressure ratios varied within a narrow range with the applied initial vertical effective stress for the rigid lateral boundary conditions but did not suggest any definitive trends. Thus, it can be said that the
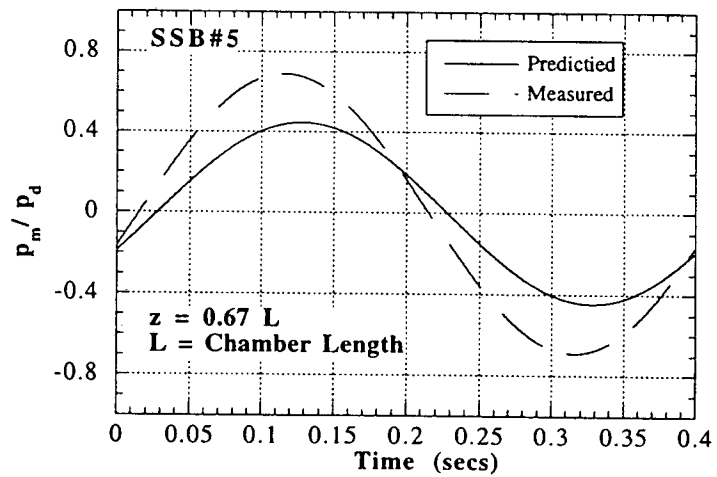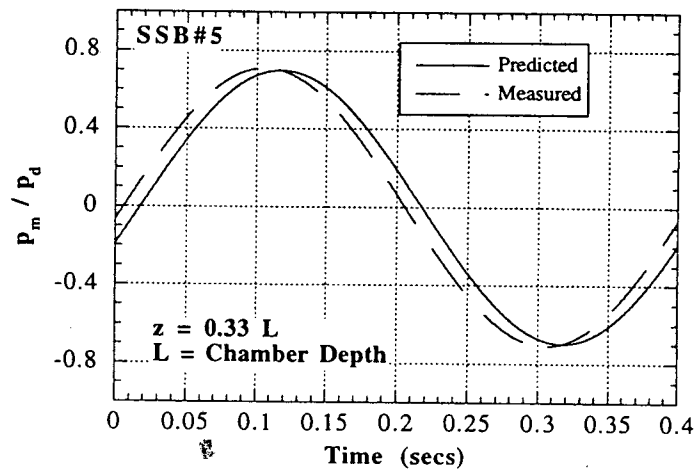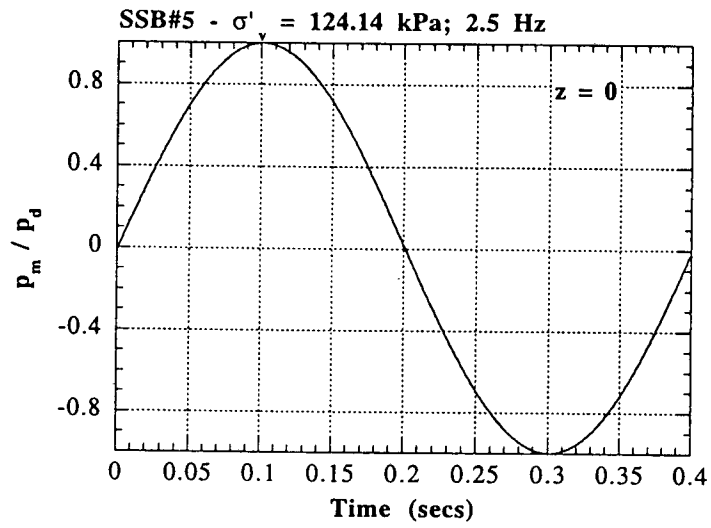
Fig. 8.8: Predicted and Measured Pore Water Pressure During Seaquake Loading
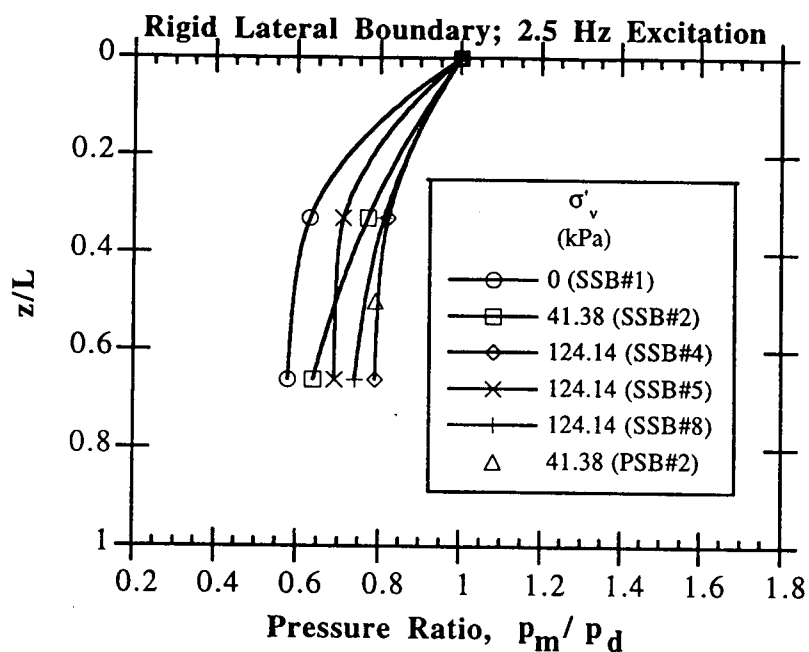
Fig. 8.9: Pressure Ratio as a Function of Initial Vertical Effective Stress for a Rigid Boundary
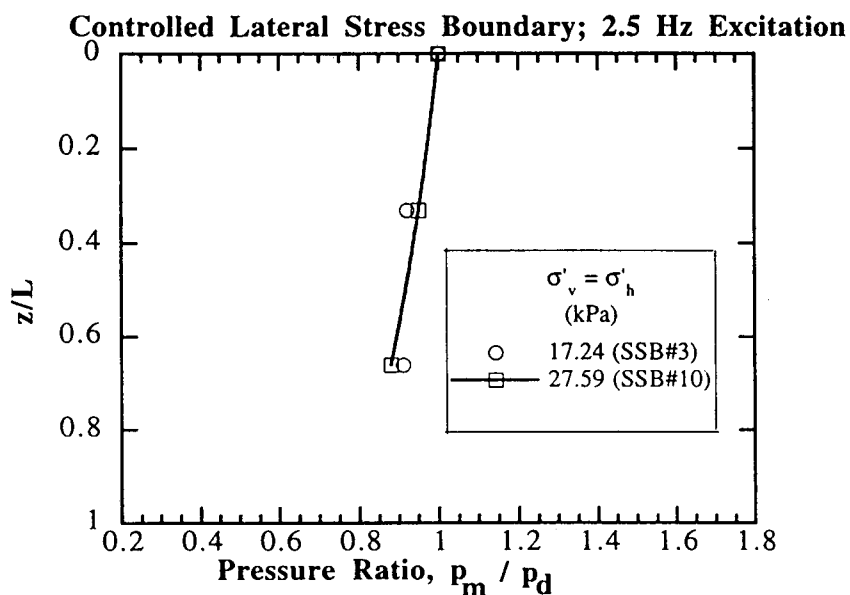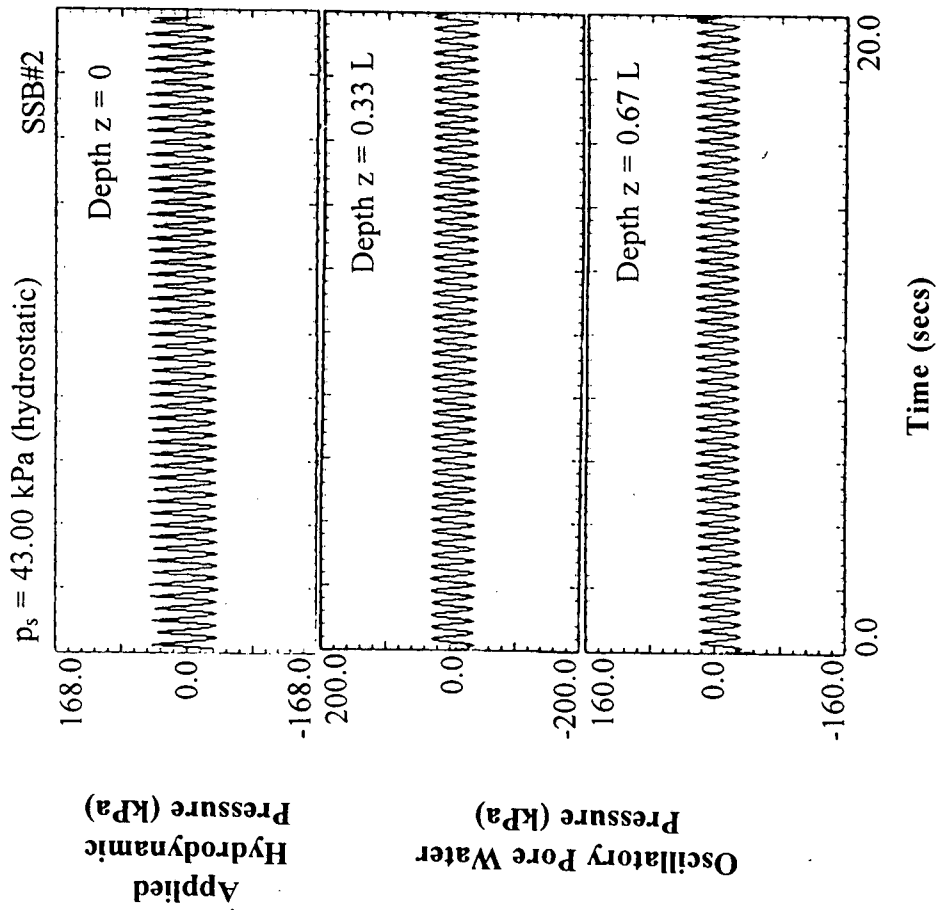

Fig. 8.10: Pressure Ratio as a Function of Initial Mean Effective Stress for a Controlled Lateral Stress Boundary

Phase Lag w.r.t. p_d After			
20 cycles		40 cycles	
z = 0.33 L	4.2 degs.	z = 0.33 L	12.85 degs
z = 0.67 L	12.0 degs	z = 0.67 L	17.14 degs

SSB#2

p_s = 43.00 kPa (hydrostatic)

Depth z = 0

Depth z = 0.33 L

Depth z = 0.67 L

Applied Hydrodynamic Pressure (kPa)

Oscillatory Pore Water Pressure (kPa)

Time (secs)

Fig. 8.11: Pore Water Pressure Response During Seaquakes - SSB#2 (Rigid Lateral Boundary, σ'_v = 41.38 kPa)
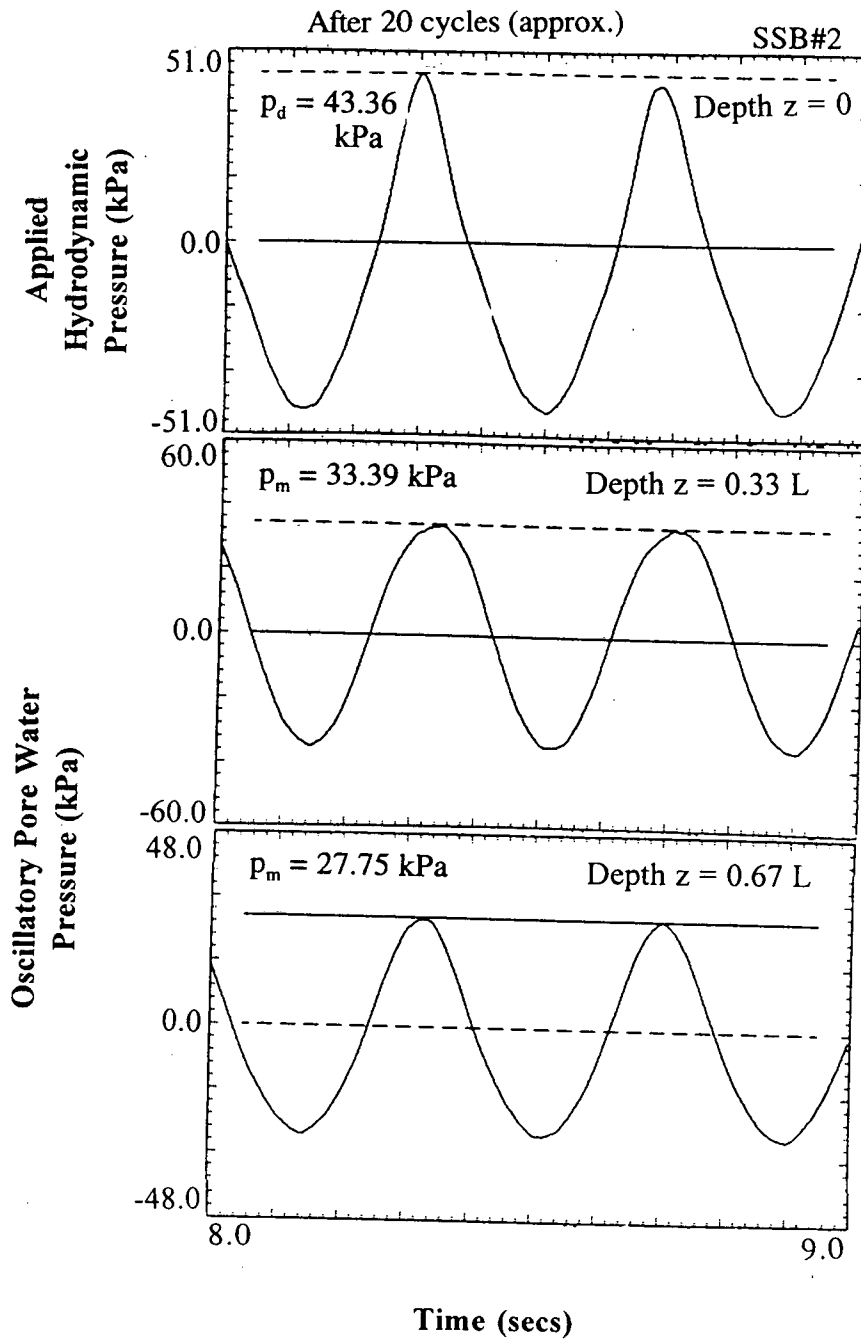
Fig. 8.12: Seaquake-Associated Seabed Pressure and Oscillatory Water Pressure in the Soil Mass - SSB#2 (Rigid Lateral Boundary, σ'_v = 41.38 kPa)
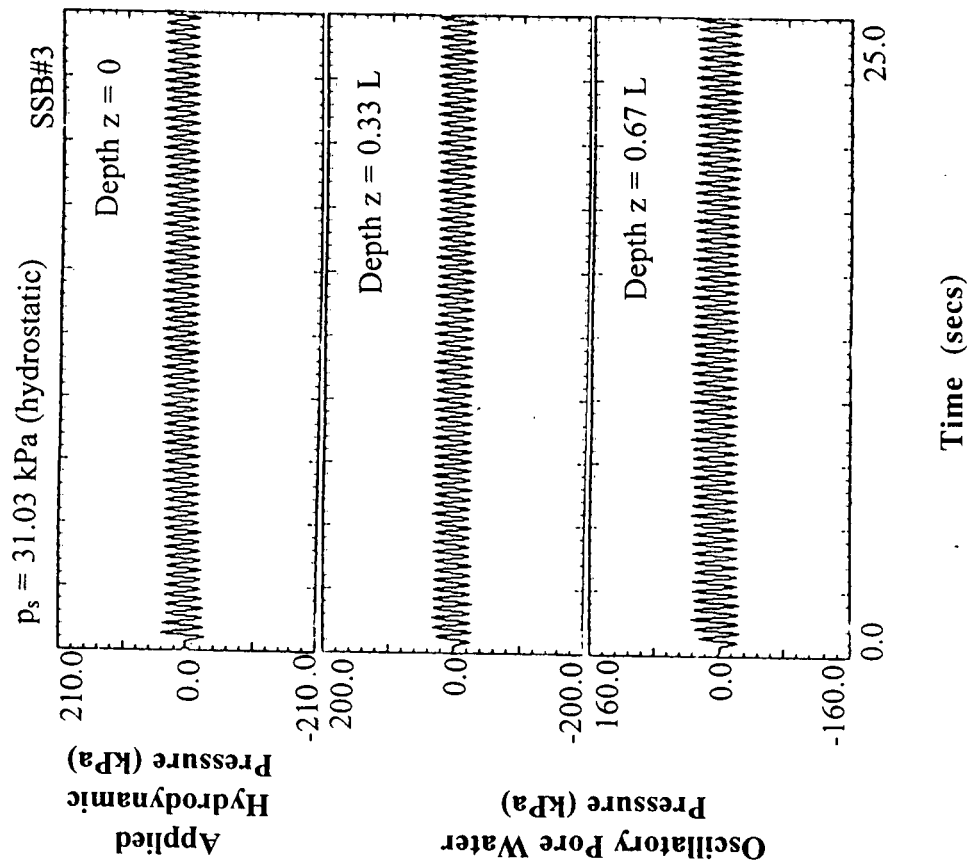
Fig. 8.13: Pore Water Pressure Response During Seaquakes - SSB#3
(Flexible Boundary, $\sigma'_v = \sigma'_h = 17.24$ kPa)
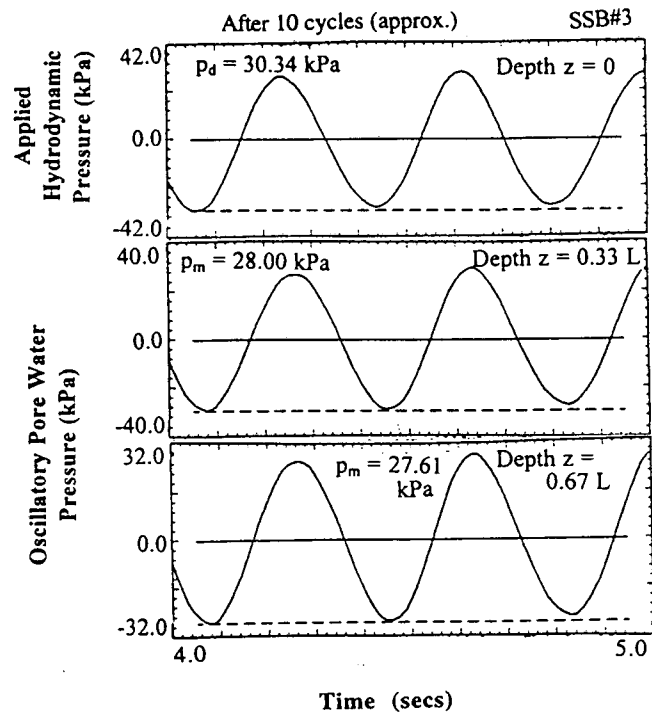
Fig. 8.14: Seaquake-Associated Seabed Pressure and Oscillatory Water Pressure in the Soil Mass - SSB#3 (Flexible Boundary, $\sigma'_v = \sigma'_h = 17.24$ kPa)
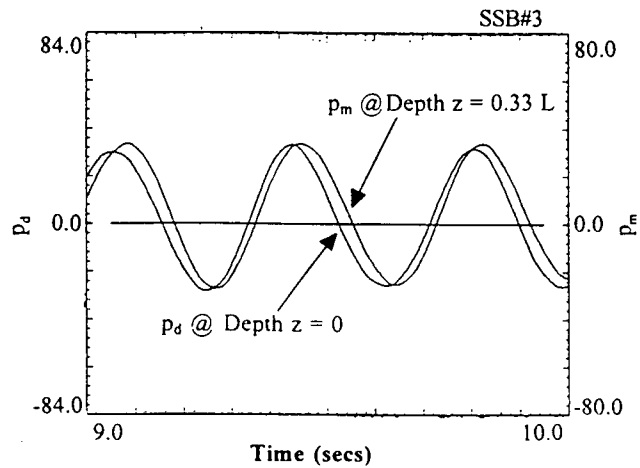
Fig. 8.15: Illustration of Phase Lag Between Seaquake Associated Seabed Pressure and Measured Pore Water Pressure at z = 0.33L in the Soil Mass - SSB#3 (Flexible Boundary, $\sigma'_v = \sigma'_h = 17.24$ kPa)

194

initial applied effective stress in the soil did not have any distinct impact on the degree of attenuation for either type of boundary conditions. However, the flexible lateral boundary consistently generated higher pressure ratios than the rigid lateral boundary. Therefore, it can be inferred that the compressibility of the soil skeleton may have some impact on the degree of attenuation since the flexible boundary allows for more compression in the soil during application of hydrodynamic pressure than a rigid boundary. No definitive correlation could be established between the phase lag and the initial effective stress condition of the sand. The phase lag of the measured pore water pressure at any point and the applied hydrodynamic seabed pressure generally increased with depth for a rigid lateral boundary test condtion with excitation frequency of 2.5 Hz, and typically the phase lag measured at z/L = 0.67 in the soil mass was within a narrow band ranging from 18 degrees to 24 degrees for these tests (Fig. 8.16). For tests conducted at higher frequencies no clear pattern of the phase lag variation with depth could be observed. Generally, the phase lag measured at z/L = 0.67 in the soil mass increased with frequency.
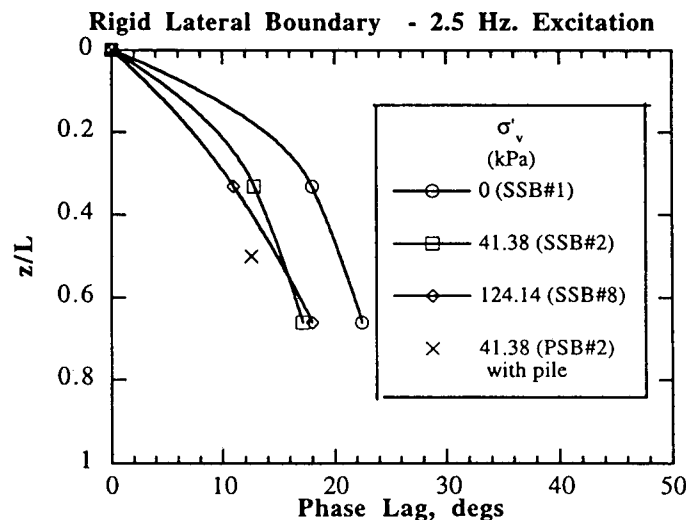
Fig. 8.16: Phase Lag as a Function of Initial Vertical
Effective Stress for a Rigid Lateral Boundary

8.3.2.3 Effect of Predominant Frequency of Excitation

The predominant frequency of vertical excitation was the most obvious factor that correlated to attenuation and phase lag of the oscillatory pore water pressure in the seabed as seen in Figs. 8.2, 8.3 (frequency of excitation of 2.5 Hz) and Figs. 8.17, 8.18 (frequency of excitation of 10 Hz). Doubling the frequency from 2.5 Hz to 5.0 Hz increased the attenuation by about 30%, and increasing the frequency from 5 to 10 Hz increased the attenuation further by about 40% (Fig. 8.19).

8.3.2.4 Effective Stress Oscillation

The effective stress in underwater deposits of the soil is held constant if the external water level, and the consequent total stress, is changed slowly. However, as evident from the preceding section, this is not true when the boundary water pressure varies so quickly that the change of water pressure on the surface of the deposit is not experienced uniformly throughout the deposit. This introduces a change in the effective stress in the soil during seaquake loading. At any given point in the soil mass, the change in the effective stress must be equal to the difference between the applied hydrodynamic pressure, P_d and the measured pore water pressure, P_m in the soil mass, discounting inertial effects and assuming no side wall shear effects. This difference represents the excess pore water pressure in the soil mass. Since the applied seaquake loading is periodic in nature, the induced excess pore water pressure component is also periodic. If the excess water pressure reaches or exceeds the ambient effective stress in the soil mass, the soil skeleton will instantaneously assume a liquefied state at that point. Conversely, if the excess pore pressures become less than the ambient effective stress in the soil mass, the vertical effective stress at that point attains values greater than on the surface. The increase in effective stress exerts compressive forces on the soil skeleton that can potentially densify the sand. The excess pore water component for Test SSB#2, conducted at a frequency of 2.5 Hz, is shown in Fig.8.20 It is obvious that at times of 0.17 to 0.37 sec after the start
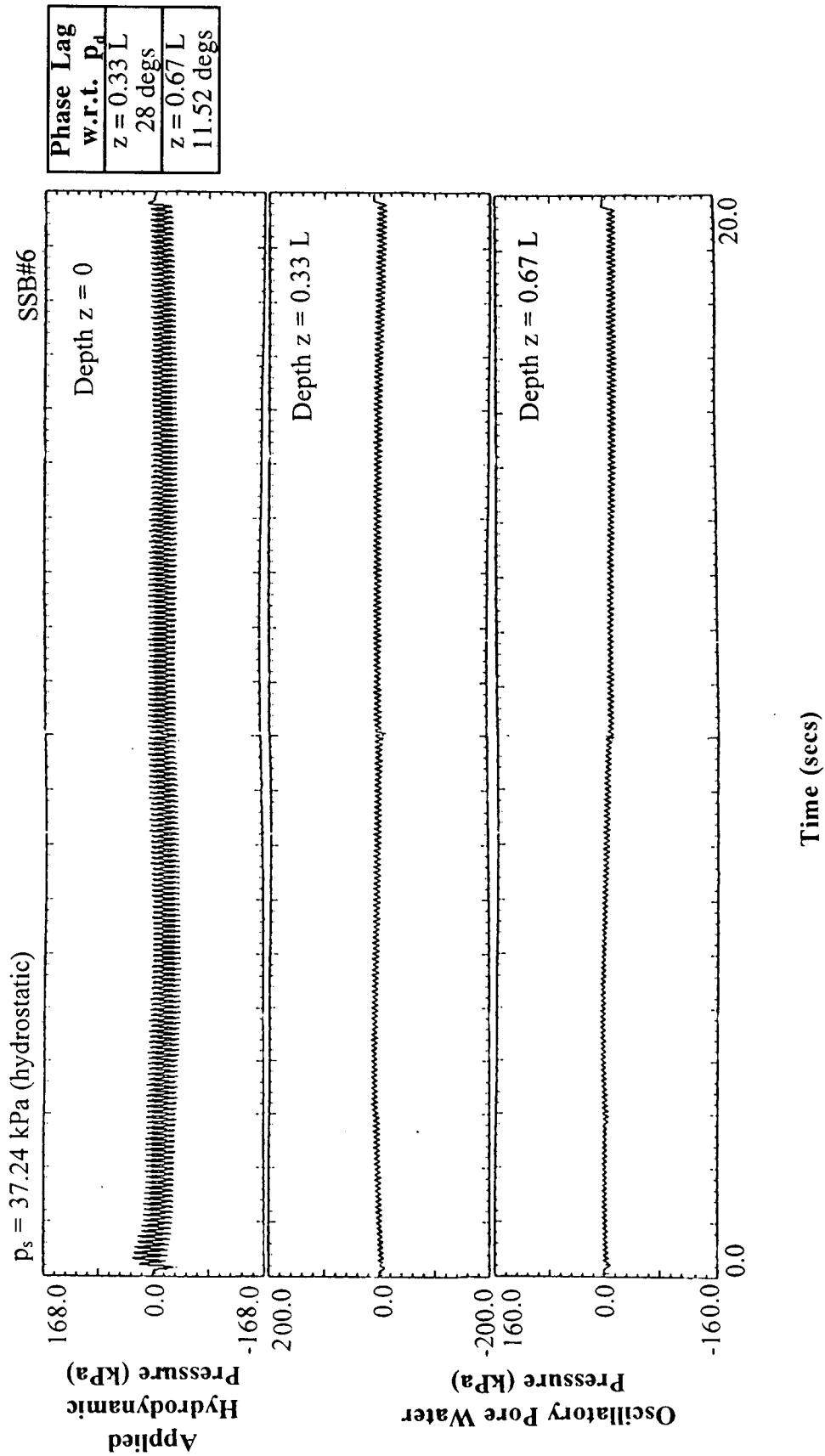
Fig. 8.17: Pore Water Pressure Response During Seaquakes - SSB#6
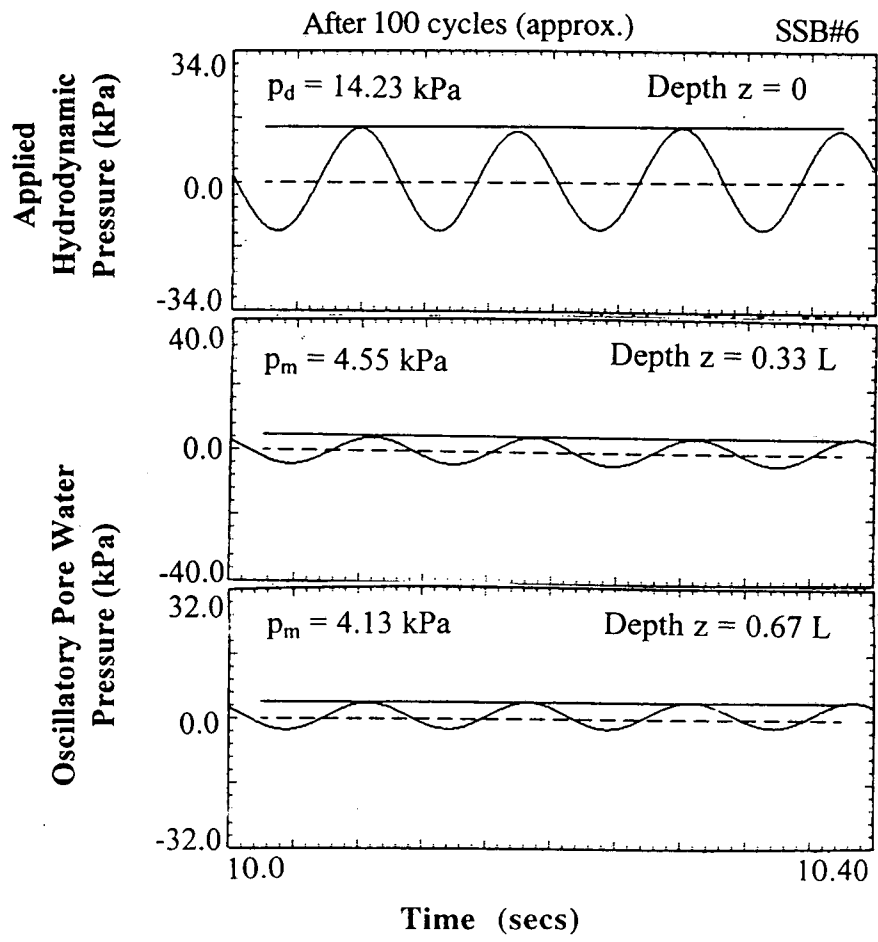(BC3, σ'_v = 124.14 kPa, Ω = 10 Hz)

197

Fig. 8.18: Seaquake-Associated Seabed Pressure and Oscillatory Water Pressure in the Soil Mass After 100 cycles - SSB#6 (BC3, σ'_v = 124.14 kPa, Ω = 10 Hz)
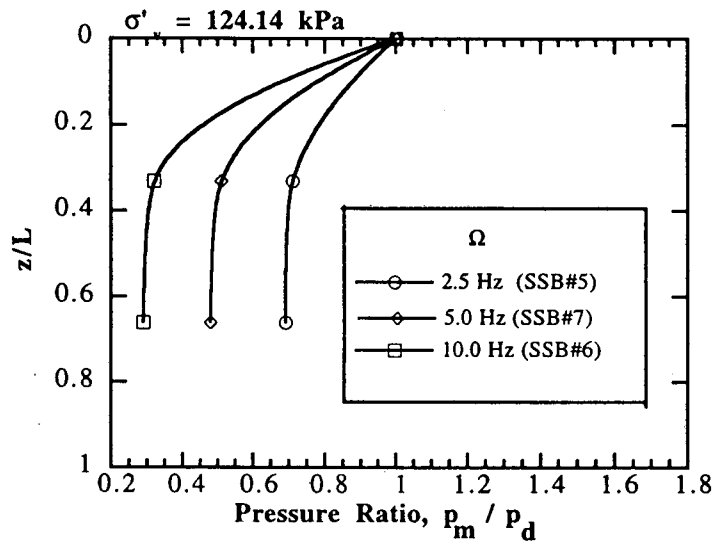
198

Fig. 8.19: Pressure Ratio as a Function of Frequency of Excitation for a Rigid Lateral Boundary Condition
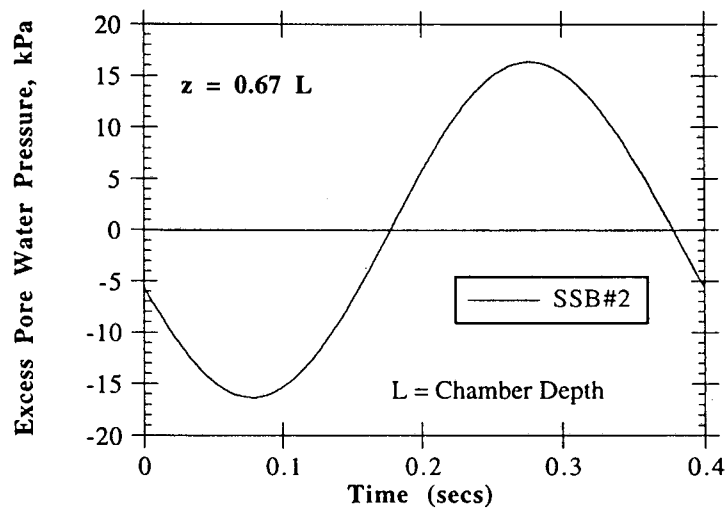

Fig. 8.20: Excess Pore Water Pressure Variation During Seaquake Loading - SSB#2

Fig. 8.21: Soil Surface After the Seaquake Loading in Test SSB#2

of a given loading cycle, a decrease in effective stress can be expected and an increase in effective stress will occur in the time domain outside of the above range. The peak positive excess pore water pressure was about 71% of the initial interpretated mean effective stress, σ'_m of 20 kPa, therefore, a degradation in shear strength of about 71% could be expected instantaneously at the indicated depth. Fig. 8.21 shows the sand surface in the chamber after Test SSB#2. Spots of fine sand can be seen on the surface which is indicative of the fact that instantaneous liquefaction may have occurred at some points in the chamber because of this phenomenon.

8.4 Axial Pile Behavior During Seaquake Loading of Seabed

8.4.1 Testing Summary

A summary of the pile-seabed interaction tests is presented in Table 8.7. Pile response to simulated seaquake loading for an M = 8.0 seismic event was studied for a rigid lateral boundary condition (BC3 i.e. $\sigma'_h = 0$) at different applied vertical effective stress, σ'_v ranging from 41.38 kPa to 303.45 kPa and under different bias loads levels varying from zero to 65% of the static capacity. The mean effective stress in the soil mass was interpreted using a procedure shown in Appendix J. The interpreted initial mean effective stress was 20 kPa for Tests PSB#2, PSB#3 which were conducted at an excitation frequency of 2.5 Hz. The interpreted initial mean effective stress, σ'_m was higher for Tests PSB#4, PSB#5, PSB#7, PSB#9, PSB#10, PSB#11, PSB#14 and PSB#15 and were conducted at an excitation frequency of 10 Hz to model the diffusion characteristics of the pore water pressure as explained in Section 8.2. The applied hydrodynamic pressure, pile-head load, pile-head movement and the pore water pressure were recorded during the seaquake loading and are also tabulated in Table 8.7. For piles that did not experience failure during the seaquake loading were loaded to failure to estimate the permanent loss in capacity. The results of the most relevant tests are discussed here, while the results of the remaining tests are attached in the Appendix L.

8.4.2 Pore Water Pressure Response During Driving

The pile was driven using the same technique as in the ground shaking tests. The pore water pressures measured during driving for typical tests are shown in Figs. 8.22 and 8.23. Unlike the pore pressures measured during the driving process for the ground shaking tests, where the pile was driven offset from the center, there was no residual build-up of pore water pressure as driving progressed. The magnitude of the peak value of the pore water pressure was about 10% of σ'_m , i.e., 20 kPa, for lower applied effective

201

Table 8.7: Summary of Pile-Seabed Interaction Tests

* Test No.	Interpreted Mean Effective Stress σ'_m (kPa)	Applied Bias Hydro-static Pressure (kPa)	Applied Hydro-dynamic Pressure Amp. (kPa)	Freq. of the Applied Hydro-dynamic Pressure (Hz)	Bias Load - % of Static Capacity	Pore Water Pressure Amplitude at Mid-depth (kPa)	Phase Lag (deg.)	Percent Loss in Capacity	No. of Blows per 25.4 mm during the final phase of driving	Net Pile Head Movement (mm)	Remarks
PSB#1	20	21.00	17.79	2.5	0	16.00 @ 0.33 L	12.0	NM	4.0	NM	-
PSB#2	20	31.03	28.97	2.5	46	22.97	13.0	100	4.0	Failure	within 2 secs
PSB#3	20	40.00	37.24	2.5	20	32.52	13.8	100	4.0	Failure	@8 secs
PSB#4	56	24.21	20.68	10.0	0	5.17	37.4	NM	8.0	+0.6	
PSB#5	112	24.97	16.55	10.0	0	4.80	57.0	NM	15.0	0	-
PSB#7	112	25.39	21.00	10.0	65	3.80	35.0	100	14.0	Failure	@ 6 secs
PSB#9	56	25.74	20.00	10.0	0	9.50	57.0	5	8.0	0	-
PSB#10	134	31.03	30.05	10.0	0	4.75	43.0	4	20.0	0	-
PSB#11	134	24.64	20.68	10.0	65	7.10	43.0	100	21.0	Failure	@ 9 secs
PSB#14	134	32.33	30.60	10.0	20	9.50	52.0	7	20.0	-0.6	-
PSB#15	134	32.00	20.68	10.0	40	4.75	42.0	20	21.0	-1.8	-

NM = Not Measured
* = Rigid Lateral Boundary (BC3)
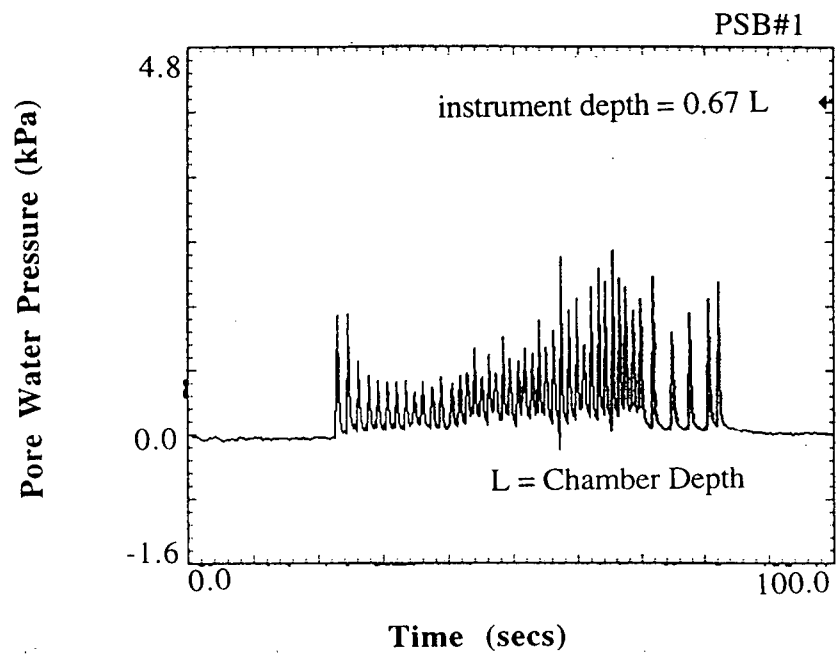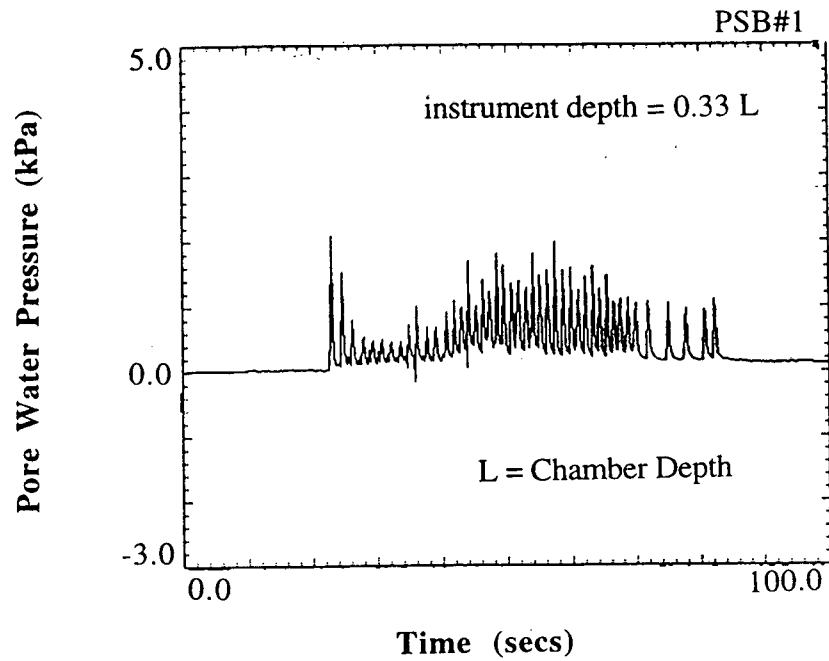
Fig. 8.22: Pore Water Pressures Measured During Pile Driving- PSB#1
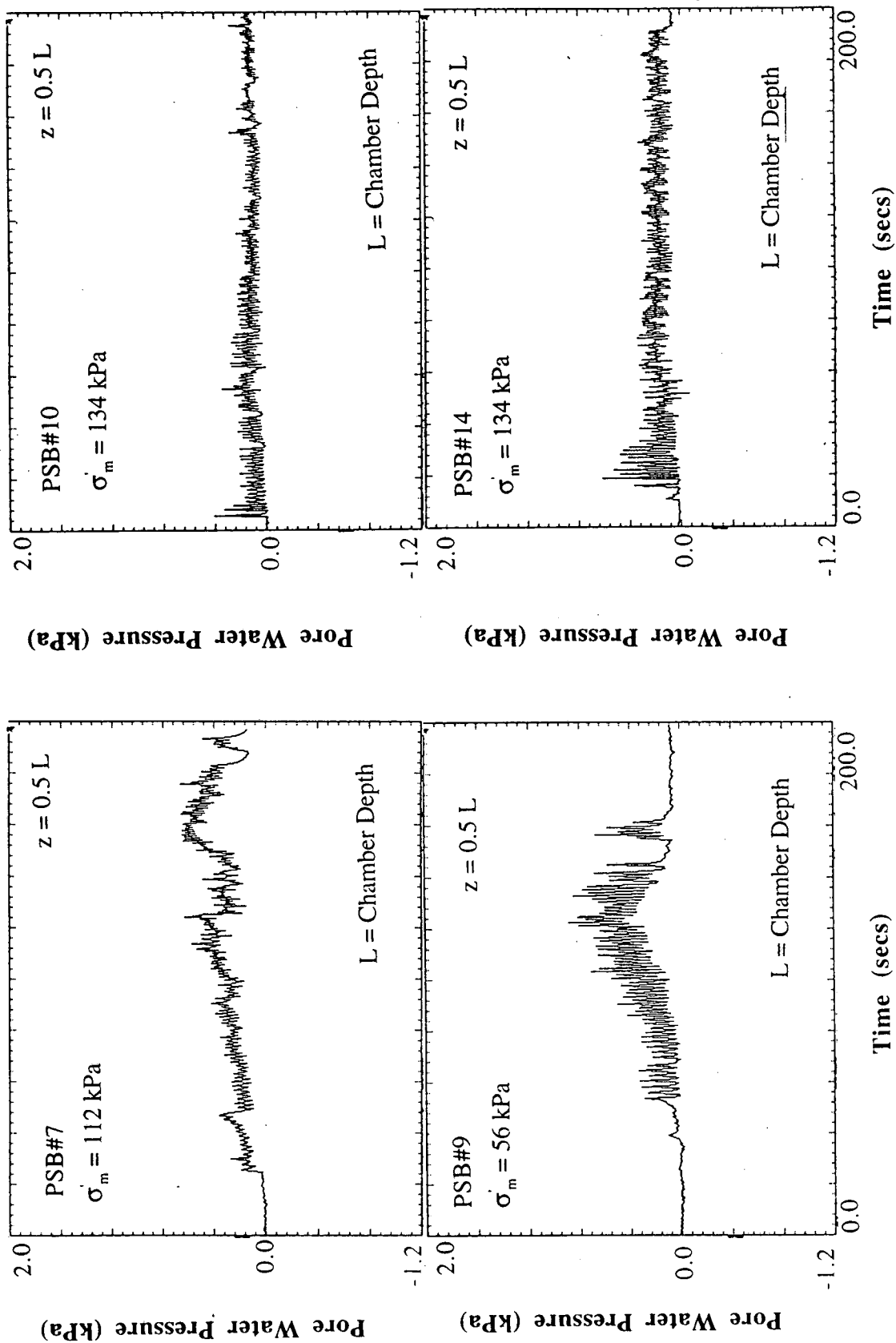
Fig. 8.23: Pore Water Pressures Measured During Pile Driving- PSB#7, PSB#9, PSB#10, PSB#4

stresses and decreased to 0.2% at σ'_m of 134 kPa. This suggests possible dilation of the sand due to increase in relative density under high confining stress.

8.4.3 Mechanism of Pile Response

Experiments were conducted at two sets of frequencies to model the diffusion characteristics of the pore water in the prototype condition. Tests conducted at σ'_m of 20 kPa and 2.5 Hz represented the top 4.5 m of a pile (approximately) and tests conducted at σ'_m of 134 kPa and 10 Hz represented a 36 m long pile. In both cases, the simulated seaquake loading generated oscillatory pore water pressure in the soil mass with almost the same degree of attenuation and phase lag as that observed in the case without the pile. The pore water pressures measured 25.4 mm from the pile at the mid-depth of the chamber are tabulated in Table 8.6. Unlike the ground shaking tests, the pore water pressures during the seaquake tests were much higher than those generated during pile driving.

The excess pore water pressure time histories computed from the applied hydrodynamic pressure and the pore water pressure response of the soil at mid-depth of the chamber are shown normalized by σ'_m in Figs 8.24 and 8.25 for tests conducted at excitation frequencies of 2.5 Hz and 10 Hz respectively. These figures clearly show that the peak value of the resulting excess pore water pressure time history at mid-depth of the chamber was about 45 to 50% of σ'_m for a test condition representing a 4.5 m long pile σ'_m = 20 kPa and 2.5 Hz excitation frequency) and 10% to 20% for higher values of σ'_m longer simulated piles up to 36 m in length. This suggests that the degradation in the soil strength per cycle of loading is higher in top 4.5 m and decreases for longer piles. The degradation indicated from these tests are conservative since the excitation frequency is limited to 10 Hz due to limitations in the testing machine and does not conform to the scaling rules. At frequencies higher than 10 Hz much lesser degradation can be expected.

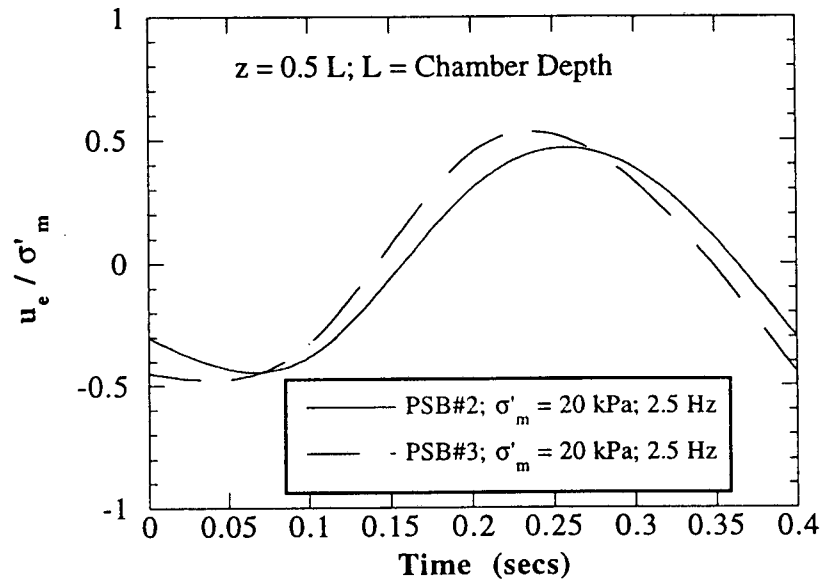In order to develop a better understanding of the axial response of a biased loaded

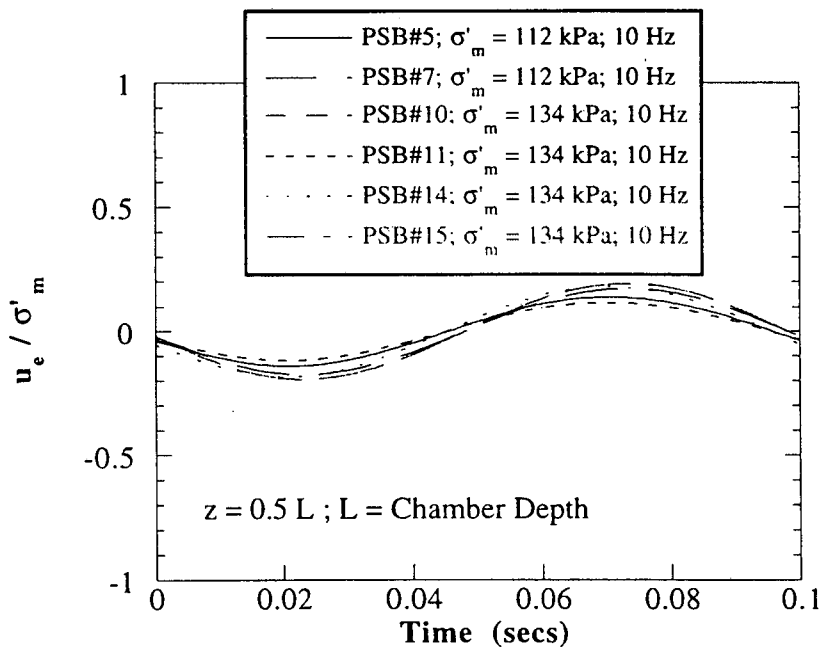**Fig. 8.24: Variation of Normalized Excess Pore Water Pressure with Time for Pile-Seabed Interaction Tests at σ'_m of 20 kPa**

Fig. 8.25: Variation of Normalized Excess Pore Water Pressure with Time for Tests Conducted at σ'_m Higher than 20 kPa

pile to seaquake loading, pile behavior in the absence of bias load was analyzed. The typical pile behavior in such a situation is illustrated in Fig. 8.26 for test PSB#10. Test PSB#10 represents a condition for a 36-m-long pile. The applied hydrodynamic pressure excites an oscillatory pore water pressure with an amplitude of 15% of the applied pressure which lags behind the applied surface pressure. As explained earlier, this establishes cycles of high and low excess pore water pressures in the soil mass. During the phase in a cycle of seaquake loading when low excess pore water pressure is established, the momentary increase in effective stress causes the soil to compress and to settle relative to the pile, which causes a slight downward shear stress on the pile, which in turn ultimately causes the pile to move downwards. Conversely, the external forces of the same nature act in the opposite direction on the pile when positive excess pore water pressures are established. Consequently, the pile ratchets upwards. This can be easily recognized from Fig. 8.27. The amplitude of the oscillatory pile movement observed in response to oscillations in the pile-head load and elastic response of the soil skeleton was about 0.22 mm. It is important to realize that there is very little net pile-head movement under no bias load and pile motion is primarily oscillatory. Similar observations were made during tests PSB#4, PSB#5, and PSB#9 at other confining stresses. The fluctuations in the pile-head load in these tests ranged from 5 N to 25 N.

In constrast , under biased tension loads as seen in Test PSB#2 (Fig. 8.28), the pile tends to ratchet upwards progressively during times when positive excess pore water pressure is established in every cycle of seaquake loading. Excursions in pile-head load occur as a result of inertial feedback from the superstructure represented by the spring mass system as well as the frictional resistance offered by the insert sleeve to the pile motion. In this particular case, the pile ultimately failed at about 1.5 sec after the start of the seaquake loading. Similar behavior was observed for biased-loaded tension piles when tested under different effective stresses. Results for PSB#3, conducted at $\sigma'_m = 20$ kPa and bias
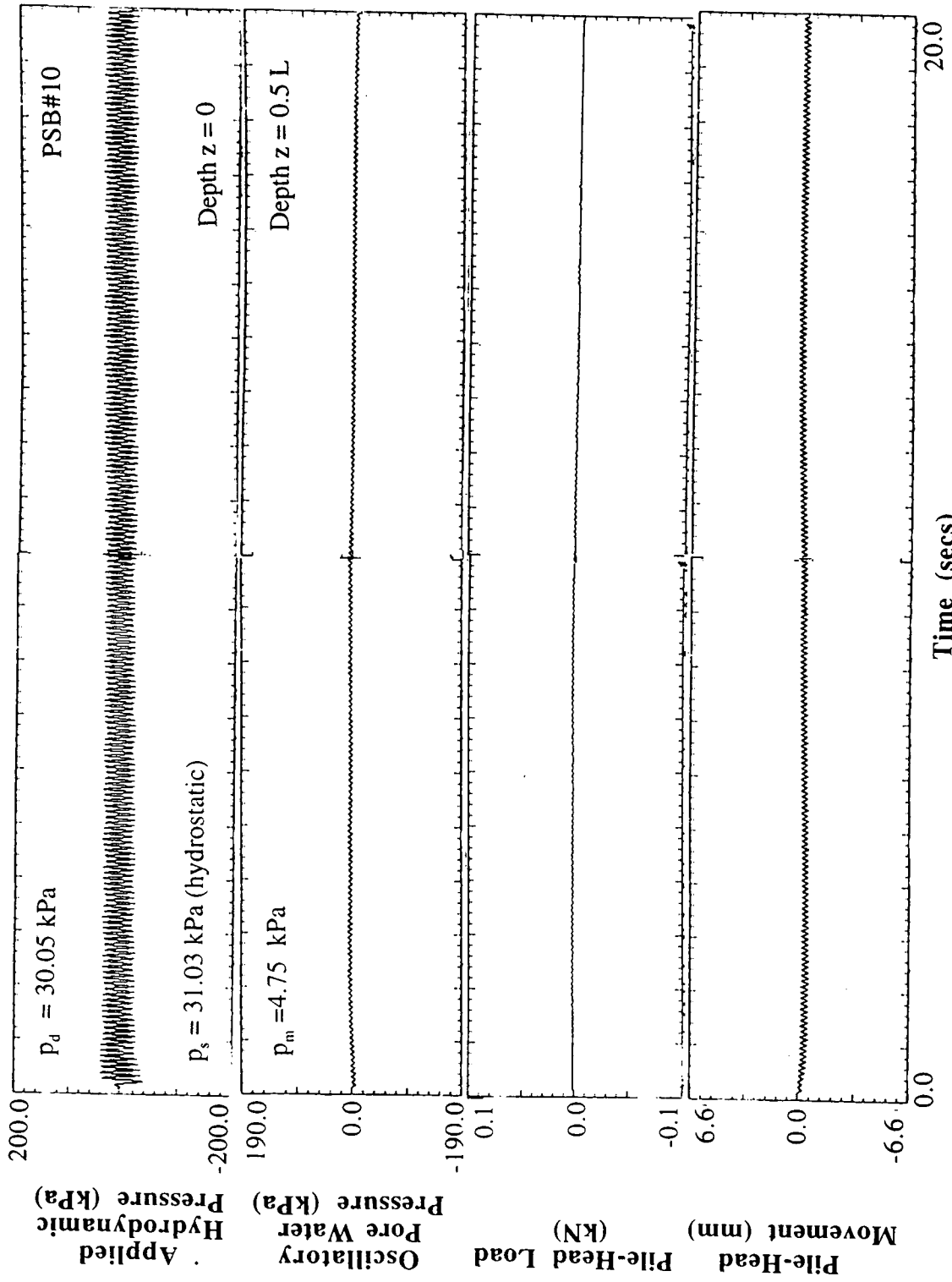
Fig. 8.26: Time History Measurements of Soil and Pile Response During Seaquake Loading Without Any Bias Load - PSB#10
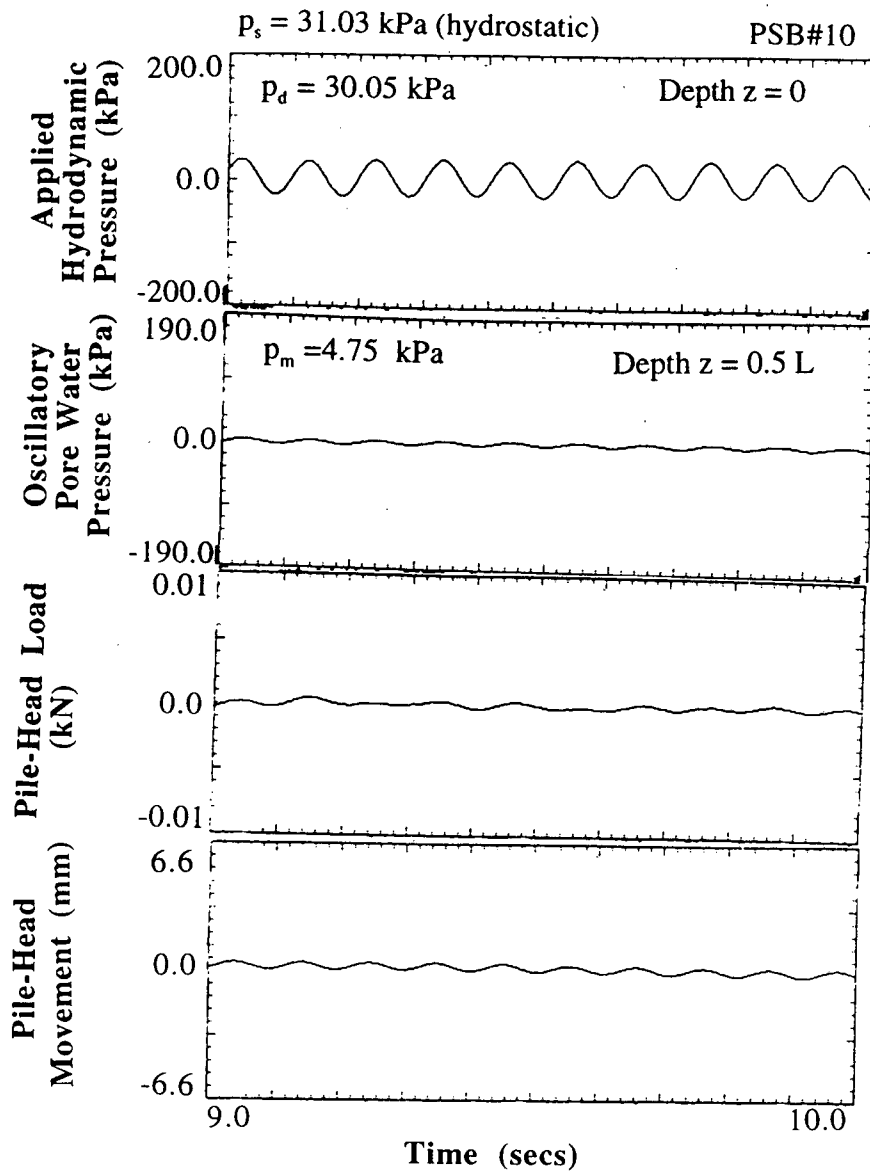
208

Fig. 8.27: Time Window Illustrating Mechanism of Pile Response During Seaquake Loading Without Bias Load - PSB#10

loading of 20%, and PSB#7, conducted at an initial effective stress of 112 kPa and bias loading of 65% are shown in Appendix L

From the above description of pile behavior, it is clear that the biased-loaded model piles, depending upon the duration of seaquake loading, will ultimately fail or experience complete extraction independent of the level of bias loading up to a scaled pile penetration of 36 m. The rate of extraction depends upon the level of bias loading, the ratio of the peak excess pore water pressure generated in the soil mass and the initial effective stress. From Figs 8.27 and 8.28 and Table 8.6, it is evident from the comparison of Tests PSB#2 and PSB#15 that for the same level of bias loading and different levels of initial effective stress, the rate of pile extraction was higher in Test PSB#2 which had a higher ratio of peak excess pore water pressure to σ'_m (0.50) as compared to Test PSB#15 (0.20). In fact, complete pile failure was observed in the former test, while the pile demonstrated mobility with sustained bias loading but did not fail in the latter test during the seaquake loading .

For tests conducted at σ'_m of 134 kPa and 10 Hz., for generally the same ratio of excess pore water pressure and σ'_m, the rate of pile extraction increased with increase in bias loading (Figs. 8.28, 8.29 and 8.30), ultimately leading to failure at 65% bias loading

In summary any safety criteria must consider the following:
i) The duration of the seaquake loading
ii) The amplitude of the applied hydrodynamic pressure
iii) The magnitude of the peak excess pore water pressure generated in the soil mass, which depends upon the frequency of excitation and the compressibility of soil solid-pore water system.

8.4.4   Suggested Degradation Factors

Based on the summary of the pile response results for a M = 8.0 simulated seaquake loading in deep water (depth = 200 - 300 m), it is seen that for σ'_m of 20 kPa,
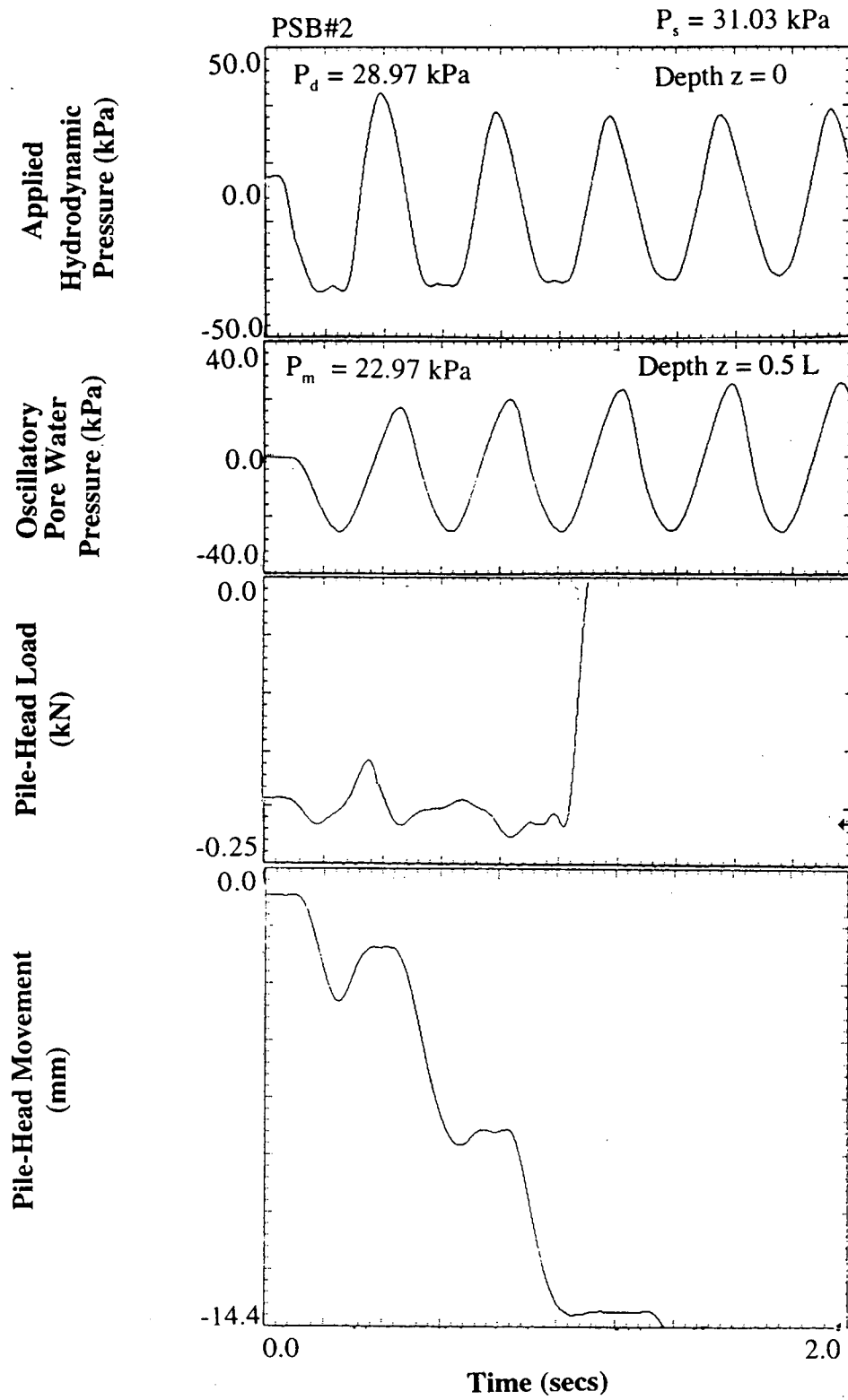
Fig. 8.28: Time History Measurements of Soil and Pile Response During Seaquake Loading with 46% Bias Loading at $\sigma'_m = 20$ kPa - PSB#2
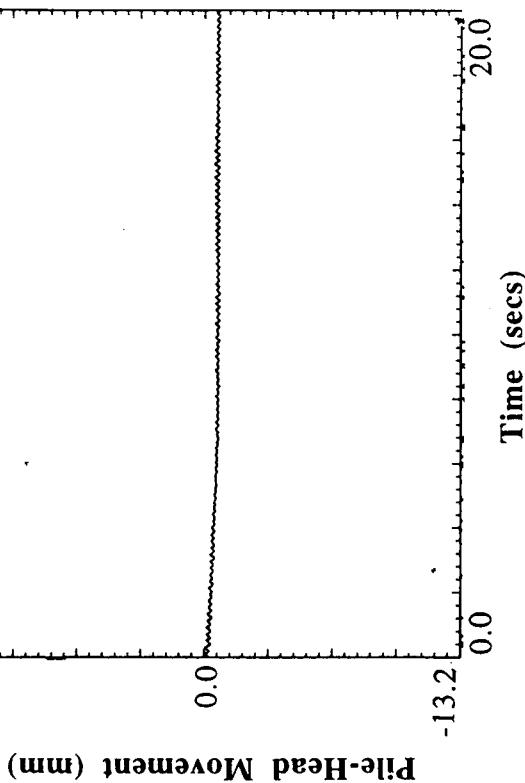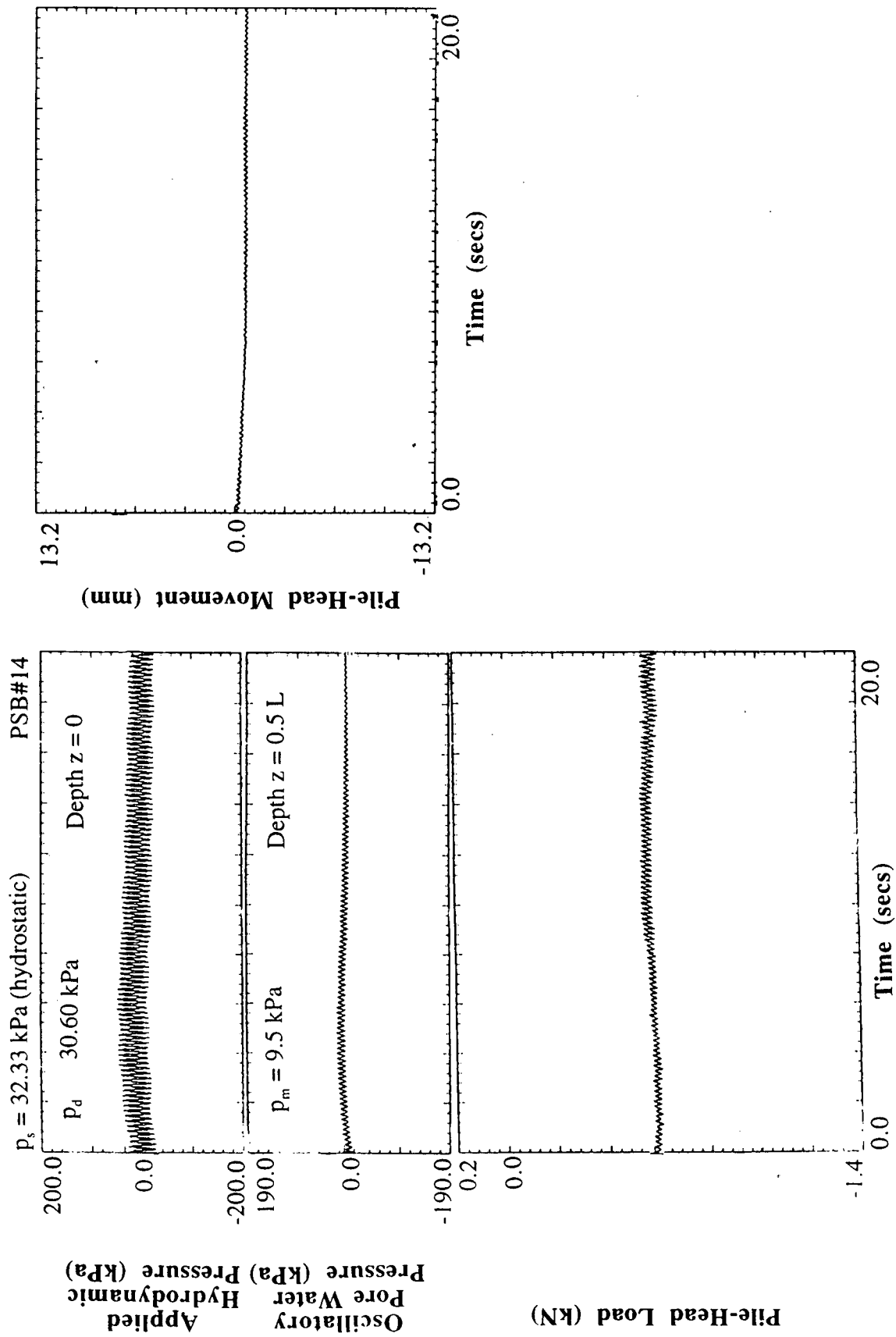
Fig. 8.29: Time History Measurements of Soil and Pile Response During Seaquake Loading with 20% Bias Loading at $\sigma'_m = 134$ kPa
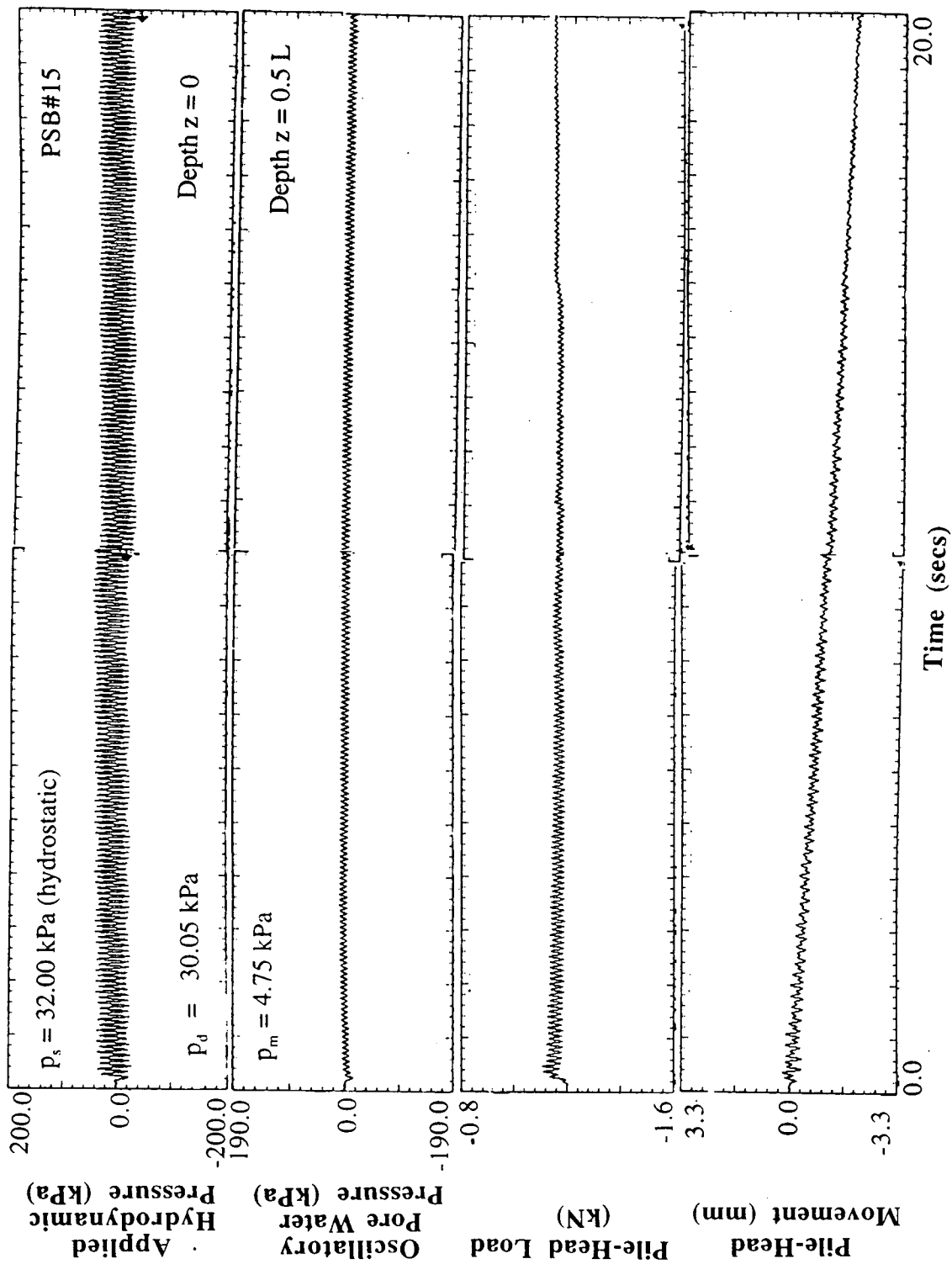
212

Fig. 8.30: Time History Measurements of Soil and Pile Response During Seaquake Loading With 40% Bias Loading at σ'_m =134 kPa

213

the piles failed completely during M = 8.0 simulated seaquake loading even under biased loads as low as 20%, which suggests that a degradation of 100% in soil strength is appropriate for stability analysis of 4.5-m-long piles. Failure was slightly delayed at σ'_m of 112 kPa and 65% bias tension load level.as compared to that at σ'_m of 20 kPa. At σ'_m of 134 kPa , pile failure occurred at 65% bias loading at about 9 secs (unscaled). The extraction rate was about 0.19 mm/sec (unscaled). The rate decreased to 0.12 mm/sec in proportion to the biased load level at 40% applied load and decreased further to 0.06 mm/sec in proportion to the biased load level at 20% applied load. From Table 8.6 for loaded piles at σ'_m of 134 kPa that did not fail, the temporary loss in capacity was limited to the peak value of the excess pore water pressure measured in every cycle of loading. The permanent loss in capacity was about 20% at 40% bias load level and was about 7% at 20% bias load level. These values may be overly conservative since the frequencies of excitation could not be appropriately scaled for tests conducted at σ'_m of 112 kPa and higher in accordance with the scaling rules because of the limitations of the testing machine requiring pile behavior to be evaluated against a fixed time duration of 20 secs and not compressed with increasing effective stress (simulated depth). In other words, piles that failed at 65% of bias loading and σ'_m of 134 kPa at approximately 9 secs during the seaquake loading would have been stable under a compressed time scale of 2.5 secs (20 secs factored by 1/8) in keeping with the scaling rules. A degraded resistance of 0.35 times the static resistance, or $\phi = 0.65$, is therefore appropriate for a 36-m-long pile. The value of ϕ in the lower 31.5 m of a 36-m-long pile can then be computed as follows:

(ϕ for 4.5 m) x 4.5 + (ϕ for 31.5 m) x 31.5 = (ϕ for 36 m) x 36

Since ϕ for 4.5 m = 0,

(0.00)4.5 + (ϕ for 31.5 m) x 31.5 = (0.65) 36

ϕ for 31.5 m = 0.74

ϕ can be inferred for σ'_m of 112 kPa. The rate of extraction of the pile at 65% bias loading was about 0.33 mm/sec (unscaled). In the absence of tests at varying bias load

levels at σ'_m of 112 kPa. The bias load level at which the piles would remain stable is estimated based on the linear relationship between bias load and extraction rate established earlier. The rate of extraction of about 0.19 mm/sec (unscaled) which is the condition for stability for σ'_m of 138 kPa is assumed to condition for stability for σ'_m of 112 kPa as well. This yields a bias load of 37%. Therefore, a ϕ of 0.37 can be considered appropriate for σ'_m of 112 kPa or 27-m-long pile.

It must be noted that these degradation factors are independent of the ground shaking effects and must be applied to the degraded static capacity obtained from ground shaking tests.

Figure 5.27 is replotted as Fig. 8.31, showing 1-ϕ for ground shaking and 1-ϕ for seaquake loading for M = 8.0 and a 250 m water depth at epicentral distance of 75 km.
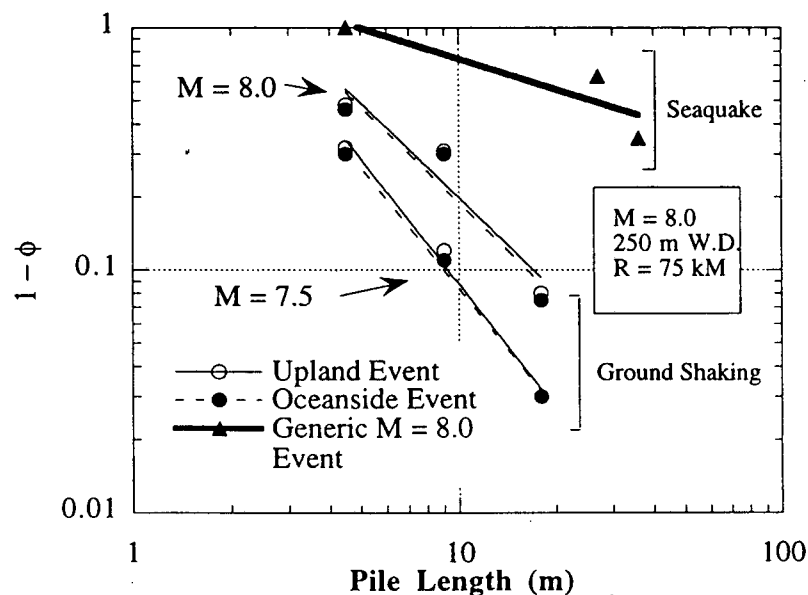
Fig. 8.31: Seismic resistance factor, ϕ, as a function of pile length for Ground Shaking and Seaquake Loading

8.5 Relative Effects of Horizontal Ground Shaking and Seaquakes

Figure.8.27 shows the pile response during seaquake loading. The pile in this case was loaded in tension to 45% of the static capacity under a σ'_m of 20 kPa, representing the top 4.5 m depth of a pile. The peak excess pore water pressure generated in the soil mass at about 50% of the chamber depth was about 50% of σ'_m. The pile failed within two cycles of seaquake loading (about 5 sec in the prototype). The instantaneous cyclic degradation in soil strength due to oscillatory pore water response established close to the pile caused the pile to ratchet upwards, consequently leading to the complete extraction of the pile. For comparison refer this behavior to Fig. 5.14. Figure 5.14 shows the result of a horizontal ground shaking under similar conditions in which the pile was loaded to 60% of its static capacity. It is clear that the mechanism of development of excess pore water pressure in the soil mass was different during the seaquake loading and ground shaking. During ground shaking, residual build-up of excess pore water pressure was observed, whereas seaquake loading generated only oscillatory excess pore water pressure response. However, the residual excess pore water pressure developed in the soil during horizontal ground shaking was much less than the peak value of excess pore water pressure developed during the seaquake loading. Unlike the complete failure that occurred during the seaquake loading, the pile only experienced mobility with some loss of its static capacity under ground shaking, which demonstrates that the seaquake loading produced more severe effects than did the horizontal ground shaking. This can also be judged based on the overall performance of piles under seaquake loading. From a comparison of degradation factors for stability conditions during horizontal ground shaking and seaquake loading independently, it is clear that degradation for a 36 m long pile was about 6% during horizontal ground shaking and 35% during seaquake loading. Therefore, seaquakes need serious consideration for offshore pile design.

216

8.6 Summary

(i) Seaquakes during M = 8.0 simulated seismic events induce hydrodynamic pressures ranging from 15 - 50 kPa in water depths ranging from 200 to 300 m

(ii) The seaquake-induced hydrodynamic loading on the seabed generates oscillatory excess pore pressure in the seabed, where the seaquake-associated seabed pressure is propagated into the seabed with attenuation and phase lag.

(iii) The degree of attenuation and the phase lag are greatly influenced by the predominant frequency of vibration of the seabed

(iv) Oscillatory pore water pressures introduce alternate increase and decrease in effective stress in the soil mass which causes piles driven into sand and carrying bias tension loads to ratchet upwards during every cycle of loading, ultimately causing complete extraction. Failure of a bias loaded tension pile during seaquake loading is therefore dependent on the duration of the seaquake loading.

(v) The rate of extraction of the pile is influenced by the ratio of the peak excess pore water pressure, the initial effective stress of the soil and the bias load level on the pile

(vi) The mechanism of generation of excess pore pressures in the seabed during horizontal ground shaking is different than that during seaquake loading, with latter being more severe.

(vii) While horizontal ground shaking may not have a major impact on the degradation of soil strength in prototype piles in saturated sands, seaquakes in deep water may affect the stability of offshore piles greatly and therefore need consideration in the design of offshore piles

(viii) Although the experiments were conducted on short piles, the results apply qualitatively to longer piles more typical of offshore structures.

Chapter 9

SUMMARY, CONCLUSIONS AND RECOMMENDATIONS

9.1 Summary

Model-scale experiments were conducted in a vibrated calibration chamber to study the effect of horizontal ground shaking and the coupled effect of vertical motion of the seabed and the induced seaquake independently, on the performance of offshore tension piles driven into sand. Pile response to horizontal ground shaking was studied for various bias tension load levels using typical offshore California-type simulated seismic events (Oceanside event of 1986, and Upland event of 1991) of Richter magnitudes 7.0, 7.5 and 8.0 with the epicenters 75 km from the pile location. Conditions leading to stability, mobility, and the failure were established for the top 4.5 m of prototype piles based on the results. Chapter 5 presents a detailed analysis of the results of the horizontal ground shaking tests. The seaquake effect was studied for typical M = 8.0 simulated seismic events in deep water (225 - 300 m). The effects of the influence of duration of the seaquake, predominant frequency of vibration and the initial effective stress in the soil and boundary conditions in the test chamber on the phenomenon of propagation of the seaquake-induced pore water pressure during simulated seismic events of Magnitude 8.0 were studied through parameteric tests. The results of the seaquake tests are described in Chapter 8.

9.2 Conclusions

9.2.1 Pile Response to Horizontal Ground Shaking

(i)   Pile failure during M = 8.0 events was catastrophic and occurred at a relatively low level of bias loading (75%) as compared to M = 7.0 and M = 7.5 events.

(ii) Significant reductions in the frictional uplift capacity of the soil occurred after M = 7.5 and M = 8.0 events.

(iii) The signature of simulated seismic events had relatively little influence on the condition of pile extraction of pile extraction for piles driven in saturated medium-dense sand during California-type seismic events.

9.2.2 Soil and Pile Response During Seaquakes

(i) The seaquake induced in the overlying seawater during the vertical excitation of the seabed in an earthquake generates oscillatory excess pore water pressure in the seabed, where the seaquake-associated seabed pressure is propagated into the seabed with attenuation and phase lag.

(ii) The degree of attenuation and the phase lag are greatly influenced by the predominant frequency of vibration of the seabed.

(iii) The mechanism of generation of excess pore water pressures in the seabed during horizontal ground shaking is different from that during seaquake loading, with the latter being more severe.

(iv) While horizontal ground shaking may not have a major impact on the degradation of soil strength in prototype piles in saturated sands, seaquakes in deep water may affect the stability of offshore piles greatly and therefore need consideration in the design of offshore piles.

9.3 Recommendations

(i) The condition modelled in these experiments is representative of an offshore site comprising of relatively coarse clean sand. Therefore, these results cannot be considered applicable for sites comprising of silty fine sand or layered soils with sand capped by clay layers. Experiments need to be conducted to investigate pile behavior under these conditions.

(ii). The stability of plugs in open-ended piles is questionable during vertical and horizontal ground shaking. This may be a much more serious issue during seaquake loading where gradients in pore water pressure at the bottom and top of the plug that occur during seaquake loading due to phase lag in the pore water pressure may destroy the plug completely, resulting in loss in compressive capacity. The conclusions developed in this study should be extended for open-ended pipe piles loaded in compression.

(iii). Similar studies should be conducted on closely spaced groups of piles, as the induced pore water pressures and the potential for uplift failure may be increased by the presencea of neighboring piles.

REFERENCES

Ambraseys, N., "A Damaging Seaquake," Short Communication, Earthquake Engineering and Structural Dynamics, Vol. 13, 1985, pp.421-424.

API, "Recommended Practice for Planning, Designing and Constructing Fixed Platforms," American Petroleum Institute, API RP2A, 19th Edition, 1993.

Arnold, P., Bea, R. G., Idriss, I., Reimer, R. B., Beebe, K. E., and Marshall, P. W., "A Study of Soil-Pile-Structure Systems in Severe Earthquakes," Paper No. 2749, Offshore Technology Conference, Houston, Texas, 1977.

Arulanandan, K., Anadrajah, A., and Abghari, A., "Centrifuge Modelling of Soil Liquefaction Susceptibility," Journal of the Geotechnical Engineering, ASCE, Vol. 109, No. 3, March, 1983, pp. 281-300.

Barends, F. B. J., Discussion of "Oscillatory Pore Pressure and Liquefaction in SeaBed Induced by Ocean Waves," by Zen, K., and Yamazaki, H., Soil Mechanics and Foundation Engineering, Vol. 30, No. 4, December, 1990, pp. 147-161.

Bea, R. G., Nour-Omid, S. and Coull, T. B., "Design for Dynamic Loadings," Paper Presented to 3rd BOSS Conf., Boston, 1982.

Bea, R. G., "Pile Capacity for Axial Cyclic Loading," Journal of Geotechnical Engineering, ASCE, Vol. 118, No. 1, 1992, pp. 34-50.

Bell, J. M., and Hoffman, R. A., "Design Earthquake Motions Based on Geologic Evidence," Proceedings of the ASCE Geotechnical Engineering Division Specialty Conference, Earthquake Engineering and Soil Dynamics, Vol. 1, June, 1978, pp. 231-271.

Blaney, G. W., Kausel, E., and Rosset, J. M. , "Dynamic Stiffness of Piles," Proc. 2nd Int. Conf. on Num. Methods in Geomechanics, Blacksburg, ASCE, 1976, pp. 1001-1012.

Boore, D.,"The Effects of Simple Topography on Seismic Waves : Implications for the Accelerations Recorded at Pacoima Dam, San Fernando Valley, California," Bull. Seism. Soc. Am., Vol. 63, No. 5, Oct. 1973, pp. 1603-1609.

Bureau, G. J., "Influence of Faulting on Earthquake Attenuation,", Proceedings of the ASCE Geotechnical Engineering Division Specialty Conference, Earthquake Engineering and Soil Dynamics, Vol. 1, June, 1978, pp. 290-307.

Castro, G., and Poulos, J., "Factors Affecting Liquefaction and Cyclic Mobility," Liquefaction Problems in Geotechnical Engineering, ASCE, National Convention, September, 1976, pp. 105-138.

Chameau, J.-L., and Clough, G. W., " Probabilistic Pore Pressure Analysis for Seismic Loading," Journal of Geotechnical Engineering, ASCE, Vol. 109, No. 4, April, 1983.

Chan, S. F., and Hanna, T. H., "Repeated Loading on Single Piles in Sand," Journal of Geotechnical Engineering Division, ASCE, 106 (GT2),1980, pp. 171-188.

Chen, C.-H. and Penzien, J., "Seismic Modeling of Deep Foundations," Earthquake Engineering Research Center, Report No. UCB/EERC-84/19, November, 1984.

Cheney, J. A., Brown, R. K., and Dhat, N. R., "Modeling Free-Field Conditions in Centrifuge Models," Journal of Geotechnical Engineering, ASCE, Vol. 116, No. 9, September, 1990, pp. 1347 - 1367.

Coe, C. J., Prevost, J. H., and Scanlan, R. H., "Dynamic Stress Wave Reflections/Attenuation: Earthquake Simulation in Centrifuge Soil Models," Earthquake Engineering and Structural Dynamics, Vol. 13, 1985, pp. 109-128.

Drnevich, V. P., "Long-Tor Resonant Column Testing Manual," Purdue University, 1994.

Finn, W. D., and Siddharthan, R., "Response of SeaFloor to Ocean Waves," Journal of Geotechnical Engineering, ASCE, Vol. 109, No. 4, 1983, pp. 556-571.

Finn, W. D. L., and Gohl, W. B., "Centrifuge Model Studies of Piles Under Simulated Earthquake Lateral Loading," Geotechnical Special Publication No. 11, Ed. by T. Nogami, ASCE, April, 1987, pp. 21-38.

Finn, W. D. L., Lee, K.W., and Martin, G. R., "An Effective Stress Model for Liquefaction," Journal of the Geotechnical Engineering Division, ASCE, 103 (GT6), 1977, pp. 517-533.

Finn, W. D. L., and Martin, G. R., "Analysis of Piles Foundations for Offshore Structures Under Wave and Earthquake Loading," Proceedings of the 2nd International Conference on Behavior of Offshore Structures, Imperial College, London, England, Paper No. 38, 1979, pp. 497-502.

Foda, M. A., Tzang, S.-Y., and Maeno, Y., "Resonant soil liquefaction by water waves," Proceeding of Int. Conf. on Geotechnical Engineering for Coastal Development, CEO-COAST, '91, Vol. 1, pp. 549-554.

Fredlund, D. G.," Density and Compressibility Characteristics of Air-Water Mixtures," Canadian Geotechnical Journal, Vol. 13, 1976, pp. 386-396.

Gazetas, G., and Dakoulas, P., "Local-Soil and Source-Mechanisms Effects in the 1986 Kalamata (Greece) Earthquake," Earthquake Engineering and Structural Dynamics, Vol. 19, 1990, pp. 431-456.

Gudehus, G., and Hettler, A., "Cyclic and Monotonic Model Tests in Sand," Proc. 10th Int. Conf. on Soil Mech. and Foundation Engineering, Stockholm, Vol. 2, 1981, pp. 211-214.

Hardin, B. O. , and Drnevich, V. P., "Shear Modulus and Damping in Soils: design equations and curves," Journal of the Soil Mechanics and Foundations Division, ASCE, Vol. 98, No. SM6, 1972, pp. 603-624.

Harrop-Williams, K. O., "Earthquake-Induced Shear Stress in Soils," Journal of Geotechnical Engineering, ASCE, Vol. 114, No. 12, December, 1988, pp. 1437-1441.

Hauksson,E., and Jones, L.M., "The July 1986 Oceanside (M_L = 5.3) earthquake sequence in the continental borderland, Southern California," Bulletin of the Seis. Soc. of America, Vol. 78, No. 6, 1988, pp. 1885-1906.

Hauksson,E., and Jones, L.M., "The 1988 and 1990 Upland Earthquakes: left-lateral faulting adjacent to the central transverse ranges," Journal of Geophysical Research, Vol.96, No. B5, 1991, pp. 8143-8165.

Huang, A.-B., Ma, M.-Y., and Lee, J. S., "Numerical Simulation of a Calibration Chamber," in Calibration Chamber Testing, Ed. by A.-B., Huang, Elsevier, 1991, pp. 175-184.

Hushmand, B., Crouse, C. B., and Martin, G., "Site Response and Liquefaction Studies Involving the Centrifuge," Soil Structure Interaction, Edited by Cakmak, A. S., 1988.

224

Iai, S., "Similitude for Shaking Table Tests on Soil-Structure-Fluid Model in 1 g Gravitational Field," Japanese Society of Soil Mechanics and Foundation Engg., Soils and Foundations, Vol. 29, No. 1, 1989, pp. 105-118.

Ishihara, K., and Haeri, S. M., "Geotechnical Aspects of the June 20, 1990 Manjil Earthquake in Iran," Soils and Foundations, Japanese Society of Soil Mechanics and Foundation Engineering, 1990.

Kobayashi, H., Sakuta, M., Okamoto, O., and Hirakawa, S.,"Safety Consideration of the TLP on earthquake wave propagated through seawater," Proceedings of 24th OTC, TX, Vol. 2, OTC 6888, pp.139-145.

Lambson, M. D., "Behavior of Piles Under Axial Cyclic Loading," Proceedings of the 20th Annual OTC Conf., May, 1988, pp. 129-138.

Lee, C. Y., and Poulos, H. G., "Influence of Excess Pore Pressures On Axial Offshore Pile Response," Journal of Geotechnical Engineering, ASCE, Vol. 19, 1988, pp.73-92.

Lehane, B. M. , Jardine, R. J., Bond, A. J. , and Frank, R., "Mechanisms of Shaft Friction in Sand from Instrumented Pile Tests," Journal of Geotechnical Engineering, ASCE, Vol. 119, No. 1, 1993, pp. 19-35.

Levacher, D. R. , and Sieffert, J-G., "Tests on Model Tension Piles," Journal of Geotechnical Engineering, ASCE, Vol. 110, No. 12, 1984, pp. 1735-1748.

Liou, G.-S., Penzien, J., and Yeung, R., "Response of Tension-Leg Platforms to Vertical Seismic Excitations," Earthquake Engineering and Structural Dynamics, Vol. 16, 1988, pp. 157-182.

Martin, P. P., and Seed, H. B., "APOLLO, A Computer Program for the Analysis of Pore Pressure Generation and Dissipation in Horizontal Sand Layers During Cyclic or Earthquake Loading," Report No. EERC 78-21, Earthquake Engineering Research Center, 1978.

Matasovic, N., and Vucetic, M., "Cyclic Characterization of Liquefiable Sands," Journal of Geotechnical Engineering, ASCE, Vol.119, No. 11, November, 1993.

Matlock, H. S., Foo, H. C., and Bryant, L. M., "Simulation of Lateral Pile Behavior Under Earthquake Motion," Proc. of Conf. on Earthquake Engineering and Soil Dynamics, ASCE, Vol. 2, 1978, pp. 600-619.

Matlock, H. S., and Foo, H. C., "Axial Analysis of Piles Using a Hysteretic and Degrading Soil Model," Proc. Conf. Num. Methods in Offshore Piling, Institution of Civil Engineers, London, 1979, pp. 165-185.

Matso, K., "Lessons from Kobe", Civil Engineering, ASCE, April, 1995, pp. 42-47.

Mayne, P. W. , and Kulhawy, F. H., "Ko-OCR Relationships in Soil," Journal of the Geotechnical Engineering Division, ASCE, Vol. 108, No. GT6, June, 1982, pp. 863-875.

Nauroy, J. F., Brucy, F., Tirant, P. Lea and Kervadec, J.-P., "Design and Installation of Piles in Calcareous Formations," Proc. 3rd Int. Conf. Num. Methods in Offshore Piling, Nantes, 1986, pp. 461-480.

Novak, M., "Dynamic Stiffness and Damping of Piles," Canadian Geotechnical Journal, 11 (4), 1974a, pp. 574-598.

Novak, M., "Effect of Soil on Structural Response to Wind and Earthquake," International Journal of Earthquake Engineering and Structural Dynamics, Vol. 3, No. 1, 1974b, pp. .

Ochoa, M., "Response of Tension Piles to Simulated Seismic Motion in Saturated Fine Sand," Ph. D. thesis, Department of Civil and Environmental Engineering, University of Houston, December, 1990, pp. 286.

Okusa, S., "Wave-Induced Pressures in Beds of Sand," Journal of the Hydraulics Division, ASCE, Vol. 96, No. 2, 1985, pp. 517-532.

O'Neill, M. W., and Raines, R. D., "Load Transfer for Pipe Piles in Highly Pressurized Dense Sand," Journal of Geotechnical Engineering Division, ASCE, Vol. 117, No. 8, 1208 - 1226.

O'Neill, M. W., Vipulanandan, C., and Ochoa, M., "Laboratory Scale Modeling of Pullout Behavior of Bias-Loaded Tension Piles During Earthquakes," Paper No. 6809, Offshore Technology Conference, 1992.

Orphal, D. L., and Lahoud, J. A., "Prediction of Peak Ground Motion From Earthquakes," Bulletin of the Seismological Society of America, Vol. 64, No. 5, 1974, pp. 1563-1574.

Otani, J., "Nonlinear Pile Group Model for Transient Dynamic Response Analysis," Ph.D. thesis, Department of Civil and Environmental Engineering, University of Houston, 1990, pp. 218.

Penzien, J., and Watabe, M.,"Characteristics of 3-Dimensional Earthquake Ground Motions," Earthquake Engineering and Structural Dynamics, Vol. 3, 1975, pp. 365-373.

PMB Engineering, Inc., PAR Pile Analysis Program, Users Manual, Theoretical Manual, Reference Manual, San Francisco, California.

Poulos, H. G., "Cyclic Axial Response of Single Pile," Journal of Geotechnical Engineering Division, ASCE, 107(GT1), 1981, pp. 41-58.

Poulos, H. G., "Cyclic Degradation of Pile Performance in Calcareous Soils," Analysis and Design of Pile Foundations, Ed. by J. R. Meyer, ASCE, 1984, pp. 99-118.

Poulos, H. G., "Marine Geotechnics," published by Academic Division of Unwin Hyman Ltd, London, 1988.

Pyke, R., "NonLinear Soil Models For Irregular Cyclic Loadings," Journal of the Geotechnical Engineerig, ASCE, Vol. 105, No. GT6, June, 1979.

Randolph, M. F., Discussion : "The Use of Physical Models in Design," Proceedings 7th ECSMFE, Brighton, Vol. 4, 1979, pp. 338-339.

Ross, H. E., Jr., "Dynamic Response of Laterally Loaded Offshore Piling," Sea Grant Report 70-224, Texas A & M University, 1970.

Saxena, S. K., and Reddy, K. R., "Dynamic Moduli and Damping Ratios for Monterey No. 0 Sand by Resonant Column Tests," Soils and Foundations, Japanese Soc. of Soil Mechanics and Foundation Engineering, Vol. 29, 1989, pp. 37-51.

Schnabel, P. B., Lysmer, J., and Seed, H. B., "SHAKE - A Computer Program for Earthquake Response Analysis of Horizontally Layered Sites," Report No. EERC 72-12, Earthquake Engineering Research Center, 1972, University of California at Berkeley.

Schnabel, P. B., Seed, H. B. and Lysmer, J., "Modification of Seismograph Records for Effects of Local Soil Conditions," Bull. Seism. Soc. Am., Vol. 62, No. 6, Dec. 1972, pp. 1649-1664.

Schofield, A. N., "Cambridge Geotechnical Centrifuge Operations," Geotechnique 30, No. 3, 1980, pp. 227-268.

Seed, H. B., et al., "Relationships of Maximum Acceleration, Maximum Velocity, Distance from Source and Local Site Conditions for Moderately Strong Earthquakes," Bull. Seism. Soc. Am., Vol. 66, No. 4, August, 1976, pp. 1323-1342.

Seed, H. B., and Rahman, M. S., "Wave Induced Pore Pressure in Relation to Ocean Floor Stability of Cohesionless Soils," Marine Geotechnology, Vol. 3, No. 2, February, 1978, pp. 123-149.

Seed, H.B., Idriss, I. M., Makdisi, F., and Banerjee, N., "Representation of Irregular Stress Time Histories by Equivalent Uniform Stress Series in Liquefaction Analysis," Earthquake Engineering Research Center, Report No. EERC 75-29, 1975, University of California, Berkeley.

Seed, H.B., and Idriss, I. M., "Influence of Soil Conditions on Ground Motions During Earthquakes," Journal of Soil Mechanics and Foundation Division, ASCE, Vol. 95, No. SM1, January, 1969, pp. 99-137.

Seed, H. B., and Idriss, I. M., "Simplified Procedure for Evaluating Soil Liquefaction Potential," Journal of the Soil Mechanics and Foundations Division, ASCE, Vol. 97, No. SM9, September, 1971, pp. 1249-1273.

Sherif, M. A. , "Damping Ratio for Dry Sands, " Journal of Geotechnical Engineering Division, ASCE, Vol. 103, No. GT7, 1977, pp. 743-755.

Swinianski, J., and Sawicki, A., "A Model of Soil-Pile Interaction Owing to Cyclic Loading," Canadian Geotechnical Journal, Vol. 28, 1991, pp. 11-19.

Sun, K., and Nogami, T., "Earthquake Induced Hydrodynamic Pressure on Axisymmetric Offshore Structures," Earthquake Engineering and Structural Dynamics, Vol. 20, 1991, pp. 429-440.

Tazoh, T., Shimizu, K., and Wakahara, T.,"Seismic Observations and Analysis of Grouped Piles," Geotechnical Special Publication No. 11, Ed. By T. Nogami, ASCE, April, 1987, pp. 1-20.

Trifunac, M. D., and Brady, A. G., "Correlations of peak acceleration, velocity and displacement with earthquake magnitude, distance and site conditions," Earthquake Engineering and Struct. Dyn., Vol. 4, 1976, pp. 455-471.

Trifunac, M. D., "Prelimnary Empirical Model for Scaling Fourier Amplitude Spectra of Strong Acceleration in Terms of Modified Mercalli Intensity and Recording Site Conditions," Earthquake Engineering and Structural Dynamics, Vol. 7, 1979, pp. 63-74.

Vaid, Y. P., and Negussey, D. "Relative Density of Pluviated Sand Samples," Soils and Foundations, Vol. 24, No.2, June, 1984, pp. 101-105.

Vesic, A. S., "Expansion of Cavities in Infinite Soil Mass," Journal of Soil Mechanics and Foundation Division, ASCE, Vol. 98, No. SM3, March, 1972, pp. 265-290.

Wang, J. N., and Kavazanjian Jr., "Pore Pressure Development During Non-Uniform Cyclic Loading," Japanese Society of Soil Mechanics and Foundation Engineering, Soils and Foundations, Vol. 29, No. 2, June, 1989, pp. 1-14.

Weissman, K., and Prevost, J. H., "Centrifugal Modelling of Dynamic Soil-Structure Interaction," Earthquake Engineering and Structural Dynamics, Vol. 18, 1989, pp. 1145-1161.

Whitman, R. V., and Klapperich, H., "Model Tests for Earthquake Simulation of Geotechnical Problems," Soil Dynamics and Liquefaction, Edited by Cakmak, A.S., 1987.

Williams, A. N., and Mau, S-T., "Earthquake Response of Submerged Circular Arch," Journal of Waterways, Port, Coastal, and Ocean Engineering, ASCE, Vol. 114, No. 4, July, 1988.

Yamamoto, T., Takahashi, S., and Schuckman, B., "Physical Modeling of Sea-SeaBed Interactions," Journal of Engineering Mechanics, ASCE, Vol. 109, No. 1, February, 1983.

Zeghal, M., and Elgamal, Ahmed-W., "Analysis of Site Liquefaction Using Earthquake Records," Journal of Geotechnical Engineering, ASCE, Vol. 120, No. 6, June, 1994.

Zen, K., and Yamazaki, H., "Mechanism of Wave-Induced Liquefaction and Densification in SeaBed," Japanese Society of Soil Mech. and Foundation Engg., Soils and Foundations, Vol. 30, No. 4, 1990, pp. 90-104.

Zen, K., and Yamazaki, H., "Oscillatory Pore Pressure and Liquefaction in SeaBed Induced By Ocean Waves," Japanese Society of Soil Mechanics and Foundation Engineering, Soils and Foundations, Vol. 30, No. 4, December, 1990, pp. 147-161.

CONVERSION FACTORS, SI TO U.S. CUSTOMARY UNITS OF MEASUREMENTS

Divide	By	To Obtain
millimetres	0.0000001	Angstroms
centimetres	2.54	inches
metres	0.3048	feet
kilometres	1.609344	miles (U.S. statute)
square metres	0.00064516	square inches
square metres	0.09290304	square feet
cubic metres	0.02831685	cubic feet
cubic metres	0.7645549	cubic yards
kilograms	0.001	grams
kilograms	0.4535924	pounds (mass)
kilograms	907.1847	tons (2000 pounds)
kilograms per cubic metres	16.01846	pounds (mass) per cubic foot
kilograms per cubic metres	0.59327631	pounds (mass) per cubic yard
newtons	4.448222	pounds (force)
pascals	6894.757	pounds (force) per square inch
kilograms per square metre	4.882428	pounds (force) per square foot
kilometres per hour	1.609344	miles per hour
radians	0.01745329	degrees (angle)
Celsius degrees	5/9	Fahrenheit degrees

APPENDIX A

TIME HISTORIES OF SCALED OCEANSIDE EVENT

EXTENDED RECORD, M = 7.0, E.D. = 75 KM

(a)

EXTENDED RECORD, M= 7.0, E.D.= 74 KM

(b)
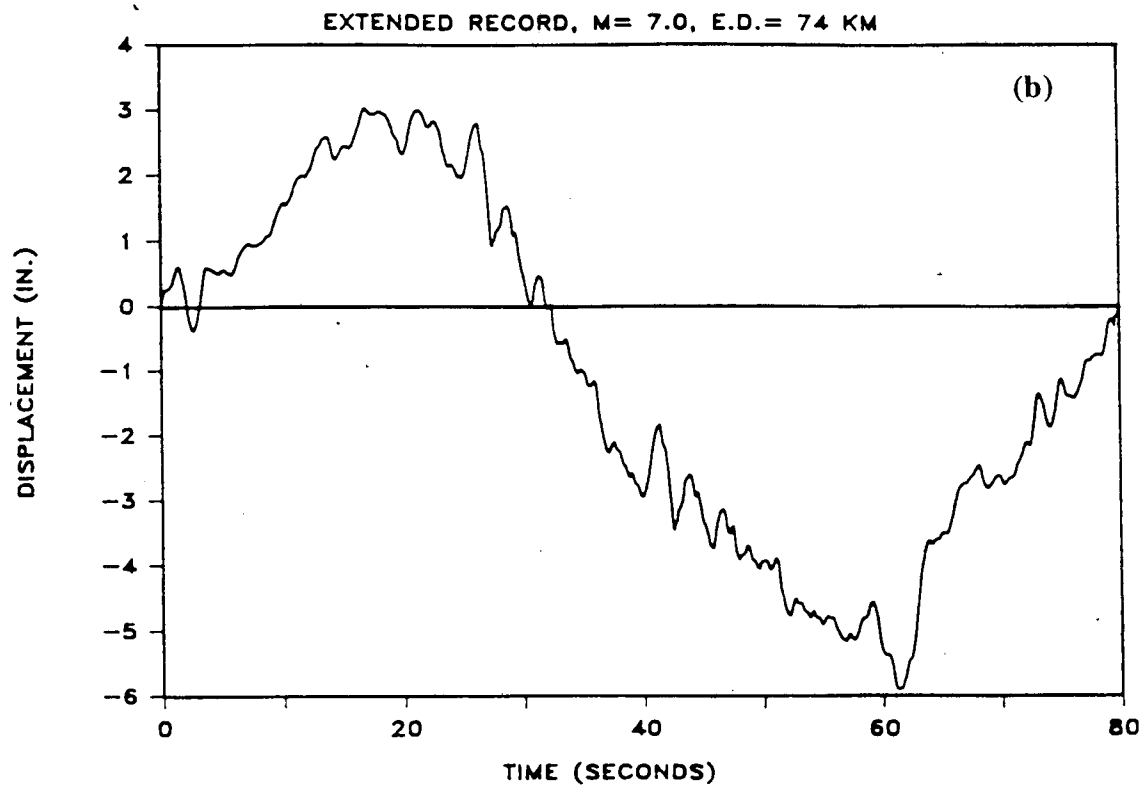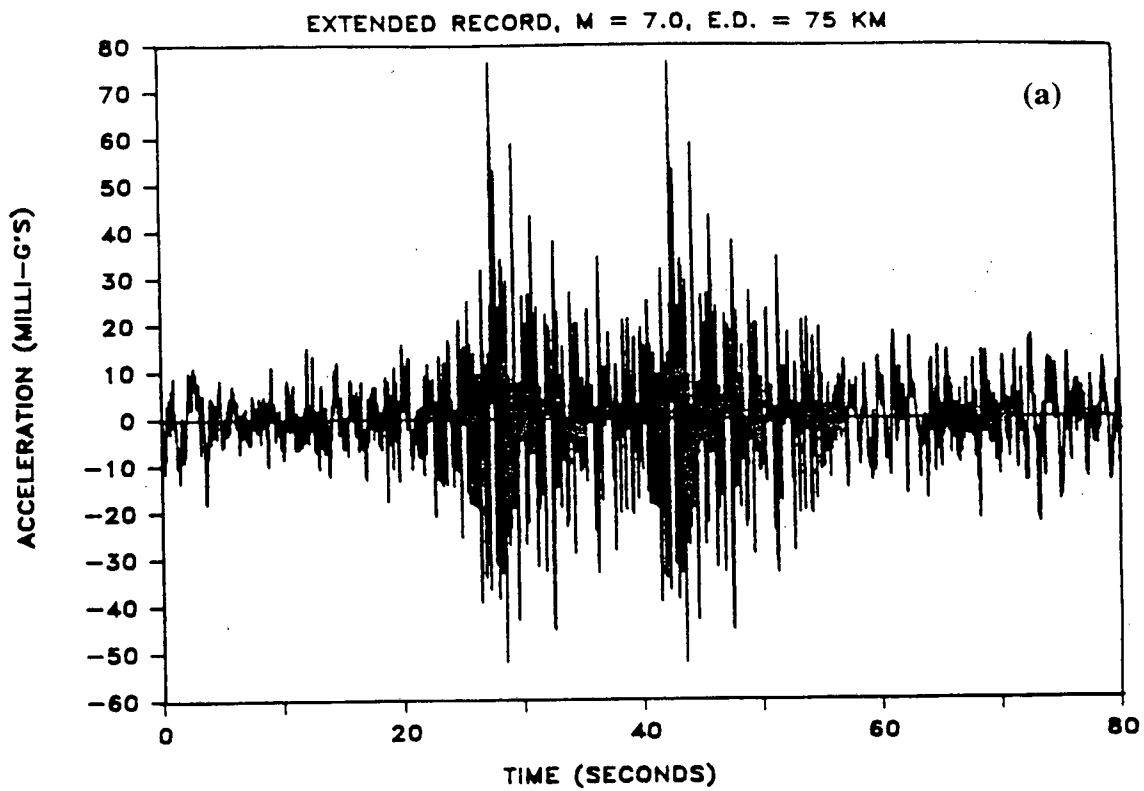
Fig. A.1: Time Records for the Scaled M = 7.0 Oceanside Event (a) Extended Acceleration and (b) Displacement [After Ochoa (1990)]

234
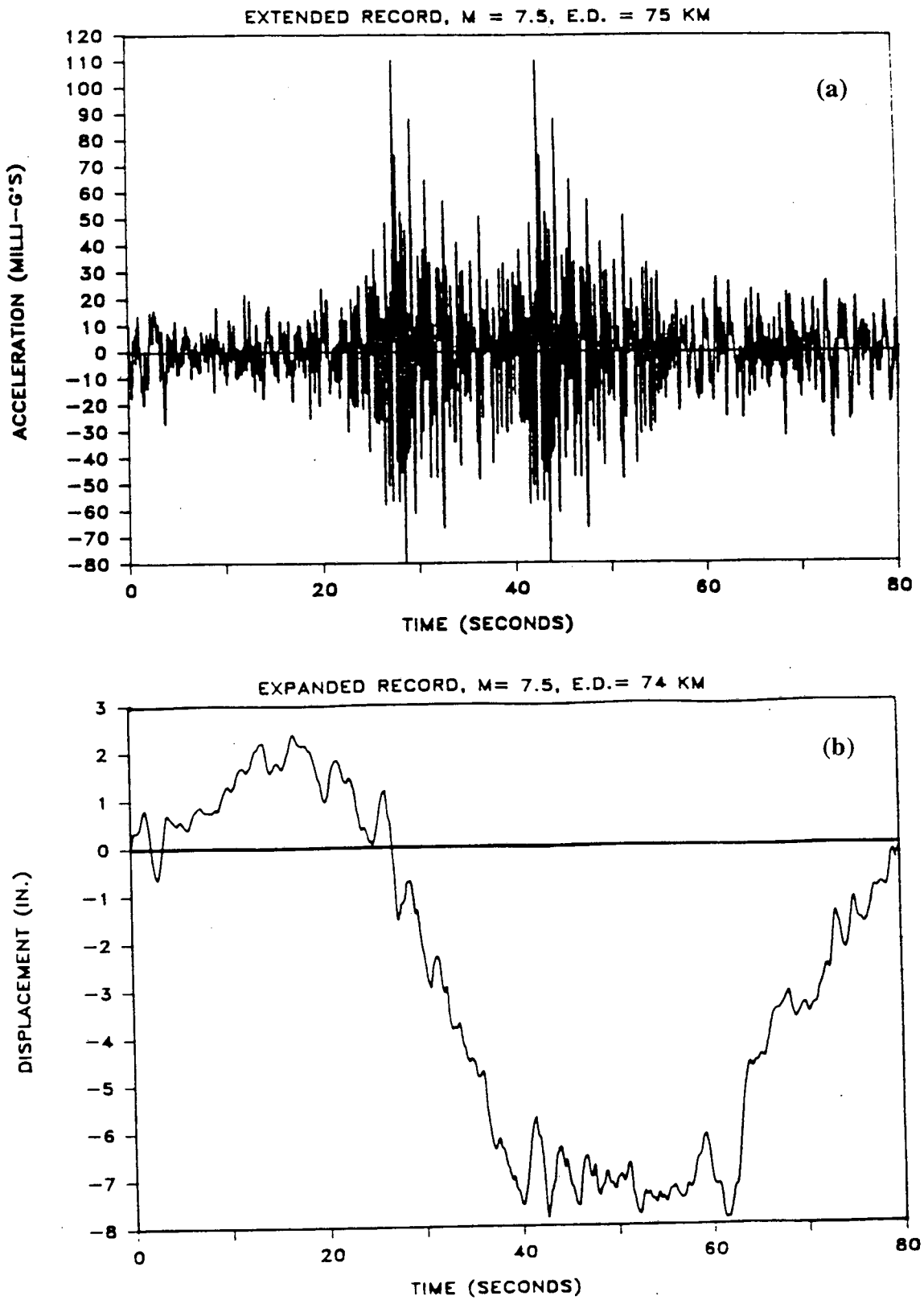
Fig. A.2: Time Records for the Scaled M = 7.5 Oceanside Event (a) Extended Acceleration and (b) Displacement [After Ochoa (1990)]

235
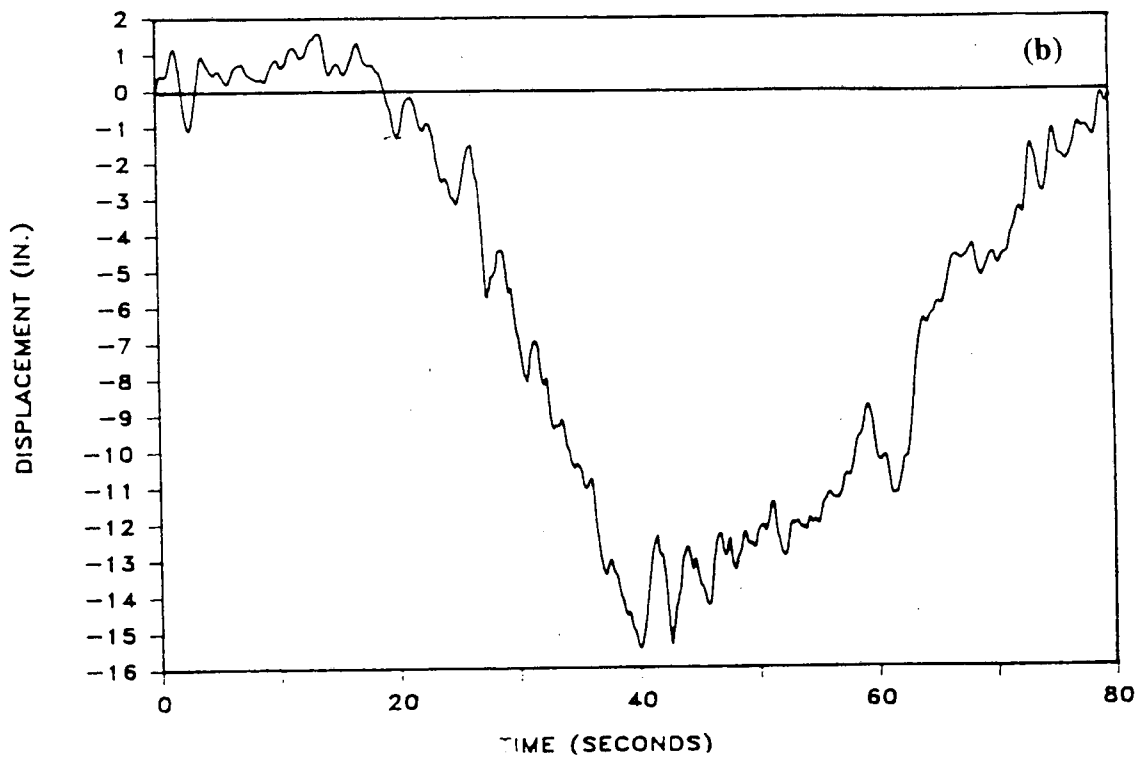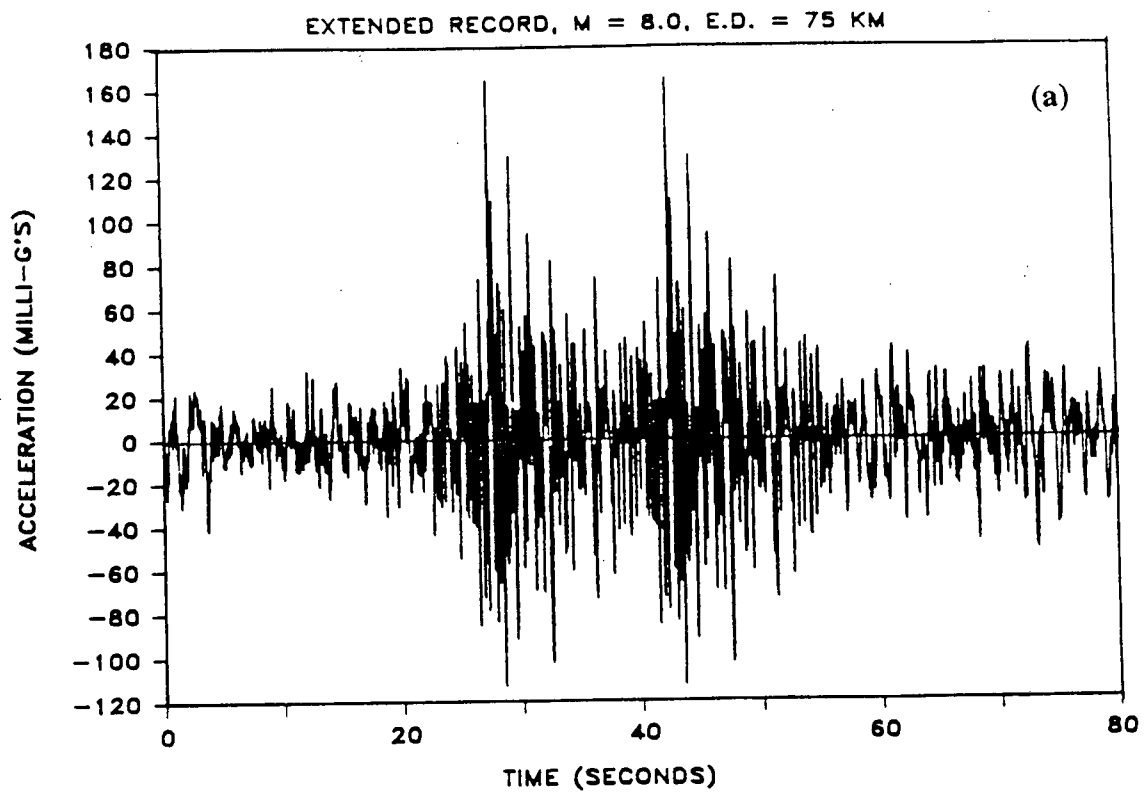
Fig. A.3: Time Records for the Scaled M = 8.0 Oceanside Event (a) Extended Acceleration and (b) Displacement [After Ochoa (1990)]

236

APPENDIX B

CALIBRATION CONSTANTS FOR INSTRUMENTS

PILE-HEAD STRAIN GAGE
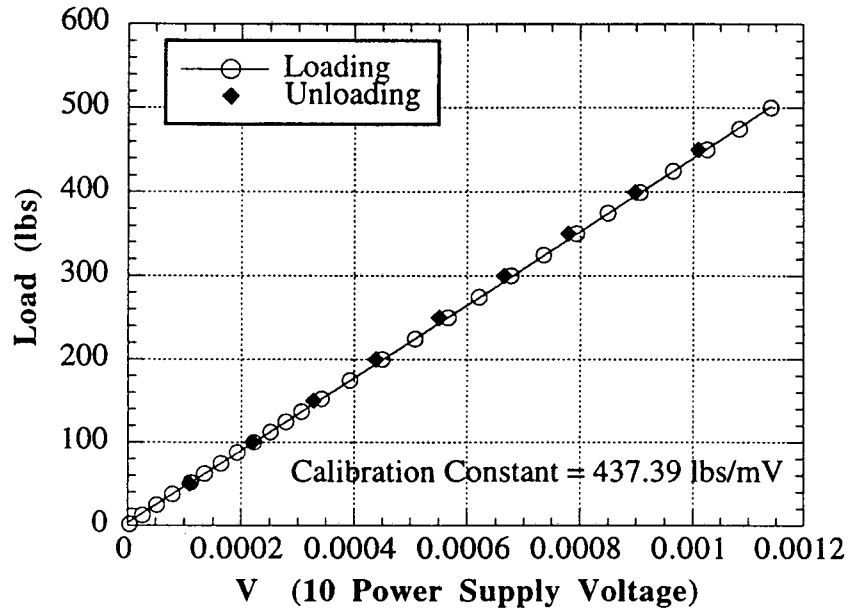
Fig. B.1: Calibration Constant for Pile-Head Strain Gage

Table B.1: Calibration Constants

LVDT	0.007614 V / 10V Power Supply / 0.001 in.
Pore Water Pressure Transducers	
PDCR 81 - S. No. 7383	8.56 mV/10V Power Supply / psi
PDCR 81 - S. No. 7592	7.21 mV/ 10V Power Supply / psi
Keller -PSI - S. No. 710P-130-0015	0.333 V /15V Power Supply / psi
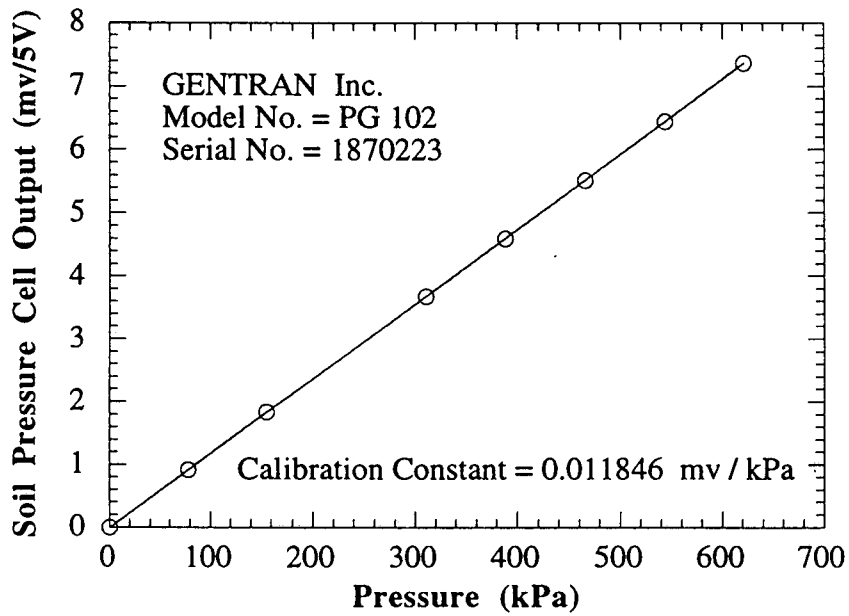
Fig. B.2: Calibration Constant for the Soil Total Pressure Cell

APPENDIX C

'B' PARAMETER TEST RESULT
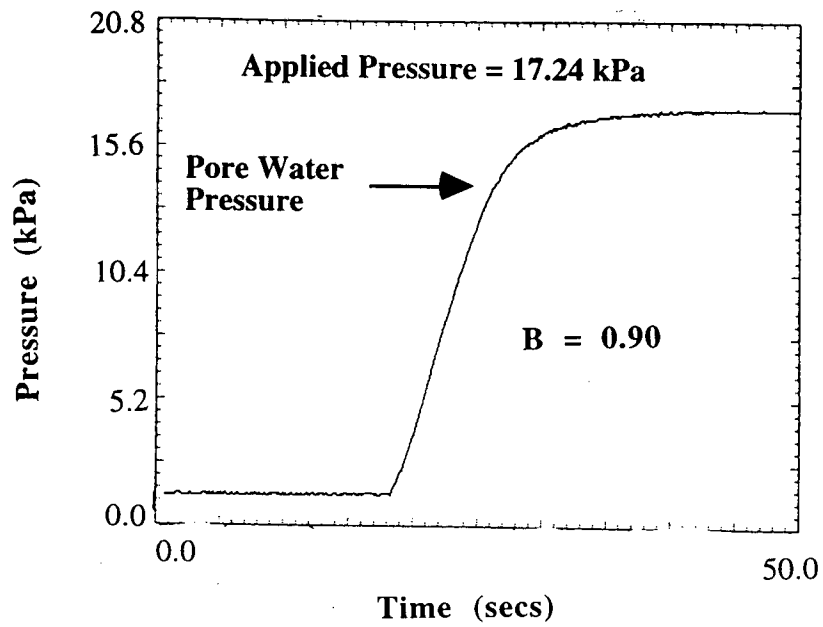
Fig. C.1: Pore Water Pressure Response to Applied Chamber Pressure with all Drainage Ports Closed - 'B' Parameter Check

APPENDIX D
SPRING CONSTANT FOR MASS-SPRING SYSTEM
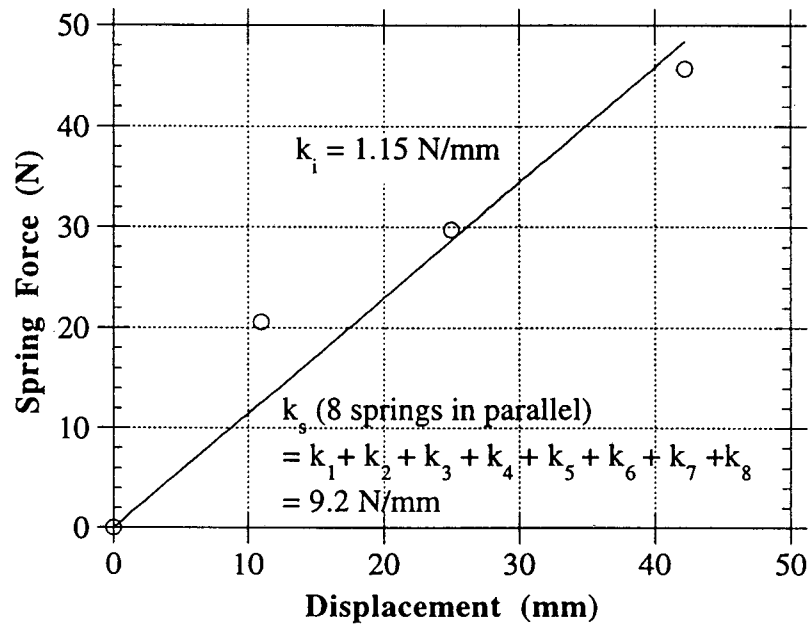
Fig. D.1: Spring Constant for the Mass-Spring System

APPENDIX E

Load-Depth Relationships
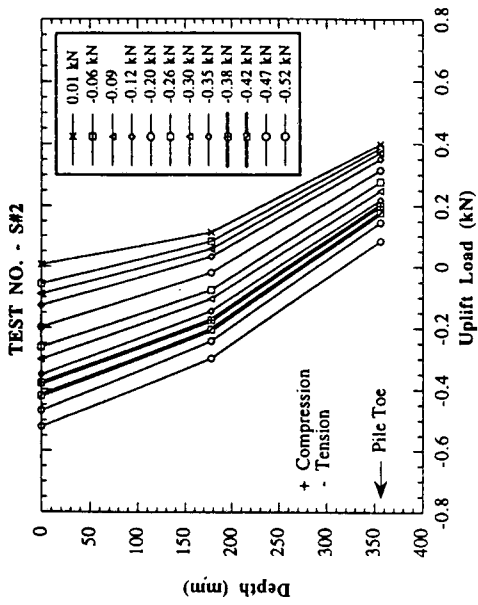
Fig. E-2: Load-Depth Relationships, Test S#2
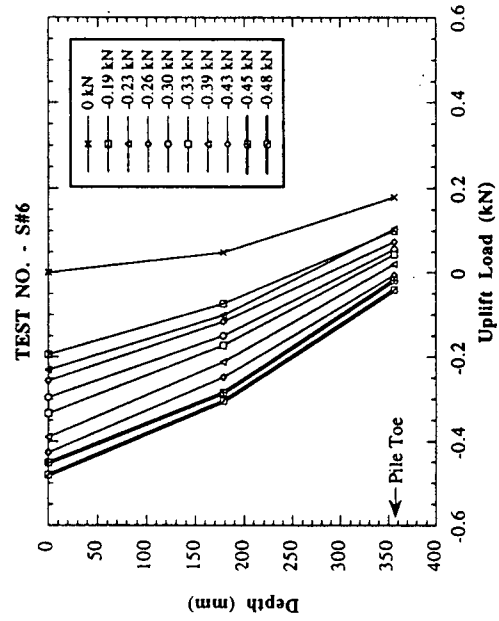
Fig. E-4 : Load-Depth Relationships, Test No. S#6
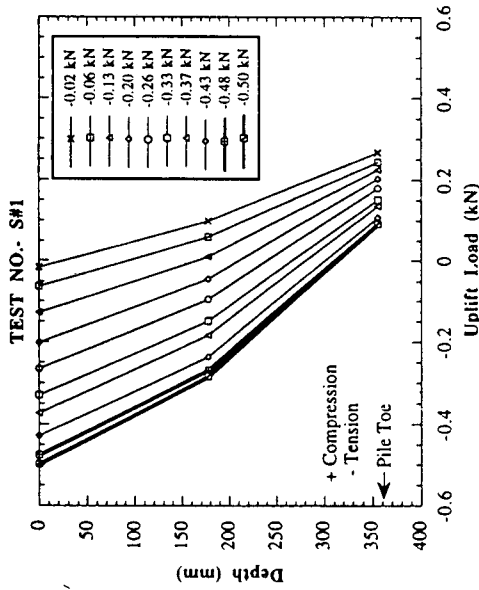
Fig. E-1: Load-Depth Relationships, Test No. S#1
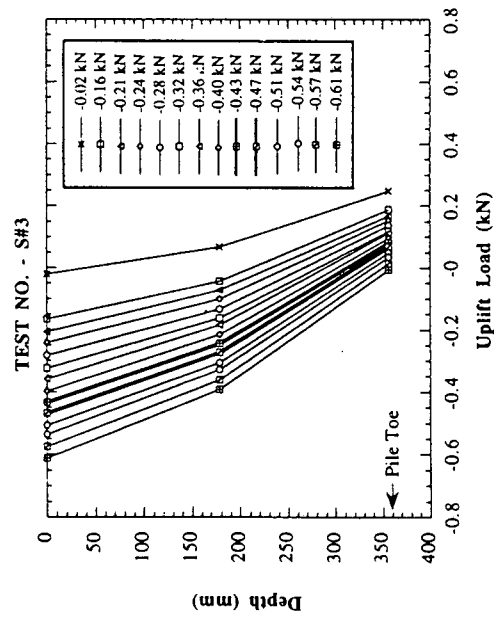
Fig. E-3 : Load-Depth Relationships, Test No. S#3

245
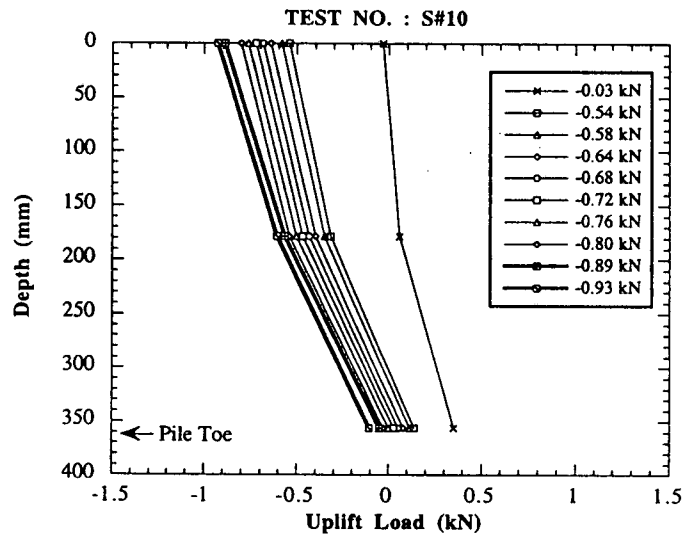
Fig. E.5: Load-Depth Relationships, Test No. S#10

APPENDIX F

Pore Water Response During Pile Driving
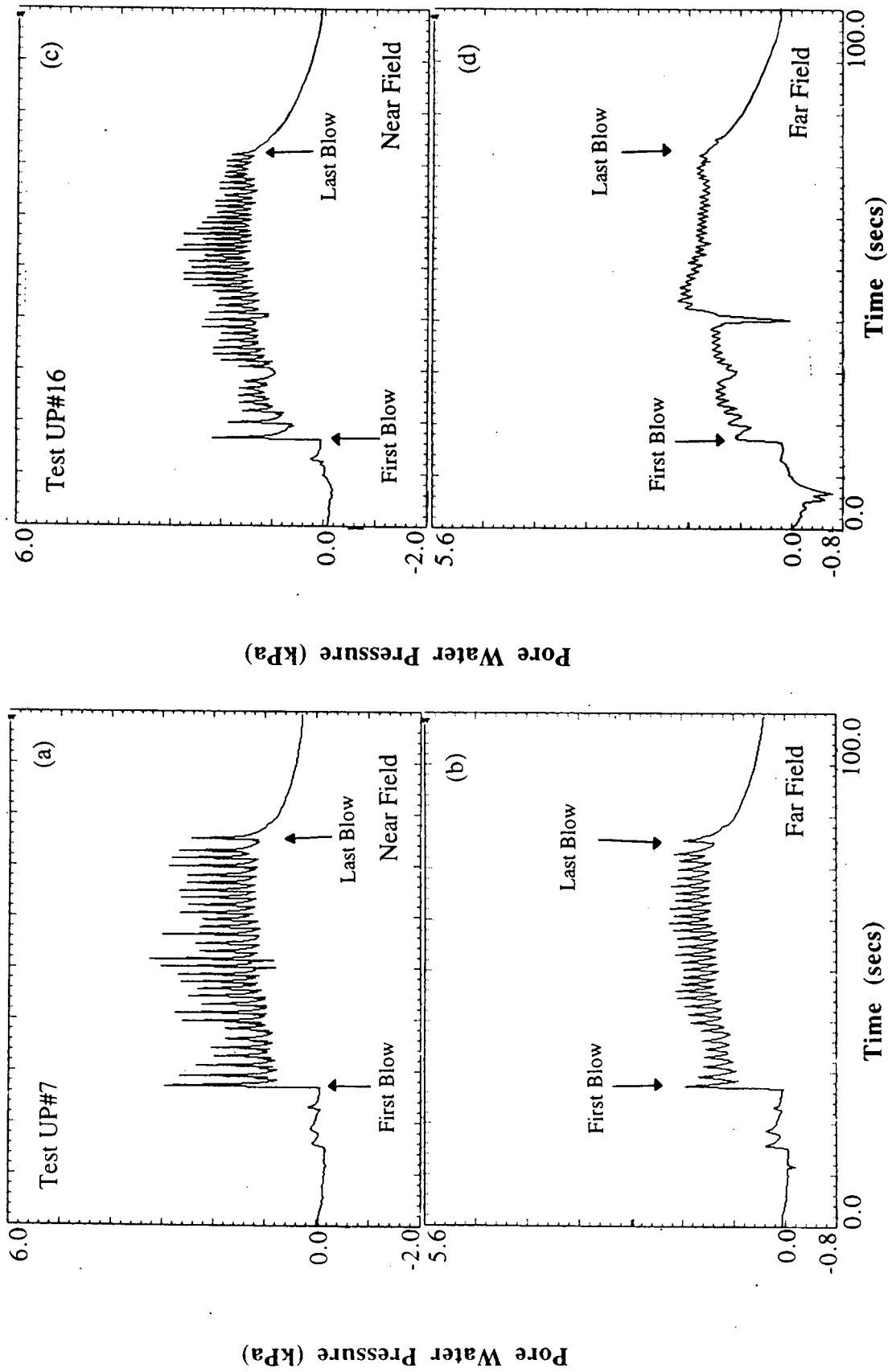
Fig. F.1: Pore Water Pressure Response During Driving Tests UP#7(a,b), and Tests UP#16(c,d)

248
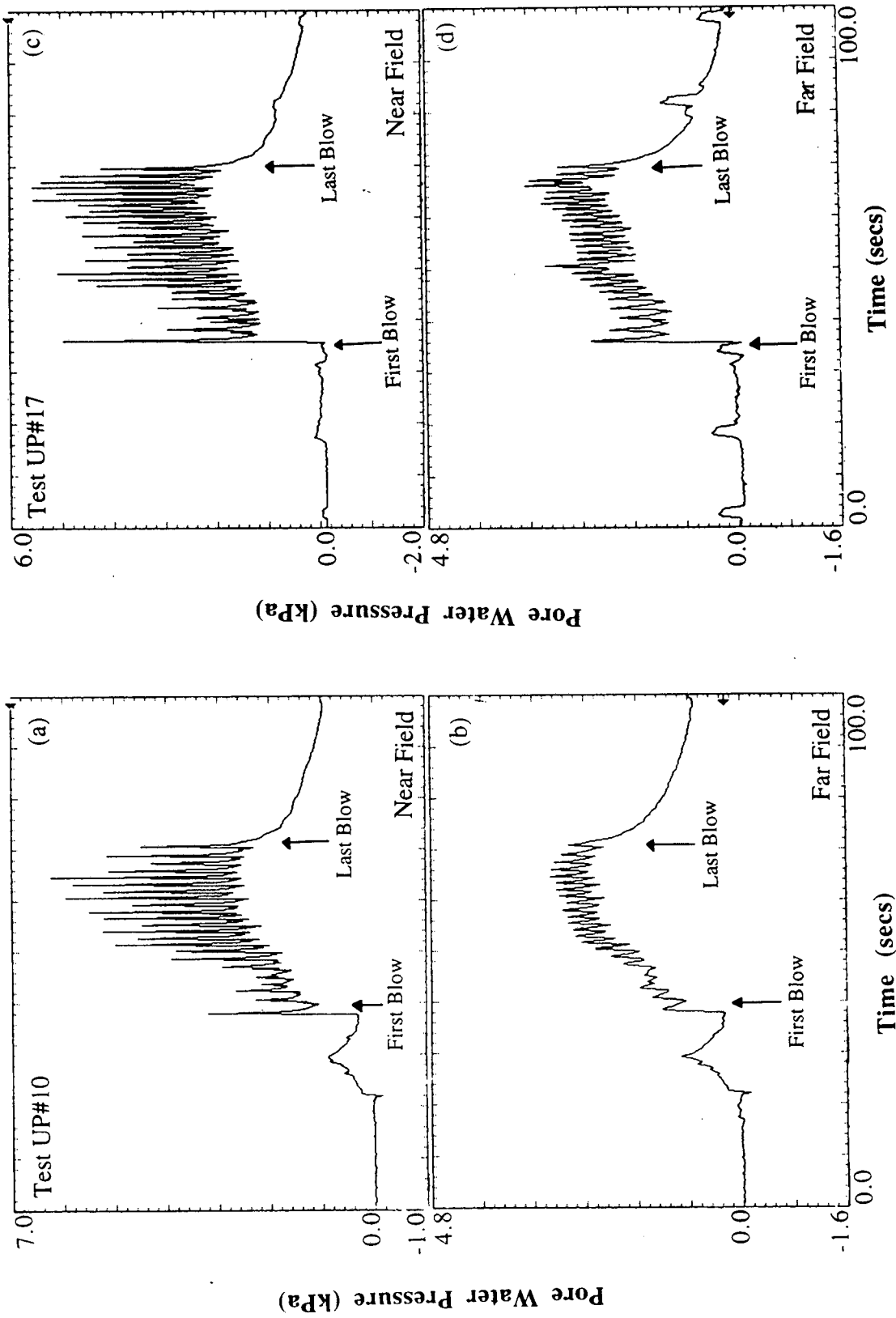
Fig. F.2: Pore Water Pressure Response During Driving Tests UP#10(a,b), and Tests UP#17(c,d)

249

APPENDIX G

Additional Data from Ground Shaking Tests
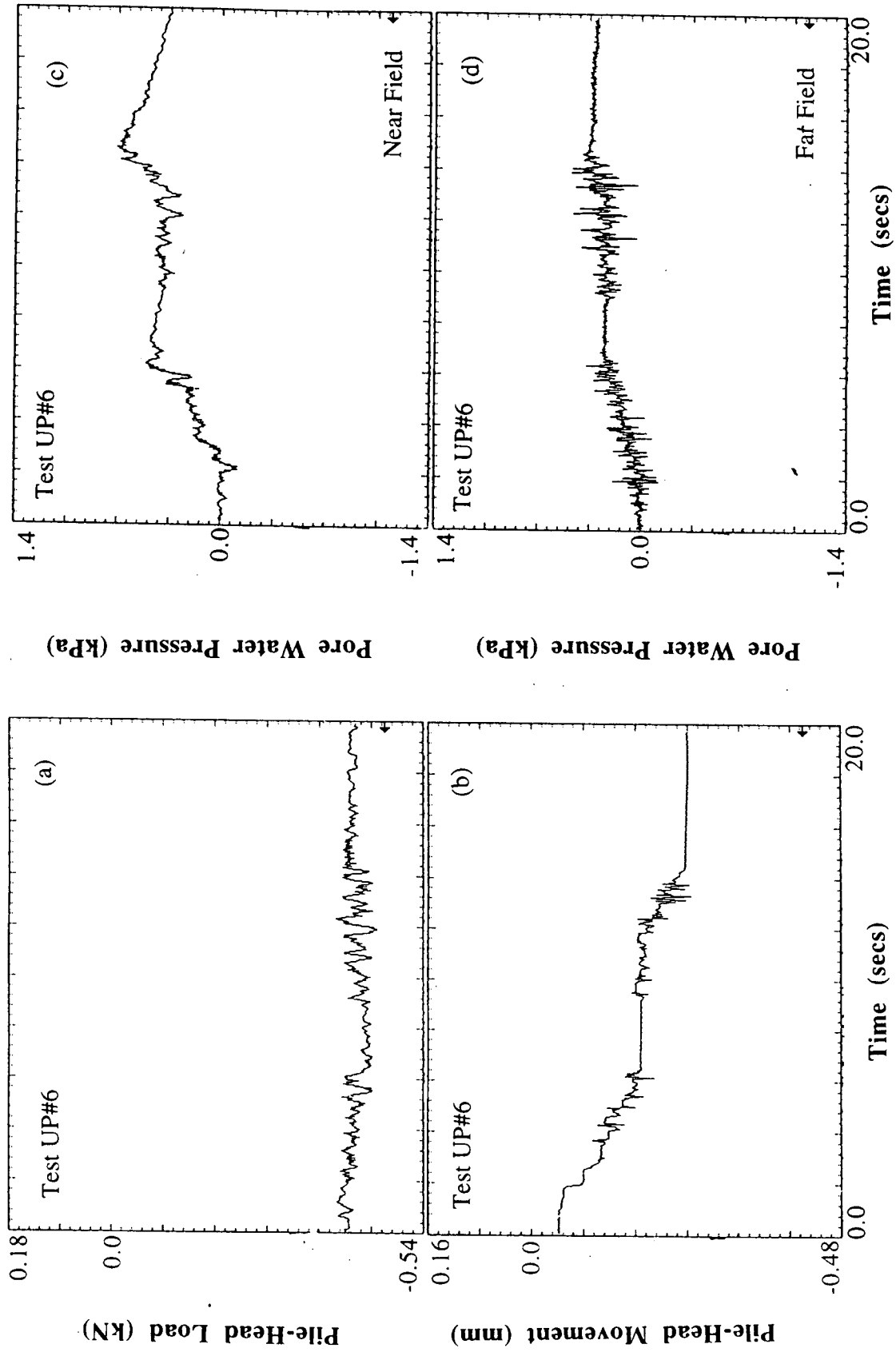
Fig. G.1: Time History Measurements During Shaking Test UP#6
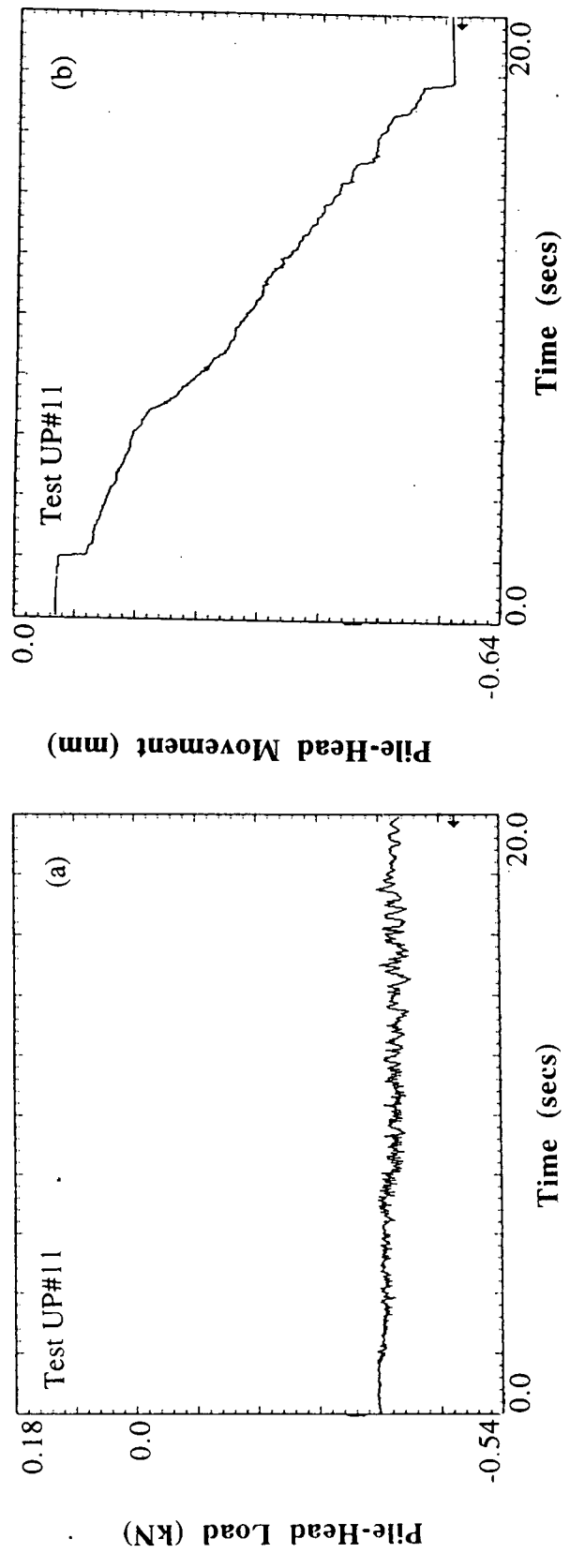
Fig. G.2: Time History Measurements During Shaking Test UP#11

Note: No Pore Water Pressure Data Available
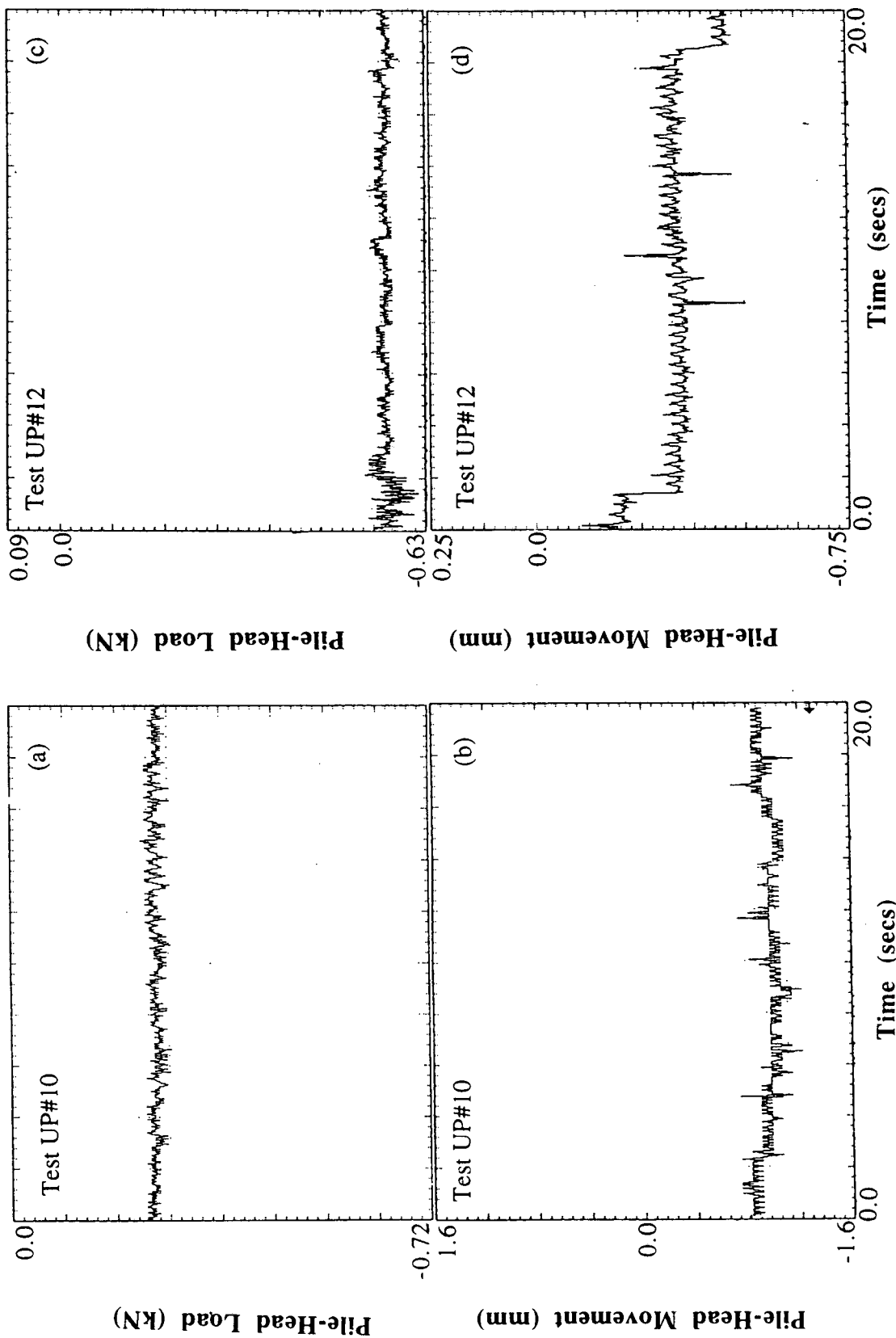
Fig. G.3: Time History Measurements During Shaking Test UP#10(a,b) and Test UP#12(c,d)

253
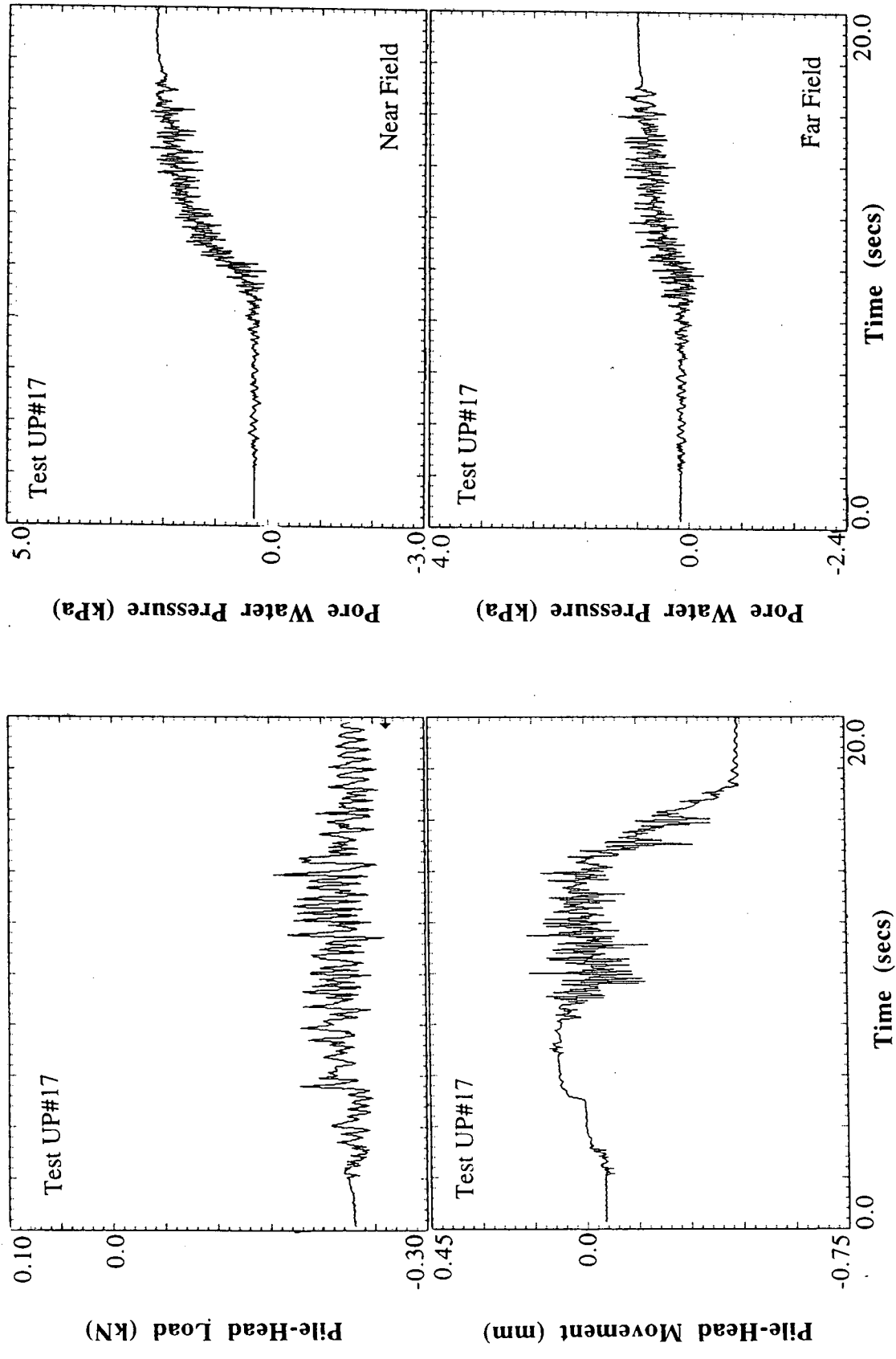
Fig. G.4: Time History Measurements During Shaking Test UP#17

254
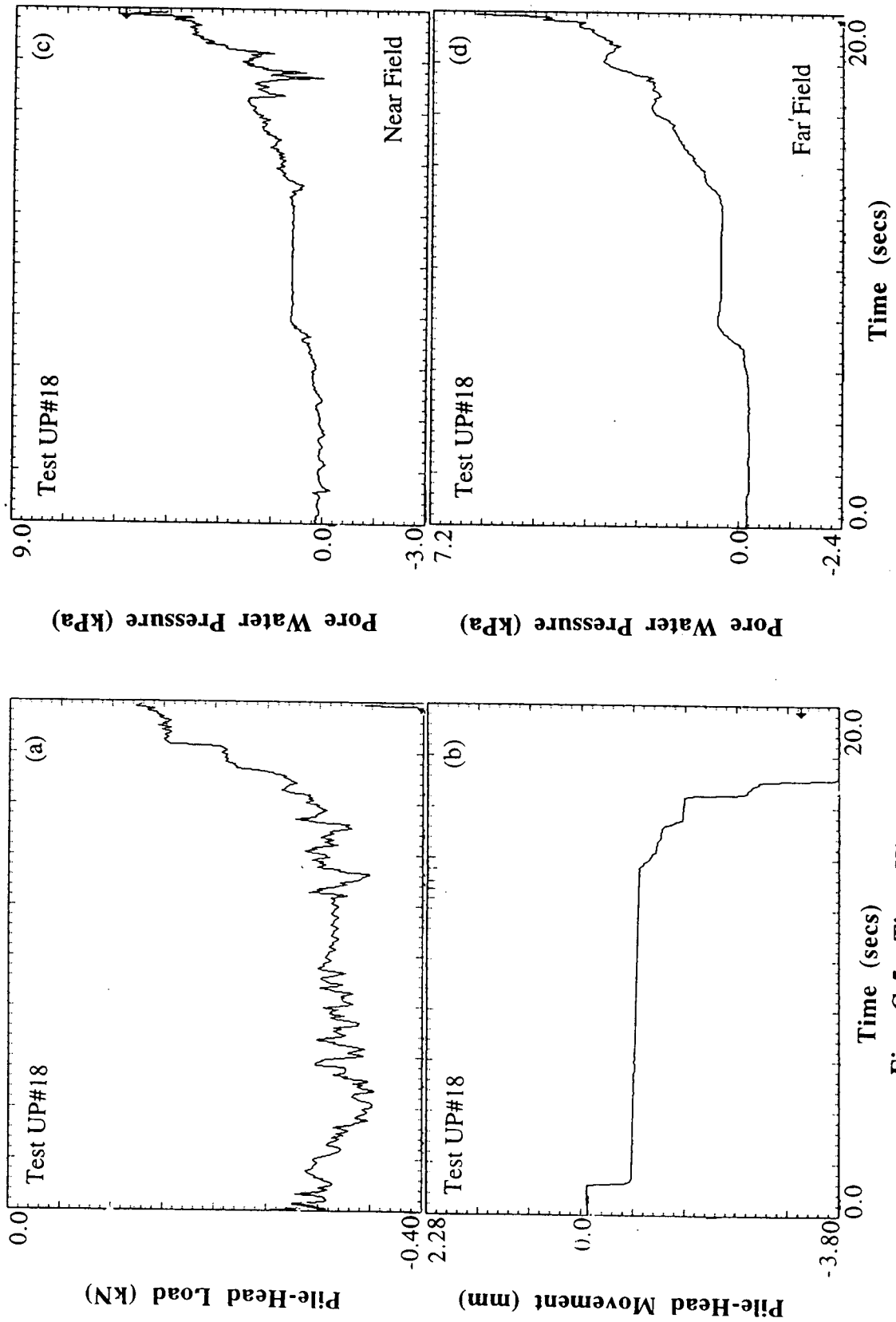
Fig. G.5: Time History Measurements During Shaking Test UP#18

255
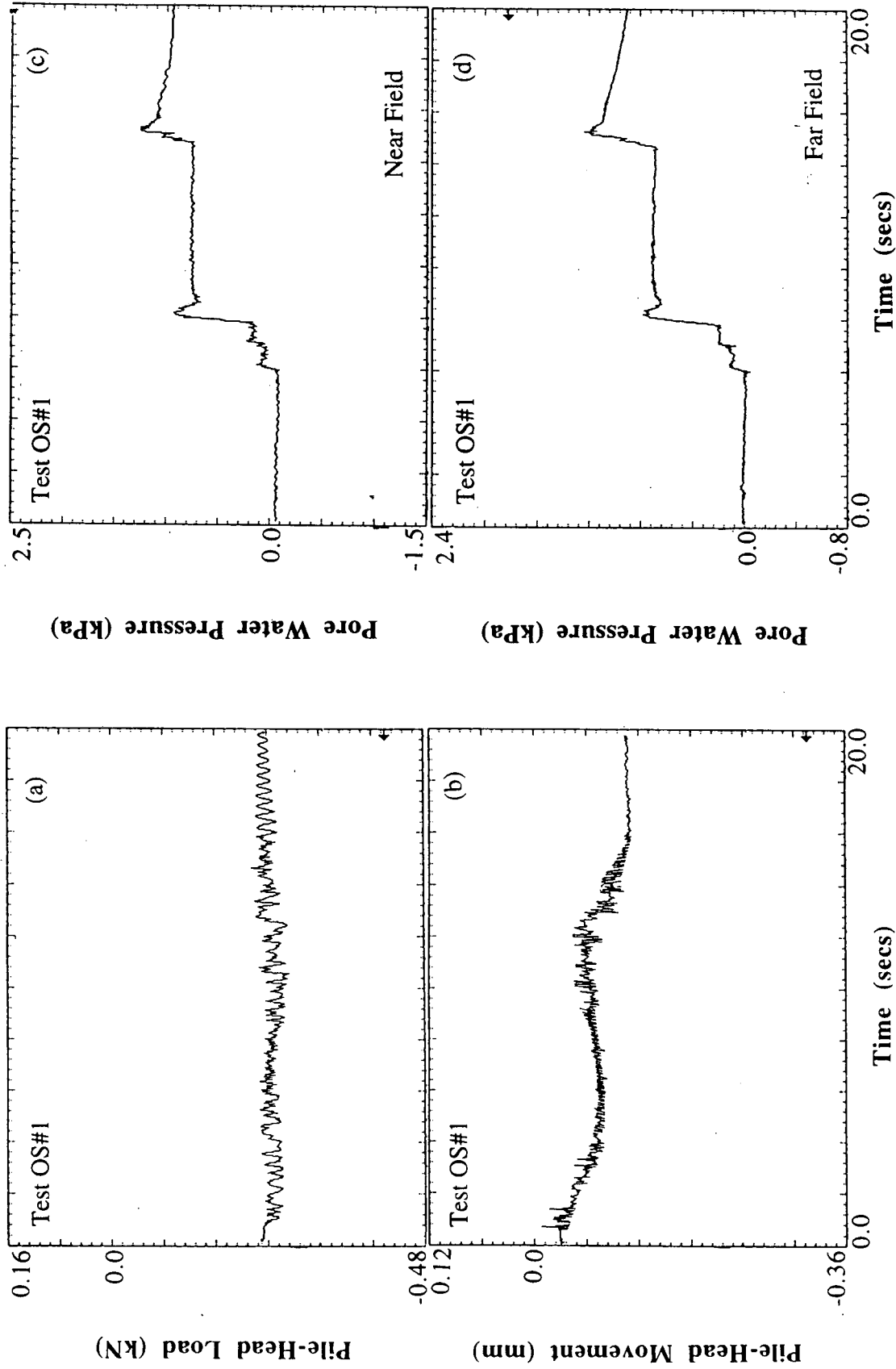
Fig. G.6: Time History Measurements During Shaking Test OS#1

256
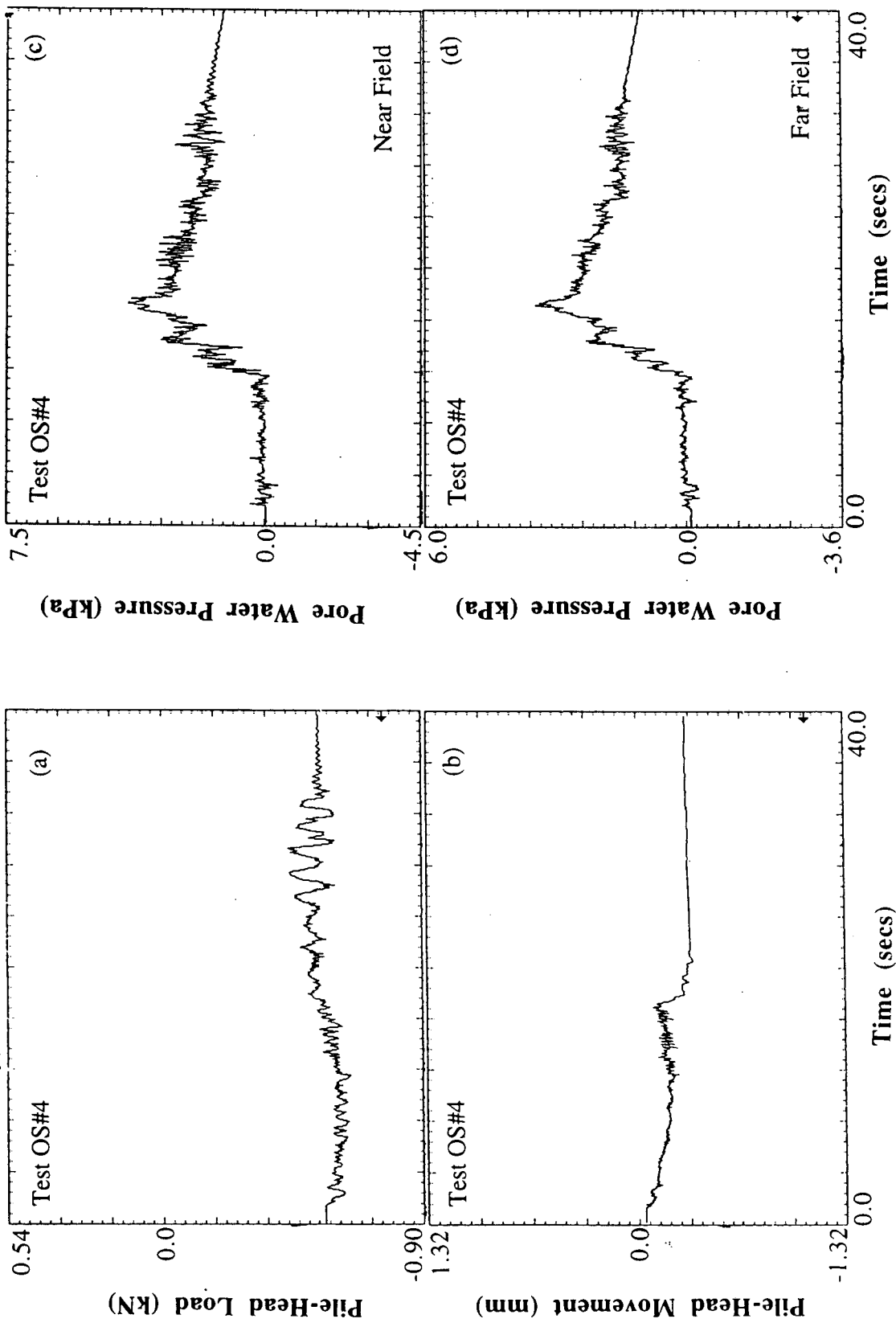
Fig. G.7: Time History Measurements During Shaking Test OS#4

257
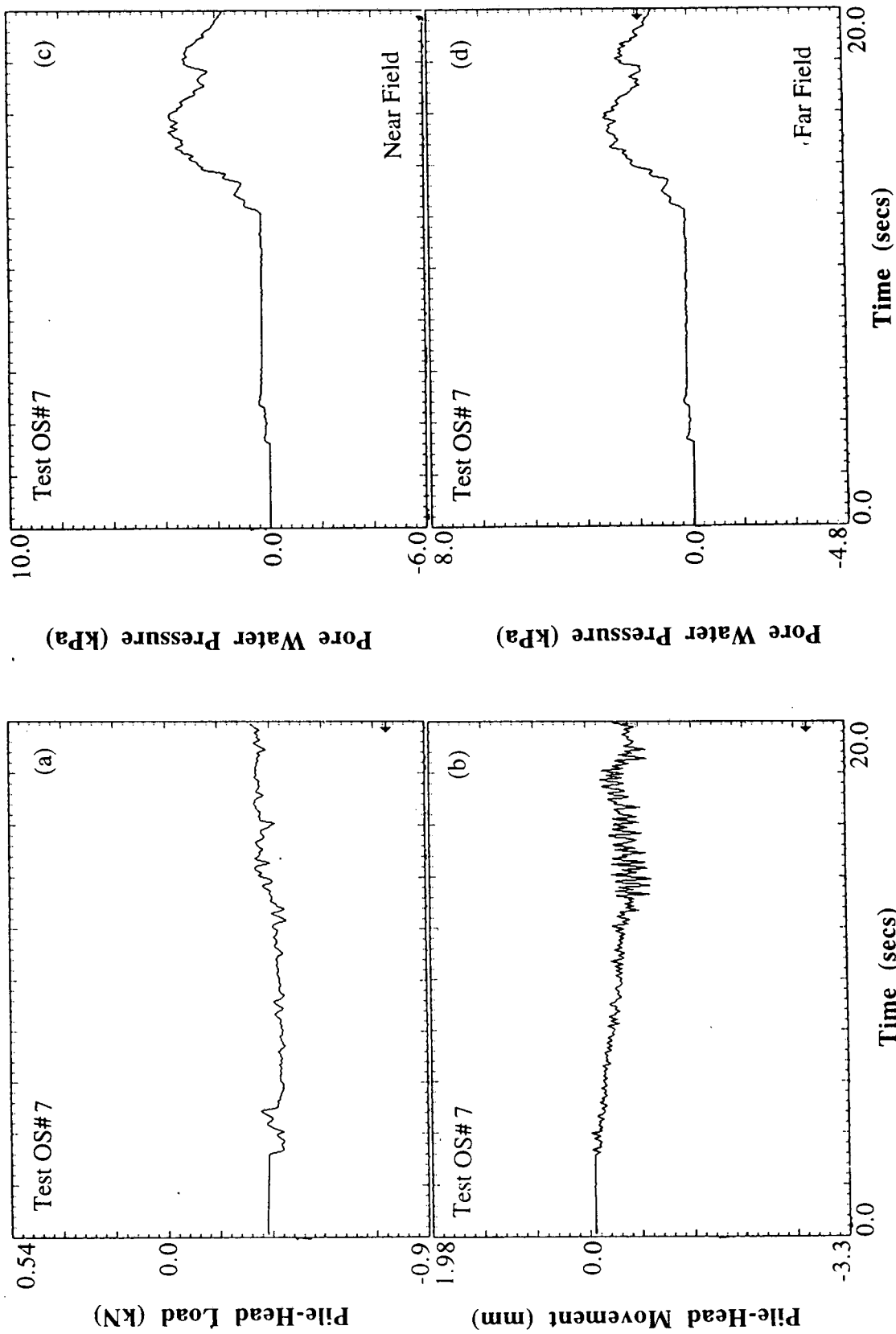
Fig. G.8: Time History Measurements During Shaking Test OS#7

258

APPENDIX H
Load-Movement Curves
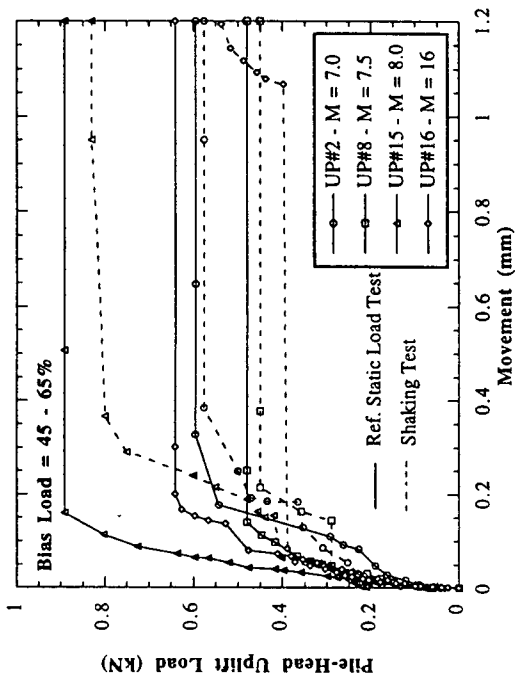
Fig. H.1: Load Movement Curves, Tests OS#2, OS#3, OS#4, and UP#1
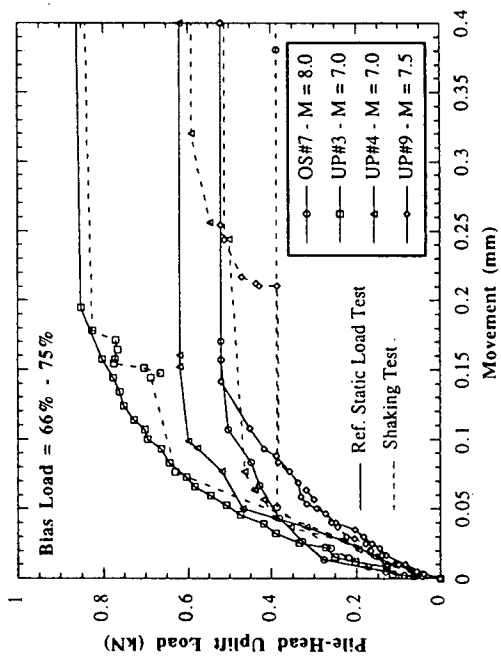
Fig. H.2: Load Movement Curves, Tests UP#2, UP#8, UP#15, and UP#16
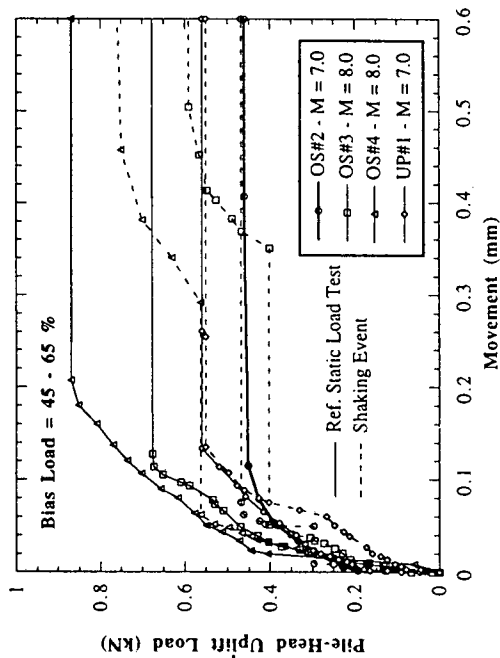
Fig. H.3: Load Movement Curves, Tests OS#7, UP#3, UP#4, and UP#9
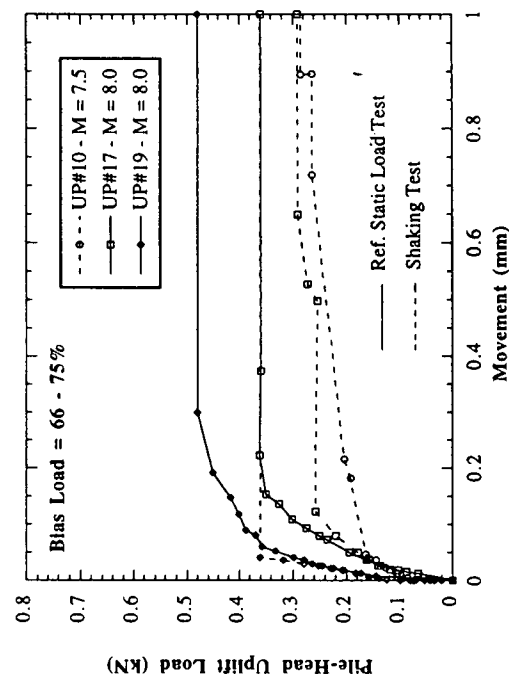
Fig. H.4: Load Movement Curves, Test UP#10, UP#17, and UP#19
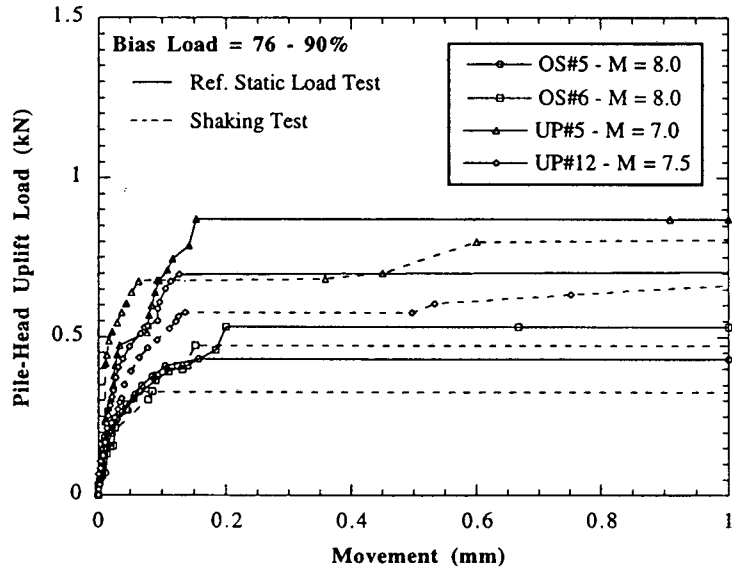
Fig. H.5: Load Movement Curves, Tests OS#5, OS#6, UP#5, and UP#12
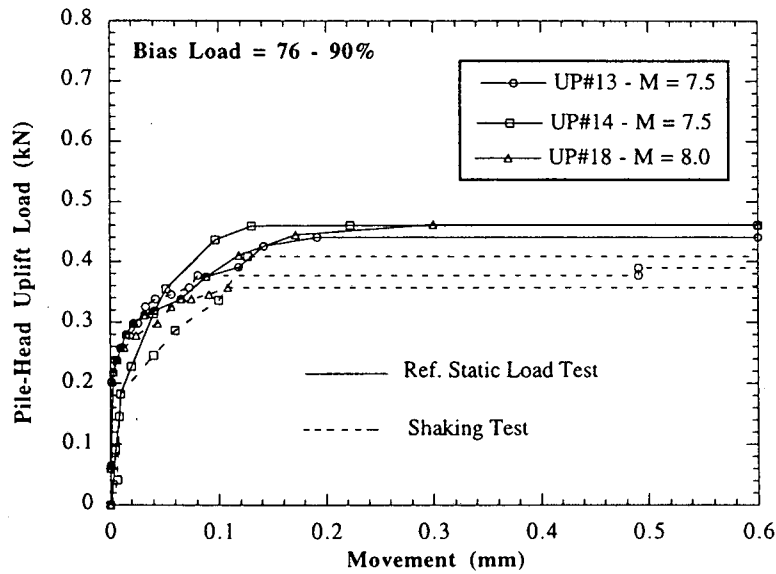
Fig. H.6: Load Movement Curves, Tests UP#13, UP#14, and UP#18

261

APPENDIX I

f-w AND p-y CURVES FOR PAR

The f-w curves for use in PAR were constructed using the following procedure:

The f-w curves along the pile length were not obtained for the model tests, only the load-displacement relationships at the pile-head were available. So, the measured load-displacement values in the model were converted first to those of the prototype by multiplying the load by the square of the static scaling factor (n_s^2) and the displacement by the static scaling factor (n_s). The computation for test R1 is shown in Table I.1.

In the prototype, it was assumed that the distribution of skin friction along the pile length is triangular and the area of the triangle is the load on the pile-head. This triangle was then subdivided into the desired number of elements (5 elements in this case), as shown in Fig. I.1. The area of each element in the triangle represented the amount of skin friction lumped to that node. These areas were: 0.01, 0.08, 0.16, 0.24, 0.32, and 0.19, respectively (with a total of 1.00), i.e., the first node resisted 1% of the total load, the second one, 8% of the total load, and so on. For a rigid pile, the displacments at all the nodes will be the same, as the elastic extension under the load is neglibile. Therefore, at any known displacement the axial soil reaction at the pile-head was obtained by multiplying the above areas to give the resistance (F) at each node. Thus, establishing the f-w curves at all the pile nodes, after dividing the respective values of F by the corresponding perimeter area of the pile.

For example, in test R1 (prototype), the f-w curve at node 1 was constructed as follows:

The displacement w_{p1} is the same as w_p (at the pile-head) (i.e., 0.006, 0.013 0.022 mm and so on) and the load transferred at node 1, F_{p1}, was 1% of the the total load on the pile (1% of F_{pt}, i.e., 0.101, 0.247, 0.422 kN and so on). At node 2, the displacements were also the same but the total load F_{pt} was multiplied by 8% and so on, as shown in Table I.2.
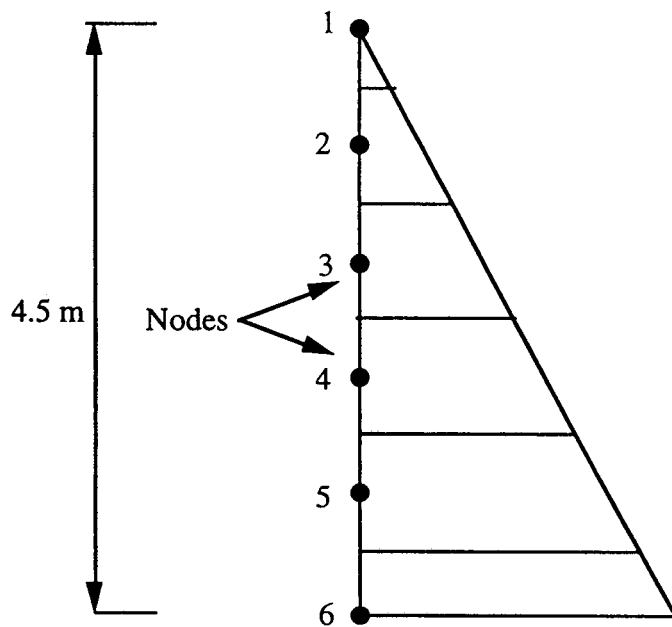
262

**Fig. I.1: Distribution of Load in Different Elements of the Pile,
The Pile is Divided into 5 Elements and 6 Nodes**

Table I.1: Static Load-Displacement Relationships , Test R1

Model Displ. w_m (mm)	Model Shear Resistance F_m (kN)	Prot. Dis. w_p (mm)	Prot. Shear Resistance F_p (kN)
0.00483	0.045	0.006045	10.13
0.1041	0.110	0.01303	24.65
0.0178	0.188	0.0222	42.24
0.0277	0.223	0.0346	50.11
0.0462	0.273	0.0578	61.36
0.0553	0.309	0.0692	69.55
0.0678	0.332	0.0848	74.66
0.1016	0.379	0.127	85.30
0.1651	0.436	0.206	98.18

Table I.2: F-w Curves of the Prototype at the Pile Nodes for Test R1

w_p (mm)	F_{pt} (kN)	F_{p1} = 0.01F_{pt} (kN)	F_{p2} = 0.08F_{pt} (kN)	F_{p3} = 0.16F_{pt} (kN)	F_{p4} = 0.24F_{pt} (kN)	F_{p5} = 0.32F_{pt} (kN)	F_{p6} = 0.19F_{pt} (kN)
0.006	10.13	0.101	0.810	1.621	2.431	3.242	1.925
0.013	24.65	0.247	1.972	3.944	5.916	7.888	4.684
0.022	42.24	0.422	3.379	6.758	10.138	13.517	8.026
0.0346	50.11	0.501	4.009	8.018	12.026	16.035	9.521
0.0578	60.36	0.604	4.829	9.658	14.486	19.315	11.468
0.0692	69.55	0.696	5.564	11.128	16.692	22.256	13.214
0.0848	74.66	0.747	5.973	11.946	17.918	23.891	14.185
0.127	85.30	0.853	6.824	13.648	20.472	27.296	16.207
0.206	98.18	0.982	7.854	15.709	23.563	31.418	18.654

p-y Curves

The p-y curves used in the PAR analysis of the prototype pile were generated using the recent API criteria (API, RP 2A-LRFD, 1993) for sand . Assuming $\phi' = 36$ degs. for the prototype sand, the ultimate lateral bearing capacity for the sand at a given depth is given by the smallest value of

$$p_{us} = (C_1*H + C_2*D) * \gamma' * H, \text{ and} \tag{I.1}$$

$$p_{ud} = C_3 *D* \gamma' * H, \tag{I.2}$$

where

p_u = ultimate lateral resistance (kN/m) (s = shallow, d = deep),

γ' = effective soil weight (kN/m^3),

H = depth (m),

C_1, C_2, and C_3 = coefficients expressed as a function of ϕ' (angle of internal friction), and

D = average pile diameter from surface to depth , m

For $\phi' = 36$ degs, C_1= 3.33, C_2 = 3.66, C_3 = 60., k (initial modulus of subgrade reaction) = 24271 kN/m^3

The lateral soil resistance-deflection relationships for sand at any specific depth, H, is given by the following expression:

$$P = A \, p_u \tanh [\, (k \, H \, y) / (A \, p_u) \,],\qquad\qquad (I.3)$$

where

$A = (3 - 0.8 \, H / D) \geq 0.9$ for static loading,

p_u = ultimate lateral capacity at depth H, kN/m,

k = initial modulus of subgrade reaction (kN/m^3),

y = lateral deflection in m,

$\dot{H}$ = depth in m.

Substituting values in (I.1), (I.2), and (I.3), the p-y curves were generated at each of the six nodes for the the 4.5 m long prototype pile shown in Fig. I.1. These curves are shown in Fig I.2
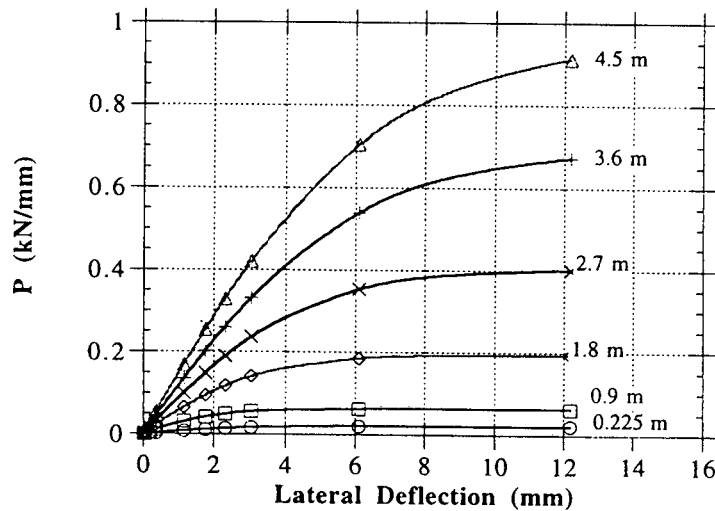
Fig. I.2 : Static p-y Curves at Different Nodes
for the Prototype Pile

APPENDIX J

Vertical Stress Transfer to Chamber Base

The distribution of the vertical stress in the soil deposited by raining inside a pile testing chamber is influenced by the test chamber boundary conditions. An experimental investigation by Al-Douri, et al.(1993) identified that the value of the applied overburden pressure, the roughness of the internal wall of the chamber and the dimensions of the chamber, affected the sand bed response in test chambers and consequently the behavior of model foundations tested in the sand bed. They developed a simple theoretical equation to predict the vertical stress distribution in the soil. The vertical stress at any depth, z, as shown in Fig. J.1, can be expressed by

$$q = q_0 e^{(-z/z_0)} + (\gamma z_0) (1 - e^{(-z/z_0)}) \tag{J.1}$$

where

$q_0 = q (z = 0)$ is the overburden pressure at the top surface of the soil,

γ = bulk unit weight of the soil,

$z_0 = R / 2\mu K$.

R is the radius of the chamber, μ = coefficient of friction between the soil and the chamber wall, and K is defined as the ratio of the horizontal pressure to the vertical pressure in the soil, i.e., the lateral pressure coefficient

Interpretation of the seaquake tests required the knowledge of the initial vertical stress profile in the sand bed. This led to an independant study were measurements were taken of the vertical stress at the base of the sand inside the testing chamber when different overburden pressures were applied to the soil surface. The sand was deposited by raining inside the chamber in a manner similar to that followed during the signature or the seaquake tests. Prior to deposition, a calibrated total soil pressure cell, Gentran Inc., model PG - 102

266

was placed at the base of the chamber for measurement of the vertical stress. The soil deposition then continued up to a depth 25.4 mm short of the top rim of the chamber. At this point, the top rubber bladder and the plate were assembled. Calibration for the soil pressure cell has been presented in Appendix B.

The top rubber bladder was then connected to an air supply panel, and the pressure in the bladder was gradually increased from 0 to 82 kPa. Stabilized readings from the transducers were recorded at two stages of applied pressure 41 kPa, and 82 kPa. Table J-1 summarizes the results of the tests performed. Results presented are average of 3 trials. From the results, it can be seen that there is about a 30 - 35% reduction in the vertical stress at the bottom of the soil which is proportional to the overburden pressure. This reduction can be attributed mainly to the developed skin friction on the wall surface. Arching causes a reduction in the vertical stress appearing at sections down the test chamber.

The second column in Table J.1 shows the values of the vertical stress at the base of the chamber predicted using (J.1) with the following parameters.

$\mu = 0.5$ (lower bound value for siliceous sand-teflon interface)

$K = (1 - \text{Sin } \phi) = 0.41$ for $\phi = 36$ degrees

$\gamma = 16.85 \text{ kN/m}^3$ (average bulk density obtained during testing)

$z = 508$ mm

$R = 254$ mm

(J.1) predicts the measured values within 20% and hence can provide a reasonable estimate of the initial overburden stress distribution in the chamber for other values of applied overburden pressures.

Table J.1: Measured and Predicted Vertical Stress at the Bottom of Silica Sand Bed

Overburden Pressure (kPa), q_o	Measured Vertical Stress at the Bottom , q_b (kPa)	Predicted Vertical Stress at the Bottom, q_b (kPa)
41	28	24
82	53	42
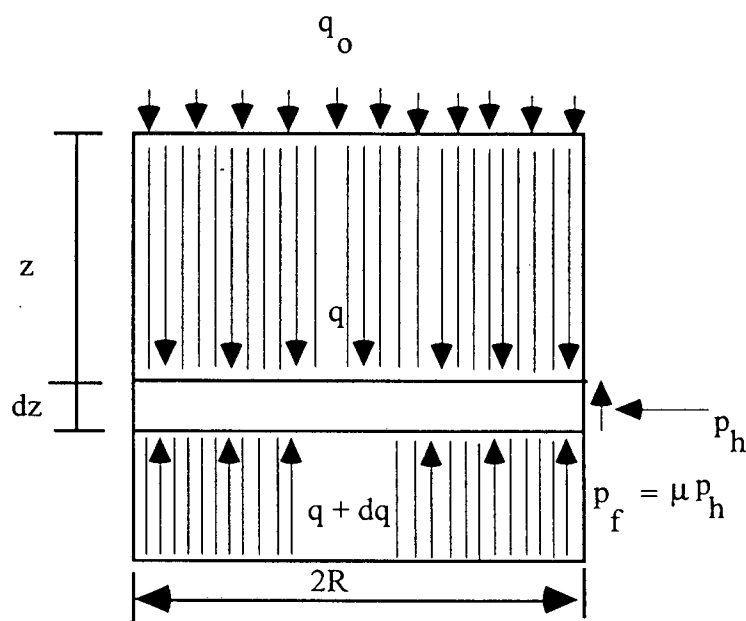
Fig. J.1 Stresses Acting Upon a Horizontal Section of the Soil in the Cylindrical Chamber

Using (J.1), the vertical effective stress transferred at the base of the sand in the chamber for known values of overburden stress applied to the top of sand surface in the chamber were computed and tabulated in Table J.2.

Table J.2: Interpreted Mean Effective Stress in the Chamber

Overburden Pressure Applied Soil Surface (a) kPa	Predicted Vertical Effective Stress at the Base of the sand (b) kPa	Mean Vertical Effective Stress, $\sigma_v' = \dfrac{(a + b)}{2}$ kPa	Interpreted Mean Effective in the Chamber, $\sigma_m' = \dfrac{(1 + 2K)\,\sigma_v'}{3}$ kPa
41.38	24	33	20
124.14	61	93	56
250.00	115	183	112
303.45	139	221	134

APPENDIX K

SEA-SEABED INTERACTION TEST RESULTS
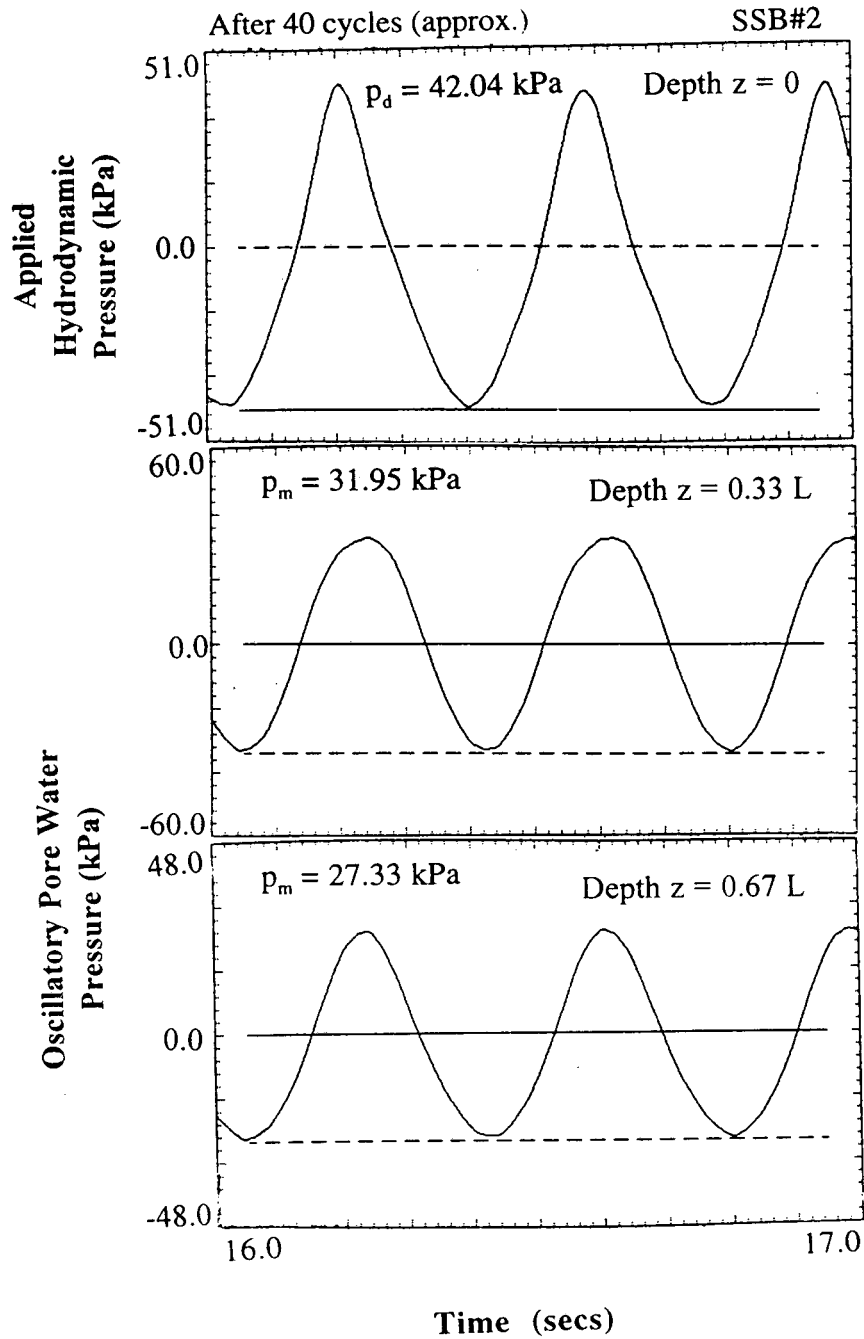
Fig. K.1: Measurements of Seaquake-Associated Seabed Pressure and Oscillatory Pore Water Pressure in the Soil Mass After 40 cycles of Loading - SSB#2

271

Phase Lag w.r.t. p_d
z = 0.33 L 12 degs
z = 0.67 L 17 degs

p_s = 37.24 kPa (hydrostatic)   SSB#4

Depth z = 0

Depth z = 0.33 L

Depth z = 0.67 L

84.0

0.0

-84.0

80.0

0.0

-80.0

64.0

0.0

-64.0

0.0

10.0

Time (secs)

Applied Hydrodynamic Pressure (kPa)

Oscillatory Pore Water Pressure (kPa)
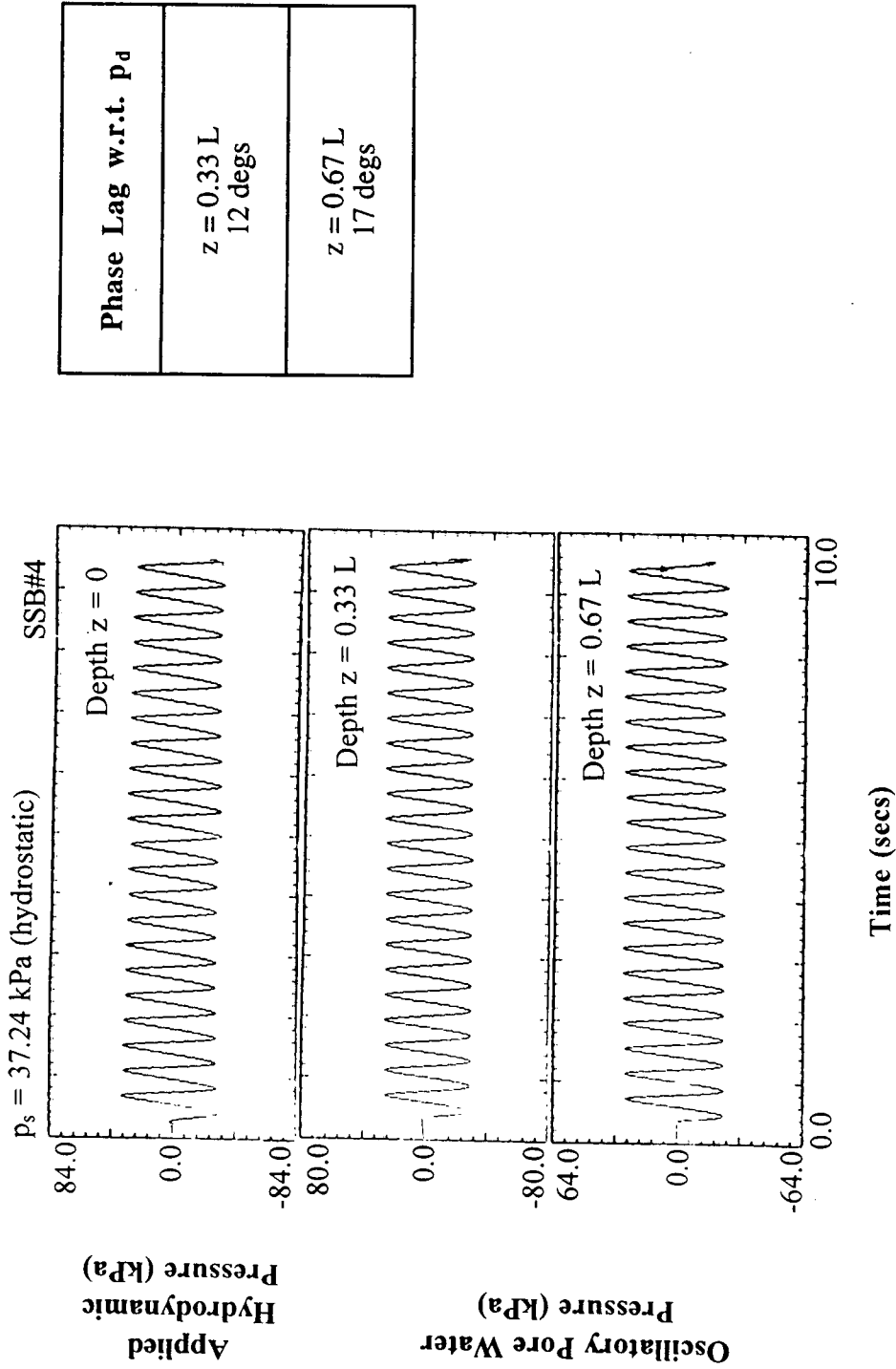
Fig. K.2: Pore Water Pressure Response During Seaquake Loading - SSB#4
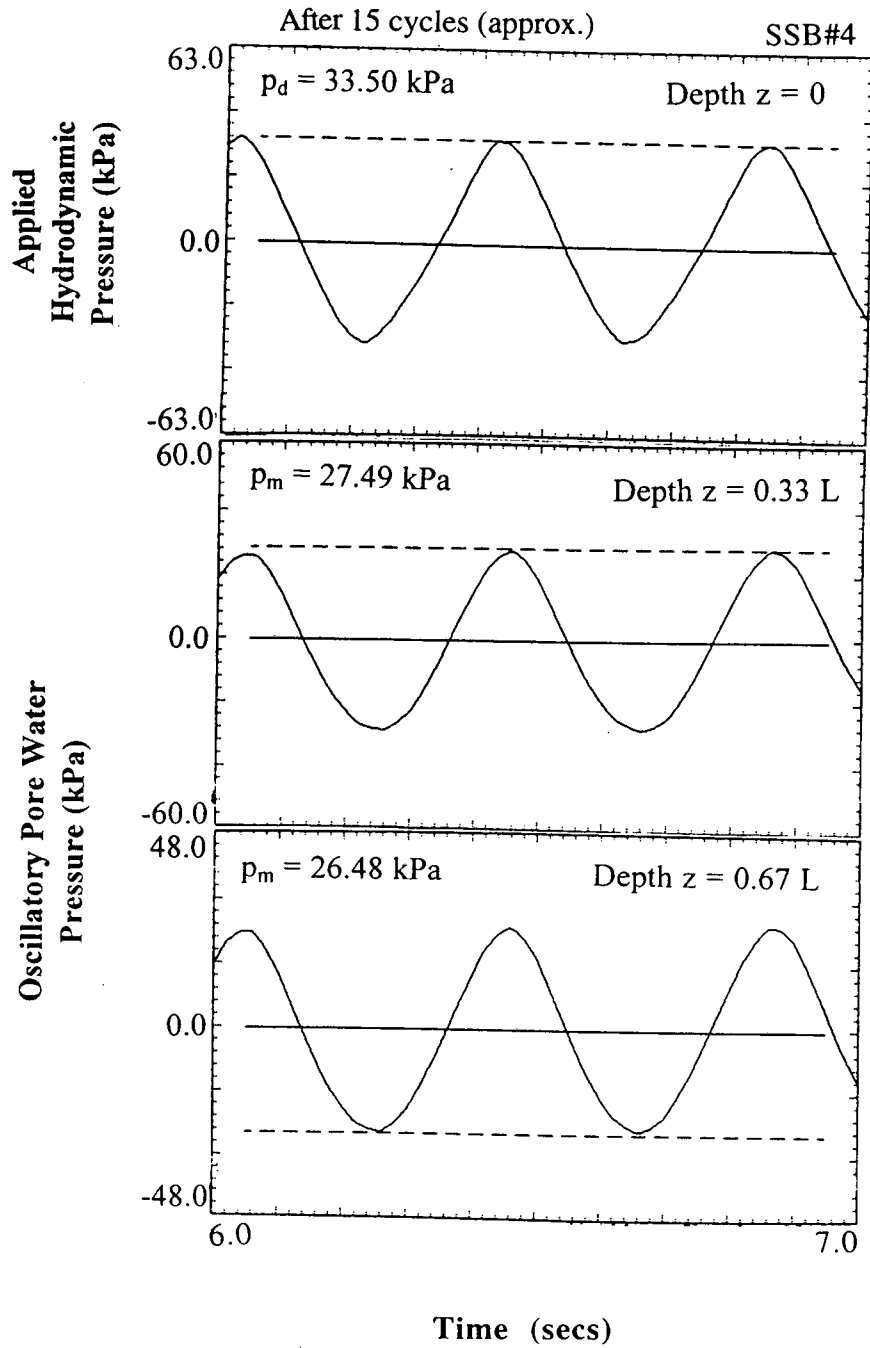
Fig. K.3: Measurements of Seaquake-Associated Seabed Pressure and Oscillatory Pore Water Pressure in the Soil Mass After 15 cycles of Loading - SSB#4
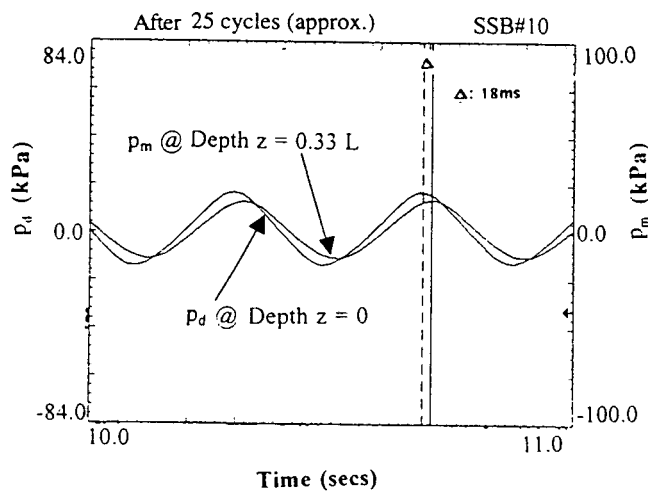
273
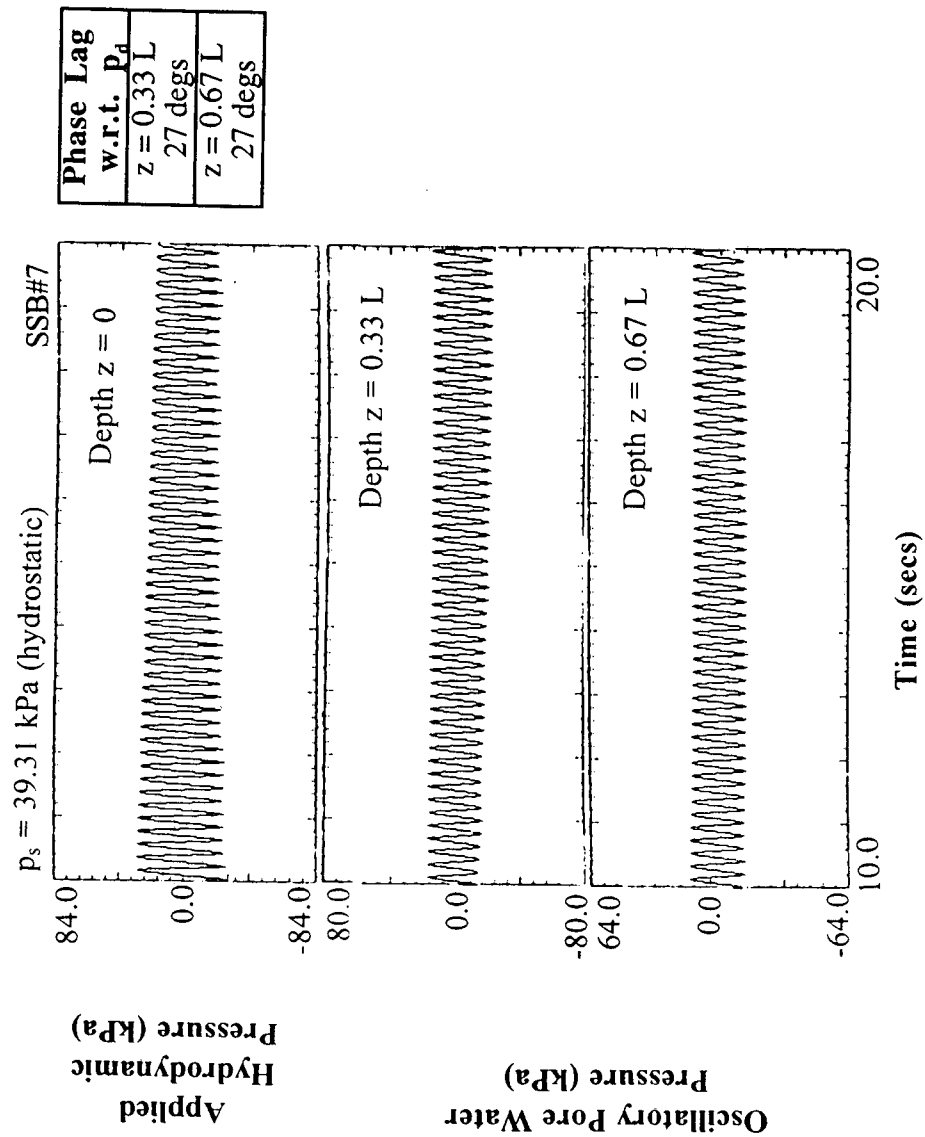
Fig. K.4: Pore Water Pressure Response During Seaquake Loading - SSB#7
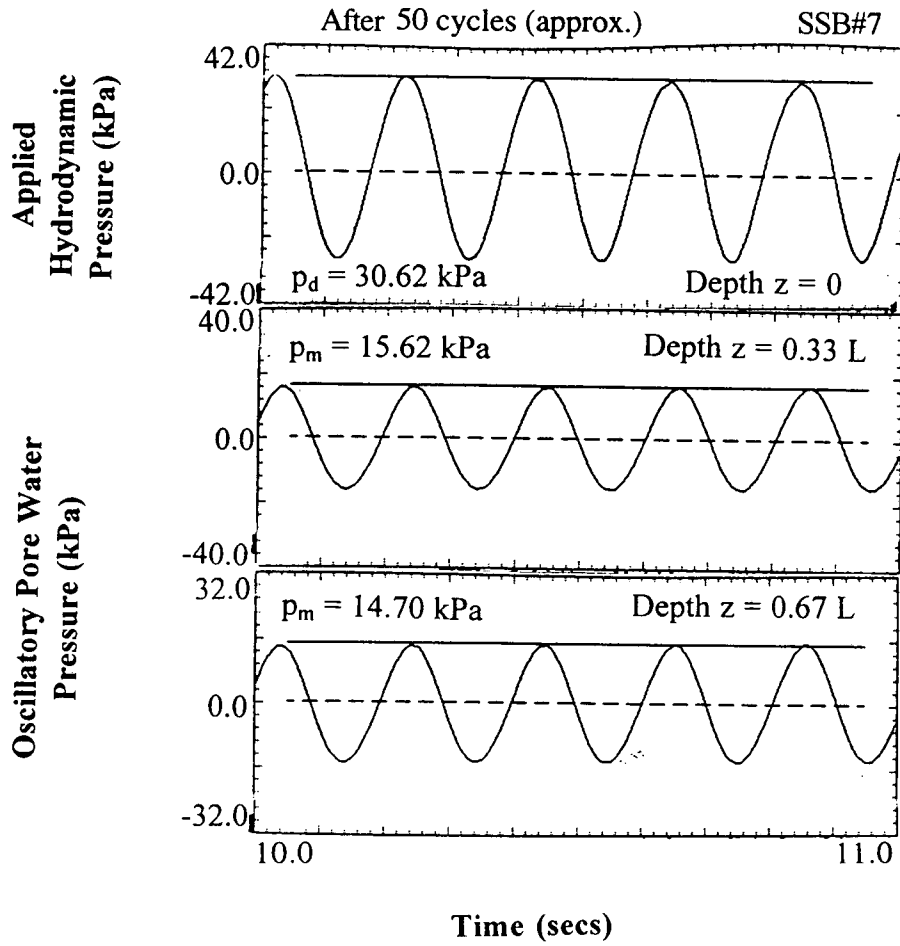
Fig. K.5: Measurements of Seaquake-Associated Seabed Pressure and Oscillatory Pore Water Pressure in the Soil Mass After 50 cycles of Loading - SSB#7
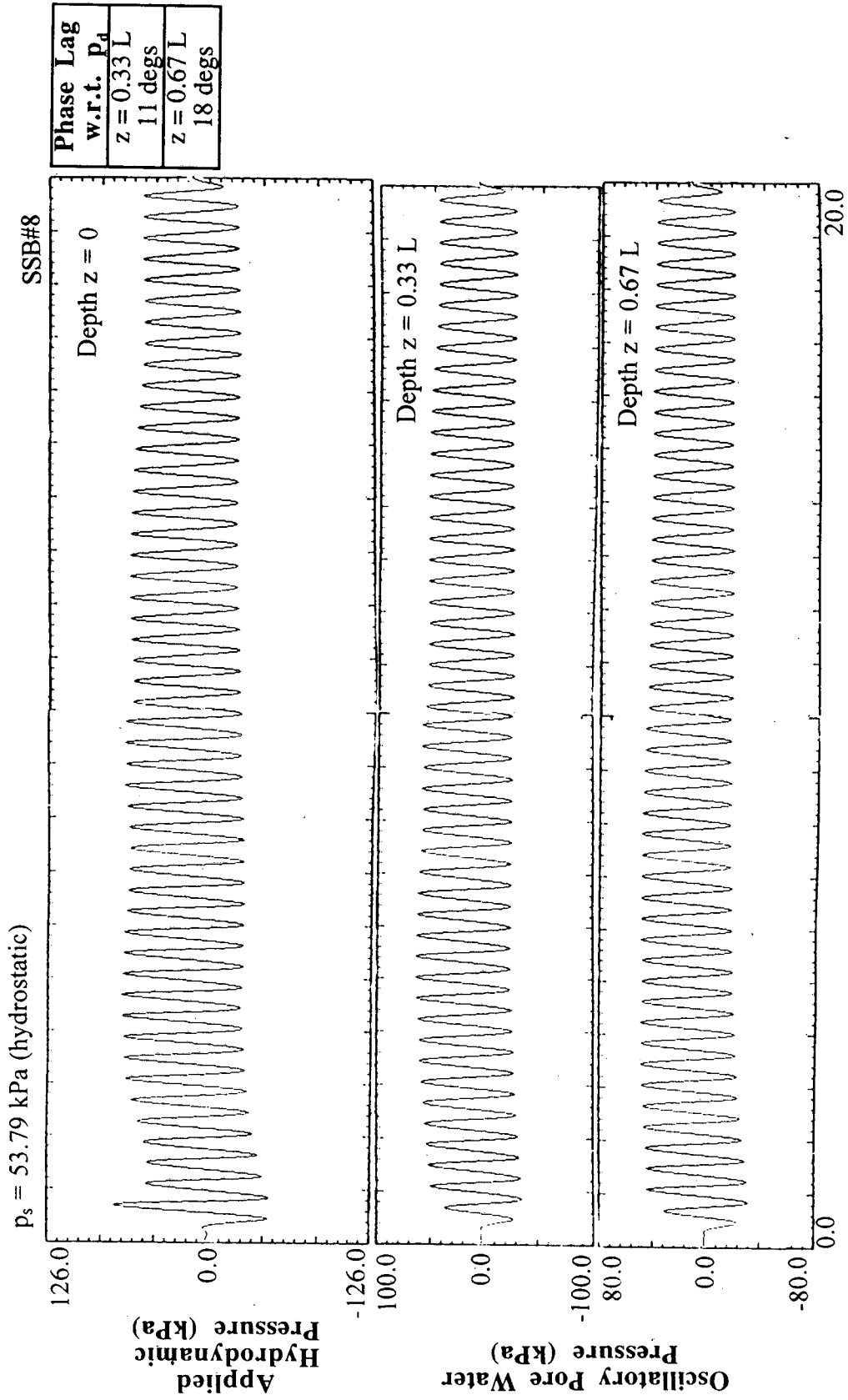
Fig. K.6: Pore Water Response During Seaquake Loading - SSB#8
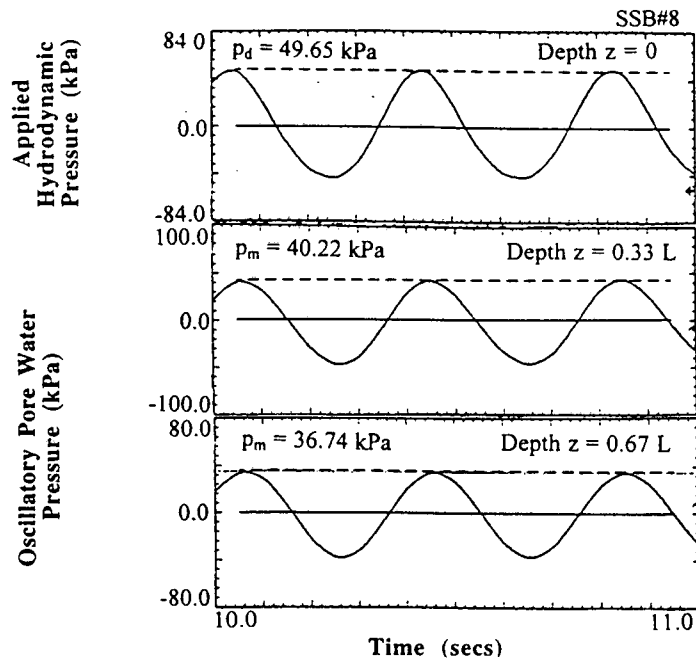
Fig. K.7: Measurements of Seaquake-Associated Seabed Pressure and Oscillatory Pore Water Pressure in the Soil Mass After 25 Cycles of Loading - SSB#8
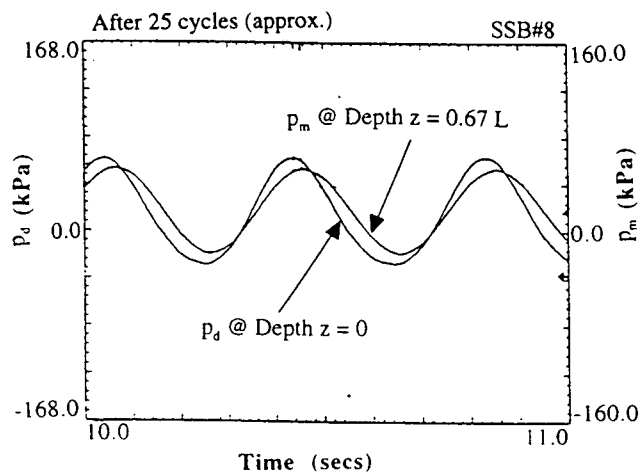
Fig. K.8: Illustration of Phase Lag Between the Seaquake-Associated Seabed Pressure and Oscillatory Pore Water Pressure at z = 0.67L - SSB# 8

277
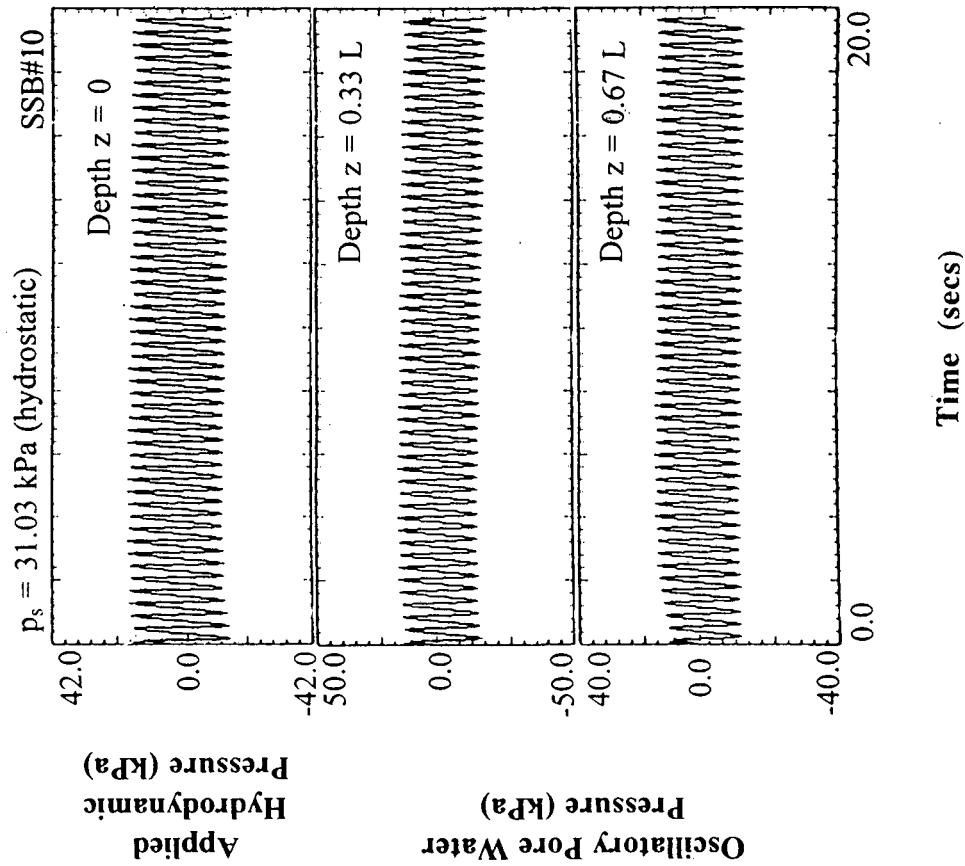
Phase Lag w.r.t. p_d
$z = 0.33$ L 14.4 degs
$z = 0.67$ L 21.6 degs

Fig. K.9: Pore Water Pressure Response During Seaquake Loading - SSB#10

278
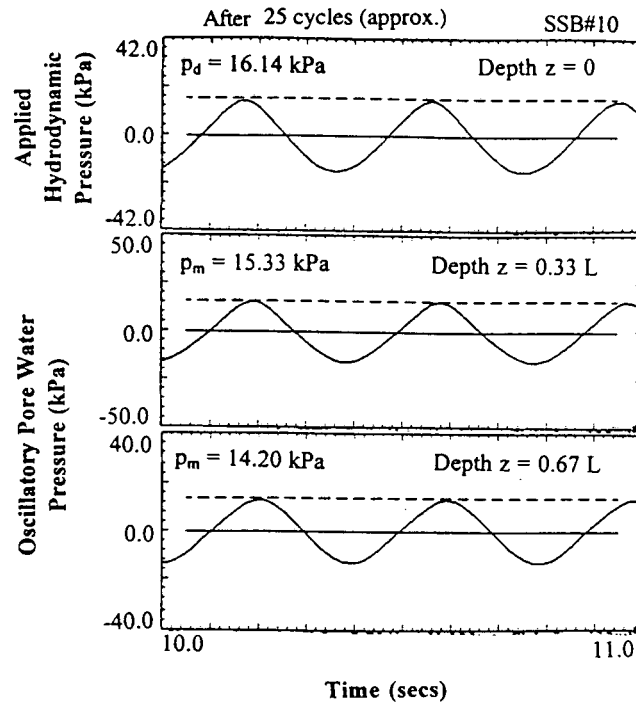
Fig. K.10: Measurements of Seaquake-Associated Seabed Pressure and Oscillatory Pore Water Pressure in the Soil Mass After 25 Cycles of Loading - SSB#10

Fig. K.11: Illustration of Phase Lag Between the Seaquake-Associated Seabed Pressure and Oscillatory Pore Water Pressure at z = 0.33L - SSB# 10

279

APPENDIX L

PILE RESPONSE TO SEAQUAKE TEST RESULTS
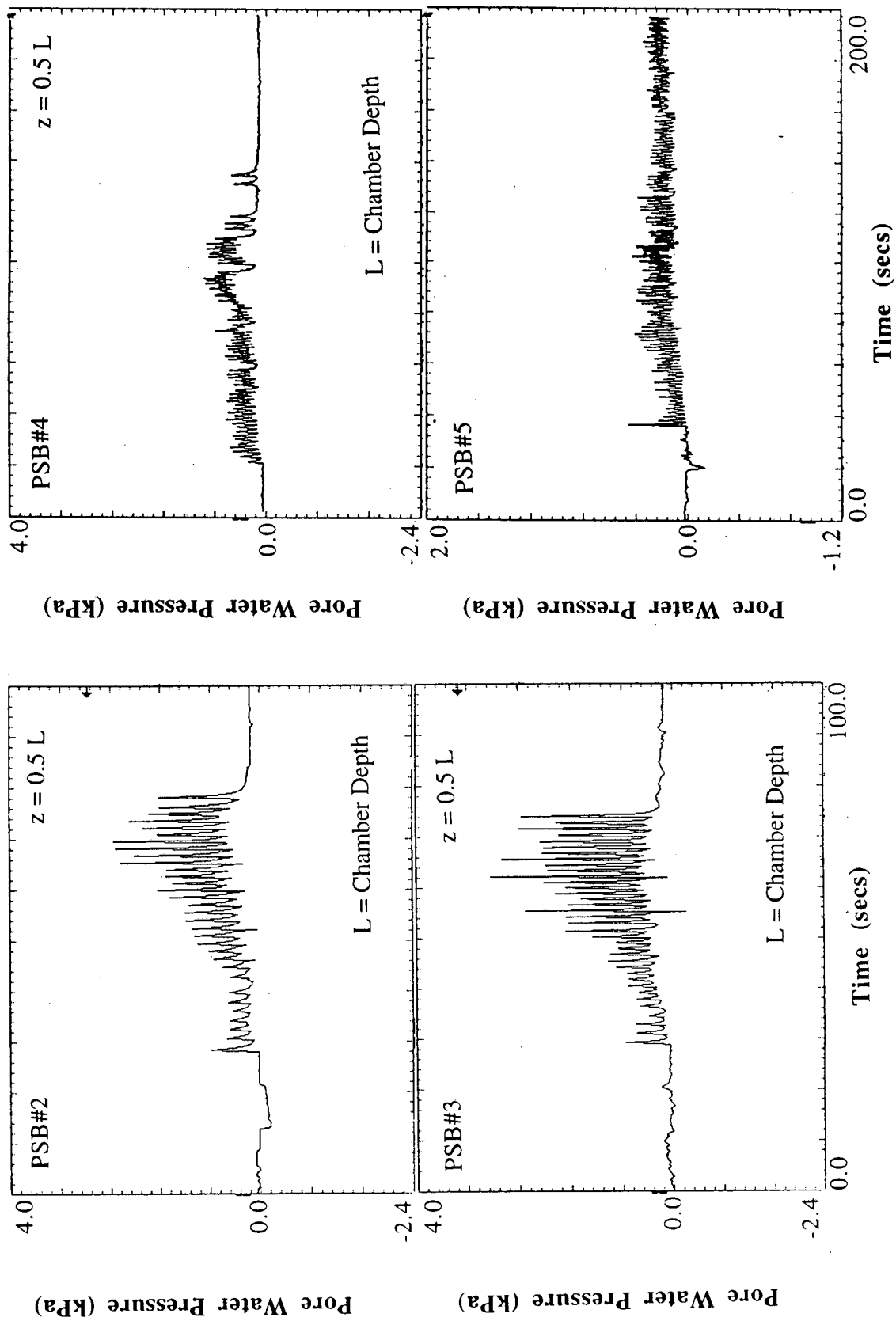
Fig. L.1: Pore Water Pressure Measured During Driving - PSB#2, PSB#3, PSB#4, and PSB#5

281
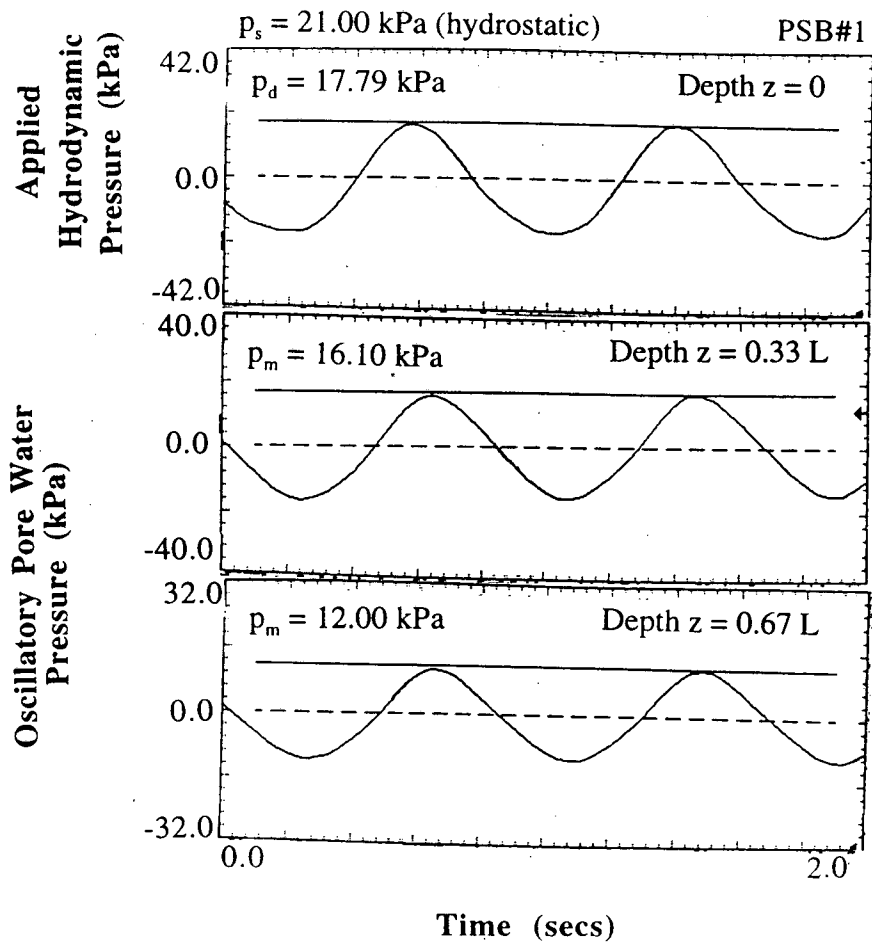
Fig. L.2: Measurements of Seaquake-Associated Seabed Pressure and Oscillatory Pore Pressure in the Soil Mass Near the Pile - PSB#1
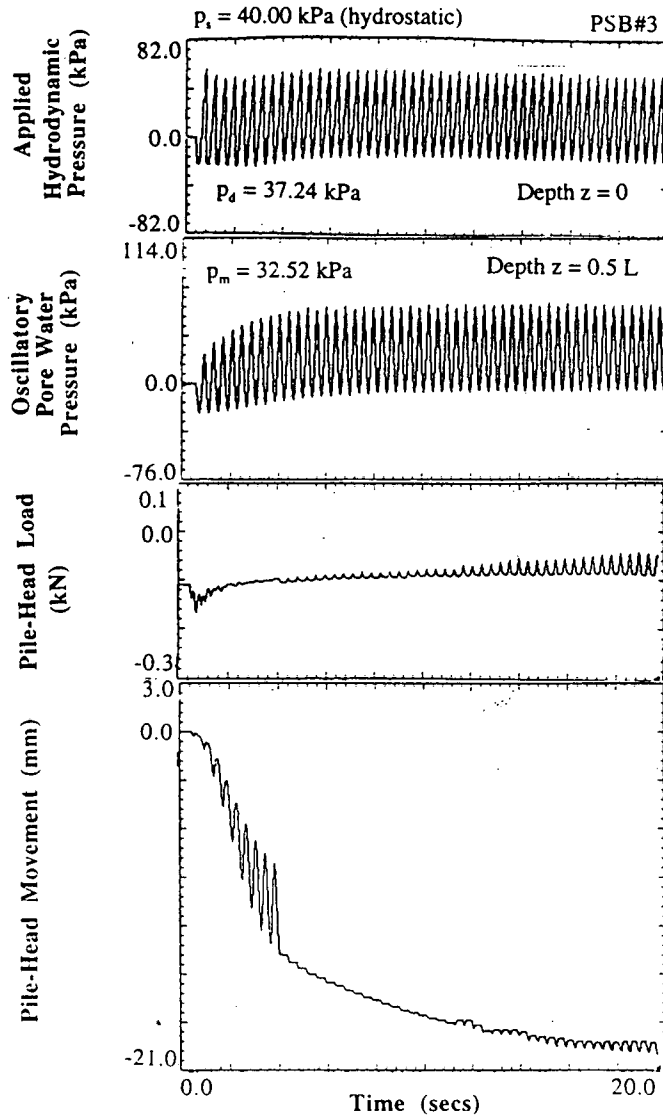
Fig. L.3: Time History Measurements of Soil and Pile Response During Seaquake Loading With 20% Bias Loading at σ'_m = 20 kPa - PSB#3
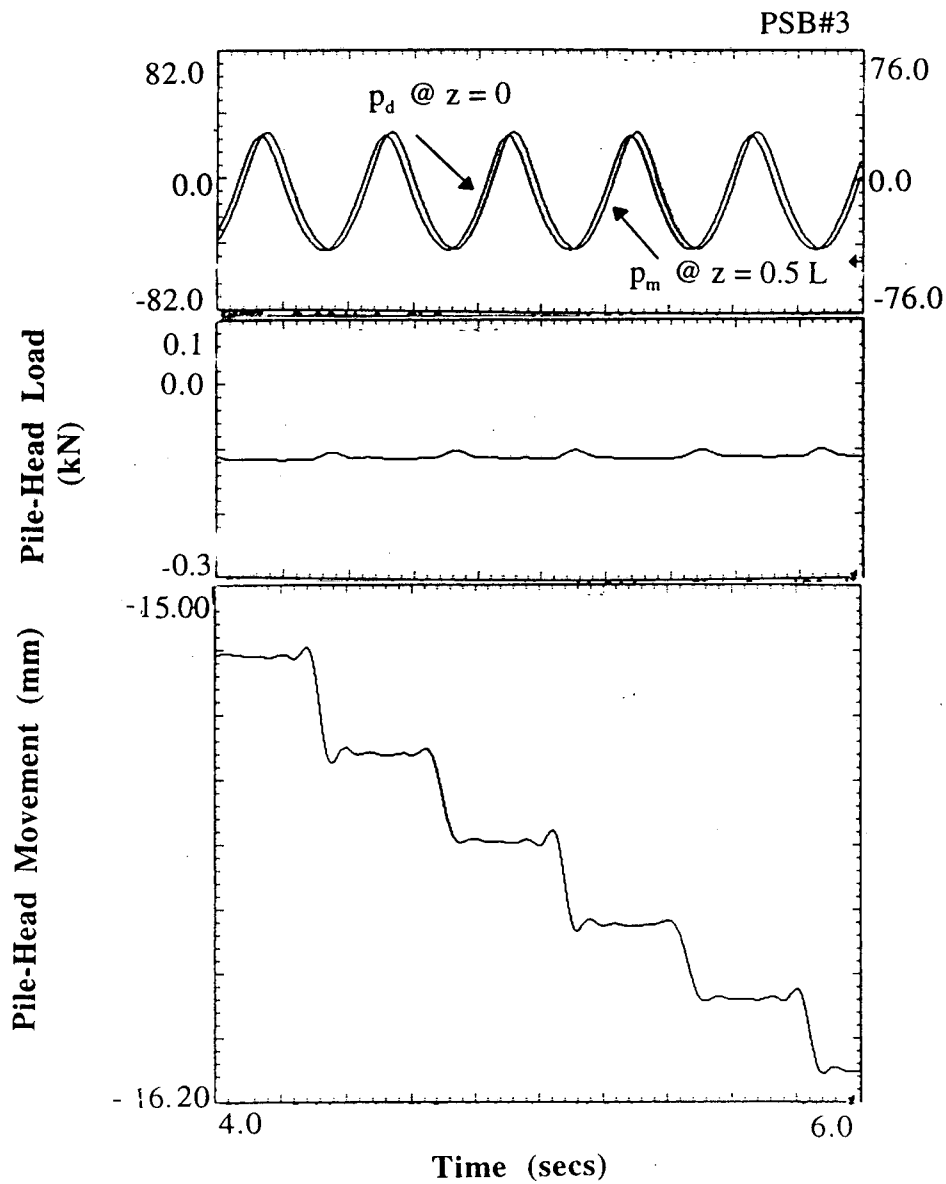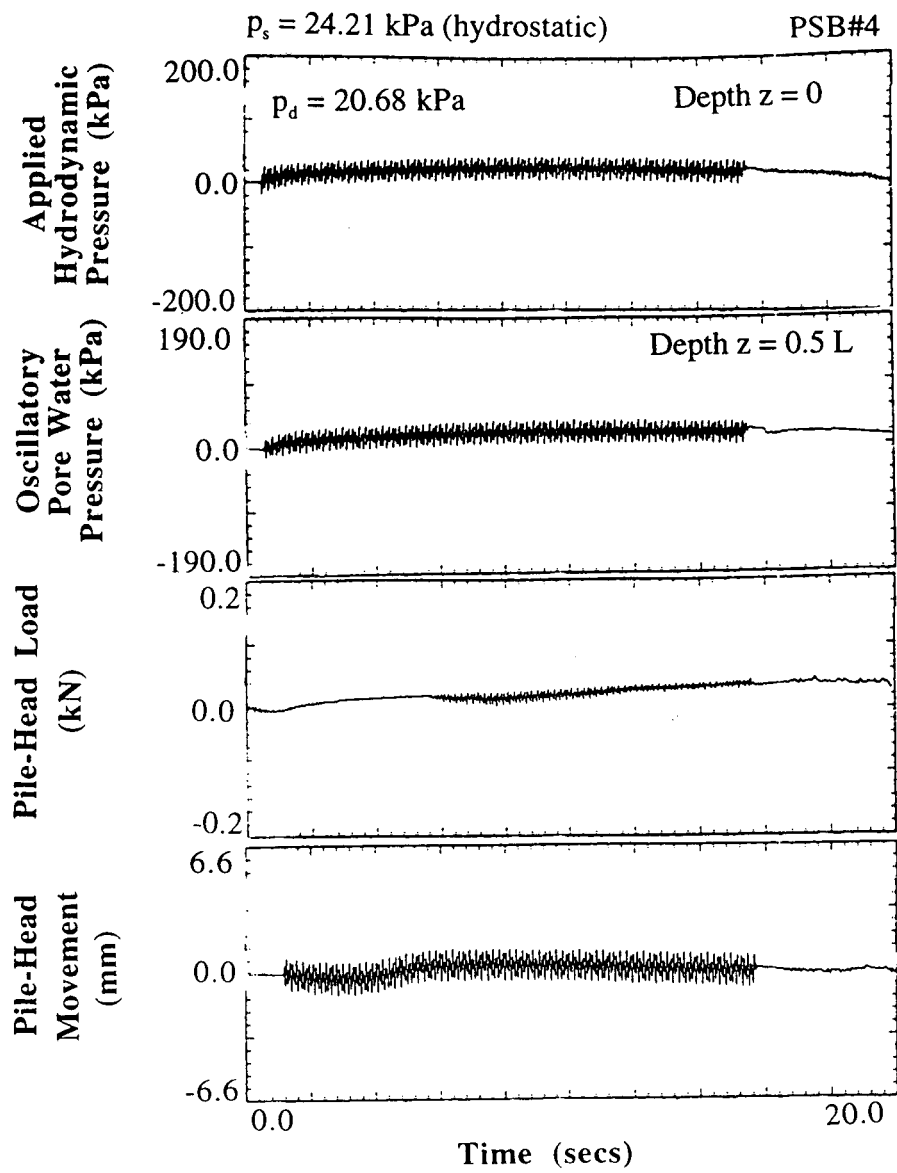
PSB#3

p_d @ $z = 0$

p_m @ $z = 0.5$ L

Fig. L.4: Time Window Illustrating Mechanism of Pile Response During Seaquake Loading With 20% Bias Loading at $\sigma'_m = 20$ kPa - PSB#3

Fig. L.5: Time History Measurements of Soil and Pile Response During Seaquake Loading Without Bias Load at σ'_m = 56 kPa - PSB#4
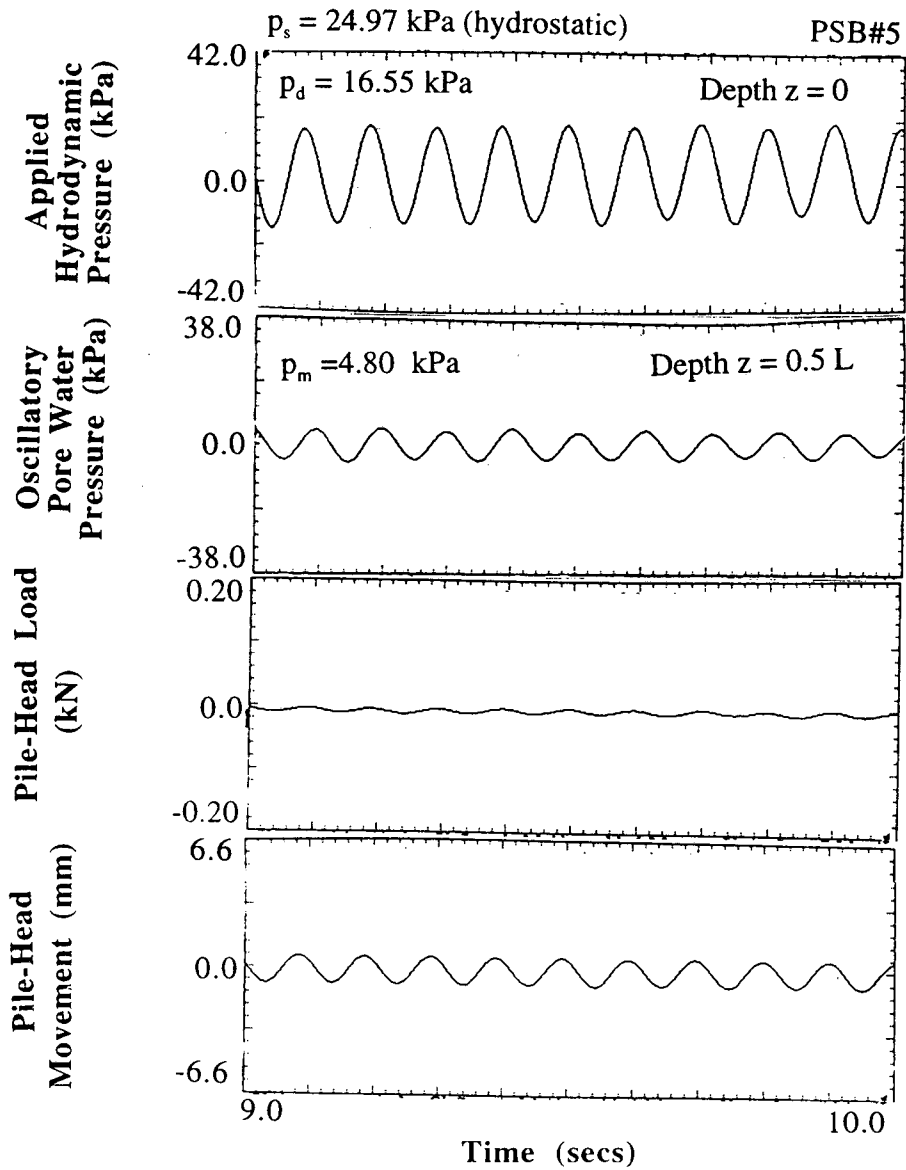
Fig. L.6: Time History Measurements of Soil and Pile Response During Seaquake Loading Without Bias Load at σ'_m = 112 kPa - PSB#5
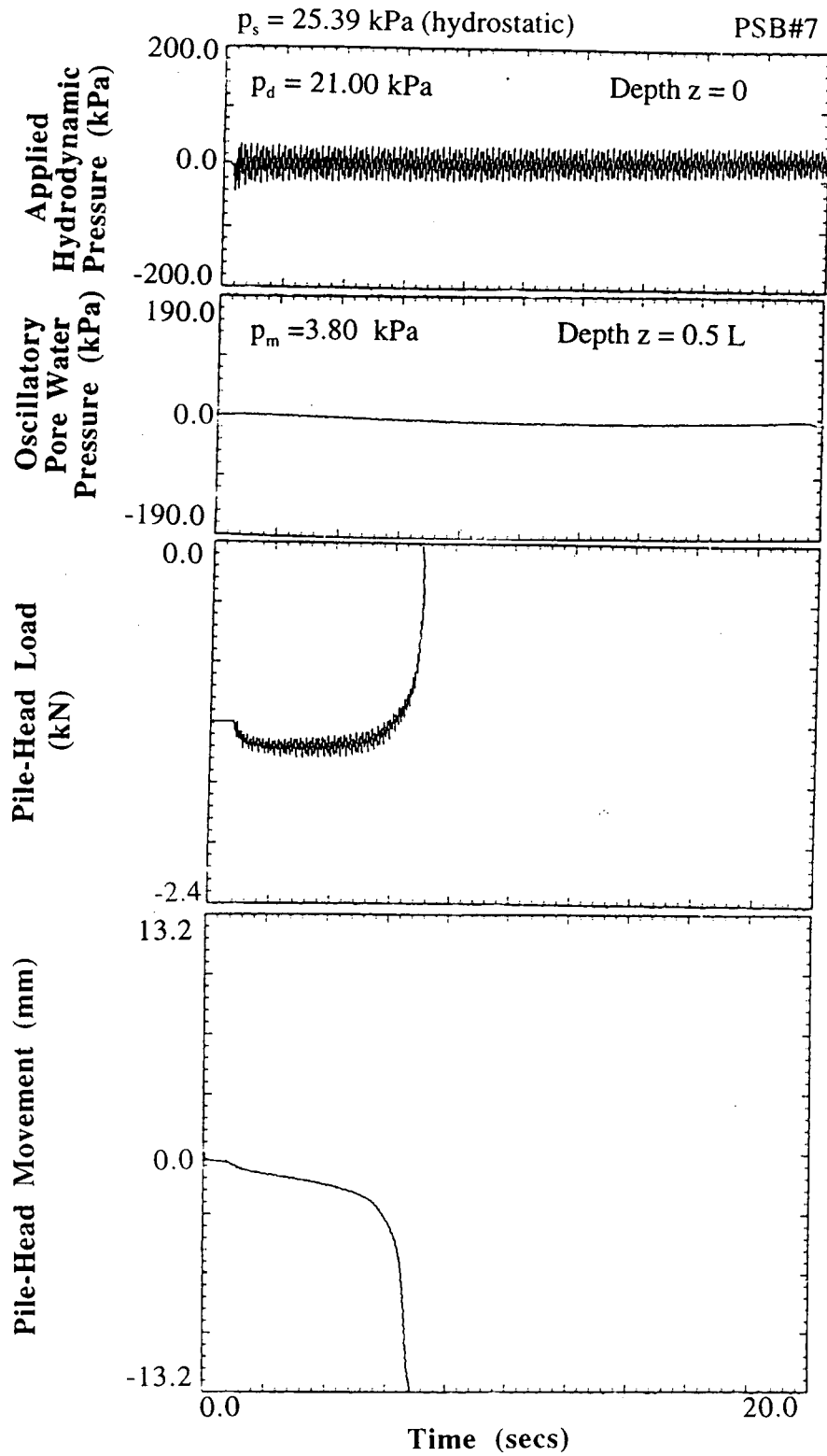
Fig. L.7:   Time History Measurements of Soil and Pile Response During Seaquake Loading With 65% Bias Loading at $\sigma'_m = 112$ kPa - PSB#7
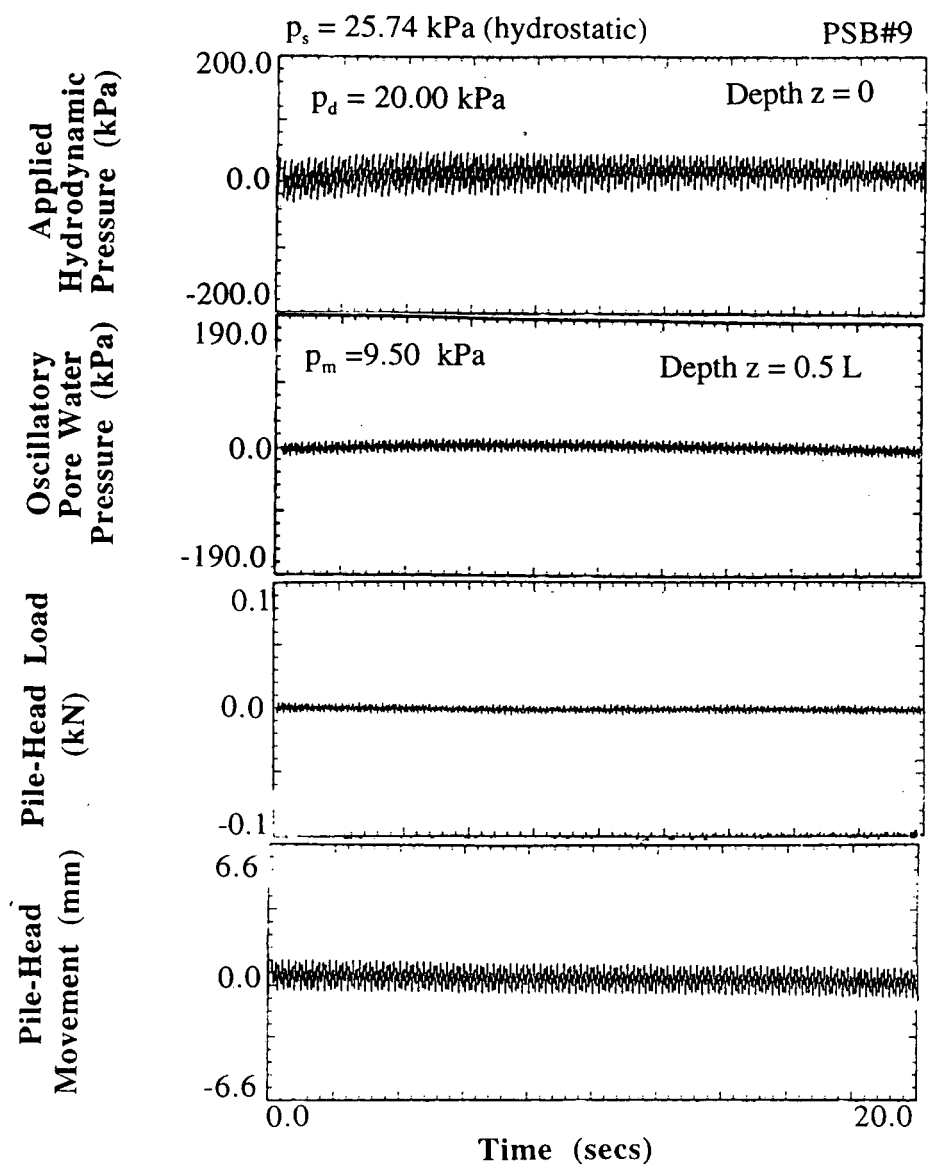
Fig. L.8: Time History Measurements of Soil and Pile Response During Seaquake Loading Without Bias Load at σ'_m = 56 kPa - PSB#9
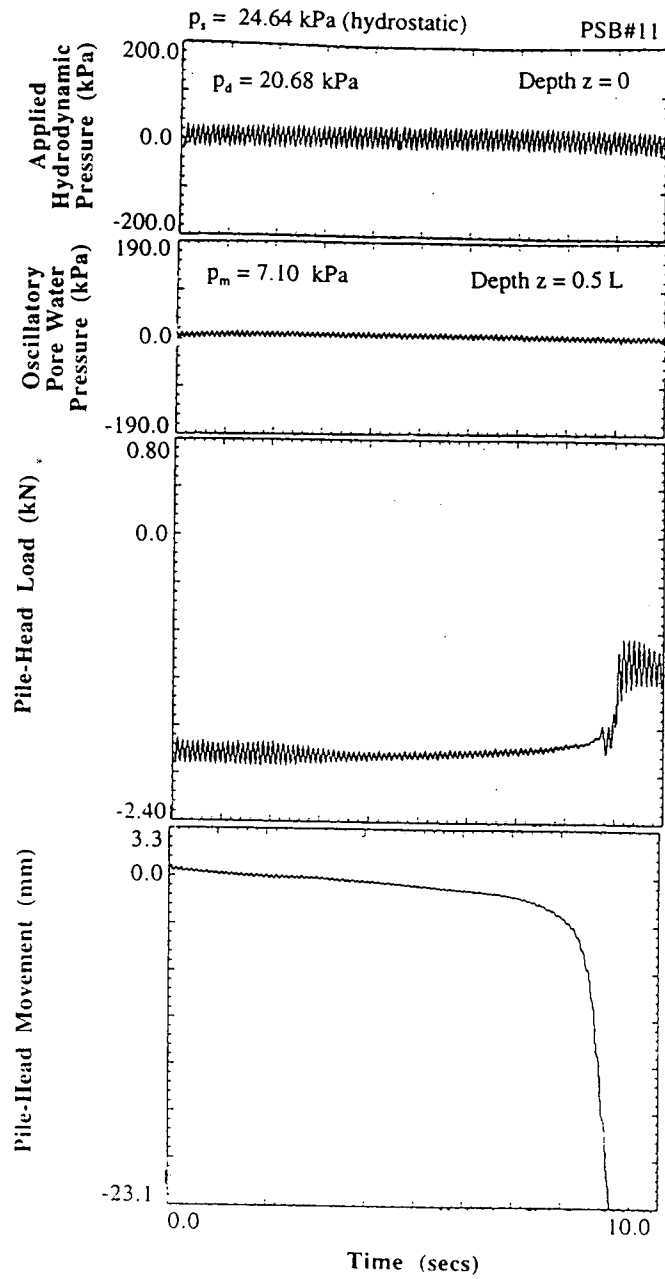
Fig. L.9: Time History Measurements of Soil and Pile Response During Seaquake Loading With 65% Bias Loading at σ'_m = 134 kPa - PSB#11